Ultrafast Optical Studies of Phonons and Phase Transitions in $Ge_2Sb_2Te_5$ thin films

Submitted by **Ashawaraya Shalini**, to the University of Exeter

as a thesis for the degree of Doctor of Philosophy in Physics,

June 2013.

I certify that all material in this thesis which is not my own work has been identified and that no material has previously been submitted and approved for the award of a degree by this or any other University.

.....

Abstract

This dissertation reports the results of optical studies of epitaxial (e), polycrystalline (p) and amorphous (a) $Ge_2Sb_2Te_5$ (GST) thin films. The dynamic properties of GST films in all three (e/p/a) phases were investigated by a time-resolved optical pump-probe technique in which a femtosecond pump pulse of 55 fs duration was used to excite the sample. The intensity and polarization of the reflected probe beam respectively provide information about the transient reflectance (R) and anisotropic reflectance (AR) induced in the sample, that in turn provide the information about the crystal structure, phonon spectrum, and ultimately phase transitions within the sample. The study of an epitaxial sample provides an opportunity to explore the character of the modes within the phonon spectrum.

The epitaxial GST film was grown upon a homoepitaxial layer of GaSb grown upon a GaSb wafer. We observed a 6.7 THz coherent optical phonon (COP) in GaSb(001). The dependence of the signal strength upon the pump and probe polarization was explained in terms of a model that considered both Transient stimulated Raman Scattering (TSRS) and the action of a Surface Space-Charge (SSC) field. The presence of the 6.7 THz transverse COP in the AR channel and its four fold dependence on pump and probe polarization suggests a three-dimensional T_2 character. The COP amplitude was maximum when the probe was polarized parallel to the cube edge (GaSb[100]) and the pump polarization was set parallel to a face diagonal (GaSb[110]). The results were fully understood using a microscopic model of selective bond breaking. The AR response of e-GST/GaSb(001) reveals the presence of a 3D 3.4 THz transverse optical phonon. The mode amplitude was independent of pump polarization indicating that the mode is excited by a SSC field. This SSC field could exist within the GST, if the distorted rock-salt structure of GST lacks inversion symmetry, or GaSb, which has the non-centrosymmetric zincblende structure, leading to impulsive excitation of phonons at the GST/GaSb interface. The mode in GST was inferred to be T_2-like. The observation of a T_2-like phonon mode confirms that GST is cubic in structure and challenges previous studies where 1D or 2D character was assigned to the 3.4 THz mode.

While pump-probe measurements displayed the presence of a 3D 3.4 THz mode in the AR response of e-GST/GaSb(001), a 4.5 THz mode was observed in both R and AR channels for p-GST(37 nm)/Si(001) and a-GST(57 nm)/Si(001). The mode character was identified

to be either of A or E type by comparing the frequency with frequencies reported in the literature. Additional Raman microscope measurements confirmed the presence of the modes observed in the pump-probe measurements and also revealed additional frequencies. The differences in the frequencies observed from the different samples are quite small suggesting the presence of similar bonds that are modified to some extent by the different structural environment found within each sample. After exposure to high pump fluence the original modes disappeared and were replaced by new modes with frequencies at 4.2 THz and 3.1 THz in e-GaSb, 4.2 THz in e-GST, 3.5 THz in p-GST and 3.6 THz in a-GST. The difference in the final frequencies observed for p and a-GST sample may result from the difference in stack structure affecting the time-dependent temperature profile in each sample.

The dependence of the temperature profile on the sample stack was understood from an experimental study of the phase transition between the amorphous and crystalline states induced by exposure to a series of amplified laser pulses. The dependence of the crystalline area and its reflectivity upon the number of pulses and fluence was described using a simple algebraic model. The results justify the assumption of one-dimensional heat flow. The growth velocity of the crystalline region was calculated to be 7-9 m/s.

Apparatus and methods were developed to extend the time-resolved optical studies described previously. Firstly, an apparatus was constructed for the measurement of the wavelength dependent sample reflectance with a white-light pulse. A reference arm was employed to allow normalization and hence removal of the intensity noise arising in the laser regenerative amplifier system. Secondly an electrical measurement apparatus was constructed to allow combined electro-optical measurements in future. Switching of GST vertical memory cells was successfully demonstrated. The cells were fabricated on a borosilicate substrate with TiW top and bottom electrodes. A DC voltage of 4.5 to 6 V was required to induce switching, while in pulsed measurements, the device demonstrated switching in response to a pulse with minimum duration of 100 ns.

Acknowledgements

This dissertation would not exist without the support of the kind and intellectual people around me, only some of whom it is possible to give particular mention here.

First of all, I would like to sincerely thank my Ph. D. supervisor Prof. Robert J. Hicken, who has the attitude and the substance of a genius. He has provided his timely remarks and guidance being its experiments, writing, presentations or discussion. I am grateful to him for giving me such great few years in research. This thesis would not have been possible without his motivation and persistent help.

I would like to thank Prof. G. P. Srivastava for his valuable discussions and suggestions regarding phonon interaction and Raman tensor properties. He has also done some theoretical calculations to generate the phonon dispersion curves that I have used in background chapter of my thesis. I would like to acknowledge with much appreciation the role of Dr Yanwei Liu for training me in optical alignment procedures. He has been a very active member for the set up and analysis of data, especially the fitting of anisotropic reflectance signal of e-GaSb and e-$Ge_2Sb_2Te_5$ films. The data produced in chapter 4 is a joint effort of Dr Yanwei Liu and myself.

I would also like to thank my group in Exeter. Thanks to Dr Uday Al Jarah for answering my questions and helping me in the lab. I have spent a lot of time with Uday sharing the lab and hayloft. He has been a great companion. Thanks to Mr Martin Simpson for his help in conducting electrical measurements in a short time. Thanks to Dr Leigh Shelford and Dr. Paul S Keatley for the critical reading of my chapters. I would thank Dr Prim Gangmei for his general Ph. D. advice. Thanks to Wei, Haidar and Reem for making this such an enjoyable place to work.

Thanks to all my mentors so far but special thanks to Dr. Manish Sharma (from IIT Delhi) for his help and motivation to do Ph. D.

Many thanks to my Parents Shiv Kumar Sharma and Susheela Sharma for their invaluable advice and emotional support. They have been the loveliest and most respected people on this earth. Thanks to my lovely sister Kirty for always standing by my side, and thanks to my brother Yash. I would also thanks to all my extended family members and friends for providing me the welcome distraction from my work.

Lastly thanks must go to my husband, Avinash Takale for his love and patience. More than anything I would thank him for handling the long distance (US-UK) relationship under a lot of social and work pressures that has meant many personal sacrifices. I would have never managed to finish this work without his support and understanding.

List of Contents

1. Introduction 22

2. Background 29

2.1 Crystal structure and Phonon properties 29

2.1.1 Lattice 29

2.1.3 Brillouin Zone 32

2.1.4 Crystal Structure 33

2.1.5 Group theory and Symmetry Operations 35

2.1.6 Phonons 39

2.1.7 Irreducible representations 41

2.1.8 Lattice dynamics of a linear chain 42

2.2 Non linear optics and Raman scattering 47

2.2.1 Introduction to optical processes at an interface 47

2.2.2 Linear optics 49

2.2.3 Non linear optics 52

2.2.4 Light Scattering 56

2.2.5 Macroscopic Theory of Inelastic Light Scattering by Phonons 58

2.2.6 Raman Tensor and Selection rules 61

2.2.7 Atomic displacement pattern: Phonon representation 64

2.3 Phase Change Materials 65

2.3.1 Storage principle 65

2.3.2 Structure and Resonant bonding 66

2.3.3 Non thermal melting 69

3. Experimental Technique 71

3.1 Introduction 71

3.2 Generalized Reflection Coefficients 72

3.3 Time resolved pump probe set up 77

3.4 Measuring spot size 79

3.5 Optical bridge detector 81

3.6 Rotation signal calculation 82

3.7 Lock-in amplifier....86
3.8 Typical AR signal....87
3.9 Fitting the experimental curve....89

4. Observation of T_2-like coherent optical phonons in epitaxial $Ge_2Sb_2Te_5$/GaSb(001) films....91

4.1 Introduction....91
4.2 Experimental Method: Optical Pump Probe....93
4.3 Results and Discussion....94
4.3.1 Reflectivity and Rotation Signal....94
4.3.2 Fitting time resolved R and AR measurements....96
4.3.3 Phonon characterization in GaSb....99
4.3.4 Theory of Transient Stimulated Raman Scattering (TSRS)....103
4.3.5 A microscopic model for the response of GaSb(001)....106
4.3.5 Fitting the dependence of the phonon amplitude and phase upon the pump polarization....111
4.3.7 Phonon characterization in GST /GaSb(001)....113
4.3.8 Effect of elevated pump fluence and phase transition....122
4.4 Conclusion....127

5. Coherent Phonons of Crystalline and Amorphous $Ge_2Sb_2Te_5$ thin films: a fingerprint of structure and bonding....128

5.1 Introduction....128
5.2 Sample details and experimental method....129
5.3 Results and discussion....130
5.3.1 Reflectance and Anisotropic Reflectance signal....130
5.3.2 Coherent optical phonons (COP)....133
5.3.3 Effect of high pump fluence....138
5.4 Conclusion....142

6. Crystallization of $Ge_2Sb_2Te_5$ films by amplified femtosecond optical pulses....144

6.1 Introduction....144
6.2 Experimental Method....145
6.2.1 Sample detail....145
6.2.2 Optical pump probe configuration for marks writing....146

6.2.3 Generation of longer pulses....147
6.3 Results and Discussion....148
6.3.1 Experimental Results....149
6.3.2 Mark area and laser fluence relation....157
6.3.3 Dependence of reflectance upon the fluence and number of pulses: Theoretical Model....159
6.4 Summary....171

7. Development of an optical set-up using white-light probe....173
7.1 Introduction: Motivation for a white-light probe....173
7.2 Jobin Yvon Spectrometer System....173
7.3 Laser System....175
7.4 Measurement Procedure....176
(i) Monochromator power up/Initialization....176
(ii) Image Acquisition....177
(iii) Spectral Acquisition....177
7.5 Alignment....178
7.6 Results....180
7.6.1 System Calibration....180
7.6.2 silver/silver reflectance spectra....181
7.6.3 Silver and gold spectra....183
7.6.4 White-light spectra Calibration: Gold/Silver (theory)....185
7.6.5 GST Spectra....188
7.6 Conclusion....190

8. Electrical testing of $Ge_2Sb_2Te_5$ vertical cells....191
8.1 Introduction....191
8.2 Sample fabrication....191
8.2.1 Phase change memory cell....192
8.2.2 Device fabrication....193
8.3 High frequency measurements: Theory....199
8.3.1 Characteristic Impedance of an electrical transmission line....199
8.3.2 The load effect....201
8.3.3 Coaxial cable....204
8.4 Building the electrical test set up....205

8.4.1 DC set up 206
8.4.2 DC set up with an external resistor 208
8.4.3 Pulsed measurement set up 210
8.5 Conclusion 213

Chapter 9 Summary and Future work 214
9.1 Summary 214
9.2 Future work 219
9.2.1 pump probe measurements on an e-GST(111) surface 219
9.2.2 Extension of white-light probe set up 220
9.2.3 Electrical testing using impedance matching network 220

Appendix 1 Fitting the time resolved reflectance and anisotropic reflectance data 221

Appendix 2 Mode Calculations for epitaxial $Ge_2Sb_2Te_5$(111) surface 226

Bibliography 229

List of Figures

Figure 2.1: A conventional unit cell for the fcc lattice 30

Figure 2.2: (a) fcc crystal structure with primitive cell (b) the reciprocal lattice of fcc structure 33

Figure 2.3: rocksalt structure: the conventional unit cell of the rocksalt structure, which has a fcc lattice with two basis atoms Na and Cl.....34

Figure 2.4: Conventional unit cells of (a) the diamond and (b) the zincblende crystal structure 35

Figure 2.5: The carbon atoms along the [111] direction in diamond.....38

Figure 2.6: Phonons: optical and acoustic vibrations in (a) the longitudinal and (b) the transverse direction.....40

Figure 2.7: Phonon dispersion curve in GaSb along [001] direction in the Brillouin zone.....44

Figure 2.8: Phonon dispersion curves for (a) Ge and (b) PbTe. 45

Figure 2.9: Various optical processes that occur at an interface.....48

Figure 2.10: Graphical representation of non-linear optics……..... 51

Figure 2.11: Energy level diagram for Rayleigh and Raman scattering 57

Figure 2.12: Schematic demonstration of the Raman effect for a diatomic molecule.....58

Figure 2.13: The Raman spectrum consists of a Stokes and anti-Stokes line.....61

Figure 2.14: Typical I-V curve for crystalline and amorphous $Ge_2Sb_2Te_5$.....66

Figure 2.15: Changing Ge coordination during the crystalline to amorphous phase transition 68

Figure 2.16: Schematic diagram demonstrating the origin of resonance bonding for Sb.....69

Figure 3.1: p and s-components of the incident, reflected and transmitted light at an interface....73

Figure 3.2: The schematic diagram displaying rotation θ and ellipticity ε in the reflected light from a sample....76

Figure 3.3: The typical set up of time resolved optical pump probe experiments....78

Figure 3.4: Beam profiler images of pump and probe spots and their overlap....81

Figure 3.5: Schematic diagram of polarizing beam splitter....82

Figure 3.6: The detection of the difference signal from optical bridge detector....83

Figure 3.7: Block diagram of a lock-in amplifier....87

Figure 3.8: Transient Rotation (or Anisotropic reflectance signal):....89

Figure 4.1: Typical time resolved (a) R, (b) AR signals for GST/GaSb(001) and (c) R, (d) AR signals of GaSb(001) with the pump and probe electric fields aligned parallel to the [110] and [100] axes respectively....95

Figure 4.2: Dependence of frequency, amplitude and phase of phonon oscillations in GaSb upon the orientation of the pump and probe electric fields....101

Figure 4.3: Dependence of the amplitude of slow transient upon the orientation of the pump and probe electric fields....101

Figure 4.4: Zincblende crystal structure of GaSb in (a) 3 dimensions and (b) viewed along the [001] axis....108

Figure 4.5: Dependence of the amplitude and phase of the 3.4 THz mode observed in GST/GaSb(001)....114

Figure 4.6: Variation of features of the AR signal from the GST/GaSb(001) sample as the pump and probe polarization was varied....116

Figure 4.7: The dependence of transient AR signal upon orientation of the GST/GaSb(001) sample. 118

Figure 4.8: (a) Unit cell of ideal rock-salt structure to understand the phonons origin in GST. 121

Figure 4.9: Power spectra obtained from AR and R signals measured with a pump fluence of 0.42 mJ/cm^2 123

Figure 4.10: Effect of elevated pump fluence upon the transient R and AR signals obtained from GaSb(001). 125

Figure 4.11: Effect of elevated pump fluence upon the transient R and AR signals obtained from GST/GaSb(001) 126

Figure 5.1: Sample stack: (a) for epitaxial (b) polycrystalline and (c) amorphous GST films with 225 composition 129

Figure 5.2: Typical pump probe signals of e-/p-/a-GST films. 132

Figure 5.3: Raman spectra for e-/p-/a-GST samples 135

Figure 5.4: The peak fitting of the FFT power spectrum of the AR signal for the polycrystalline GST sample 136

Figure 5.5: (a) The multipeak fitting of the Raman spectrum of the e-GST/GaSb(001) sample. (b) The spectrum in panel (a) is zoomed in to show the fitting of GST signal at lower wavenumbers. 137

Figure 5.6: Effect of pump fluence on transient AR and R signal in p-GST 140

Figure 5.7: Effect of high pump fluence on transient AR and R signal in a-GST 141

Figure 5.8: The peak fitting of the FFT power spectrum of the R signal obtained after exposure of the a-GST sample to higher fluence and rescanning at low pump fluence 142

Figure 6.1: Sample stack: GST 20 nm sputter deposited on a Si substrate with different thicknesses of ZnS-SiO_2 for the underlayer and capping layer. 145

Figure 6. 2: Experimental set up: the pump-probe configuration is shown. Pump and probe beam are focused onto the sample in the focal plane of the optical microscope..... 146

Figure 6.3: Set up using electro-optic modulator to generate ns pulses..... 148

Figure 6.4: Single pulse excitation: Microscopic images obtained after excitation by a 60 fs pulse for different pump fluence.. 149

Figure 6.5: 2000 pulse excitation: Microscopic images obtained after excitation by 2000 pulses of 60 fs duration. 150

Figure 6.6: Dependence of Reflectivity and Area of crystalline mark upon increasing fluences:..... 152

Figure 6.7: Microscope images for varaible number of pulses and F_{avg}: obtained after excitation by 200 pulses (far left) of 60 fs duration with an increment of 50 pulses for each successive mark until 600 pulses (far right). F_{avg} is fixed in each row (labeled)..... 154

Figure 6.8: Dependence of Reflectivity and Area of crystalline mark upon increasing number of pulses. 155

Figure 6.9: Reversible transition between crystalline and amophous phases. 156

Figure 6.10: Equation (6.7) has been used to calculate the dependence of mark area upon the number of pulses for different fluences used within the experiments. 160

Figure 6.11: The dependence of mark area upon number of pulses has been calculated from equation (6.10) for different fluences used within the experiments. 161

Figure 6.12: Flow chart for the Crystallization model: representing the process of calculating the optical parameters after every successive laser pulse 163

Figure 6.13: Transient temperature distributions: calculated using the analytical model for F_{avg} = 2.33 mJ/cm^2 and a pulse duration of 60 fs. 164

Figure 6.14: Area (a) and reflectivity (b) of crystallize mark calculated using the analytical model for increasing fluence. 165

Figure 6.15: Area (a) and reflectivity (b) of the crystallized mark calculated using the analytical model for increasing number of pulses applied. 166

Figure 6.16: Calculated average fluence F_{avg} (for a single laser pulse) required to induce melting at the centre of the irradiated region at increasing depths within the GST layer for different crystalline volume fractions. 167

Figure 6.17: Growth of the crystalline material from the inner perimeter and central region of the annular rings with increasing pulse number. 169

Figure 6.18: Measurements of the inner diameters of the annuli in Figure 6.7 for two fluences as functions of increasing laser pulse number. 170

Figure 6.19: Effect of fluence and number of pulses on crystalline area. 171

Figure 7.1: Optical design of iHR 320 174

Figure 7.2: White light generator assembly 175

Figure 7.3: LabView panel for the initialization of the monochromator 176

Figure 7.4: Image acquisition of reflected probe beams 177

Figure 7.5: Spectral acquisition of reflected probe beams using LabView program 178

Figure 7. 6: Alignment of white light probe beam to measure the reflectance spectra of the sample 179

Figure 7. 7: Mercury spectral lines 181

Figure 7. 8: Image acquisition of reflected beams 182

Figure 7.9: (a) Intensity spectra of reflected beams (b) Intensity ratio of two beams 183

Figure 7.10: (a): Image acquisition for gold and silver mirror 184

Figure 7.11: Ratio of gold/silver reflectance spectra obtained from the experiment, calculations, and manufacturer's data 188

Figure 7.12: Intensity spectra for (a) GST and (b) Silver mirror 189

Figure 7.13: (a) Normalized reflactance spectra of GST and (b) Image acquisition for GST and silver mirror 189

Figure 8.1: Structure of a GST memory cell. The vertical line cell is sandwiched between a TiW top and bottom electrode. 192

Figure 8.2**:** The steps for the contact photolithography and lift-off process. 198

Figure 8.3**:** (a) Optical microscope image of bottom electrode; (b) reflection and (c) transmission microscopy images of the top electrode. 198

Figure 8.4: Equivalent circuit of a unit length of transmission line. 200

Figure 8.5: Reflection of an electrical pulse from an open circuit. 202

Figure 8.6: The reflection of an electrical pulse from a short circuit. 203

Figure 8.7: DC test set up to switch the memory cells 206

Figure 8.8: The device current is plotted with respect to applied dc voltage 207

Figure 8.9: DC test set up with an external resistor 208

Figure 8.10: (a) plots the device current and (b) device voltage against the applied voltage 209

Figure 8.11: Test set up to perform pulsed measurements 210

Figure 8.12: (a) Scope response for an applied pulse and (b) Equivalent circuit for 200 kΩ external resistor 212

,

Figure A.1: Crystal directions for an epitaxial GST(111) sample. **E** represents the pump electric field in (111) plane at an angle φto the x-axis. 226

List of Tables

Table 2.1: Notation for irreducible representations of T_d point group…… 42

Table 4.1: Parameter values obtained by fitting equation 1 to example R and AR signals from the GaSb and GaSb/GST samples……....99

Table 5.1: Comparison of pump-probe and Raman frequencies……135

Table A.1: Observability of phonon modes for various orientations of crystals of T_d (and O_h) point group symmetry……..228

Declaration

Chapter 2. Background

This chapter introduces the physics required to understand and explain the experimental results. This chapter is compiled by me, and the relevant authors, text and figures are clearly referenced.

Chapter 3. Experimental Technique

This chapter explains about the optical pump-probe technique in detail. The set up was established before I started my PhD project. The alignment in the pump-probe technique was a joint effort of Dr. Yanwei Liu and myself.

Chapter 4. Observation of T2 modes in epitaxial GST/GaSb(001)

The samples studied in this chapter were provided by Mr Wolfgang Braun of the Paul Drude Institute, Berlin. Dr. Yanwei Liu and I performed the measurements on epitaxial GaSb. The epitaxial GST sample was measured by myself using a s-polarized probe. The discussion and data analysis was shared between us. However the fitting of the anisotropic reflectance signal on both the samples was performed by Dr. Yanwei Liu. The results of this chapter are explained using the TSRS mechanism provided by Merlin's theory and the SSC mechanism given by Cho. The work of these authors is referenced throughout the chapter.

Chapter 5. Comparison of crystalline and amorphous phases of GST

The measurements on p/a-GST were carried out by me in the same experimental conditions as for the other two samples of chapter 4. p-GST/Si(001) and a-GST/Si(001) samples were provided by Mr Andrew Pauza from Data Storage solution, UK. The pump-probe data analysis was done by myself and compared with the previous studies from Forst and Hase.

The Raman measurements on these samples were performed with the help of Mrs Ellen Green. She handles the micro-Raman set up in the biophysics lab in Exeter.

Chapter 6. Crystallization of amorphous GST using amplified fs pulses

This chapter explains the phase-transition mechanism for the phase transition between amorphous and crystalline state, using amplified pulses of variable fluences. The experiment was primarily set up by Dr. Yanwei Liu. The crystallization mark using a different number of pulses and fluences were made by Dr. Yanwei Liu and myself. The simple algebraic model to explain the dependence of crystallized mark and reflectivity on number of fluence was generated by Prof. Rob Hicken. A detailed theoretical model was presented by Dr. Mustafa considering the crystallization kinetics, thermal transport and optical absorption. The results of the above two models were in good agreement with the experimental data.

Chapter 7. White-light test set up

This set up was built and tested by myself using two well-known metals.

Chapter 8. Electrical testing of GST vertical cells

The vertical memory cells of GST were fabricated with the help of Dr. Behrad Gholipur at the Optoelectronic Research Centre in Southampton. The electrical testing of these cells was carried out at Exeter. Mr Martin Simpson from the Engineering department helped to conduct the electrical measurements.

Appendix

The derivation for the fitting function was provided by Prof Rob Hicken.

My supervisor Prof Rob Hicken has contributed to every part of this thesis.

For my Parents and husband

without whom I would not be here.

Chapter 1

Introduction

The study of condensed matter is one of the richest and most important fields of study in Physics. In solids, the atoms, molecules or ions, if arranged in a regular way, form crystals. Many researchers have invested great effort in studying their various properties, such as mechanical, chemical reactivity, crystal structure and electrical properties. The optical properties of solids have also drawn a lot of attention. First, the standard laws of reflection and refraction of light generated by conventional light sources were founded. Later, the invention of the laser in 1961 [1], provided a completely new dimension to the analysis of the optical properties of materials. After the invention of ultrafast lasers in 1976 [2], with pulses of duration shorter than the time scale of ionic motion in materials and associated high electric-field intensities, there has been rapid technological development in this field. Femtosecond lasers have made a significant contribution to the study of non-linear optics (NLO) and laser-induced phase transitions. NLO has received thorough investigation with the observation of many effects in different materials. Today NLO has become an important tool in the study of thin films.

Femtosecond lasers have improved the details with which a material's optical properties may be characterized. The principal feature of the femtosecond (fs) laser is the short pulse width (down to five femtoseconds) [3]. These short optical pulses allow the observation of a material's dynamics with a much better time resolution, almost 1000 or 10000 times shorter, than that provided by any other experimental technique. Therefore, the scientist can now study many important processes, such as carrier-carrier interactions and energy

transfer from electrons to the lattice in solids [4]. The applications of femtosecond lasers are not only limited to physics, but are also widely used in the fields of chemistry and biology, e.g. in chemical reactions in gases [5] and the temporal progression of luminescence in biological cells.

A material required for a specific application can be thoroughly studied by investigating its fundamental properties, such as its optical, electronic and structural behaviour, in equilibrium and in a temporarily excited physical state. The various processes in a solid, excited to a non-equilibrium transient state, occur on time scales starting from a few femtoseconds (10^{-15} s). These processes include excitation and relaxation of electron-hole pairs, redistribution of electrons, lattice vibrations, and rearrangement of atoms etc in the transient physical state. Processes that occur on such short time scales cannot be studied by electronic measurement techniques. However, electromagnetic radiation in the form of ultrashort pulses enables one to study the electron and lattice dynamics almost "instantly". Femtosecond lasers successfully probe the dynamics of the excited state with high temporal resolution. This is successfully achieved by using the complicated yet popular optical pump-probe technique. The full-width-half-maximum (FWHM) pulse duration for commercial lasers, $\tau_{pulse} \approx$ 12-50 fs, determines the temporal resolution of the technique.

Despite having a modest total energy, femtosecond lasers can produce a huge amount of peak power. This is the second important characteristic of femtosecond lasers. Since the laser pulses squeeze the energy into short time packets, femtosecond lasers can deliver a greater power density than a nanosecond laser with the same total energy. For example a pulse of 1 mJ energy with 10 ns duration provides a peak power of 0.1 MW whereas the same pulse energy with 100 fs duration gives 10 GW of peak power, 10^5 times higher. In our experiments, we use pulses that have ~50 fs duration and up to 5 μJ of energy, giving a peak power of 0.1 GW. Therefore, a femtosecond pulse, while carrying 1000 times less energy than a flying butterfly, is able to achieve a peak power more comparable to the electric power demand of a small country [6]. Or viewed another way, the electric field of a short pulse is millions of times greater than the field with which the nucleus of an atom attracts its electrons. Therefore such short pulses have energies high enough to manipulate the fundamental properties of matter. When an ultrashort pulse with small energy is focused to a tiny spot, it is capable of generating an electron-hole plasma in any material

almost instantaneously. It then becomes possible to precisely machine materials with ultrashort pulses of such small energy that they do not cause heat damage to the regions surrounding the cut. Such a capability can be applied in material processing and laser surgery [7].

Additionally, these short laser pulses may be used to induce a non-thermal melting process. If an ultrashort pulse with a pulse duration shorter than the phonon emission time [8] is applied to the material, it immediately excites the electrons to a much higher temperature than the rest of the lattice. This leads to bond softening and destabilization of the lattice due to the generation of electron-hole pairs and finally results in what is called non-thermal melting. This unique non-equilibrium state is achieved by excitation of at least 10% of the valence electrons. This process has been confirmed theoretically with a lower limit of carrier density of approximately 10^{22} carriers/cm^3 [9,10]. The non-thermal phase transition is also known as ultrafast melting (UF melting) [10]. However, it is still not clear whether the metastable transient phase achieved by strong electronic excitation can lead to a final structural change. After a few femtoseconds, the electrons transfer their energy to the lattice by carrier-carrier and carrier-phonon interactions, followed by a thermal structural transition on a longer time scale.

Several materials, such as silicon [11-13], gallium arsenide [13-15], indium antimonide [16], aluminium [17] and diamond [18], have been observed to undergo a non-thermal phase transition. But no non-thermal effect has been reported yet in phase-change materials such as $Ge_2Sb_2Te_5$ (GST). These chalcogenide-based phase change alloys are a key component for the memory device industry because, first, they can be used to construct devices that are non-volatile in nature (i.e these devices retain data when the power is interrupted) and second, these alloys have two stable phases (crystalline and amorphous) which can be reversed with the application of laser pulses of different fluences. It requires pulses of tens of nanoseconds duration to accomplish amorphization (WRITE or RESET) or crystallization (ERASE or SET) operations in existing optical phase-change products. Recently however, there have been many studies of the phase-transition mechanism in data-storage materials with fs laser sources [19-22]. In this thesis, femtosecond laser pulses are used to understand excited carrier and phonon dynamics that could result in a non-

thermal transition [23] followed by a structural transformation, in three different phases of GST.

In this context, it is important to establish a clear difference between a classical thermal process and electronic excitation induced non-thermal phenomena. A transition induced by a picosecond or nanosecond laser is thermal whereas femtosecond lasers can induce non-thermal transitions which become thermal on longer time scales. Recently it has been reported [24] that a significantly smaller energy fluence is required to induce crystallization in GeSb with pulses shorter than a picosecond.

In this thesis, femtosecond optical measurement techniques are used to investigate the carrier dynamics prior to the phase transition in GST. The response of the alloy to optical pulses of different polarizations is explored. These measurements probe the optically-induced birefringence, for various orientations of the pump and probe electric field, in what is known as the specular optical Kerr effect (SOKE). The observation of electron dynamics and the behaviour of optical phonons on femtosecond time scales can provide information about the non-thermal nature of the transition process. Characterization of properties of the phonon, such as frequency, amplitude and relaxation time, can help determine structural properties of the GST material, while large-amplitude phonons can also be considered as a precursor to the phase transition itself.

Over the past decade, the optical pump-probe technique has proved to be a powerful tool for the investigation of ultrafast dynamics in novel materials. The principle of the pump-probe experiment is the following. The beam of laser pulses is split into two parts known as the pump and probe beams. First, the pump beam is aligned to hit the sample under investigation and generate some kind of excitation. The probe beam is then used to measure the state of the sample. The probe beam passes along a variable optical delay line so that it can arrive at the sample before, with, or after the pump laser pulse. The intensity and polarisation rotation of the reflected probe beam are recorded. By measuring the probe signal with respect to time delay, it is possible to explore with high temporal resolution the processes induced by the pump beam.

In this thesis, I present the results of several experiments that have been performed in order to characterize the very popular phase-change material $Ge_2Sb_2Te_5$ (GST). The primary focus of my research work is to investigate the non-thermal behaviour of GST using the time-resolved pump probe technique. The purpose is to study the excitation of optical phonons and charge carriers at short time scales in different phases of GST. I have spent most of my time (2+ years) on this experiment and its associated analysis. However, I have also worked on other related projects to understand the behaviour of GST material in detail, namely the phase transition between the amorphous and crystalline phases of GST by amplified femtosecond pulses of varying pump fluence, the spectral response of GST detected with a white-light probe pulse, and electrical switching in vertical GST cells.

Chapter 2 explains the crystal structure and phonon properties relevant to this thesis. Group theory and allowed symmetry operations of the zinc blende and rock salt structures are discussed to understand the Raman active modes at the zone centre. The macroscopic theory of inelastic light scattering is presented to understand the Raman tensors and their selection rules. A brief introduction to linear optics is provided which is then extended to explain non-linear phenomena and in particular the SOKE effect. The final section covers the structure of GST and the principles by which it can be used to store data. Resonant bonding is discussed to identify the coordination number difference in the crystalline and amorphous phases of GST. An introduction to non-thermal melting is provided at the end. This chapter provides an extensive background review. However the literature of most immediate relevance will also be discussed at the beginning of each chapter in which experimental results are presented.

In Chapter 3, the experimental set-up of the time-resolved pump-probe technique is described. The chapter begins with an introduction of anisotropic materials, which have different permittivity values along the ordinary and extraordinary ray directions. The expressions for the reflection coefficients reflected from a uniaxial material are given. The measurement of optical rotation and ellipticity is described in terms of the optical reflection coefficients, followed by details of the optical bridge detector, which contains a polarizing beam splitter and two photodiodes orthogonal to each other. It is then mathematically proven that the difference of photodiode signals is proportional to the rotation of the incident polarization.

Chapter 4 presents the time-resolved pump probe measurements of the reflectivity and anisotropic reflectivity of an epitaxial $Ge_2Sb_2Te_5$/GaSb(001) sample using 800 nm wavelength, 55 fs pulses. The excitation of coherent optical phonons (COP) and charge carriers on few femtosecond time scales is studied to understand the possible non-thermal nature of the phase change process. The response of the alloy to optical pulses of different polarizations is described. This chapter also presents an additional study performed on an epitaxial GaSb(001) film to determined the substrate contribution to the signal from the epitaxial GST sample. A theory due to Merlin [25], which explains phonon generation by impulsive and displacive mechanisms, is described in detail. The theory is applied to zincblende and rock salt structures indicating the presence of T_2 phonons in GST and GaSb. A microscopic model is also presented which explains the four-fold behaviour of the COP and optically-induced linear birefringence for different pump and probe polarization angles. Finally, the behaviour of the materials at high pump fluence is also examined.

In chapter 6, the crystalline-to-amorphous structural phase transition induced in GST by exposure to amplified pulses is described. The description of the area of the mark and its reflectivity with respect to the applied pump fluence is explained in detail. The results strongly support a simple algebraic model which claims that thermal transport within the sample is purely vertical. A detailed theoretical model is presented in this chapter in which consideration of the heat flow, crystallization kinetics and effective medium theory leads to a growth of optical reflectivity and mark area that is in good agreement with our experimental results.

Chapter 7 describes an experimental method in which a white-light probe pulse may in future be used in a time-resolved pump probe set up. The idea is to use two probe beams, where one can measure the sample excitation and the other can be used as a reference. This chapter explains the step-by-step procedure of setting up the alignment. Gold and silver mirrors were used to verify the system functionality since the spectral response for these two metals is well known.

Chapter 8 explains the principles of high-frequency measurements of electrical switching in GST memory cells. The fabrication of GST vertical cells is also described. The GST

cells have demonstrated successful DC switching at a voltage between 4.5 to 6V. The set up was also used to demonstrate switching by pulses with a minimum duration of 100 ns. However, the programming current could not be measured due to impedance mismatch problems.

Chapter 2

Background

In this section, I explain the concept of the direct and reciprocal lattice, the Brillouin zone, and the crystal structure. I describe the face-centred cubic and zincblende structures in detail since these are of most direct relevance to the discussion of the experimental results that will be presented later in the thesis. Information about their symmetry operations and phonon dispersion curves is also presented. In the following section, I also present background about the various scattering processes and allowed modes in Raman scattering, which are again specific to the structure of the sample. A brief section on phase-change materials and their phase transitions is presented.

2.1 Crystal structure and Phonon properties

2.1.1 Lattice

A lattice is defined as an infinite regular arrangement of points with identical surroundings. The position vector of any point in three-dimensional lattice is defined in terms of the translational vector **T**, from a chosen lattice point. If $\mathbf{a}_1$, $\mathbf{a}_2$, and $\mathbf{a}_3$ are three independent primitive translation vectors, then **T** is written as [26],

$$\mathbf{T} = n_1\mathbf{a}_1 + n_2\mathbf{a}_2 + n_3\mathbf{a}_3 ,$$

----------(2.1)

where n_1, n_2 and n_3 are any integers. The region formed by these three primitive vectors is known as a primitive unit cell, which contains only one lattice point. Since the lattice points have identical surroundings, the whole space can be generated by translation of the primitive unit cell. A region that contains more than one lattice point cannot be a primitive unit cell. A total of 14 distinct types of three-dimensional lattice can be realized, known as Bravais lattices, which are grouped into seven lattice systems. Out of the seven systems, the cubic lattice system is characterized by $a_1 = a_2 = a_3$ and $\hat{\mathbf{a}}_1 . \hat{\mathbf{a}}_2 = \hat{\mathbf{a}}_2 . \hat{\mathbf{a}}_3 = \hat{\mathbf{a}}_3 . \hat{\mathbf{a}}_1 = 0$. There are three different lattice types within this system known as simple cubic (sc), face-centred cubic (fcc) and body-centred cubic (bcc). We will only consider the fcc lattice in this chapter.

Figure 2.1 shows the conventional unit cell for the fcc structure, where a is the side of the conventional unit cell known as the cubic lattice constant.

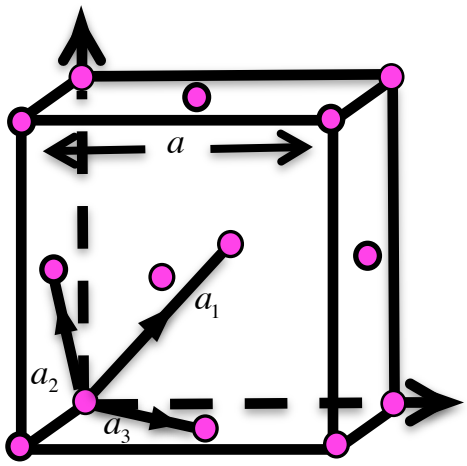

Figure 2.1: fcc: A conventional unit cell for the fcc lattice with 8 lattice points at the corner of the cell and 6 lattice points located at the center of each face. a_1, a_2, and a_3 represent the primitive lattice vectors

Therefore, the primitive lattice vectors for the fcc lattice are defined as

$$\mathbf{a}_1 = \frac{a}{2}(0,1,1),$$

$$\mathbf{a}_2 = \frac{a}{2}(1,0,1),$$

$$\mathbf{a}_3 = \frac{a}{2}(1,1,0),$$

----------(2.2)

And the volume of the primitive unit cell is

$$\Omega = |\mathbf{a}_1.(\mathbf{a}_2 \times \mathbf{a}_3)| = {a^3}/{4}\,.$$

----------(2.3)

The conventional unit cell for the simple cubic (sc) lattice is a unit primitive cell. However, the body-centered cubic (bcc) and face-centered cubic (fcc) lattices have more than one lattice point in the conventional cells and therefore are not primitive.

2.1.2 Reciprocal Lattice

The reciprocal lattice vectors **G** of a three-dimensional direct lattice are defined by the following relationship:

$$\mathbf{exp}(\mathbf{iG}.\mathbf{T}) = \mathbf{1} \quad .$$

----------(2.4)

The reciprocal lattice vectors have the dimension of [1/length]. The reciprocal lattice is important for the study of crystalline solids. The space generated by the reciprocal lattice points is called the reciprocal space (or **G**-space or momentum space). The reciprocal lattice vectors may be written in the form

$$\mathbf{G} = m_1\mathbf{b}_1 + m_2\mathbf{b}_2 + m_3\mathbf{b}_3\,,$$

----------(2.5)

where m_1, m_2 and m_3 are any integers and $\mathbf{b}_1, \mathbf{b}_2$ and $\mathbf{b}_3$ are the primitive lattice vectors of the reciprocal lattice, which may be defined in terms of the primitive lattice vectors of the direct lattice as follows:

$$\mathbf{b}_1 = \frac{2\pi}{\Omega}(\mathbf{a}_2 \times \mathbf{a}_3)\,,$$

$$\mathbf{b}_2 = \frac{2\pi}{\Omega}(\mathbf{a}_3 \times \mathbf{a}_1)\,,$$

$$\mathbf{b}_3 = \frac{2\pi}{\Omega}\,(\mathbf{a}_1 \times \mathbf{a}_2)\,,$$

----------(2.6)

where as described before Ω is the volume of the primitive unit cell of the direct lattice. The volume of the primitive unit cell of the reciprocal lattice is defined as

$$\Omega_{\mathrm{rl}} = |\mathbf{b}_1 \,.\, (\mathbf{b}_2 \times \mathbf{b}_3)| = {}^{(2\pi)^3}/_{\Omega}\,.$$

----------(2.7)

Now using equations (2.2) and (2.6), the primitive lattice vectors of the fcc reciprocal lattice are

$$\mathbf{b}_1 = \frac{2\pi}{\mathrm{a}}\,(-1,1,1)\,,$$

$$\mathbf{b}_2 = \frac{2\pi}{\mathrm{a}}\,(1,-1,1)\,,$$

$$\mathbf{b}_3 = \frac{2\pi}{\mathrm{a}}\,(1,1,-1)$$

----------(2.8)

The volume of the primitive unit cell defined by vectors $\mathbf{b}_1, \mathbf{b}_2$ and $\mathbf{b}_3$ in reciprocal space is

$$\Omega_{\mathrm{rl}} = 4\,({}^{2\pi}/_{\mathrm{a}})^3\,.$$

----------(2.9)

It is interesting to note that the reciprocal lattice of the fcc direct space lattice is itself a bcc lattice.

2.1.3 Brillouin Zone

A primitive cell has a volume equal to the Wigner-Seitz cell, which is constructed as follows: choose a lattice point and draw lines joining all nearby points. Construct perpendicular planes bisecting these planes. The smallest volume enclosed in this way is called the Wigner-Seitz (W-S) cell. The W-S cell of the reciprocal lattice is known as the first Brillouin zone (BZ). Likewise the 2nd (and higher order) BZs are defined as the additional volumes enclosed by perpendicular bisectors to 2nd (and higher) nearest neighbours.

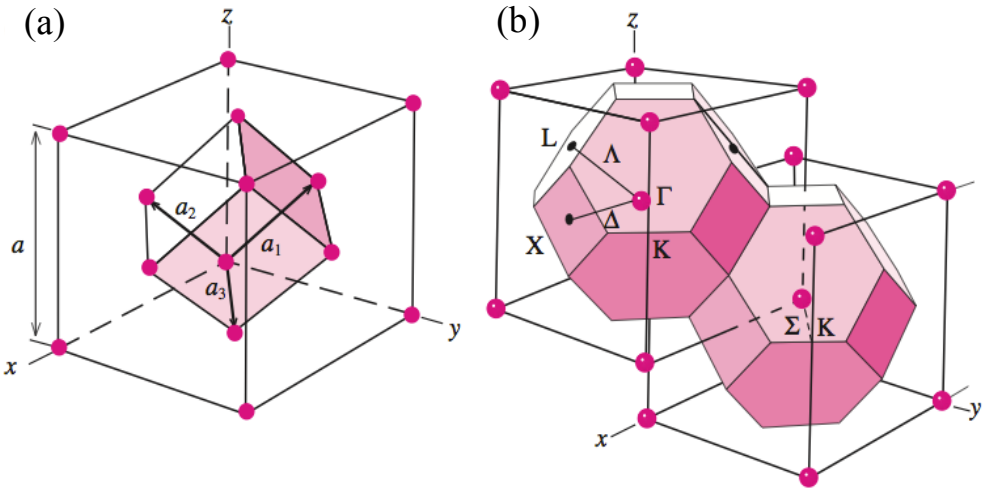

Figure 2.2: (a) fcc crystal structure with the primitive cell; (b) the reciprocal lattice of the fcc structure [30]

Fig 2.2(a) shows the fcc crystal structure with its primitive lattice vectors $\mathbf{a}_1$, $\mathbf{a}_2$, and $\mathbf{a}_3$. Fig 2.2(b) shows the reciprocal lattice of the fcc structure. The first BZ of the reciprocal lattice of the fcc lattice (i.e a bcc lattice) is a truncated octahedron with a total of 14 faces (8 regular hexagons and 6 squares). Special high symmetry points are denoted by Γ, X, and K, while high symmetry lines joining some of these points are labeled as Δ and Σ.

Each BZ has a volume equal to

$$\Omega_{\mathrm{BZ}} = \Omega_{\mathrm{rl}} = |\mathbf{b}_1 . (\mathbf{b}_2 \times \mathbf{b}_3)| .$$

----------(2.10)

2.1.4 Crystal Structure

A crystal or crystalline solid is a regular three-dimensional arrangement of atoms exhibiting long-range order and symmetry [26]. It is usually defined as the combination of a lattice and a basis, where the lattice is an infinite set of points that each have an identical environment, and the basis defines an atom or group of atoms assigned to every lattice point. The lengths of the edges of a unit cell and the angles between them are called the lattice parameters or lattice constants.

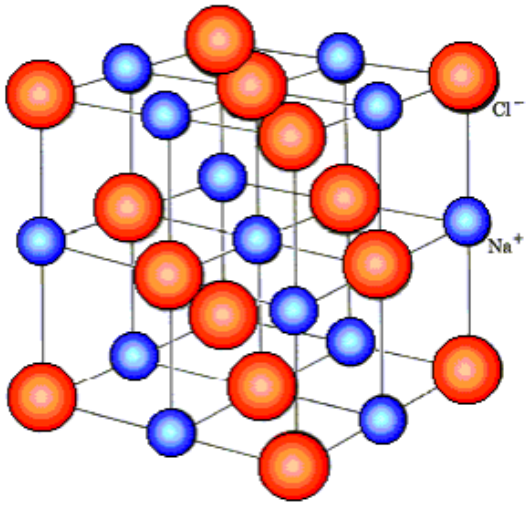

Figure 2.3: rocksalt structure: the conventional unit cell of the rocksalt structure, which has a fcc lattice with two basis atoms, Na and Cl

Crystal Structure with fcc lattice

There are four simple structures with the fcc lattice.

- The rocksalt (or NaCl) structure
- The zincblende (or ZnS) structure
- The diamond structure
- The CaF_2 structure

2.1.4 (a) Crystal structure of rocksalt (or NaCl)

In this structure, each fcc lattice point is assigned a basis of two atoms (or one unit) of NaCl: Na (group 1) atom at $(0, 0, 0)$ and Cl (group 7) atom at $(½, ½, ½)$ (or vice versa). The coordination number for an atom within this structure is 6. The conventional unit cell for the rocksalt structure is shown in figure 2.3.

2.1.4 (b) Crystal Structure of zincblende and diamond

Zincblende is another type of crystal structure with an underlying fcc lattice and two basis atoms. As shown in fig 2.4(a) and (b), one of the two basis atoms is placed at $(0, 0, 0)$ and

the other atom is at $\left(\frac{1}{4},\frac{1}{4},\frac{1}{4}\right)$. Each atom in this structure is tetrahedrally bonded to atoms of the other type. When the two basis atoms are identical, the zincblende structure turns into the diamond crystal structure. Therefore, the diamond crystal structure is characterized by a centre of inversion at the midpoint between two basis atoms. Fig 2.4(a) and (b) display the diamond and zincblende crystal structures respectively. Compound semiconductors composed of atoms from group 3 and 5 of the periodic table tend to crystallize in the zincblende structure, whereas the crystals of group 4 elements such as C (diamond), Si and Ge etc exhibit the diamond structure.

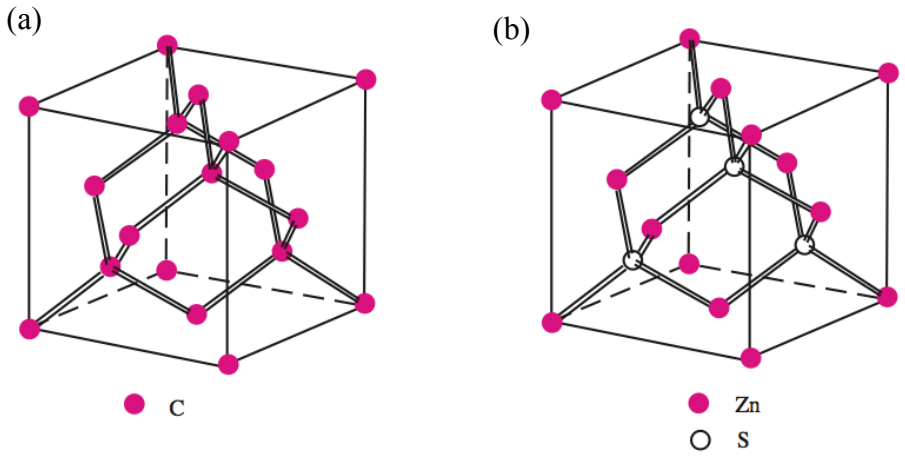

Figure 2.4: Conventional unit cells of (a) the diamond and (b) the zincblende crystal structure [30]

2.1.5 Group theory and Symmetry Operations

We observed in the previous section that the reciprocal lattice of a fcc lattice is a bcc lattice, which is highly symmetrical. A careful examination of the first BZ shows that it remains unchanged under various rotations and reflections. These operations are known as the symmetry operations of the BZ. The symmetry of the BZ (or reciprocal lattice) results from the symmetry of the direct lattice and therefore it is ultimately related to the symmetry of the crystal.

There are two important consequences of these symmetries upon the electron band structure. First, if there are two wave vectors **k** and **k′** in the BZ, that can be transformed into one another by a symmetry operation of the crystal then the electronic energies associated with these two wave vectors must be identical. The symmetry points or axes within the Brillouin zone (or reciprocal lattice), which are involved in these transformations, are said to be equivalent. In fig 2.2(b), the first BZ of the fcc lattice contains six square faces containing the high-symmetry point labelled X in the center. These six faces including the X points are equivalent and can be transformed into one another through rotations by 120°. Therefore it is necessary to calculate the energies of the electron at only one of the six equivalent square faces containing the X point.

The second and more important consequence of the crystal symmetry is that wave functions can be expressed in a form so that they have specific transformation properties under the symmetry operations of the crystal. These are called symmetrized wave functions. The standard wave functions of electrons in atoms are an example of symmetrized wave functions, which are usually labelled according to their transformation properties under rotations, i.e. as s, p, d, f, etc. An s wave function is unchanged by any type of rotation, a p wave function transforms under rotation like the three components of a vector, and the d wave function under rotation can transform like the five components of a symmetric second rank tensor. For a given operator, some of the matrix elements defined from this set of basis functions may be found to vanish, giving rise to selection rules. Similarly, wave functions in crystals can also be classified according to their transformation properties under the symmetry operations of the BZ (or crystal), and selection rules for operators acting on these wave functions can be determined. The set of all possible symmetry operations of a crystal can be grouped into a point group or a space group. The symmetry operations of the point group such as rotations or reflections are those that leave one point fixed while leaving the crystal invariant. On the other hand, all possible symmetry operations, including translations, are contained within the space group. The mathematical treatment of the properties of groups is Group Theory.

Symmetry Operations of the zincblende and rocksalt structures

Figure 2.4(b) shows the structure of the zincblende crystal. As described in the previous section, zincblende crystal structures consist of a fcc lattice with two basis atoms which are displaced relative to each other by one quarter of the body diagonal, i.e. along the [111] direction. The volume defined by the primitive lattice vectors forms a primitive cell, which is repeated at each lattice site. The point group of the zincblende structure has 24 elements and is denoted by T_d. The corresponding space group is denoted as T_d^2 (or F$\bar{4}$3m in the international notation).

The point group symmetry operations of the zincblende crystal are defined with respect to the origin placed at one of the two atoms in the primitive unit cell. With this choice of coordinates, the 24 operations are divided into five classes as listed below:

E:

eight C3 operations: clockwise and counterclockwise rotations of 120 deg about the $[111], [\bar{1}11], [1\bar{1}1]$ and $[11\bar{1}]$ axes, respectively;

three C2 operations: rotations of 180 deg about the [100], [010], and [001] axes, respectively;

six S4 operations: clockwise and counterclockwise improper rotations (defined as a rotation followed by a reflection) of 90 deg about the [100], [010], and [001] axes, respectively;

six σ operations: reflections with respect to the $(110), (1\bar{1}0), (101), (10\bar{1}), (011)$ and $(01\bar{1})$ planes, respectively.

In the diamond structure, the two atoms in the primitive unit cell of the zincblende crystal are identical. In this case, if we choose the origin at the midpoint of these two identical atoms, the crystal structure remains invariant under inversion with respect to this origin. However, if we choose the origin at one of these identical atoms, then the crystal is no longer invariant under inversion with respect to this new origin, but is unchanged under inversion plus a translation by the vector (a/4)[1, 1, 1], where a is the length of the unit cube. This can be visualized by drawing the carbon atoms in the diamond structure along

the [111] direction as described in fig 2.5 below.

Figure 2.5: The carbon atoms along the [111] direction in diamond [30]

The point group of the diamond structure is generated from the T_d group by adding the inversion operation. This point group has 48 elements, and is denoted as O_h. The space group is denoted as O_h^7 (or Fd3m in the international notation).

The rocksalt crystal structures consist of a fcc lattice with two basis atoms displaced relative to each other by half of the body diagonal i.e. along the [111] direction. The coordination number of each atom in this structure is 6 with the octahedral sites fully occupied by cations/anions and the tetrahedral sites empty. Each cation is coordinated with 6 anions at the vertices of an octahedron, and similarly, each anion is coordinated with 6 cations. The system remains invariant under inversion symmetry. Therefore the point group for rocksalt contains the symmetry operations of the T_d point group and in addition has a center of inversion. This structure has 48 symmetry operations and the point group is denoted as O_h (space group O_h^5 or $Fm\bar{3}m$ in the international notation).

If the point group of a crystal structure contains an inversion center as one of its symmetry elements, then it is known as a centrosymmetric crystal. In such a point group, for every point (x, y, z) there is an indistinguishable point (-x, -y, -z) within the unit cell. Crystals without an inversion center are known as non-centrosymmetric crystals and display certain physical properties, such as the piezoelectric effect. For the structures discussed above, rocksalt and the diamond structure are centrosymmetric and hence do not display any piezoelectric property. On the other hand, the zincblende structure does contain a centre of inversion as one of its symmetry elements. This crystal is non-centrosymmetric and hence exhibits piezoelectricity.

2.1.6 Phonons

A phonon is a quantum of vibrational energy of a crystalline solid [26]. It can also be defined as an elementary excitation with which a quantum energy of $\hbar\omega(q)$ is associated. The concept of the phonon is similar to that of the photon which is a quantum of electromagnetic energy. As the phonon does not have any mass and it originates from relative motion of atoms, it is a quasiparticle with a momentum $\hbar\mathbf{q}$. The variation of the phonon frequency ω versus wave vector $\mathbf{q}$ is known as the phonon dispersion relation $\omega = \omega(q)$.

Optical vs Acoustic, Longitudinal vs Transverse

Phonons in a crystal containing more than one basis atom per unit cell are classified as either acoustic or optical phonons.

Optical phonons are associated with the out-of-phase movement of the basis atoms in a primitive unit cell. Infrared radiation can excite these phonons in ionic crystals such as sodium chloride. The electric field of the light will move every positive ion in the direction of the field, and every negative ion in the opposite direction, generating the crystal vibration. For an optical phonon, the neighboring atoms move against each other and hence create an electric dipole moment, which varies with respect to time. These phonons possess a non-zero frequency at the center of the Brillouin zone. Such phonons are called infrared-active, whereas the phonons which indirectly interact with light through Raman scattering are called Raman active. Optical phonons can further be abbreviated as transverse (TO) or longitudinal (LO) according to whether their displacements are perpendicular or parallel to the direction of the wave vector $\mathbf{q}$.

The atoms vibrating in phase with each other are known as acoustic phonons. At infinite wavelength, the frequency of the acoustic phonons at the zone center tends to zero and corresponds to a simple displacement of the crystal. These phonons can also be categorized as transverse acoustic (TA) or longitudinal acoustic (LA) according to the direction of displacement of the atoms. The schematic diagrams for LA, TA, LO and TO phonons are presented in figure 2.6.

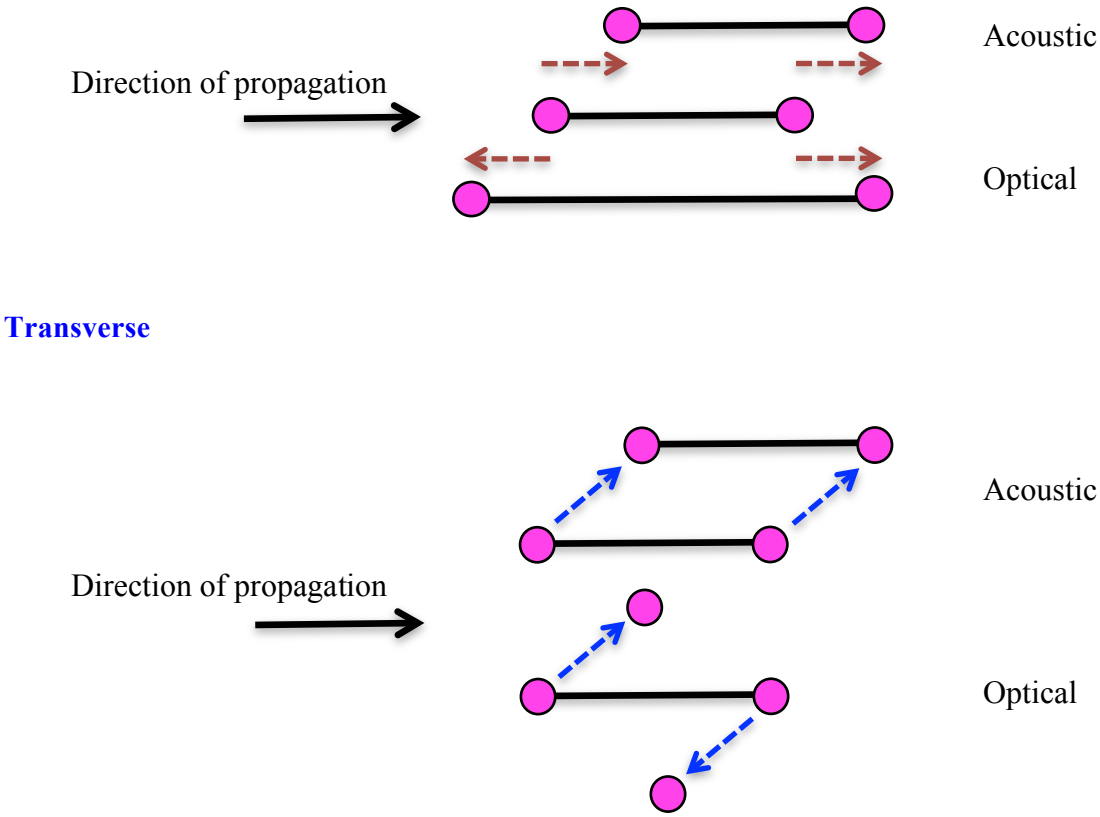

Figure 2.6: Phonons: optical and acoustic vibrations in (a) the longitudinal and (b) the transverse direction.

In a diamond structure, e.g. Si, the optical phonons are triply degenerate at the zone center whereas in the zincblende structure, e.g. GaSb, the optical phonons split at the zone center into a nondegenerate longitudinal optical phonon (LO) and doubly degenerate transverse (TO) phonons. The frequency of the LO phonon is higher than that of the TO phonons. The reason for the splitting lies in the ionic nature of the bonds in the zincblende crystal structure. For example in GaSb, Ga has three electrons in its outer orbital while Sb has five electrons. While making a bond, a Sb atom contributes more electrons to the covalent bond than a Ga atom. Therefore, the electrons participating in the bond spend more time near the Sb atom than Ga, which polarizes the bond by making the Sb atoms slightly more negatively charged than the Ga atoms. The long-wavelength excitation of such a structure causes an additional restoring force due to Coulomb attraction between the positively and

negatively charged particles. The additional force results in the increase of the frequency of the LO phonon relative to that of the TO phonons.

On the other hand, in the diamond structure, the bonding between two atoms is purely covalent and the atoms do not carry any charge. Consequently, there is no additional force associated with LO phonons, leading to triply degenerate optical phonons at the zone center.

2.1.7 Irreducible representations

The effect of symmetry operations (such as rotation) on a coordinate system can be represented by a transformation matrix. If *x, y, z* are transformed to *x', y', z'* under a four-fold rotation about the *x*-axis such that *x'* = *x*, y' = z and *z'* = -*y* then the transformation matrix can be represented as

$$M = \begin{pmatrix} 1 & 0 & 0 \\ 0 & 0 & 1 \\ 0 & -1 & 0 \end{pmatrix}.$$

The set of transformation matrices for all the symmetry operations in a group is known as a representation of the group. If these representations of a group cannot be reduced further then they are known as an irreducible representation.

Let us consider the zincblende crystal structure. As described in the previous section, it belongs to the T_d point group with 24 symmetry operations. It can be shown that the number of irreducible representations is identical to the number of classes. The T_d point group has five irreducible representations with the sum of their squares equivalent to the total number of symmetry operations. The only possible combination of five squares that adds up to 24 is $2\times1^2 + 2^2 + 2\times3^2$ [27]. This indicates that there are five irreducible representations referred to as A_1 and A_2 (two irreducible representations of dimension one), E (one irreducible representation of dimension two) and T_1 and T_2 (two irreducible representations of dimension three).

The A_1 and A_2 representations are related to the A_{1g} and A_{2u} modes, where A_{1g} and A_{2u} denote the 1-D phonon modes with and without inversion symmetry, respectively. The

presence of inversion symmetry or not is denoted as gerade (g) and ungerade (u), respectively.

There are three common notations for the irreducible representations of the T_d point group symmetry. These are summarized in the table below.

Koster notation[a]	BSW notation	Molecular notation
Γ_1	Γ_1	A_1
Γ_2	Γ_2	A_2
Γ_3	Γ_{12}	E
Γ_4	Γ_{15}	T_2
Γ_5	Γ_{25}	T_1

Table 2.1: Notation for irreducible representations of T_d point group [27]

The symmetry group of the diamond structure is O_h and it is derived from the T_d point group by including the additional inversion operation i. It has therefore 48 elements: the 24 symmetry operations the same as T_d plus those of T_d followed by i. Referring to the properties of the T_d group, it is obvious that O_h has ten classes: five classes are the same as those of T_d while the remaining five are obtained by multiplying the first five operations with the inversion symmetry. Likewise, there are ten irreducible representations and ten phonon modes. Five of them correspond to odd transformations the same as the T_d group and the remaining five are even transformations obtained from T_d operations followed by inversion.

2.1.8 Lattice dynamics of a linear chain

Monatomic linear chain

Let us consider a monatomic chain with an infinitely large number, N, of atoms separated by distance a. Suppose that at a particular time, the n^{th} atom in chain has a displacement u_n from its equilibrium. Then from Newton's second law of motion and Hooke's law, the equation of motion of the n^{th} atom can be described as [26],

$$m\frac{d^2u_n}{dt^2} = \Lambda[(u_{n+1} - u_n) + (u_{n-1} - u_n)]\,. \qquad \text{----------(2.11)}$$

Here m is the mass of the atom and Λ is the force constant.

The solution of equ (2.11) can be written as

$$u_n = A\exp[i(qx - \omega t)]\,,$$

----------(2.12)

where A is the amplitude of motion of the n^{th} atom.

Keeping the value of displacement u_n in equation (2.11) gives the dispersion relation [26]:

$$\omega = 2\sqrt{\frac{\Lambda}{m}}\left|sin\ \frac{qa}{2}\right|.$$

----------(2.13)

In this case, we have only one allowed mode of vibration, either longitudinal in which case atoms vibrate along the direction of wave propagation, or transverse where atoms vibrate perpendicular to the wave. The dispersion curve in equation (2.13) shows (i) the translational symmetry $\omega(q + G_n) = \omega(q)$ and (ii) $\omega(q)$ is a symmetric function between +q and –q.

Diatomic linear chain

In this case, consider an infinitely large chain of 2N atoms forming N unit cells. The length of each unit cell is 2a with 2 atoms per unit cell of mass m_1 and m_2. Following the same procedure as used in solving the monatomic chain problem, the dispersion relation comes out to be

$$\omega^2 = \Lambda\left(\frac{1}{m_1} + \frac{1}{m_2}\right) \pm \Lambda\left[\left(\frac{1}{m_1} + \frac{1}{m_2}\right)^2 - \frac{4}{m_1 m_2} sin^2 qa\right]^{\frac{1}{2}},$$

----------(2.14)

which implies that there are two modes of phonon dispersion curve in a diatomic linear chain: a optical phonon mode, where the atoms in the unit cell move in opposite directions, and acoustic phonon modes, where the atoms move in the same direction. Fig 2.7 below explains the longitudinal and transverse atomic vibrations in the acoustic and optical branches in GaSb crystal along the [001] direction (i.e along Γ – X symmetry line) in the

Brillouin zone.

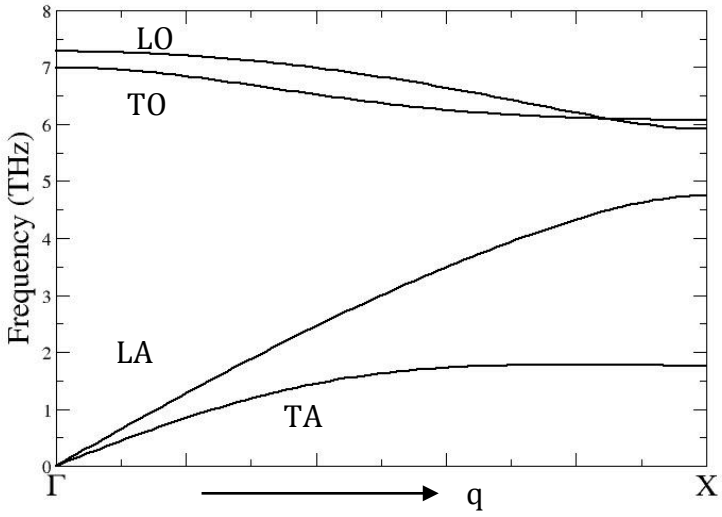

Figure 2.7: Phonon dispersion curve in GaSb along the [001] direction in the Brillouin zone [28]

The total number of phonon modes in a crystal is given by, D.p, where D denotes the dimension of the crystal and p describes the number of basis atoms in a unit cell. The total number of phonon modes can be divided into D acoustic branches and D(p-1) optical branches.

The phonon dispersion curves for Ge (diamond structure) and PbTe (with the rock-salt structure) are shown in fig 2.8(a)/(b) respectively. The Brillouin zone for each of these three structures has the same shape – a truncated octahedron and Γ – X is one of the principal symmetry directions. For the diamond structure (two identical basis atoms in the unit cell), there are three acoustic (LA, TA_1, TA_2) and three triply degenerate (at the zone centre) optical (LO, TO_1, TO_2) branches. For GaSb, there are three acoustic modes (LA, TA_1, TA_2) and three optical modes split at the zone centre into one longitudinal (LO) mode and doubly degenerate transverse (TO_1, TO_2) modes (shown in Fig 2.7). The optical modes of PbTe are also split at the zone centre into one LO and two doubly degenerate TO modes. The frequency for the longitudinal mode is higher than that of the transverse vibrations.

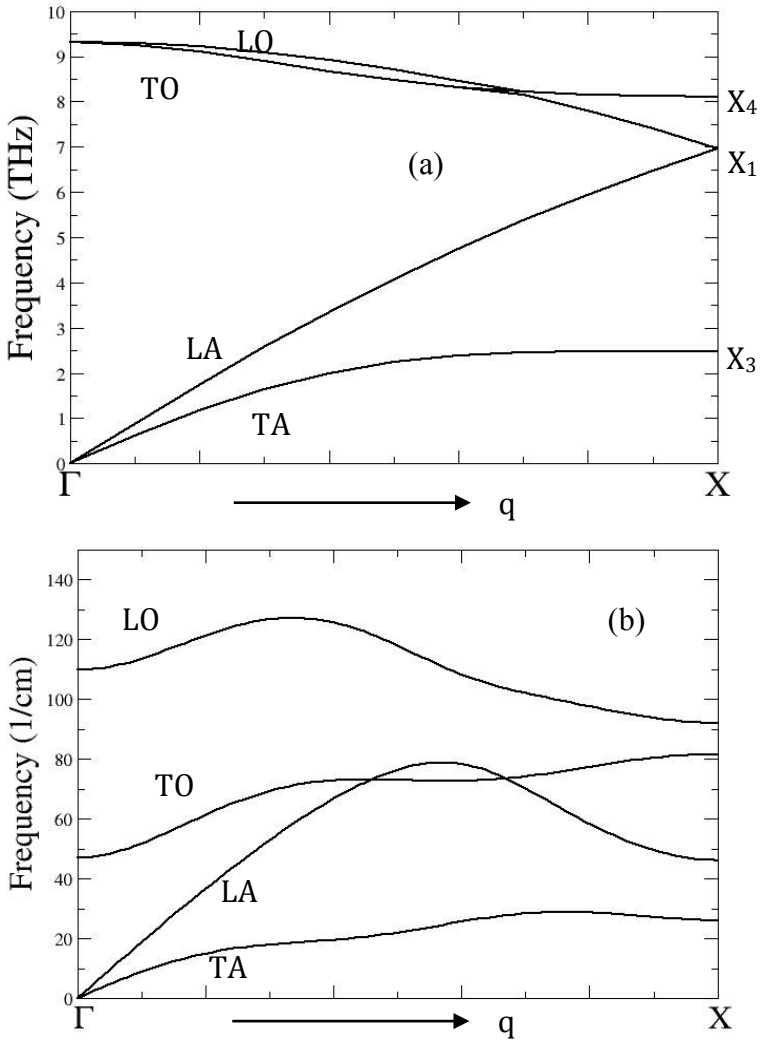

Figure 2.8: Phonon dispersion curves for (a) Ge and (b) PbTe. The optical phonons are split at the zone center for PbTe structure [28].

It is important to know a relation between the frequency of transverse and longitudinal vibrations in a crystalline solid to study our solid materials. As explained in the previous discussion, for the optical mode, the atoms vibrate against each other, generating a finite polarization density **P**, which gives rise to a macroscopic electric field **E** and electric displacement **D**.

$$\mathbf{D} = \epsilon\mathbf{E} = \mathbf{E} + 4\pi\mathbf{P} \, .$$

----------(2.15)

where ϵ is the dielectric tensor of the medium. **D** and **E** satisfy the electrostatic equations as

$$\nabla . \mathbf{D} = 0,$$

----------(2.16)

and,

$$\nabla \times \mathbf{E} = 0.$$

----------(2.17)

In a cubic crystal, **D** ∥ **E** ∥ **P**, and it can be shown from equations (2.16) and (2.17) that either

$$\mathbf{D} = 0, \ \mathbf{E} = -4\pi\mathbf{P},$$

----------(2.18)

which describes an LO mode, or

$$\mathbf{E} = 0,$$

----------(2.19)

which describes a TO mode, i.e. a non-vanishing electric field is associated with long wavelength LO vibrations.

In the presence of a polarization density **P** and a long-range electrostatic field **E**, the vibrations experience an electrostatic restoring field (called the local field $\mathbf{E}_{loc}$ or $\mathbf{E}_{eff}$), which is given by the Lorentz relation

$$\mathbf{E}_{eff} = \mathbf{E} + \frac{4\pi\mathbf{P}}{3}.$$

----------(2.20)

Substituting equation (2.18) and (2.19) into equ (2.20),

$$\mathbf{E}_{eff} = -\frac{8\pi\mathbf{P}}{3}, \quad \text{for the LO mode.}$$

----------(2.21)

and

$$\mathbf{E}_{eff} = \frac{4\pi\mathbf{P}}{3}, \quad \text{for the TO mode.}$$

----------(2.22)

Therefore, for LO vibrations, $\mathbf{E}_{eff}$ reduces the polarization while it adds to the polarization for TO vibrations. The Lyddane-Sachs-Teller relation relates the LO and TO frequencies as [26],

$$\omega_{LO}^2 = \frac{\epsilon_r(0)}{\epsilon_r(\infty)}\omega_{TO}^2 ,$$

----------(2.23)

where $\epsilon_r(0)$ and $\epsilon_r(\infty)$ are the static and optical dielectric constants of the crystal. In an ionic crystal the LO and TO frequencies will be split by $\omega_{LO} - \omega_{TO}$.

2.2 Non linear optics and Raman scattering

2.2.1 Introduction to optical processes at an interface

The band gap of semiconductors falls in the energy range of zero to 6 eV [27]. Photons of sufficient energy can excite electrons from the top of filled valence bands to the bottom of conduction bands. Therefore a lot of information about the electronic properties of a semiconductor can be obtained from their optical spectra. However, photons can also interact with lattice vibrations and with electrons localized on defects, making optical techniques useful for studying phonons and electronic excitations.

Figure 2.9 shows schematically some of the optical processes that can occur when a medium is illuminated by light. At the surface of the medium, a part of the incident light is reflected and the rest is transmitted following the standard laws of reflection and refraction (which are obtained from momentum conservation). Inside the transmitted medium, various interesting optical phenomena can take place. Some of the radiation may be absorbed or scattered while the remainder passes through the sample. Some of the absorbed electromagnetic waves may be lost as heat or reemitted at a different frequency to the incident light. The latter process is referred to as photoluminescence.

While most of the light traveling through a medium is either transmitted or absorbed, a very tiny fraction is scattered, in all directions, by inhomogeneities inside the medium. These inhomogeneities may be static or dynamic. An example of a dynamic fluctuation is the density fluctuation associated with an acoustic wave. Inelastic scattering of light by acoustic waves is generally referred to as Brillouin scattering [27,29]. This was proposed theoretically by Brillouin and Mandelstam. Inelastic scattering of light by other elementary excitations, such as optical phonons, is known as Raman scattering. (Sir C.V. Raman

received the Nobel Prize in Physics in 1930 for discovering this effect in 1928 in Calcutta, India. The effect was named after him). In a typical luminescence process, electrons in the sample are excited electrically or optically. After some energy loss (relaxation), the excited electrons return to the ground state while emitting light at a different frequency. In a Raman or Brillouin process light is scattered by oscillations or instabilities inside the sample. An important difference between these two processes is that luminescence involves the real excitation of electrons, whereas in light scattering virtual excitations of electrons are sufficient.

In general, reflection and absorption are the strongest optical processes because they involve the lowest order of interaction between the electromagnetic waves and the atomic vibrations inside the medium. Light scattering involves two such interactions and therefore tends to be weaker. In this chapter, I will first present the fundamental optical properties of semiconductors and linear optical processes, and then a detailed description of nonlinear optical properties, which involve higher-order optical interactions, will be provided. This is followed by a macroscopic theory of Raman scattering by phonons in solids.

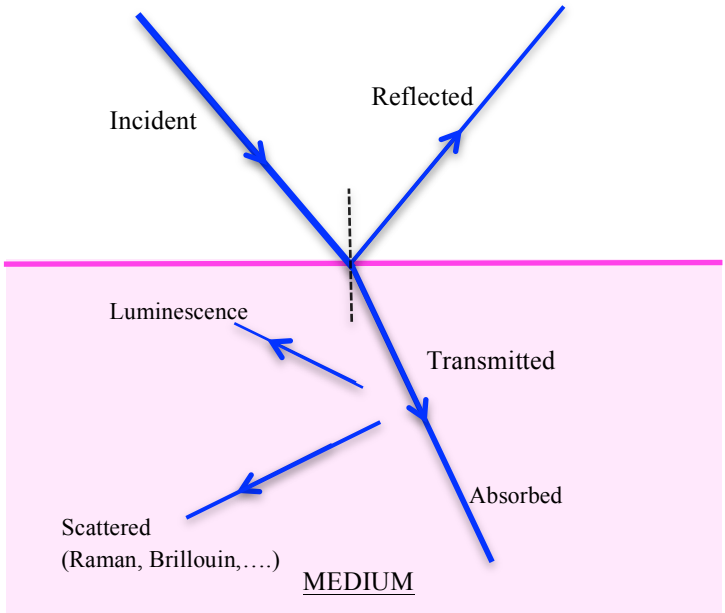

Figure 2.9: Various optical processes that occur at an interface [27]

2.2.2 Linear optics

Maxwell described the interaction of electromagnetic radiation with matter in terms of four well known equations. He also concluded that light is an electromagnetic wave. The exact form of these equations depends upon the system of units used, although their general form remains the same. The Maxwell equations in cgs units are written as

$$\nabla . \mathbf{D} = 4\pi\rho ,$$

$$\nabla . \mathbf{B} = 0 ,$$

$$\nabla \times \mathbf{E} + \frac{1}{c}\frac{\partial \mathbf{B}}{\partial t} = 0 ,$$

$$\nabla \times \mathbf{H} - \frac{1}{c}\frac{\partial \mathbf{D}}{\partial t} = \frac{4\pi}{c}\mathbf{J} ,$$

----------(2.24)

where, **E** is the electric field and **B** is the magnetic flux density. ρ and **J** describe the free charge density (not including bound charges) and free current density respectively. The bound charges contribute to the electric displacement **D** and magnetic field **H**.

For linear isotropic media, **D** and **H** can be described by,

$$\mathbf{D} = \mathbf{E} + 4\pi\mathbf{P} ,$$

$$\mathbf{B} = \mathbf{H} + 4\pi\mathbf{M} .$$

----------(2.25)

and

$$\mathbf{J} = \sigma\mathbf{E} ,$$

----------(2.26)

where **P** is the electric polarization due to the separation of bound charges in a medium, σ is the electrical conductivity and **M** is the magnetic dipole polarization (or magnetization) in the medium due to bound currents induced by the applied fields.

In the linear case, the electric or magnetic field induces polarization or magnetization linearly proportional to the field magnitude. Generally this is valid only for weak applied fields. For isotropic materials, the direction of polarization is the same or opposite to the applied field,

$$\mathbf{P} = \chi \mathbf{E} .$$

----------(2.27)

where χ is the dielectric susceptibility which is independent of the electric-field intensity and is a scalar quantity in this case.

For anisotropic media, the proportionality factor becomes a second-rank tensor so that

$$\begin{pmatrix} P_x \\ P_y \\ P_z \end{pmatrix} = \begin{pmatrix} \chi_{xx} & \chi_{xy} & \chi_{xz} \\ \chi_{yx} & \chi_{yy} & \chi_{yz} \\ \chi_{zx} & \chi_{zy} & \chi_{zz} \end{pmatrix} \begin{pmatrix} E_x \\ E_y \\ E_z \end{pmatrix}.$$

or

$$P_i = \chi_{ij}^{(1)} E_j ,$$

----------(2.28)

where *j* is summed over x, y and z axes and the superscript indicates that this is a first-order term. Anisotropy can be a natural existing property of the material or it can be induced by applied fields. Birefringence is an example of a linear optical effect, which can occur in an anisotropic material where the orthogonal components of incident light have different propagation velocities.

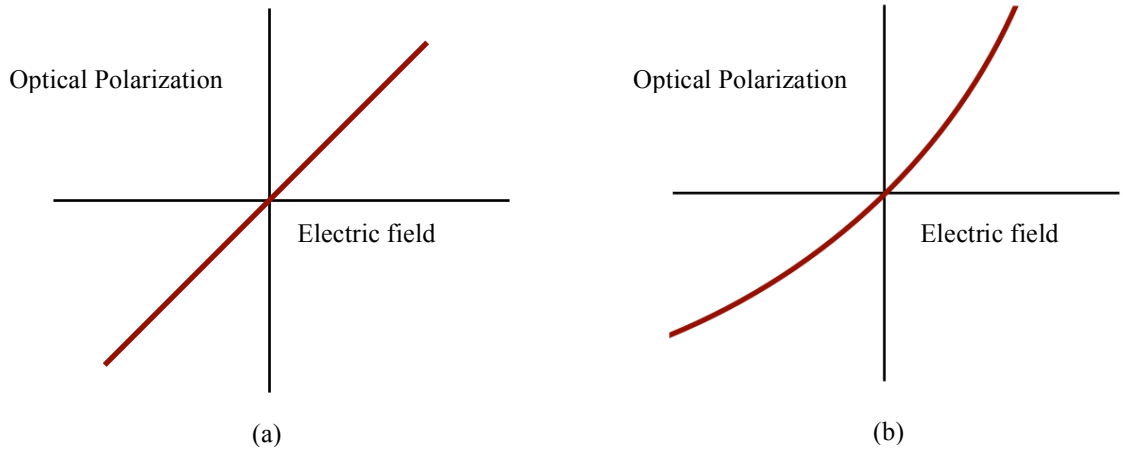

Figure 2.10: Graphical representation of non-linear optics: (a) shows the linear response of electrical polarization with respect to an applied electric field and (b) represents that for a high intensity field where the response is non-linear.

2.2.3 Non linear optics

Nonlinear optics refers to the case that the optical propagation medium exhibits a non-linear response to the applied electromagnetic field. The part of the light-induced electric polarization which depends non-linearly upon the electric field of the light is called the non-linear polarization. When light propagates in a transparent medium, its electric field induces an electric polarization in the medium. At low light intensities, the electric polarization is proportional to the electric-field strength. The nonlinear contributions become important at high optical intensities.

History:

The origin of nonlinear optics is associated with J. Kerr, who observed the change in the refractive index of organic liquids and glasses in the presence of an electric field. Kerr collimated sunlight and then passed it through a prism to an isotropic sample, which was placed between two cross polarizers (i.e. the polarizers' axes are perpendicular to each other). The set up could be used to vary the color of the light incident upon the sample. A static electric field at 45^{o} to the axis of each polarizer was applied to the sample. The transmitted intensity was observed to vary quadratically with the applied voltage. This phenomenon is known as the Kerr effect or the quadratic electro-optic effect. The effect originates because the electric field induces birefringence in the material. When light with high intensity propagates through a medium, there is a change (usually an increase) in the refractive index in proportion to the optical intensity *I*. The non-linear refractive index n is described as

$$n = n_0 + n_2 I \,,$$

----------(2.29)

where n_0 is the linear refractive index, I is the optical intensity and n_2 is the nonlinear refractive index (or material-dependent Kerr coefficient).

The invention of the laser in 1960 [1] offered light sources with huge electric-field intensity. Second-harmonic generation was the first nonlinear-optical phenomenon to be observed. P. A. Franken and coworkers focused a pulsed ruby laser into a quartz crystal and showed that light with a frequency double that of the laser frequency was generated [30].

Later, Mayer and Gires demonstrated the optical Kerr effect (OKE). A strong light pulse from a ruby laser pumped the sample and a weak probe beam from a xenon flashlamp was used to record the sample response to the pump. The polarizations of pump and probe beams were set 45^{o} from each other. The high-intensity pump beam induces a birefringence in the material that causes a rotation of the polarization of the probe beam. The probe beam was reflected from a dichroic mirror to the detector through a polarizer, which rejected the original polarization of the probe. Therefore, the amount of light reaching the detector was related to rotation of polarization of the probe beam, which was proportional to the disturbance in the sample, and in turn, was directly related to the pump intensity. Since the intensity is proportional to the square of the electric field, the OKE is also known as the intensity-dependent refractive index.

While the optical Kerr effect is similar to the quadratic electro-optic effect, where a strong static electric field depolarizes the probe beam, the OKE has many more diverse applications.

2.2.3.1 Nonlinear Phenomena

If high optical intensity beams are applied to a material, then the electric polarization and induced magnetization can depend nonlinearly on higher powers of the applied fields. Therefore the polarization of the material includes contributions from non-linear susceptibility tensor components and may be written as [31, 32]

$$P_i = \chi_{ij}^{(1)} E_j + \chi_{ijk}^{(2)} E_j E_k + \chi_{ijkl}^{(3)} E_j E_k E_l + \cdots,$$

----------(2.30)

where $\chi^{(n)}$ describes the nth order susceptibility which is a tensor of rank (n+1). Therefore the second-order dipolar susceptibility $\chi^{(2)}$ is a tensor of rank 3 and is represented by a 3×3×3 matrix.

The susceptibility tensor may also depend upon the presence of phonons as

$$\chi_{ij}^{(1)} = \chi_0 + \frac{\partial \chi}{\partial Q} Q + \frac{\partial^2 \chi}{\partial Q^2} Q^2 + \cdots,$$

----------(2.31)

where χ_0 is the linear susceptibility, which is a tensor of rank 2, Q represents the atomic displacement, and then the expression includes higher order susceptibility terms which when contracted with the atomic displacement vector, yields a nonlinear susceptibility tensor of rank 2.

Non-linear optical effects arise due to the polarization dependence of the higher order electric field in equ 2.30.
The second-order non-linear polarization is generated by $\chi^{(2)}$. Therefore, the non-linear polarization includes a term that varies quadratically with the electric field of the incident light. It is observed in materials which lack a centre of inversion symmetry.

For centrosymmetric crystals, $\chi^{(2)}$ is symmetric and so must vanish. This may be illustrated by considering an electric field

$$E_\omega(t) = E_0\,(e^{i\omega t} + e^{-i\omega t}),$$

applied to a centrosymmetric medium. The second-order polarization of the medium is written as

$$P^{(2)}(t) = \chi^{(2)} {E_\omega}^2(t)$$

----------(2.32)

For a centrosymmetric crystal,

$$-P^{(2)}(t) = \chi^{(2)}\{-E_\omega(t)\}^2$$
$$-P^{(2)}(t) = \chi^{(2)}\,{E_\omega}^2(t)$$

----------(2.33)

Equation (2.32) and (2.33) can hold simultaneously only when the second order polarization is zero, indicating that $\chi^{(2)} = 0$

The quadratic dependence is responsible for phenomena such as second-harmonic generation, where the frequency of an emitted phonon is double the frequency of the incident photon, parametric amplification and optical rectification.

The next higher order term, $\chi^{(3)}$, describes a cubic dependence on the electric field. This dependence is observed in almost all media, and is the origin of the optical Kerr effect, where the incident light changes the refractive index of the material.

2.2.3.2 Specular Optical Kerr Effect

The response of the sample to incident light has two contributions: (1) from the surface:,which gives rise to a specular or diffuse reflection, the latter arising from the breakdown of momentum conservation. In specular reflection (or mirror-like reflection), the excited electrons obey momentum conservation, while in diffuse scattering, the drift velocity of the electrons is completely destroyed, so that electrons scatter to a random momentum state (i.e momentum is not conserved) [33]. (2) From the bulk, which comes from the interaction of the incident photon with a phonon, impurity or other form of scattering center within a distance which is comparable to the skin depth from the surface.
Pumping the sample surface with linearly (circularly) polarized light is used to transfer linear (angular) momentum from the photons to the electronic orbits and enhance their linear (orbital) momentum [34]. Therefore the pump-induced transient polarization of the medium contains information about the rate of relaxation of the linear (angular) momentum of electrons and transforms the polarization of a time-delayed probe beam. These processes can be regarded as pump-induced linear or circular birefringence and have also been referred to as the Specular Optical Kerr Effect (SOKE) and Specular Inverse Faraday Effect (SIFE) [35]. The pump-induced birefringence in the medium is expected to relax within a few tens of femtoseconds because of the rapid scattering of the electron momentum [36].

I have measured the SOKE in three important states of a phase-change material (GST) described in the result chapters. The SOKE shows a sharp peak in the rotation channel at zero time delay between pump and probe pulses (experiments and measurement procedure are explained in chapter 3).
The amplitudes of the transient rotation and ellipticity are related to the components of susceptibility tensor $\chi^{(3)}$ by [37]

$$\begin{pmatrix}\Delta\theta\\ \Delta\eta\end{pmatrix} = -\frac{32\,\pi^2 I_{pump}}{c|1+n|^2}\Big\{\sin 2(\theta_1-\theta_2)\cos 2\eta_1 \begin{pmatrix}\mathrm{Re}\\ \mathrm{Im}\end{pmatrix}\frac{\chi_{xxyy}+\chi_{xyyx}}{n(1-n)^2} + \sin 2\eta_1 \begin{pmatrix}-\mathrm{Im}\\ \mathrm{Re}\end{pmatrix}\frac{\chi_{xxyy}-\chi_{xyyx}}{n(1-n)^2}\Big\},$$

----------(2.34)

where (θ_1, η_1) and (θ_2, η_2) are the rotation (defined as the optical rotation of the principal axis of polarized light) and ellipticity (ratio of minor to major axis) of pump and probe beams, respectively. The incident probe beam is linearly polarized, so $\eta_2 = 0$. $\Delta\theta$ and $\Delta\eta$ are the change in rotation and ellipticity of the probe beam as it is reflected from the sample. I_{pump} is the intensity of the pump beam, n is the complex refractive index of the medium and c is the speed of light. In this case, $\chi^{(3)}$ is a tensor of rank 4 and only 2 components out of 81 are non-vanishing. The first term in this equation represents the amplitude of the SOKE and the second represents that of the SIFE.

2.2.4 Light Scattering

When a medium is illuminated by light, the incident photons may be scattered from an atom or molecule. If the scattered photons have the same frequency (and wavelength) as the incident photons, they are said to be elastically scattered and this process is known as Rayleigh scattering (1899). The intensity of scattered light is inversely proportional the wavelength ($I_s \propto \lambda^{-4}$) [29]. However, a small fraction of scattered photons (approximately 1 in 10 million) may be scattered by a phonon with the scattered photons having a frequency different from, and usually lower than, that of the incident photons. This inelastic scattering of light by molecular or crystal vibrations is known as the Raman effect (1928). It is caused by modulation of the susceptibility (or, equivalently, polarizability) of the medium by the vibrations. However, this description implies a direct interaction of the photon and the phonon. Such an interaction is very improbable and has not been experimentally verified yet. The Raman process as it occurs in the solid state involves the excitation of an electron. In Raman scattering, the molecular separation is small compared to the wavelength of light and so there is a coherence between the light beams scattered by different molecules. Einstein (1910) showed that the wavevector of the scattering fluctuation conserves momentum between the incident and scattered photons.

The Raman effect involves the absorption and subsequent emission of a photon via an intermediate quantum state of the medium. The intermediate state can either be a "real" (i.e stationary) state or a virtual state. Raman scattering can be of two types:

- When the material absorbs energy, the scattered photon has a lower energy than the incident photon (ω_I). The frequencies smaller than ω_I are denoted by ω_S and are known as the **Stokes component** ($\omega_I > \omega_S$).
- When the material loses energy, the scattered photon has higher energy than the absorbed photon. The frequencies larger than ω_I are denoted by ω_{AS} and are known as the **Anti-Stokes component** ($\omega_I < \omega_{AS}$).

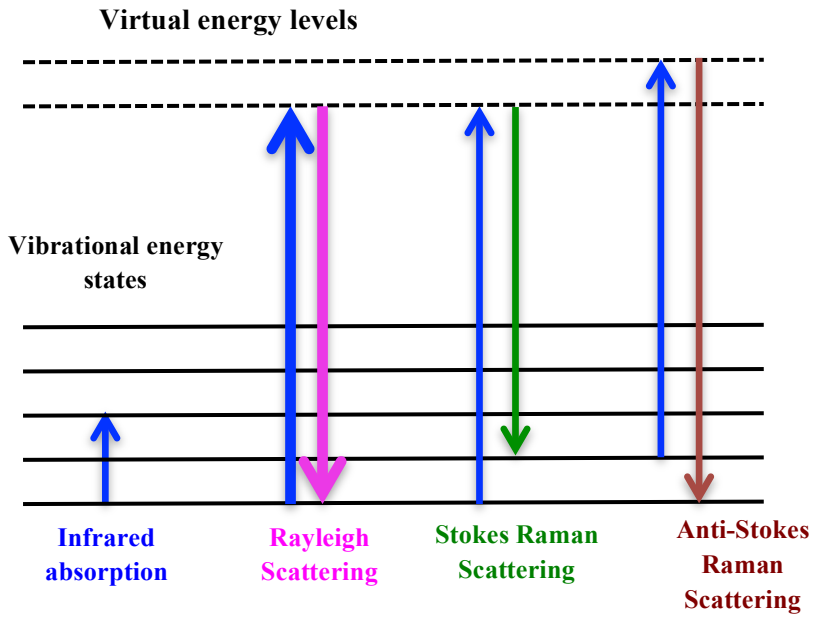

Figure 2.10: Energy level diagram for Rayleigh and Raman scattering

The spectrum of the emitted photons is termed the Raman Spectrum, and it is typically displayed in terms of the energy shift of the scattered photons relative to the Rayleigh line. The Stokes and anti-Stokes spectra form symmetric sidebands above and below the incident photon energy. The frequency shifts are symmetric because they correspond to the energy difference between the same upper and lower resonant states.

In infrared spectroscopy, the molecules absorb specific frequencies that are characteristic of their structure. Fig 2.11 shows the energy levels involved in the different types of scattering.

2.2.5 Macroscopic Theory of Inelastic Light Scattering by Phonons

Electromagnetic radiation can induce a macroscopic polarization in a material. Consider an infinite system with its response to an electromagnetic field described by the electric susceptibility $\boldsymbol{\chi}$. $\boldsymbol{\chi}$ is a second rank tensor. When a sinusoidal plane electromagnetic field described by

$$\mathbf{E}(\mathbf{r}, t) = \mathbf{E}(\mathbf{k}, \omega)\cos(\mathbf{k}\cdot\mathbf{r} - \omega t),$$

----------(2.35)

is present in this medium, it leads to a local sinusoidal polarization $\mathbf{P}(\mathbf{r}, t)$ given by:

$$\mathbf{P}(\mathbf{r}, t) = \mathbf{P}(\mathbf{k}, \omega)\cos(\mathbf{k}\cdot\mathbf{r} - \omega t).$$

----------(2.36)

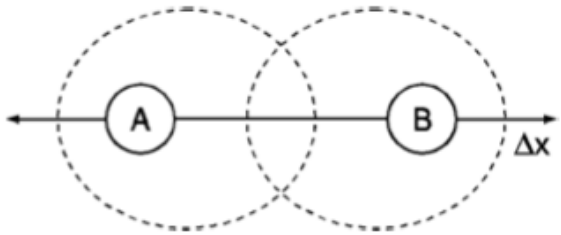

Figure 2.11: Schematic demonstration of the Raman effect for a diatomic molecule

Its frequency and wavevector are same as those of the incident radiation while its amplitude is given by

$$\mathbf{P}(\mathbf{r}, t) = \chi(\mathbf{k}, \omega, \mathbf{Q})\mathbf{E}(\mathbf{r}, t),$$

----------(2.37)

$$\mathbf{P}(\mathbf{k}, \omega)\cos(\mathbf{k}\cdot\mathbf{r} - \omega t) = \chi(\mathbf{k}, \omega, \mathbf{Q})\mathbf{E}(\mathbf{k}, \omega)\cos(\mathbf{k}\cdot\mathbf{r} - \omega t),$$

----------(2.38)

$$\mathbf{P}(\mathbf{k},\omega) = \chi(\mathbf{k},\omega,\mathbf{Q})\mathbf{E}(\mathbf{k},\omega),$$

----------(2.39)

where **P** is the polarization induced in the material, **k** and ω are the wave vector and frequency of the incoming electromagnetic field, and **Q** is the atomic displacement and can be associated with a phonon wave vector **q** as,

$$\mathbf{Q}(\mathbf{r},t) = \mathbf{Q}(\mathbf{q},\omega_0)\cos(\mathbf{q}\cdot\mathbf{r} - \omega_0 t),$$

----------(2.40)

where **q** and ω_0 are the wavevector and frequency of the phonon.

The response of the system to electromagnetic radiation will change the atomic positions and that will modify **χ**. Therefore **χ** can be expanded as a Taylor series in $\mathbf{Q}(\mathbf{r},t)$:

$$\chi(\mathbf{k},\omega,\mathbf{Q}) = \chi_0(\mathbf{k},\omega) + \left(\frac{\partial\chi}{\partial\mathbf{Q}}\right)_0 \mathbf{Q}(\mathbf{r},t) + \cdots,$$

----------(2.41)

where $\boldsymbol{\chi_0}$ denotes the electric susceptibility of the medium with no fluctuations. The first term represents the elastic scattering known as Rayleigh scattering. The first derivative of the susceptibility with respect to the phonon displacement describes the first order Raman scattering (only one phonon involved), and represents an oscillatory susceptibility induced by the phonon $\mathbf{Q}(\mathbf{r},t)$. Higher order susceptibility terms (not shown here) describe Raman scattering of 2nd order (two phonons) and so on. Substituting equ (2.41) into (2.39) the polarization $\mathbf{P}(\mathbf{r},t,\mathbf{Q})$of the medium in the presence of atomic vibrations can be expressed in terms of the static polarization term $\mathbf{P}_0$ and a term $\mathbf{P}_{\text{ind}}$ that is induced by the lattice displacement as follows

$$\mathbf{P}(\mathbf{r},t,\mathbf{Q}) = \chi_0(\mathbf{k},\omega)\mathbf{E}(\mathbf{k},\omega)\cos(\mathbf{k}\cdot\mathbf{r} - \omega t) + \left(\frac{\partial\chi}{\partial\mathbf{Q}}\right)_0 \mathbf{Q}(\mathbf{r},t)\mathbf{E}(\mathbf{k},\omega)\cos(\mathbf{k}\cdot\mathbf{r} - \omega t),$$

$$\mathbf{P}(\mathbf{r},t,\mathbf{Q}) = \mathbf{P}_0(\mathbf{r},t) + \mathbf{P}_{\text{ind}}(\mathbf{r},t,\mathbf{Q}),$$

----------(2.42)

where

$$\mathbf{P_0}(\mathbf{r},t) = \chi_0(\mathbf{k},\omega)\mathbf{E}(\mathbf{k},\omega)\cos(\mathbf{k}\cdot\mathbf{r} - \omega t),$$

----------(2.43)

is a polarization vibrating in phase with the incident radiation and

$$\mathbf{P}_{\mathrm{ind}}(\mathbf{r},\mathrm{t},\mathbf{Q}) = \left(\frac{\partial\chi}{\partial\mathbf{Q}}\right)_0 \mathbf{Q}(\mathbf{r},\mathrm{t})\mathbf{E}(\mathbf{k},\omega)\cos(\mathbf{k}\cdot\mathbf{r}-\omega\mathrm{t})\,,$$

----------(2.44)

is a polarization wave induced by the phonon.

Inserting equation (2.40) leads to

$$\mathbf{P}_{\mathrm{ind}}(\mathbf{r},\mathrm{t},\mathbf{Q}) = \left(\frac{\partial\chi}{\partial\mathbf{Q}}\right)_0 \mathbf{Q}(\mathbf{q},\omega_0)\cos(\mathbf{q}\cdot\mathbf{r}-\omega_0\mathrm{t})\mathbf{E}(\mathbf{k},\omega)\cos(\mathbf{k}\cdot\mathbf{r}-\omega\mathrm{t}).$$

----------(2.45)

Using a simple trigonometric identity, $\mathbf{P}_{\mathrm{ind}}(\mathbf{r},\mathrm{t},\mathbf{Q})$ can be further expanded to show the frequency and wavevector of $\mathbf{P}_{\mathrm{ind}}$.

$$\mathbf{P}_{\mathrm{ind}}(\mathbf{r},\mathrm{t},\mathbf{Q}) =$$
$$\frac{1}{2}\left(\frac{\partial\chi}{\partial\mathbf{Q}}\right)_0 \mathbf{Q}(\mathbf{q},\omega)\mathbf{E}(\mathbf{k},\omega)[\cos\{(\mathbf{k}+\mathbf{q})\cdot\mathbf{r}-(\omega+\omega_0)\mathrm{t})\}+\cos\{(\mathbf{k}-\mathbf{q}).\mathbf{r}-(\omega-\omega_0)\mathrm{t}\}].$$

----------(2.46)

The right hand side of equation (2.46) contains two sinusoidal waves. Both have wave vectors and frequencies that are shifted compared to the incoming photon. The Stokes shifted wave has the wavevector $\mathbf{k}_{\mathrm{S}} = \mathbf{k}-\mathbf{q}$ and a frequency $\omega_{\mathrm{S}} = \omega-\omega_0$. The anti-Stokes shifted wave has the wavevector $\mathbf{k}_{\mathrm{AS}} = \mathbf{k}+\mathbf{q}$ and frequency $\omega_{\mathrm{AS}} = \omega+\omega_0$. These radiations are known as the Stokes scattered and anti-Stokes scattered light respectively. Since the phonon frequency is equal to the difference between the incident photon frequency ω and the scattered photon frequency ω_{S}, this difference is referred to as the Raman frequency or Raman shift (Stokes and anti-Stokes shifts). The Raman shift is usually expressed in wavenumbers, and has dimension of reciprocal length. The Raman spectrum is usually plotted as the intensity of the scattered radiation versus the Raman frequency. Equation (2.46) shows that the Stokes and the anti-Stokes lines have the same shift in energy from the incoming laser light. The positions of these Raman lines are located symmetrically around the Rayleigh-scattered component. Hence a peak in a spectrum can always be verified as being of Raman origin by checking that the peak also appears on the anti-Stokes side. Figure 2.13 shows the Raman spectra with Stokes and anti-Stokes line located symmetrically around the Rayleigh's scattering line.

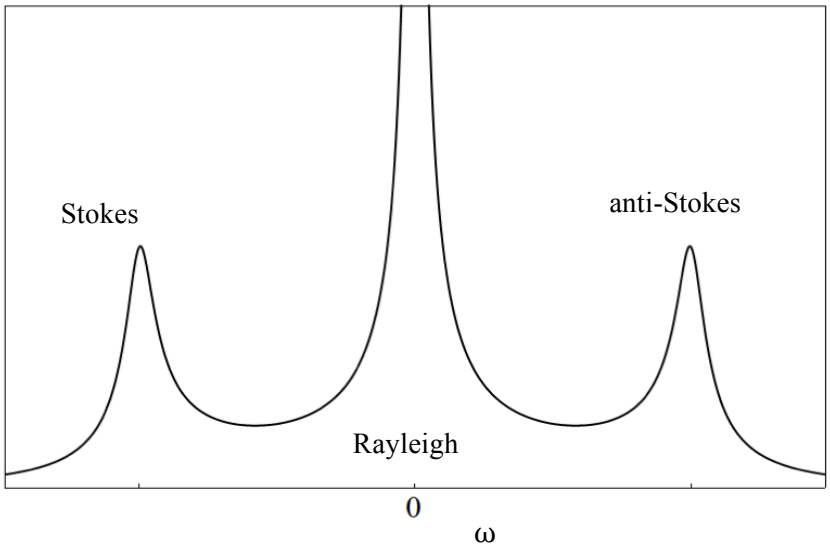

Figure 2.12: The Raman spectrum consists of Stokes and anti-Stokes lines that are located symmetrically around the Rayleigh-scattered component of the laser light.

2.2.6 Raman Tensor and Selection rules

The intensity of the scattered light can be estimated from the time-averaged power radiated by the induced polarizations $\mathbf{P}_{\text{ind}}$ into unit solid angle. The intensity depends on the polarization of the scattered radiation, $\mathbf{e}_s$, as $|\mathbf{P}_{\text{ind}} \cdot \mathbf{e}_s|^2$. If the polarization of the incident radiation is denoted by $\mathbf{e}_i$, the scattered intensity $\mathbf{I}_s$ calculated from equation (2.46) is proportional to

$$\mathbf{I}_s \propto \left| \mathbf{e}_i \cdot \left(\frac{\partial \chi}{\partial \mathbf{Q}} \right)_0 \mathbf{Q}(\omega_0) \cdot \mathbf{e}_s \right|^2 .$$

----------(2.47)

Notice that the scattered intensity is proportional to the vibration amplitude $\mathbf{Q}$ squared, indicating that there will be no Stokes scattering if no atomic vibration is present. In the present case, we will assume one-phonon scattering.

A complex tensor $\mathcal{R}$ can be defined in terms of the derivative of the susceptibility and by introducing a unit vector $\widehat{\mathbf{Q}} = \mathbf{Q}/|\mathbf{Q}|$ parallel to the phonon displacement so that

$$\mathcal{R} = (\partial\chi/\partial\mathbf{Q})_0 \widehat{\mathbf{Q}}(\mathbf{r}, t).$$

----------(2.48)

$\mathcal{R}$ is known as the Raman Tensor.

The Raman scattering intensity I_s is proportional to [27]

$$\mathbf{I}_s \propto |\mathbf{e}_i . \mathcal{R} . \mathbf{e}_s|^2 .$$

----------(2.49)

By measuring the dependence of the scattered intensity $\mathbf{I}_s$ on the incident and scattered polarizations, $\mathbf{e}_i$ and $\mathbf{e}_s$ respectively, one can deduce the symmetry of the Raman tensor and hence the symmetry of the corresponding Raman-active phonon. Therefore, Raman scattering can be used to determine both the frequency and symmetry of a zone-center phonon mode.

Additional essential requirements for Raman tensors result from the symmetries of the medium and the vibrational modes involved in the scattering. The result of these symmetry requirements is that the scattered radiation vanishes for certain choices of the $\mathbf{e}_i$ and $\mathbf{e}_s$ and the scattering geometry. These rules, known as Raman selection rules, are very useful for determining the symmetry of Raman-active phonons.

In equation (2.48), the derivative of the susceptibility with respect to phonon displacement possesses the full point group symmetry. If the representation of **Q** is contained within the representation of $(\partial\chi/\partial\mathbf{Q})$, then the Raman tensor is finite, or in other words, the phonon mode is Raman active. A simple example of Raman selection rules can be found for the centrosymmetric crystals, diamond and rocksalt. Since these crystals remain invariant under inversion, $\partial\chi/\partial\mathbf{Q}$ should remain unchanged under the same operation. However, the phonons in these crystals can be classified as having even or odd parity under the inversion operation. Because of the two identical basis atoms in a unit cell of the diamond structure, its atomic displacement pattern **Q** possesses even symmetry (even parity) and therefore R is finite (Raman active). On the other hand for the rocksalt structure, the phonons possess odd parity and therefore the Raman tensor becomes zero (Raman inactive). Hence the Raman tensor for an even-parity phonon is finite, while the Raman tensor for an odd-parity phonon must vanish in centrosymmetric crystals (within the approximation that the phonon wavevector is zero). These even-parity phonons are Raman-active while odd-parity phonons can be infrared active. Therefore Raman scattering and infrared absorption mechanisms are complementary in centrosymmetric crystals (i.e a phonon cannot be both

Raman-active and infrared-active in such crystals). Phonon modes that are neither infrared nor Raman active are termed silent modes.

Another important structure to be considered is the zincblende structure exhibited by GaSb. Its zone-center optical phonon has triply degenerate T_2 symmetry with nondegenerate LO phonon and doubly degenerate TO phonons. These three components correspond to the relative displacement of two atoms in the unit cell lying parallel to the three cubic axes of the conventional cell. GaSb lacks inversion symmetry and hence its susceptibility derivative ($\partial\chi/\partial\mathbf{Q}$) changes sign under the inversion operation. The atomic displacement pattern in this crystal also possesses odd parity. This makes the T_2 phonon modes Raman active in GaSb.

The third-rank tensor ($\partial\chi/\partial\mathbf{Q}$) for GaSb has only one linearly independent component, denoted by d. The non-zero components of the Raman tensor will depend on the atomic displacement. For an optical phonon polarized along the X axis, its Raman tensor will have two non-zero components

$$\mathcal{R}_{\mathrm{yz}}(\mathrm{X}) = \mathcal{R}_{\mathrm{zy}}(\mathrm{X}) = \mathrm{d}.$$

The Raman tensor $\mathcal{R}(\mathrm{X})$ can be expressed by a 3 × 3 matrix:

$$\mathcal{R}(\mathrm{X}) = \begin{bmatrix} 0 & 0 & 0 \\ 0 & 0 & \mathrm{d} \\ 0 & \mathrm{d} & 0 \end{bmatrix}.$$

----------(2.50-a)

Applying similar arguments to the optical phonons polarized along the Y and Z axes, the Raman tensors are

$$\mathcal{R}(\mathrm{Y}) = \begin{bmatrix} 0 & 0 & \mathrm{d} \\ 0 & 0 & 0 \\ \mathrm{d} & 0 & 0 \end{bmatrix}.$$

----------(2.50-b)

$$\mathcal{R}(\mathrm{Z}) = \begin{bmatrix} 0 & \mathrm{d} & 0 \\ \mathrm{d} & 0 & 0 \\ 0 & 0 & 0 \end{bmatrix}.$$

----------(2.50-c)

It should be noted that the zone-center optical phonon in GaSb is split into a doubly degenerate transverse optical (TO) mode and a non-degenerate longitudinal optical (LO) mode for $\mathrm{q} \neq 0$.

The Raman tensor elements for LO and TO phonons are different and expressed as d_{LO} and d_{TO} respectively. Using the Raman tensors given in equation (2.50), the selection rules for Raman scattering in GaSb can be derived. The Raman selection rules are dependent on the scattering geometry specified by four vectors $\mathbf{k}_i$, $\mathbf{k}_s$, $\mathbf{e}_i$ and $\mathbf{e}_s$, where $\mathbf{k}_i$ and $\mathbf{k}_s$ are the directions of the incident and scattered photons and $\mathbf{e_i}$ and $\mathbf{e_s}$ are the polarizations of the incident and scattered photons. The scattering configuration is then usually represented as $\mathbf{k}_i(\mathbf{e}_i, \mathbf{e}_s)\mathbf{k}_s$ [27,38].

2.2.7 Atomic displacement pattern: Phonon representation

Let us understand the origin of the T_2 excitation in a crystalline GST film in microscopic terms. In the rock-salt structure, there are two basis atoms in the unit cell.

An incident ultrafast laser pulse excites coherent phonons in a crystal by forcing atoms to vibrate in certain directions. These allowed vibrations have a specific atomic displacement pattern. This is an inherent property of any material that depends on its crystal structure. The allowed lattice vibrations in an ideal rock-salt structure involve all three axes as given below [28]:

$$\begin{aligned} d_1 &: (u_1, -v_1, -w_1); (-u_2, v_2, w_2) \\ d_2 &: (-u_1, -v_1, w_1); (u_2, v_2, -w_2) \\ d_3 &: (-u_1, v_1, -w_1); (u_2, -v_2, w_2) \end{aligned} \quad , \qquad \text{----------(2.51)}$$

where d represents the allowed displacement modes and u_i, v_i, w_i are the atomic displacement in the x, y and z direction respectively for the basis atoms (i = 1, 2). However the atomic vibration along the X-axis (expressed as u_i) is very small and can be neglected.

The allowed atomic displacements in a GaSb crystal can be represented as

$$\begin{aligned} d_1 &: (0, 0, z_1); (0, 0, z_2) \\ d_2 &: (x_1, -y_1, 0); (-x_2, y_2, 0) \\ d_3 &: (x_1, y_1, 0); (-x_2, -y_2, 0) \end{aligned} \quad . \qquad \text{----------(2.52)}$$

2.3 Phase-Change Materials

Alloys such as $Ge_2Sb_2Te_5$ (GST) have attracted great interest due to their favorable properties for phase-change memory applications [39]. The use of GST for optical disk coatings is well established, while more recently GST has also been used in the development of phase-change random access memory (PCRAM) [40] and within new paradigms for bio-inspired computing [41,42]. Phase-change materials were introduced by Stanford Ovshinsky in 1968 [43]. The popularity of GST stems from the fast and reversible phase transition that occurs between its amorphous (RESET) and cubic crystalline phases (SET), and the strong contrast in electrical conductance and optical reflectance that these phases exhibit. A lot of research has been done on this material to understand its structure, optical properties such as reflectivity and phonon behaviour, electrical properties e.g. resistance of memory cells, and transition behavior from one state to another etc. This section gives a brief description of the GST crystal structure and the principles by which GST may be used to construct a memory device.

2.3.1 Storage principle

The phase-change memory can switch between two structural states. Therefore the logical state of the memory device is determined by the structure of the device in that state. If it is crystalline, the state is equivalent to 1 or SET state. In the amorphous phase, the device is in the RESET or 0 binary state [44].

There are two types of switching phenomena: Ovonic threshold switching (OTS), which switches the material from a high-resistance to the low-resistance state and Ovonic memory switching (OMS), a reversible mechanism induced because of Joule heating. A typical *I–V* curve for a GST memory cell is shown in figure 2.14 and shows the presence of both mechanisms. At low bias the cell is in a high-resistance amorphous state. However, as a threshold voltage is reached, OTS takes place. The current value rapidly rises with a voltage snap-back, but, even after switching, the material is still amorphous. When the current is further increased, the Joule heating becomes high enough to crystallize the GST without melting. This is known as memory switching. The resistor status is read by simply

using a lower voltage. On the other hand, information storage on an optical disk relies on OMS only [45, 46]. The difference in the electron density leads to the difference in reflectivity, which makes the optical read out possible. Phase-change materials were commercialized in 1990 for optical data storage [45]. After this, threshold and memory switching have been observed in many other materials, for example nickel oxide [47], metal-semiconductor-metal structures [48], transition metal-oxides [49] etc.

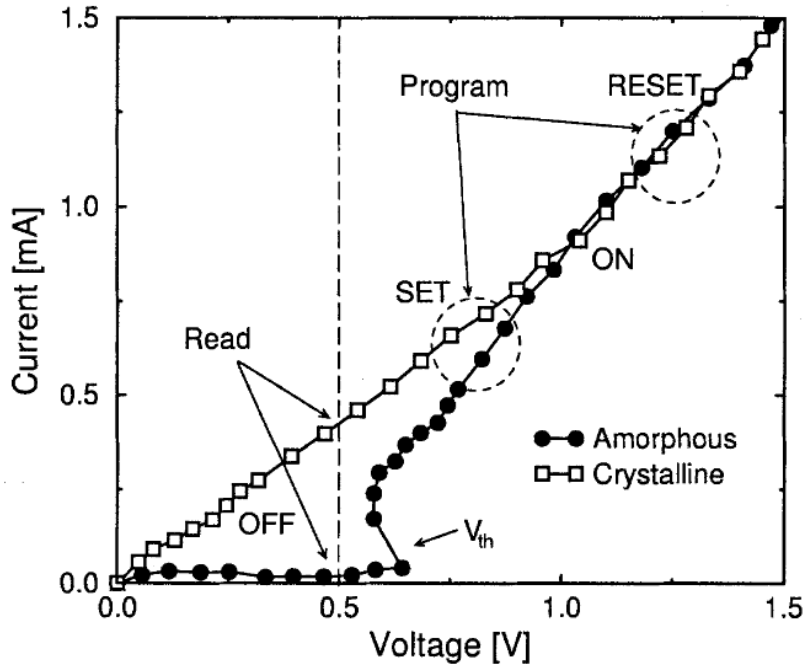

Figure 2.13: Typical I-V curve for crystalline and amorphous $Ge_2Sb_2Te_5$ [50]

2.3.2 Structure and Resonant bonding

Crystalline GST has two possible structures: a stable hexagonal and a metastable face centred cubic phase [51,52]. Since the metastable state crystallizes faster [44], GST always crystallizes in the fcc structure during the phase-change process. In reality, the rock-salt structure is slightly distorted with Te located at one sublattice position and Ge, Sb and 20% vacancies sharing the other sublattice [53]. Although the amorphous state does not have any long range order, it is important to mention that the chemical short-range order remains similar in the two phases. Early studies of the amorphous phase of phase-change materials indicated that the local coordination of the amorphous phase is inherited from its parent crystalline phase. However, there is a completely different type of bonding in the two phases. It was shown by Kolobov et al. in 2004 that Ge atoms are octahedrally coordinated in crystalline $Ge_2Sb_2Te_5$ with three shorter and three longer Ge-Te bonds. Long Ge-Te bonds are broken during amorphization, flipping the Ge atom from octahedral to tetrahedral coordination [54]. Short and strong Ge-Te bonds give more stability to the amorphous phase, making GST a suitable material for data storage. Using extended X-ray absorption fine-structure (EXAFS) spectroscopy, and assuming flipping of Ge atoms, Kolobov suggested a different local structure for the two phases of GST. Taylor et. al. in 2005 presented a model to explain the local structure of ternary chalcogenide glasses using the covalent nature of bonding [55]. A few years later in 2007 Baker et. al. demonstrated that there are Ge-Ge bonds present in the amorphous phase of GST alloy [56]. It was recently reported by Wuttig et. al that tetrahedrally coordinated Ge atoms in the amorphous phase only represent a minority, about $1/3^{rd}$ of all germanium atoms. Instead, the amorphous phase contains Ge-Ge and Ge-Sb bonds, referred to as "wrong bonds", rather than only Ge-Te bonds [57]. Therefore in the phase transition, healing of wrong bonds is as important as the umbrella flip of Ge atoms. The fast crystallization in GST stems from the fact that only a small change in the GST structure is required to reduce the strong distortion. The removal of wrong bonds and Ge atoms in tetrahedral coordination is the most significant rearrangement, but it most likely slows down the progress of fast crystallization.

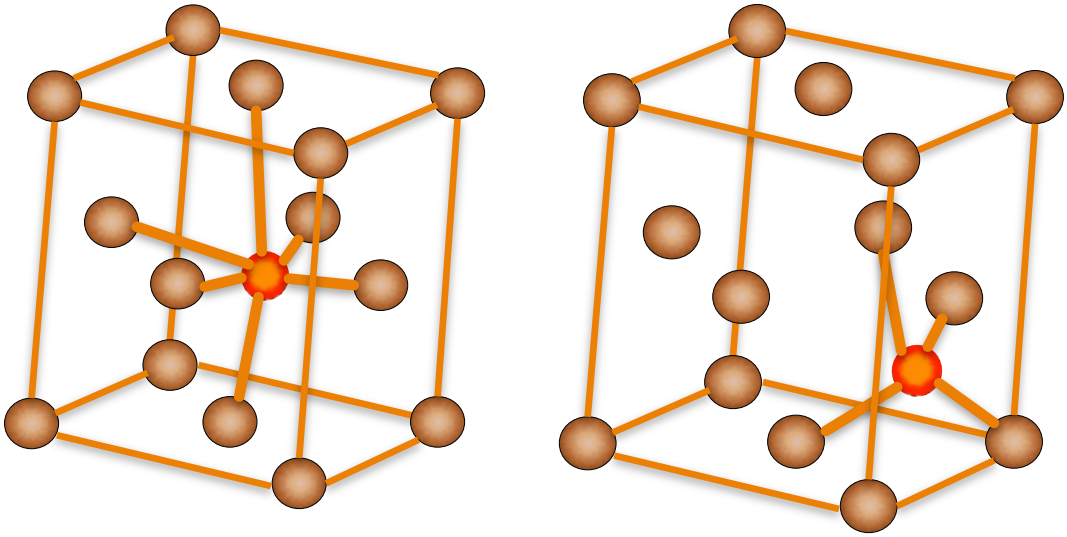

Figure 2.14: Changing Ge coordination during the crystalline to amorphous phase transition [54]

The local structure of GST glasses can be explained with the help of homo- and hetero-polar bonds. Unlike the amorphous phase, the different elements in the crystalline alloy do not follow the 8-N rule of covalent bonding. Instead the coordination number for different elements is much higher than expected from the 8-N covalent rule. Let us understand the covalent bonding in elemental Sb, which has the fcc structure. Sb atoms have five electrons in the outer shell, with one filled s-orbital and three half-filled p-orbitals (with one electron in each). These p-orbitals make three independent bonds with the adjacent atoms along the x, y and z directions. This leads to a half-filled band with zero bandgap at the Fermi energy E_F. This structure is unstable, exhibiting a Peierls distortion in the chain where alternative shorter and longer bonds lower the free energy and open up a gap at E_F.

The situation when there are more than the allowed (8-N) electrons involved in bonding, was called resonant bonding by Pauli. In Sb, half-filled p-orbitals make two bonds to the left and right as shown in fig 2.16. The Sb atom has six nearest neighbours with only three electrons to participate in covalent bonding. Sb can form bonds with adjacent atoms to the left or right or to both, which is the most likely configuration as shown in the middle of the

figure. The resonant bonding causes electron delocalization, which in turn leads to increased electronic polarizability [58].

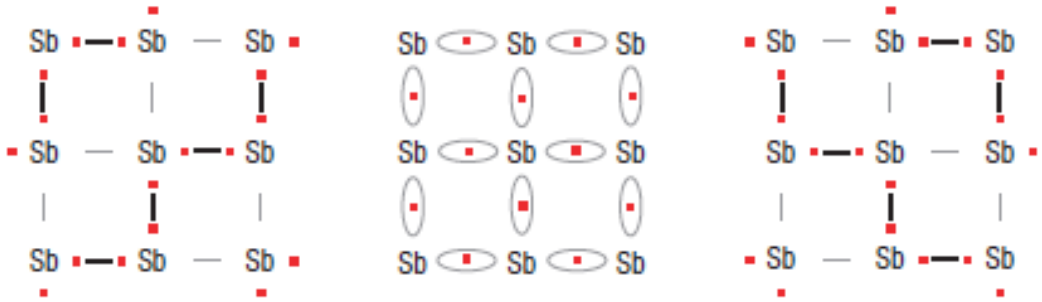

Figure 2.15: Schematic diagram demonstrating the origin of resonance bonding for Sb

2.3.3 Non thermal melting

It is of fundamental importance to study the dynamic properties of the electrons and the lattice so as to be able to explain many basic properties of a material such as conductivity, magnetism, and linear and non-linear optical properties. In order to study the carrier dynamics, a non-equilibrium state is induced by excitation with ultrafast laser pulses. The heat capacity of the electrons is much smaller than that of lattice. Therefore, when an ultrafast laser with duration shorter than the electron relaxation life time is applied to a material, it rapidly heats the electrons to a very high temperature while leaving the lattice at a relatively lower temperature. The transient two-temperature system tries to reach thermal equilibrium via carrier-carrier interaction and electron transport out of the excited region. This process occurs on timescales of a few picoseconds. In non-thermal melting, the laser induced intense excitation of bonding electrons could enhance atomic mobility without transferring significant thermal energy to the lattice. However, even with non-thermal melting, which occurs on the order of hundreds of femtoseconds, the excited carriers and lattice reach thermal equilibrium within a few picoseconds, making the subsequent transition thermal in nature.

Non-thermal melting has been observed in many materials, such as GaAs [15], Al [16] and many other semiconductors [12,13,16,59,60,61]. But no such study has been reported on

phase-change materials yet. In this thesis, we are concerned with the carrier dynamics on the femtosecond time scale, which provides information about the nonthermal dynamics of the material and the behavior of its phonons, which are a fingerprint of the structure and a precursor to the structural transition.

Chapter 3

Experimental Technique

In this chapter, a detailed description of the measurement technique is provided. The time-resolved set up in Exeter had been built before I started my Ph.D project. Dr. Yanwei Liu and I have set up a single-colour time-resolved pump-probe technique to measure phase-change materials. Therefore, the development of the measurement procedure is described in greater detail. Emphasis is also placed upon obtaining the signal from a noisy background and understanding the measured signals.

The chapter begins with a brief introduction to isotropic and anisotropic media and the form of the refractive index that gives rise to an ordinary and extraordinary ray. Expressions for Fresnel reflection coefficients are provided to describe the rotation of polarization and ellipticity induced by such a sample. The time-resolved pump-probe technique used to measure the reflectance (R) and rotation (also known as anisotropic reflectance or AR) signal using an optical bridge detector is then described in detail. A mathematical description is given to show that the difference of the two signal outputs of the optical bridge detector is equal to the rotation of the incident polarization. Finally the equation required to fit the experimental data curves is presented with its derivation given in Appendix 1.

3.1 Introduction

An optical medium can be defined in terms of its permittivity tensor. Isotropic materials have a single permittivity whereas uniaxial materials have two characteristic permittivity values. For a uniaxial material, the permittivity along the optical axis is different from that in the two orthogonal directions. The optical axis of a crystal is an axis of symmetry where all the perpendicular directions are optically equivalent. Therefore a wave transmitted along the optical axis does not suffer any birefringence. For biaxially anisotropic materials, there are two optic axes. These materials have three different values of the permittivity [62]. If linearly polarized light is propagating in a medium with its electric field perpendicular to the optic axis, then this is known as an ordinary ray. Linearly polarized light with its electric field parallel to the optical axis is called an extraordinary ray. The refractive indices for the ordinary and extraordinary rays are usually represented as n_o and n_e respectively.

3.2 Generalized Reflection Coefficients

When light is incident on a plane surface, some part of it is reflected and some is transmitted as shown in fig 3.1. The reflectivity (R) of a sample is defined as the ratio of reflected power to the incident power $R = I_r/I_i$ where I_i and I_r are the intensity of incident and reflected light respectively [63]. The wavelength and polarization of the incident light as well as the optical properties of the sample determine the reflectivity.

Polarized light passing through an optical element can be described using the Jones matrix formalism. Jones vectors describe the relative amplitude and relative phase of the electric field in the x and y directions, while the Jones matrices represent the polarized components. When polarized light crosses an optical element, the polarization of the emerging light is calculated by taking the product of the Jones vector of the incident light and Jones matrix of the optical element. The electric-field components E_p^r and E_s^r of the reflected light can be described in terms of the incident electric-field components $E_p^{(i)}$ and $E_s^{(i)}$ by

$$\begin{pmatrix} E_s^{(r)} \\ E_p^{(r)} \end{pmatrix} = \begin{pmatrix} r_{ss} & r_{sp} \\ r_{ps} & r_{pp} \end{pmatrix} \begin{pmatrix} E_s^{(i)} \\ E_p^{(i)} \end{pmatrix}.$$

----------(3.1)

By implementing the Jones matrix calculations, the reflectivity for incident light polarized at an angle θ to the plane of incidence is

$$R = \left(|r_{ss}|^2 + |r_{ps}|^2\right)\sin^2\theta + \left(|r_{pp}|^2 + |r_{sp}|^2\right)\cos^2\theta + \frac{1}{2}\left(r_{ss}r_{sp}^{*} + r_{pp}r_{ps}^{*}\right)\sin^2\theta,$$

----------(3.2)

where r_{ss}, r_{sp}, r_{ps} and r_{pp} denote the optical reflection coefficients for non-magnetic media [63].

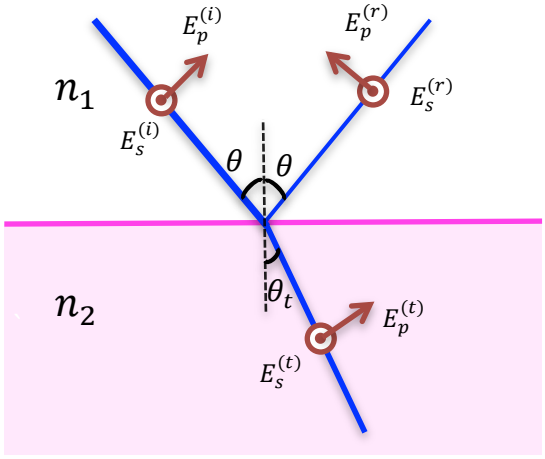

Figure 3.1: p and s-components of the incident, reflected and transmitted light at an interface

Reflection coefficients are derived in reference [64] for the case that plane waves of p or s polarization are incident on an arbitrary face of a uniaxial crystal. The expressions for the reflection coefficients reflected from a biaxial crystal are even more complicated.

Let us consider the case when the optic axis of the crystal lies in the reflecting plane making an angle φ with the x-axis, where the plane of incidence is the zx plane and the reflecting surface is the xy plane with the z axis normal to the surface. The direction cosines of the optical axis along the x, y and z axes are given as $\cos\varphi$, $\sin\varphi$ and 0 respectively.

If n_1 and k define the refractive index and wavenumber of the incident wave in medium 1 and n_o, q_o and n_e, q_e are the refractive index and wavenumber for the ordinary and extraordinary ray in medium 2 respectively, then the reflection coefficients can be expressed as

$$r_{ss=} \frac{k^2 \begin{bmatrix} \left\{(k\sin\theta - q_o)\left(\frac{q_o n_1^2}{k\sin\theta n_o^2} + 1\right)(n_o^2 - \cos^2\varphi\cos^2\theta)\right\} - \\ (q_e - q_o)\left\{n_o^2 - \cos^2\varphi\cos^2\theta + \frac{q_o}{k\sin\theta}\left(n_1^2 - \cos^2\varphi\,(2n_1^2 - \cos^2\theta)\right)\right\} \end{bmatrix}}{D},$$

----------(3.3)

$$r_{pp=} \frac{k^2 \begin{bmatrix} \left\{(k\sin\theta + q_o)\left(\frac{q_o n_1^2}{k\sin\theta n_o^2} - 1\right)(n_o^2 - \cos^2\varphi\cos^2\theta)\right\} - \\ (q_e - q_o)\left\{n_o^2 - \cos^2\varphi\cos^2\theta - \frac{q_o}{k\sin\theta}\left(n_1^2 - \cos^2\varphi\,(2n_1^2 - \cos^2\theta)\right)\right\} \end{bmatrix}}{D},$$

----------(3.4)

and

$$r_{ps} = r_{sp} = \frac{2\cos\varphi\sin\varphi\, q_o(q_o - q_e)n_1 k}{D},$$

----------(3.5)

where

$$\begin{aligned} D = &\left\{(k\sin\theta + q_o)\left\{\frac{q_o n_1^2}{k\sin\theta n_o^2} + 1\right\}(n_o^2 k^2 - \cos^2\varphi\cos^2\theta\, k^2)\right\} \\ &+ \left\{(q_e - q_o)\left[n_o^2 k^2 - \cos^2\varphi\cos^2\theta\, k^2\right.\right. \\ &\left.\left. + \frac{q_o}{k\sin\theta}(n_1^2 k^2 - \cos^2\varphi\cos^2\theta\, k^2)\right]\right\}, \end{aligned}$$

----------(3.6)

and

$$q_o^2 = k\sqrt{n_o^2 - \cos^2\theta},$$

$$q_e^2 = k\sqrt{\left(\frac{n_e^2}{n_o^2} - 1\right)(n_o^2 - \cos^2\varphi\cos^2\theta)}\,.$$

----------(3.7)

The rotation and ellipticity of the reflected light for incident p-polarised light are defined as the real and imaginary parts of the ratio of optical reflection coefficients r_{sp} and r_{pp} respectively.

$$\theta = -\mathrm{Re}\left\{\frac{r_{sp}}{r_{pp}}\right\},$$
$$\varepsilon = \mathrm{Im}\left\{\frac{r_{sp}}{r_{pp}}\right\}.$$

----------(3.8)

Similarly the rotation and ellipticity of the reflected light for incident s-polarised light are

$$\theta = \mathrm{Re}\left\{\frac{r_{ps}}{r_{ss}}\right\},$$
$$\varepsilon = \mathrm{Im}\left\{\frac{r_{ps}}{r_{ss}}\right\}.$$

----------(3.9)

The expression in equ (3.5) becomes zero when the incident beam is polarized either along the optical axis ($\cos\varphi = 0$) or perpendicular to it ($\sin\varphi = 0$) and therefore no rotation is observed. However if the beam makes an angle of 45^0 with the optical axis, then r_{ps} and r_{sp} and hence the rotation obtain their maximum values.

A schematic diagram showing the rotation and ellipticity is presented in figure 3.2. The off-diagonal components of the reflection coefficient matrix are provided in equation 3.5. If the incident light induces anisotropy or birefringence in the non-magnetic material such that the velocity of light varies with the polarization, the off-diagonal components r_{sp} and r_{ps} can again become non-zero. Consequently the incident *p* (or *s*) polarized light will induce an *s* (or *p*) electric-field component in the reflected light as per equation 3.1.

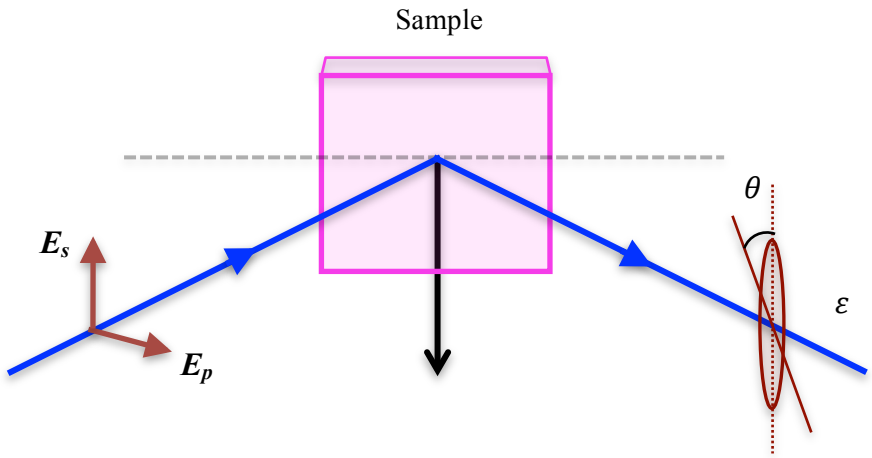

Figure 3.2: The schematic diagram displaying rotation θ and ellipticity ε in the reflected light from a sample.

Generally,

$$r_{pp} \neq r_{ss} \text{ and } E_s^{(r)}/E_p^{(r)} \neq E_s/E_p \,.$$

----------(3.10)

which implies that if the incident light is not perfectly p (or s) polarized then the plane of polarization can be rotated upon reflection. Therefore, to measure the rotation due to the optical Kerr effect, the incident light should be either p (or s) polarized.

Rotation matrix

Let us consider an incident beam of light, with its electric field defined within the (x', y') plane with electric field components $E_{x'}$ and $E_{y'}$. If we wish to instead represent the electric field in an (x, y) coordinate system which is rotated by an angle θ with respect to the (x', y') system, then the electric field components E_x and E_y are related to the components $E_{x'}$ and $E_{y'}$ by the application of a rotation matrix as shown below.

$$\begin{pmatrix} E_x \\ E_y \end{pmatrix} = \begin{pmatrix} \cos\theta & -\sin\theta \\ \sin\theta & \cos\theta \end{pmatrix} \begin{pmatrix} E_{x'} \\ E_{y'} \end{pmatrix}.$$

----------(3.11)

3.3 Time-resolved pump probe set up

This technique is used to study the ultrafast response of a sample in the presence of the SOKE (specular optical Kerr effect), MOKE (magneto optical Kerr effect), carrier-carrier (or phonon) interaction, carrier relaxation, etc. This technique requires two ultrashort pulses termed the pump pulse and probe pulse. The pump pulse optically modifies the sample by generating some excitation, then, at a variable time delay, a weaker probe pulse records the response of the sample. It then becomes possible to obtain information about the processes initiated by the pump pulse. The reflected probe beam typically exhibits only a small variation in intensity and polarization and the detector requires the reflection originating from the pump beam to be carefully excluded from the detector. This can be achieved using different optical paths, along with different polarizations for the pump and the probe beam. Therefore the probe beam can be well separated from the pump beam when specularly reflected from a sample with an even surface. However if the sample surface is rough, there is a significant amount of diffusely scattered light and then the two beams cannot be easily separated just by using a different polarization or alignment geometry. Using two different wavelengths for the pump and probe can be helpful in such cases. Depending on the wavelengths used for the pump and probe beams, the measurements can be classified as either single-colour or two-colour.

The set up for optical pump-probe experiments is shown in fig 3.3. The pulsed laser output of an amplified laser system is split into two beams: a high-intensity pump and a weaker probe pulse. The pump beam passes through a translation stage to allow up to 4 ns of time delay to be introduced between the two pulses, with a minimum step size of 1.67 fs. The probe beam is s-polarized, so that its electric field lies perpendicular to the plane of incidence, while the pump beam is linearly polarized at an angle that can be varied continuously. The pump beam intensity was modulated at a frequency of 692 Hz by an optical chopper before converging the beam at the same spot as the probe beam on the sample surface. The size of the probe beam spot was significantly smaller than the size of the pump beam spot. A beam profiler was used to obtain the optimum overlap of pump and probe beam and measure the focussed spot sizes. A CCD camera was used to confirm the overlap after replacing the sample at the position of the beam profiler. The reflected probe beam was directed to a balanced polarization bridge detector comprised of a polarizing

beam splitter and two photodiodes. The sum and difference of the photodiode outputs yield the reflectance (R) and rotation (AR) signals respectively. Each signal was sent to a separate dual-phase lock-in amplifier so that the transient R and AR signals induced by the pump beam could be extracted. A filter was placed before the bridge detector to remove the diffusely scattered pump light. This scattered light, if incident upon the detector, can significantly reduce the signal-to-noise ratio. Most of the scattered light usually comes from the chopper. The pulses must be unchirped when they arrive at the sample or else strong variations of the transient anisotropic reflectance (AR) signal may be induced close to the zero-time delay condition [65].

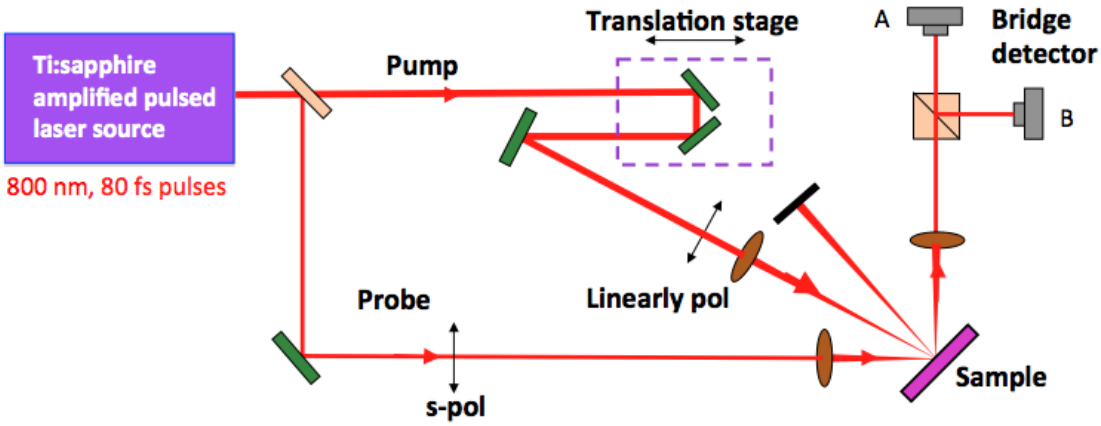

Figure 3.3: The typical set up of time-resolved optical pump-probe experiments

To identify changes in ellipticity, a quarter wave-plate is inserted just before the bridge detector with its fast axis parallel to the major axis of the polarization ellipse. It induces a phase difference of 90 deg between the orthogonal polarization components and converts rotation to ellipticity and *vice versa*.

One should also be careful in aligning the bridge detector and probe polarization because misalignment of either of these can cause an additional contribution to the measured rotation signal. These contributions are known as reflectivity breakthrough and originate from pump-induced changes in the diagonal reflection coefficients (r_{ss} and r_{pp}). These

components are found to be proportional to the transient reflectivity. Therefore the signal observed in the rotation channel appears more like that within the reflectivity channel. The reflectivity breakthrough persists for hundreds of femtoseconds [66]. When light is incident on a non-magnetic sample, there are generally two contributions to the rotation signal: the first is the SOKE peak, centred at zero time delay, which is observed when pump and probe have different polarization states, with a maximum peak amplitude when pump and probe polarizations are at +/- 45 deg to each other [67]; and the second is reflectivity breakthrough which occurs if the probe beam is not precisely p or s polarized. Therefore to precisely measure the signal and remove traces of reflectivity breakthrough from the transient rotation signal, the probe beam polarization should be gradually changed. The pump polarization must be kept linear and parallel to that of the probe polarization to remove the effect of the SOKE feature. The bridge detector should also be readjusted after the probe polarization is changed so that its static output is zero.

The basic principle and alignment procedure for two-colour measurements is the same as that for single-colour measurements. The only difference is that two different wavelengths for pump and probe are used, usually red (800 nm) and blue (400 nm).

Our ultrafast laser system consists of a Coherent Verdi 18 which is a solid-state single-wavelength green laser (532 nm) with an output power of 18W. 6W of the Verdi's power is used to pump the Mira SEED Ti:Sapphire laser, and the remaining 12W goes to the regenerative amplifier (RegA). The Mira is designed to produce ultrashort pulses of 800 nm central wavelength, <60 fs pulse width, 80 MHz repetition rate, with a mode-locked average power of more than 250 mW. These pulses are amplified in the RegA using chirped pulse amplification (CPA). The output pulses from the Mira are first stretched in the time domain by a stretcher/compressor to avoid high-intensity damage to the cavity optics within the RegA. The RegA system amplifies the nJ pulses from the 800 nm to μJ energies, with an average power of greater than 750 mW, 800 nm wavelength, and a repetition rate up to 250 kHz. These amplified pulses again pass through the stretcher/compressor to return them to <60 fs pulse width.

3.4 Measuring spot size

We define pump fluence as

$$\text{Pump Fluence} = \frac{\text{Pulse energy}}{\text{spot area}}.$$

where the pulse energy is the ratio of the applied pump power to the number of pulses per second, so that,

$$\text{Pump Fluence} = \frac{\text{applied pump power}}{\text{No of pulses} \times \text{spot area}}.$$

----------(3.12)

It is important to know the spot sizes for the pump and probe beams in order to calculate the incident fluence on the sample and to confirm that the probe spot is significantly smaller than that of the pump.

The diameter of the laser spot depends on the focal length of the focusing lens (f) and the divergence of the incident beam θ as

$$d = f\theta.$$

----------(3.13)

The spot size can be reduced either by using a focusing lens of shorter focal length, or by reducing the beam divergence, or both. In our experimental set up, the divergence of the probe beam was reduced by using a 10x beam expander placed immediately before a focusing lens of focal length 6.3 cm that converged the probe beam at the sample surface. The pump beam passed through a telescope before entering the delay stage and was finally focused at the sample by using a lens with a focal length of 25 cm.

A beam profiler was inserted at the focus of the pump and probe beams to measure their spot sizes and obtain the optimum overlap. The beam-profiler images of the pump and probe spots are shown in fig 3.4. The CCD beam profiler is a DataRay WinCAM-D UCD12, with a 6.3 × 4.8 mm^2 CCD with pixel size of 4.6 μm that can measure the full width half maxima (FWHM) and $\frac{1}{e^2}$ spot diameters with 1D and 2D intensity profiles. We were able to achieve a minimum pump spot size of 100 × 120 μm^2 and minimum probe size

of 30 × 40 μm^2. The spot sizes were monitored while moving the delay stage from one end to the other to maintain constant laser fluence. The images of the pump and probe beams were simultaneously collected by the CCD camera. It ensures the overlap of two beams on the sample at different time delays.

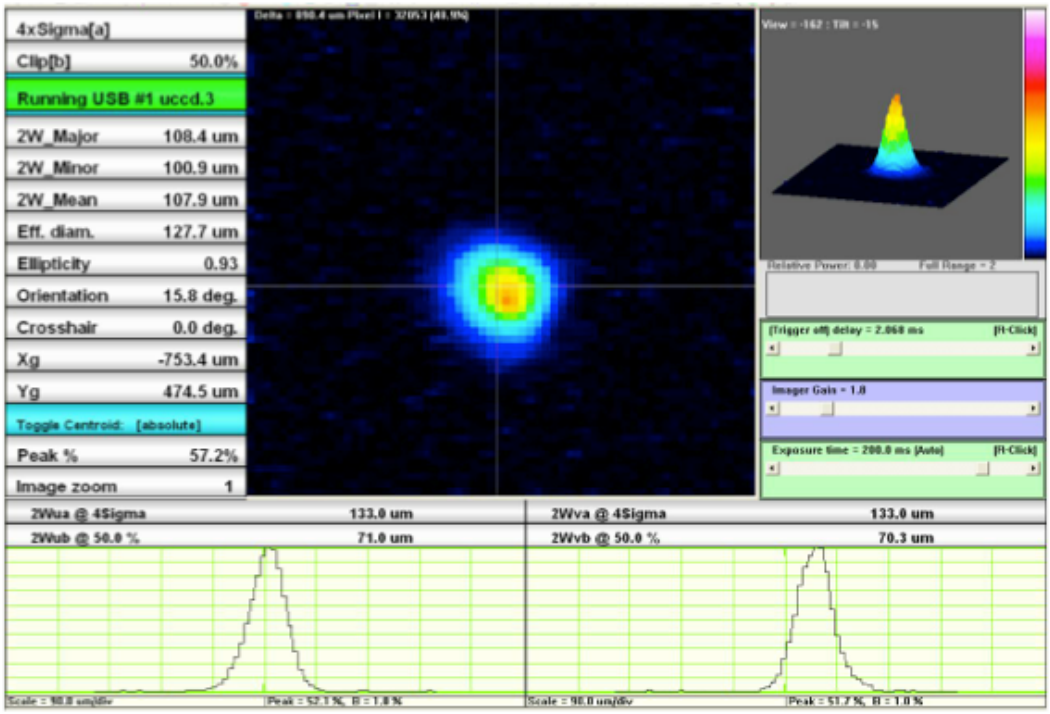

Figure 3.4: Beam-profiler image of pump and probe spot overlap

3.5 Optical bridge detector

The optical bridge detector consists of a Glan-Thompson polarizing beam splitter and two photo diodes. The beam splitter is made from a birefringent calcite material that divides the incident light into orthogonally linearly polarized (s and p polarization) components separated by an angle of 45 deg. A schematic diagram of the polarizing beam splitter is shown in fig 3.5. In a birefringent material, the value of the refractive index and hence the

velocity of propagation is different for ordinary and extraordinary waves. For the Glan-Thompson polarizing beamsplitter, the angular separation of the two beams is independent of the incident wavelength. The large-area silicon photodiodes measure the intensity of the two beams. The sum and difference of the two signals are proportional to the reflectivity and rotation of the probe polarization, respectively.

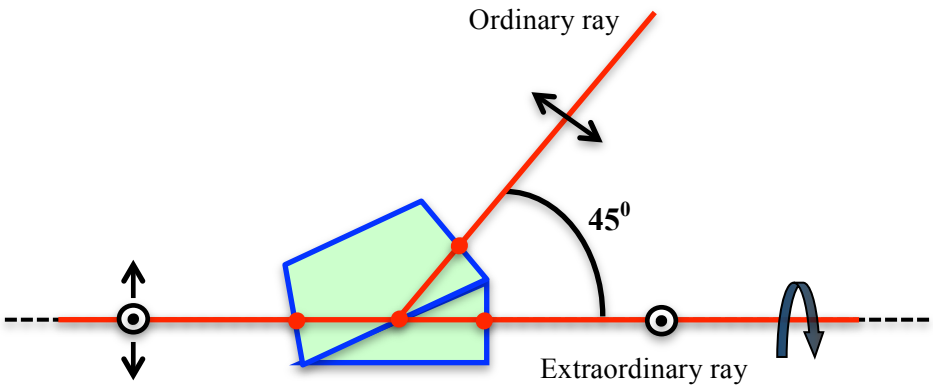

Figure 3.5: Schematic diagram of the polarizing beam splitter

The detector is aligned so that the reflected probe light is normally incident on the front face of the polarizing beam splitter. To increase the sensitivity of the detection technique, the pump beam was blocked, so as not to induce any optical modification of the sample, and then the difference signal was nulled by rotating the detector about the axis, as shown in fig 3.5 so that s and p polarized components had equal intensity. When a pump pulse induces birefringence in the sample, the polarization state of the probe beam reflected from the sample at a later time delay will change. This will cause the difference signal to change, and therefore the difference signal monitors the changes introduced by the pump beam in the sample.

3.6 Rotation signal calculation

If the probe polarization is s or p, the detector is aligned at 45 deg to the plane of incidence, so that the intensity of the two output beams of the photodetector prior to any pump-induced birefringence is

$$I_0 = \frac{{E_0}^2}{2}.$$

----------(3.14)

When the pump beam induces birefringence in the sample, the output signal from the optical bridge detector is measured as the difference in intensity incident on the two photo-diodes (shown in fig 3.6). Therefore the output difference signal can be written as,

$$S \propto I_A - I_B ,$$

----------(3.15)

where I_A and I_B are the intensities incident upon the two photodiodes.

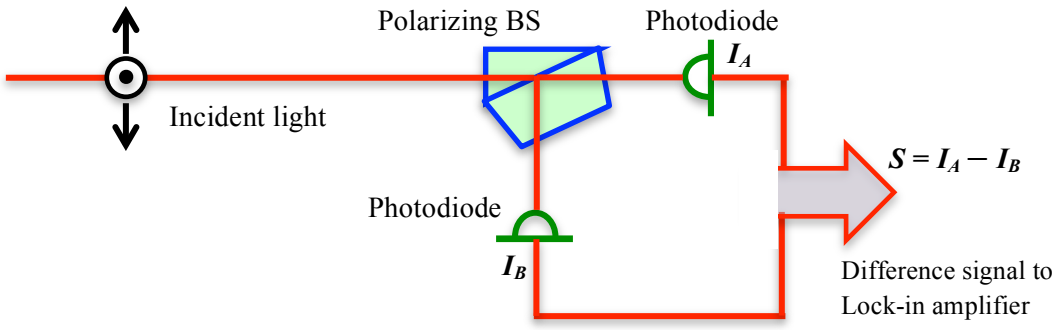

Figure 3.6: The detection of the difference signal from the optical bridge detector

Now, it will be shown here that the difference of the photodiode outputs (S) yields a signal proportional to the rotation of the probe polarization (θ).

If the reflected elliptically polarised probe beam is rotated by an angle θ by the pump-induced birefringence in the sample, then its electric field components in the x', y' coordinate system can be expressed as

$$E_x' = E_0 \cos \omega t, \text{ and } E_y' = E_0 \sin \varepsilon \sin \omega t \,,$$

----------(3.16)

where ε is the ellipticity of the probe beam. Projecting onto the x, y coordinate system, the x and y components of the electric field can be calculated using the rotation matrix.

$$\begin{pmatrix} E_x \\ E_y \end{pmatrix} = \begin{pmatrix} \cos\left(\frac{\pi}{4} + \theta\right) & -\sin\left(\frac{\pi}{4} + \theta\right) \\ \sin\left(\frac{\pi}{4} + \theta\right) & \cos\left(\frac{\pi}{4} + \theta\right) \end{pmatrix} \begin{pmatrix} E_x{}' \\ E_y{}' \end{pmatrix},$$

----------(3.17)

$$\begin{pmatrix} E_x \\ E_y \end{pmatrix} = \begin{pmatrix} \cos\left(\frac{\pi}{4} + \theta\right) & -\sin\left(\frac{\pi}{4} + \theta\right) \\ \sin\left(\frac{\pi}{4} + \theta\right) & \cos\left(\frac{\pi}{4} + \theta\right) \end{pmatrix} \begin{pmatrix} E_0 \cos \omega t \\ E_0 \sin \varepsilon \sin \omega t \end{pmatrix}.$$

----------(3.18)

Therefore,

$$E_x = E_0 \ \cos \omega t \ \cos\left(\frac{\pi}{4} + \theta\right) - E_0 \ \sin \varepsilon \sin \omega t \sin\left(\frac{\pi}{4} + \theta\right),$$

and

$$E_y = E_0 \ \cos \omega t \ \sin\left(\frac{\pi}{4} + \theta\right) + E_0 \ \sin \varepsilon \sin \omega t \cos\left(\frac{\pi}{4} + \theta\right).$$

----------(3.19)

The intensity at the first photodiode is

$$I_A = \frac{1}{2}\overline{E_x{}^2}$$

$$I_A = \frac{1}{2\tau}\int_0^{\tau} {E_0}^2 \left\{\cos \omega t \ \cos\left(\frac{\pi}{4} + \theta\right) - \sin \varepsilon \sin \omega t \ \sin\left(\frac{\pi}{4} + \theta\right)\right\}^2 dt \,,$$

----------(3.20)

where τ is the pulse width for a square pulse.

$$I_A = \frac{{E_0}^2}{2\tau}\int_0^{\tau}\left\{\cos^2\omega t\,\cos^2\left(\frac{\pi}{4}+\theta\right)+\sin^2\varepsilon\ \sin^2\omega t\ \sin^2\left(\frac{\pi}{4}+\theta\right)\right.$$
$$\left.-\frac{1}{2}\sin\varepsilon\,\sin 2\omega t\,\sin\left(\frac{\pi}{2}+2\theta\right)\right\}dt\,.$$

----------(3.21)

Neglecting second-order terms, i.e. $\sin^2\varepsilon \simeq 0$,

$$I_A = \frac{{E_0}^2}{2\tau}\int_0^{\tau}\left\{\frac{1}{2}(1+\cos 2\omega t)\cos^2\left(\frac{\pi}{4}+\theta\right)-\frac{1}{2}\sin\varepsilon\,\sin 2\omega t\,\sin\left(\frac{\pi}{2}+2\theta\right)\right\}dt\,,$$

$$I_A = \frac{{E_0}^2}{4\tau}\left\{\frac{\sin 2\omega\tau}{2\omega}\cos^2\left(\frac{\pi}{4}+\theta\right)+\frac{1}{2}\sin\varepsilon\ \frac{\cos 2\omega\tau}{2\omega}\sin\left(\frac{\pi}{2}+2\theta\right)\right\},$$

----------(3.22)

Using $\sin 2\omega\tau \simeq 2\omega$ for small τ,

$$I_A = \frac{{E_0}^2}{4}\cos^2\left(\frac{\pi}{4}+\theta\right),$$

----------(3.23)

since $\theta \ll 1$

$$I_A = \frac{{E_0}^2}{4}\left[\frac{\cos\theta}{\sqrt{2}}-\frac{\sin\theta}{\sqrt{2}}\right]^2,$$

$$I_A = \frac{{E_0}^2}{4}\cos^2\left(\frac{\pi}{4}+\theta\right) = \frac{{E_0}^2}{4}\left[\frac{1}{2}-\frac{1}{2}\sin 2\theta\right].$$

----------(3.24)

Likewise, the intensity at the second photodiode is

$$I_B = \frac{1}{2}\overline{{E_y}^2}\ ,$$

$$I_B = \frac{{E_0}^2}{4}\ \sin^2\left(\frac{\pi}{4}+\theta\right) = \frac{{E_0}^2}{4}\left[\frac{1}{2}+\frac{1}{2}\sin 2\theta\right].$$

----------(3.25)

Therefore, the difference signal generated at photodiodes A and B is

$$I_A - I_B = \frac{{E_0}^2}{4}\left[\frac{1}{2}-\frac{1}{2}\sin 2\theta\right]-\frac{{E_0}^2}{4}\left[\frac{1}{2}+\frac{1}{2}\sin 2\theta\right],$$

$$I_A - I_B \propto \frac{{E_0}^2}{4}[\sin 2\theta]\,,$$

----------(3.26)

For small θ, $\sin 2\theta \simeq \theta$. Therefore

$$\boldsymbol{I_A - I_B \propto I_0\theta}\,,$$

----------(3.27)

which demonstrates that the difference of the two photodiode signals is proportional to the optical rotation.

3.7 Lock-in amplifier

The bridge detector is connected to the lock-in amplifier by a BNC cable to recover the signal from a noisy background. There is another connection to the lock-in for the optical chopper, which provides a frequency of 692 Hz as a reference. The lock-in amplifier measures the amplitude and phase of the part of the signal that occurs at the reference frequency. A schematic of the lock-in amplifier is shown in fig 3.7. It has two inputs: a signal (to measure) and a reference (connected to input beam and lock-in) defined as

$$V_{in} = \mathrm{A}\cos\omega t \text{ and } V_{ref} = \mathrm{B}\cos(\omega t + \phi)\,.$$

----------(3.28)

Both inputs are connected to a phase-sensitive detector (PSD), which multiplies the two components, resulting in an output voltage of the form

$$V_{psd} = \mathrm{A}\cos\omega t \times \mathrm{B}\cos(\omega t + \phi)\,,$$
$$V_{psd} = {}^1\!/_2\,\mathrm{AB}\cos\phi + {}^1\!/_2\,\mathrm{AB}\cos(2\omega t + \phi)\,,$$
$$V_{psd} \propto {}^1\!/_2\,\mathrm{AB}\cos\phi\,.$$

----------(3.29)

The output of the PSD is then passed to a low-pass filter which removes the $2\omega t$ component leaving the output of the lock-in as a DC signal. For a constant reference amplitude (B), the output of the PSD is: (i) proportional to the input signal amplitude A (ii) proportional to the cosine of the phase difference between the input and reference signals

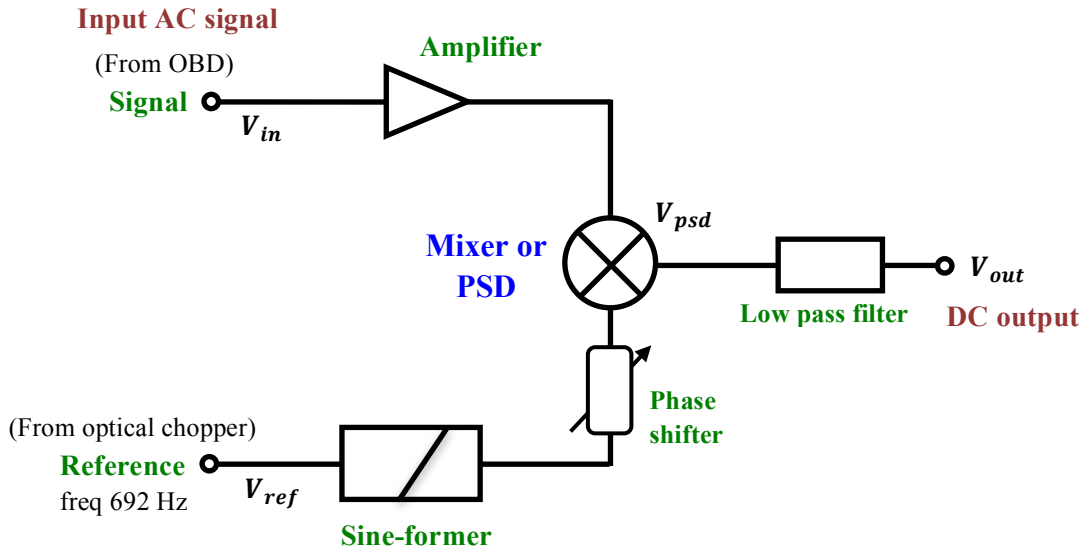

Figure 3.7: Block diagram of a lock-in amplifier

3.8 Typical time-resolved AR signal

Fig 3.8 shows the typical response of a phase-change sample ($Ge_2Sb_2Te_5$) for fixed pump and probe orientations. The rotation signal is plotted with respect to the time delay between the pump and probe pulses. The signal has been plotted on different time scales in order to make visible the different features of the time-resolved signal.

For negative time delays ($t_d < 0$), the probe pulse arrives before the pump. The reflected probe beam does not then contain any information about the sample response. This region is seen as a flat segment before the peak, which is recorded to check the offset from zero. The offset arises due to diffuse pump scatter for the fact that the repetition rate is too high and the system does not fully relax before the next pulse comes. At zero time delay ($t_d = 0$), the pump and probe beam travel the same optical lengths and coincide within the time domain. At a positive time delay ($t_d > 0$), when the pump pulse arrives before the probe pulse, the reflected probe contains information about the pump-induced excitation of the sample, resulting in a finite rotation of the probe polarization state. The optical path length of the pump beam is varied to introduce the time delay, by placing a retroreflector mounted on a 600 mm stepper motor stage.

The peak at the zero time delay in figure 3.8 results from the specular optical Kerr effect within the sample and depends upon the angle between the pump and probe polarization states [36,37]. The signal then starts to decay as the delay of the probe pulse relative to the pump pulse is increased. It exhibits oscillatory components superimposed on an exponential background. The signal is fitted by the sum of a Gaussian peak, a series of Gaussian error function and few exponentially damped oscillatory term.

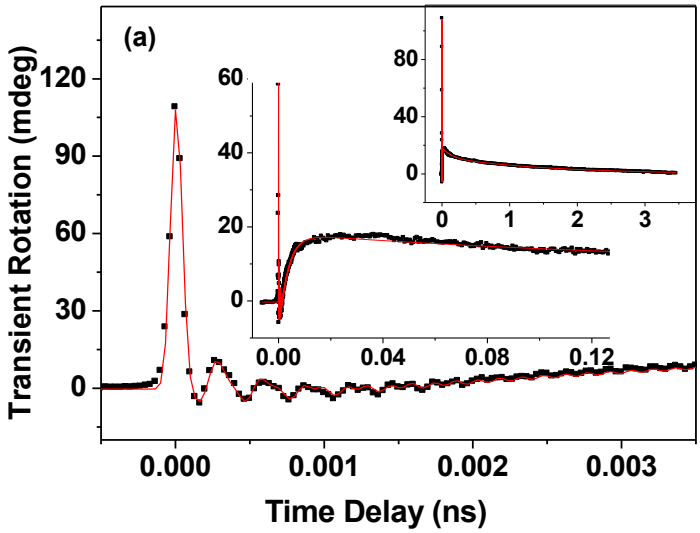

Figure 3.8: **Transient Rotation (or Anisotropic reflectance signal):** A typical time-resolved signal for $Ge_2Sb_2Te_5$ is presented for the case that the pump electric field is along the GaSb [110] axis and the probe electric field is along the [100] axis. Insets show the full scan. The solid symbols represent the experimental data whereas the red line is the fit.

3.9 Fitting the experimental curve

The pulse intensity for a Gaussian pump/probe pulse can be written as:

$$I(t) = \frac{1}{\sqrt{2\pi}w}\exp\left(-\frac{t^2}{2w^2}\right),$$

----------(3.30)

where w is the rms width of the pulse.

The measured rotation curve shows that there is no signal at negative time delay. The signal first appears when pump and probe arrive at the same time at the sample surface. As the delay time increases, the detector measures the rotation of the polarization of the probe beam. The rotation as a function of time delay is calculated as the convolution of two

Gaussian pump and probe beams with the sample response. Solving the convolution integrals gives the terms in the fitting function. The total signal measured at time delay t_d is [67],

$$S \propto A\exp\left(-\frac{(t-t_0)^2}{4w^2}\right) + \frac{B}{2}\exp\left(\frac{w^2}{\tau^2}-\frac{t-t_0}{\tau}\right)\left[1-\mathrm{erf}\left(\frac{w}{\tau}-\frac{t-t_0}{2w}\right)\right] + \frac{C}{2}\exp\left(-\frac{t-t_0}{\tau}\right)\left[1-\mathrm{erf}\left(-\frac{t-t_0}{2w}\right)\cos[\omega(t-t_0)+2\pi\beta(t-t_0)^2+\phi]\right], \quad \text{----------(3.31)}$$

where β is the chirp in the signal, and ω and ϕ are the frequency and phase of the oscillatory term respectively.

We use this formula to fit the measured rotation signal. The derivation of the first two terms of the fitting function is provided in Appendix 1. The last oscillatory term is considered to be phenomenological and is not rigorously derived.

Chapter 4

Observation of T_2-like coherent optical phonons in epitaxial $Ge_2Sb_2Te_5$/GaSb(001) films

In this chapter, I present an ultrafast optical spectroscopy study of epitaxial $Ge_2Sb_2Te_5$/GaSb(001) material to understand the excitation of coherent optical phonons (COP) and charge carriers on femtosecond time scales, which may in turn provide information about the non-thermal nature of the phase-change process. I describe the response of the alloy to optical pulses of different polarizations. An additional study on an epitaxial GaSb(001) film is also performed so as to know the contribution of the substrate to the signals observed in the $Ge_2Sb_2Te_5$/GaSb(001) sample. A microscopic model is presented which explains the four-fold behaviour of COP and optically-induced linear birefringence for certain pump and probe polarization angles. Finally, the behaviour of materials at high pump fluence is also examined.

4.1 Introduction

$Ge_2Sb_2Te_5$ (GST) is one of the compositions of choice from the phase-change material group, which has been widely targeted for use in the next generation of non-volatile memories. As explained in the background chapter, the cubic metastable crystalline phase has a distorted rock-salt structure with a high density of vacancies. The distribution of

vacancies and hence the bonding within the material, and its modification during the phase transition, remains poorly understood. Knowledge and understanding of the phonon spectrum can provide a fingerprint of the crystallographic structure while large amplitude phonons may appear as a precursor to the phase transition itself. Although several studies of coherent optical phonon (COP) dynamics have been performed upon both amorphous and polycrystalline GST [68-71], no such study has been conducted on a GST single crystal. Therefore the growth of epitaxial GST films upon GaSb(001) substrates [72] by molecular-beam epitaxy provides an opportunity to explore the character of the phonon spectrum of GST.

Time-resolved optical pump-probe measurements can provide information about both the ultrafast relaxation of photo-excited carriers and the phase and amplitude of COPs [25,73]. By varying the polarization of the pump and probe beams relative to the crystallographic axes, the symmetry of a particular COP can be deduced, and insight can be gained into the non-thermal nature of phonon excitation and the structural phase transition at large fluence. In this chapter, we present time-resolved reflectance (R) and anisotropic reflectance (AR) measurements of GaSb(001) and GST/GaSb(001). The results are interpreted in terms of a theory of transient stimulated Raman scattering (TSRS) [25]that can account for the excitation of phonons by either impulsive stimulated Raman scattering (ISRS), which can be considered to include displacive excitation of coherent phonons (DECP), or the action of an optically-induced surface space-charge (SSC) field [74]. The dependence of the signals upon the pump and probe polarizations is accounted for through use of the Raman tensor. The dominant mode observed in AR measurements of GST will be shown to be the T_2-like mode of the cubic structure. New modes observed after the application of large pump fluences are interpreted as 1- and 2-dimensional modes of Sb, while a longer-lived transient AR signal is explained in terms of the piezoelectric response of the GaSb to a SSC field.

4.2 Experimental Method: Optical Pump Probe

Time-resolved R and AR (rotation) measurements were performed upon a $Ge_2Sb_2Te_5$(15 nm)/ GaSb(50-100 nm)/ GaSb(001) structure prepared by molecular-beam epitaxy. The GST exhibits a predominant cube-on-cube growth with the GST [100] axis parallel to the GaSb[100] axis [72]. Additional measurements were performed upon a reference structure without the GST layer. Pump and probe pulses of 800 nm wavelength and 55 fs duration were generated by a Ti:sapphire regenerative amplifier system at a 100 kHz repetition rate. The linearly polarized pump pulse with a fluence of 0.85 mJ/cm^2 was directed onto the sample at close to normal incidence. The R and AR were measured by a time delayed s-polarized probe pulse with fluence of 0.2 mJ/cm^2 incident at 45° to the sample normal. Alignment of the optical measurement apparatus requires considerable care. A DataRay WinCamD-UCD12 beam profiler was used to characterize the size of the focused pump and probe spots and to optimize their overlap. At normal incidence upon the beam profiler, the intensity profiles of the spots along their principal axes were observed to be Gaussian with $1/e^2$ full widths of 100 μm × 120 μm and 30 μm × 40 μm for the pump and probe, respectively. Overlap was performed with the beam profiler at the same position and orientation as the sample. The pulse duration was adjusted by using pre-compensation within the compressor stage of the regenerative amplifier system. The same setting gave the minimum pulse width for the pump and probe beams at the sample position, namely an intensity autocorrelation width of 80 ± 2 fs that corresponds to a bandwidth-limited hyperbolic secant with full width half maximum of 55 fs. The probe beam polarization was set precisely to the s-state so as to avoid breakthrough of the transient R signal into the AR channel. The polarization of the pump and probe beams relative to the crystallographic axes of the samples was controlled by rotating the sample about its normal, and by rotating a polarizer placed in the path of the pump beam.

4.3 Results and Discussion

4.3.1 Reflectivity and Rotation Signal

The transient R response of the GST/GaSb(001) structure is shown in Fig 4.1(a) and is similar to that observed in GaSb as shown in fig 4.1(c). The red/green curve is a fit to a phenomenological fitting function. The procedure for fitting the R and AR scans is described in next section. The signal is plotted on three different time scales so as to reveal all of its principal features. The initial rise of the signal occurs within about 200 fs and is associated with photoexcitation and thermalization of an electron-hole plasma. Weak oscillations with a frequency of 4.2 – 4.5 THz are observed until about 1 ps time delay. The signal then changes sign after about 6 ps before reaching a minimum after about 70 ps. This region is well fitted by two exponential functions with relaxation times of 2.0 ± 0.1 ps and 13.1 ± 0.5 ps, which can be attributed to the interaction of the electrons with incoherent optical and acoustic phonons, respectively [75,76]. Weak superimposed oscillations with a frequency of 43 GHz are observed until about 150 ps and can be attributed to longitudinal coherent acoustic phonons propagating normal to the plane of the sample. The final relaxation towards the ambient state is well fitted by two exponential terms. The first has a relaxation time of 0.42 ± 0.05 ns and can be assigned to carrier diffusion from the pumped spot. A longer time of 5.4 ± 0.5 ns can be associated with thermal conduction within the lattice. Similar relaxation behavior has been observed previously in Si [77,78]. The form of the transient R response was found to be independent of the pump and probe polarization except for a small variation in amplitude close to zero-time delay. The similarity of the R signals obtained from the GST/GaSb and GaSb samples suggests that the signals are dominated by the response of the homo-epitaxial GaSb layer and substrate.

The AR response of the GST/GaSb(001) structure is shown in Fig 4.1(b) for the pump and probe electric fields parallel to the [110] and [100] axes, respectively. The signal contains a large peak centred at zero time delay that lies within the temporal overlap of the pump and probe pulses, two oscillatory components of 6.7 and 3.4 THz frequency superimposed on a multi-exponential background, and a slower (ns scale) relaxation. The initial peak arises from the specular optical Kerr effect (SOKE) [36], an optically-induced birefringence, and has a maximum amplitude when the pump and probe electric fields lie

45° apart. The peak occurs because the pump modifies the electron momentum distribution within the surface of the sample and is short-lived due to the small momentum relaxation time [37]. The multi-exponential background is fitted well by the sum of three terms with relaxation times of 500 fs, 3.3 ps, and 137 ps. These terms may be associated with the momentum relaxation of charge carriers, and incoherent optical and acoustic phonons respectively [23]. The slowest relaxation time of 1.6 ns is associated with relaxation of strain in the GaSb that results from its piezolelectric response to an SSC field. Oscillations of THz frequency have been widely observed in R measurements conducted on other materials [74,79-83]. If the fitted initial peak and multi-exponential background are subtracted from the AR data, then the residual is well described by the sum of two damped sinusoids (i = 1, 2) of the form $A_i \exp(-t/\tau_i)\cos(2\pi f_i t + \phi_i)$, allowing the mode amplitudes A_i, frequencies f_i, relaxation times τ_i, and phases ϕ_i to be determined.

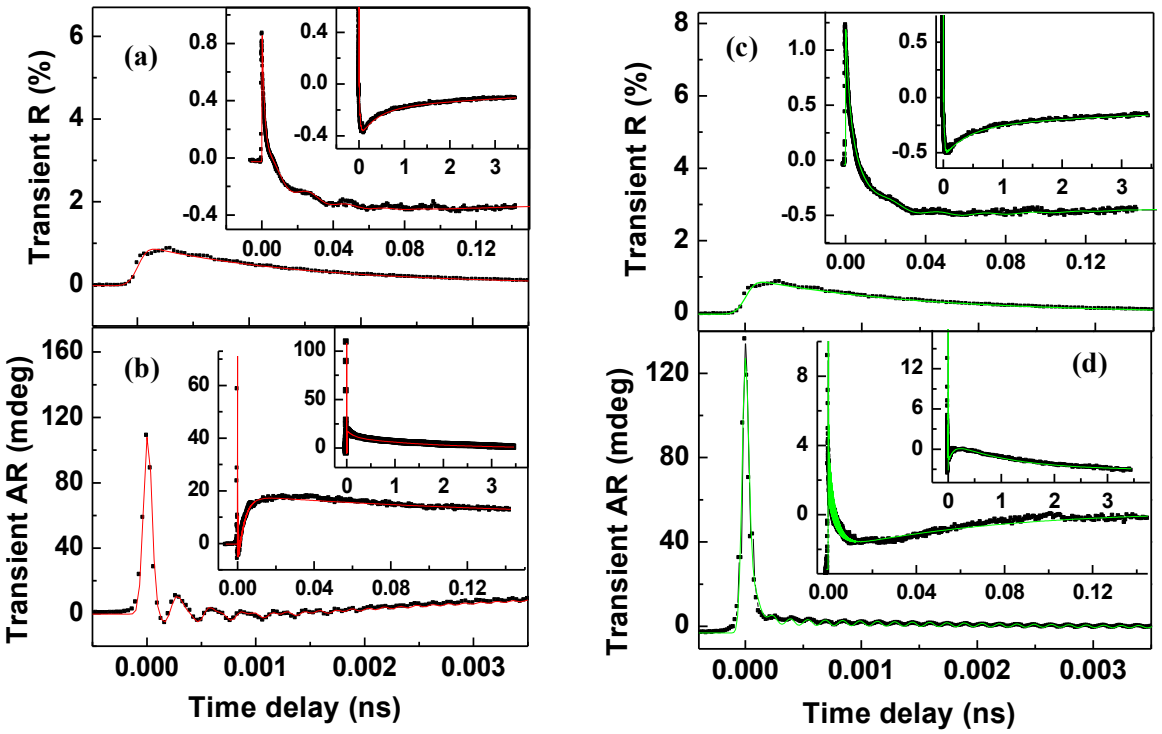

Figure 4.1: Typical time-resolved (a) R, (b) AR signals for GST/GaSb(001) and (c) R, (d) AR signals of GaSb(001) with the pump and probe electric fields aligned parallel to the [110] and [100] axes, respectively. The solid points represent the experimental data while the red/green lines are the fitted curves described within the text.

AR measurements made upon the reference GaSb substrate revealed largely similar features as shown in fig 4.1(d). However, the 3.4 THz mode was observed only in the GST/GaSb structure, confirming that it originates in the GST layer. Similar relaxation times were obtained for the multi-exponential background and long relaxation terms, albeit with some difference in the amplitudes.

4.3.2 Fitting time-resolved R and AR measurements

The R and AR data was fitted to a function with the general form

$$A\exp\left[-\frac{(t-t_0)^2}{4w^2}\right]+\sum_i\frac{B_i}{2}\exp\left[\frac{w^2}{\tau_i^2}-\frac{(t-t_0)}{\tau_i}\right]\left\{1-erf\left[\frac{w}{\tau_i}-\frac{(t-t_0)}{2w}\right]\right\}$$
$$+\sum_j\frac{C_j}{2}\exp\left[-\frac{(t-t_0)}{\tau_j}\right]\left\{1-erf\left[-\frac{(t-t_0)}{2w}\right]\right\}\cos\left[\omega_j(t-t_0)+2\pi\,\beta_j(t-t_0)^2+\phi_j\right]$$

----------(4.1)

in which t and t_0 are the times of arrival of the probe and pump, respectively.

The first term with amplitude A describes an initial Gaussian peak with $1/e^2$ full width of $2\sqrt{2}w$. A series of Gaussian error functions with amplitudes B_i, in which a simple exponential relaxation is convolved with a Gaussian impulse, is used to describe the multi-exponential background within the signal. Finally, a series of terms with amplitude C_j represent the damped oscillatory response of the phonon modes to a Gaussian impulse. The cosine factor oscillates with circular frequency ω_j, has initial phase ϕ_j, and includes a term with coefficient $2\pi\beta_j$ that describes any chirp of the phonon associated with the transient temperature profile. A constant offset was also included to account for the time-independent finite signal sometimes observed at negative time delay which can arise from diffuse scattering of the pump beam from the sample surface into the detector.

Table 4.1 shows fitted parameter values for the data obtained from the GST/GaSb(001) sample and for a comparable set of data obtained from the GaSb(001) sample shown in Figure 4.1. The pump and probe electric fields were parallel to the [110] and [100] axes of the sample, respectively. The Gaussian peak with amplitude A and 4 relaxation terms with

coefficients B_i were used to fit each of the signals. No attempt was made to fit the weak 4.2 –4.5 THz oscillations observed in the R signal from the GST/ GaSb sample. Instead a single oscillatory term was included so as to fit the low frequency oscillations observed in both samples. For the AR signals, one and two oscillatory components were required to fit the data from the GaSb and GST/GaSb samples respectively.

The fitted parameter values for the R signals are broadly similar for the two samples. The Gaussian peak is small in comparison to the other terms and so the difference in the fitted values of A is not significant. For the AR signals, the relaxation times τ_2, τ_3 and τ_4 associated with the terms with coefficients B_2, B_3, and B_4 are also similar for the two samples, although B_2 and B_3 have different signs. The relaxation times for R and AR signals are seen to be quite different, suggesting that the underlying physical processes are different.

			t_0	τ_i	$\omega_i/2\pi$	φ_i	w	offset
Reflect -ivity	GST/GaSb	A	0.00016	6 fs	–	–	–	–
		B_1	0.97	1.44 ps	–	–	–	–
		B_2	0.43	23.6 ps	–	–	–	–
		B_3	-0.21	0.38 ns	–	–	–	–
		B_4	-0.18	4.3 ns	–	–	–	–
		C_1	0.078	23 ps	46 GHz	-1.75	50 fs	-0.03
		C_2	0	–	–	–	–	–
	GaSb	A	-0.016	5 fs	–	–	–	–
		B_1	0.49	2.04 ps	–	–	–	–
		B_2	0.39	13.1 ps	–	–	–	–
		B_3	-0.14	0.424 ns	–	–	–	–
		B_4	-0.11	5.4 ns	–	–	–	–
		C_1	-0.017	50 ps	43 GHz	-3.23	40 fs	-0.04
		C_2	0	–	–	–	–	–

Rotation	GST/GaSb	A	98.91	5.0 fs	–	–	–	–
		B_1	19.23	500 fs	–	–	–	–
		B_2	-28.99	3.37 ps	–	–	–	–
		B_3	6.64	137 ps	–	–	–	–
		B_4	11.93	1.6 ns	–	–	–	–
		C_1	14.42	430 fs	3.40 THz	0.316	–	–
		C_2	1.46	2.98 ps	6.77 THz	1.530	30 fs	-0.290
	GaSb	A	97.79	0.8 fs	–	–	–	–
		B_1	48.37	45 fs	–	–	–	–
		B_2	2.32	3.24 ps	–	–	–	–
		B_3	-1.57	106 ps	–	–	–	–
		B_4	2.19	1.14 ns	–	–	–	–
		C_1	0.84	3 ps	6.77 THz	2.540	20 fs	-3.150
		C_2	0	–	–	–	–	–

Table 4.1: Parameter values obtained by fitting equation 4.1 to R and AR signals from the GaSb and GaSb/GST samples

In the case of the AR signals, the non-oscillatory components of the fitting function were subtracted from the experimental data to leave only an oscillatory residual. The residual was then fitted by the damped oscillatory function as described before. The fitted values of the frequency, relaxation time and initial phase were found to be almost identical to those obtained from the fitting of equation (4.1).

4.3.3 Phonon characterization in GaSb

Further measurements were made as the planes of polarization of the pump and probe beams were varied relative to the crystallographic axes of the sample. Figure 4.2 shows typical oscillatory components in panels (a) and (d) and the variation of their frequency, phase and amplitude in panels (b-c), (e-f) for the GaSb structure while varying either the pump or probe polarization with the other fixed. The variation of the amplitude of the ns transient in the AR response is presented in Fig 4.3(a-d). The angles φ and θ are used to define the orientation of the pump and probe electric fields relative to the [100] axis are shown in the panel (c). From panels (b) and (e) in fig (4.2), the frequency is seen to have an essentially constant value of 6.77 THz. From panels (d) and (f), the oscillations are seen to almost vanish when the probe electric field lies along <110> and have maximum amplitude when it lies parallel to <100>.

The variation of phonon phase and amplitude in fig 4.2(e) and (f) respectively suggests an overall cos(2θ) dependence upon probe polarization. Panels (a), (b) and (c) in Fig 4.2 reveal a more complicated dependence upon the pump polarization. The amplitude is a minimum when the pump electric field lies parallel to <100> but has different values when it is parallel to [110] and [$\bar{1}$10]. The range of phase of about 2 rad suggests contributions from different excitation mechanisms of different relative phases. However, when the amplitude and phase data of panels (c) and (b) in Fig 4.2 respectively, are plotted in the Argand plane, in panel (d) of fig 4.3, the data points are found to lie on a straight line. According to panels (a), (b) in fig 4.3, the longer-lived tail with 4 mdeg amplitude was observed for the probe parallel to the cube edge, while being almost independent of pump polarization. However, when the probe is polarized along the face diagonal, there is no tail observed in the signal. The tail shows a sinusoidal behavior as the probe is rotated from -90 deg to +90 deg w.r.t GaSb[100] axis when the pump polarization is fixed along GaSb[110]. The peak height of the reflectivity does not show any clear trend as the pump/probe is rotated. The error bars are comparatively larger as well. This implies that the reflectivity peak does not depend upon pump or probe polarization; the difference in the peak height comes from the experimental noise, and the peak reflectivity is constant within experimental error.

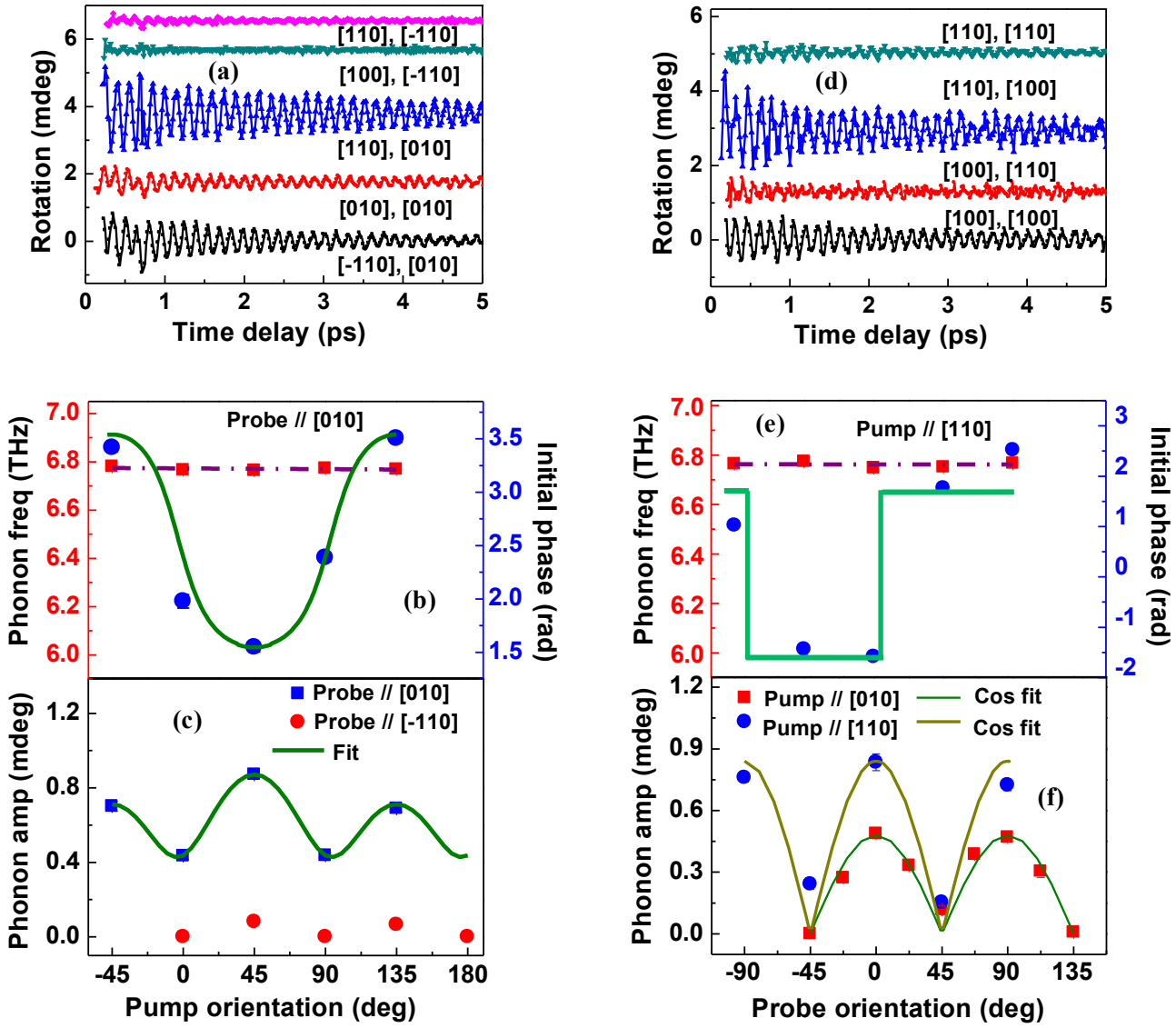

Figure 4.2: Dependence of frequency, amplitude and phase of phonon oscillations in GaSb upon the orientation of the pump and probe electric fields. Typical oscillatory components after subtraction of the initial peak and multi-exponential background are presented in (a) when the pump polarization is varied and (d) when the probe polarization is varied (Labels represent the orientations of pump and probe polarizations from the GaSb[100] axis respectively). (b) Frequency and phase, and (c) amplitude, are plotted as the pump polarization is varied. (e) Frequency and phase, and (f) amplitude, are plotted as the probe polarization is varied.

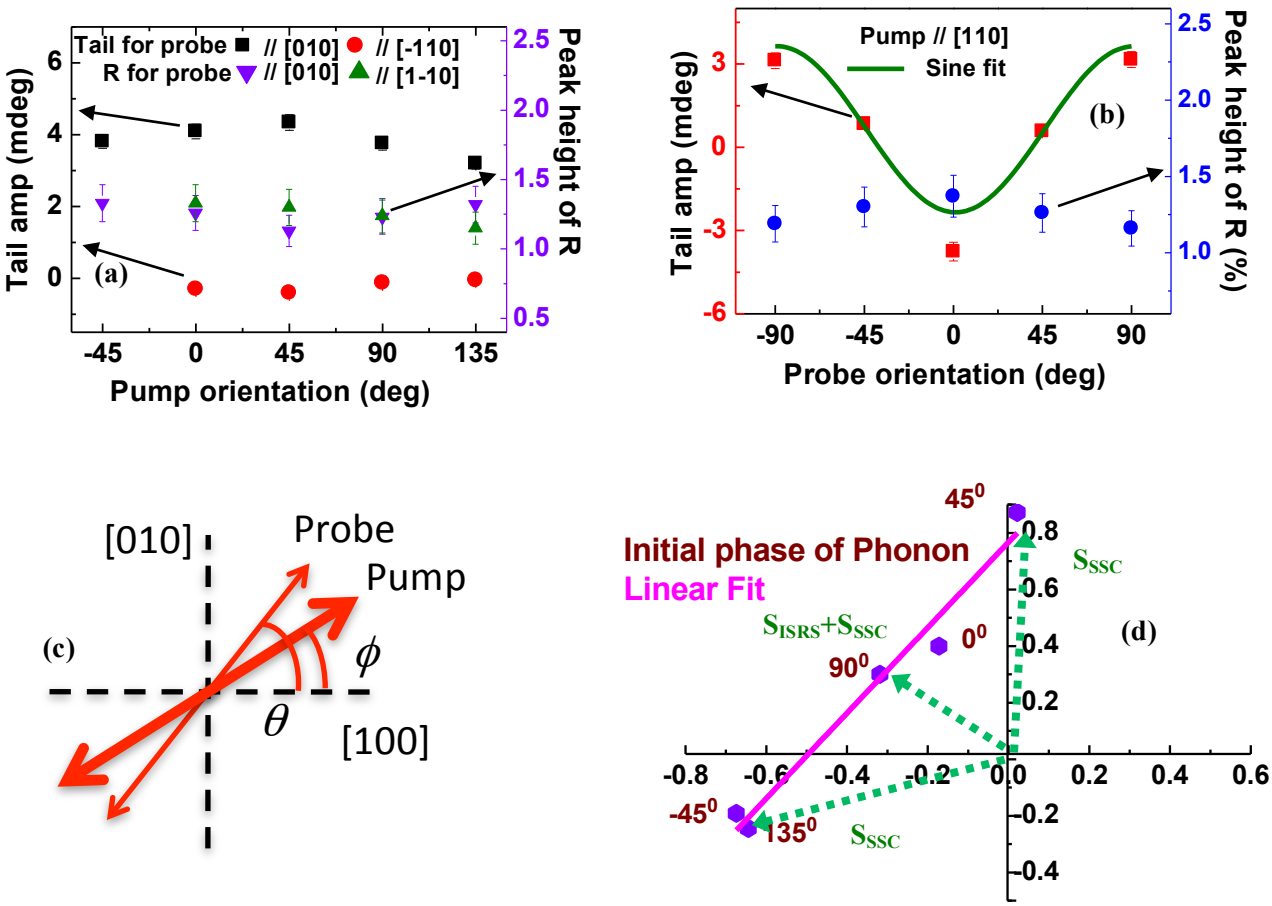

Figure 4.3: Dependence of the amplitude B_4 of the slow transient (tail) observed within the AR signal of GaSb(001) upon the orientation of (a) the pump and (b) the probe electric field. The peak R signal value is shown for comparison. The angles φ and θ used to define the orientation of the pump and probe electric fields are shown in panel (c). (d) Data from Fig 4.2 (b) and (c) are plotted in the Argand plane. The purple straight line fit in (d) has been used to generate the continuous curves in Fig 4.2 (b) and (c).

GaSb has the zincblende structure with T_d point group symmetry and A_1, A_2, E, T_1 and T_2 irreducible representations at the zone centre [29,84]. Of the associated phonon modes, only the T_2 mode is Raman active. At the center of the Brillouin zone, the three dimensional mode splits into a non-degenerate longitudinal optical (LO) phonon and doubly degenerate transverse optical (TO) phonons with slightly lower frequency [27].

Raman scattering studies [85] have observed the LO phonon at 7.08 THz while neutron-scattering [86] measurements observe both LO and TO modes and suggest that the TO phonon propagating orthogonal to the incident pump light is detected in the present experiments.

4.3.4 Theory of Transient Stimulated Raman Scattering (TSRS)

In the theory described by Merlin [25], transient stimulated Raman scattering (TSRS) observed by the time-resolved optical pump-probe technique is considered as a two-stage process involving: (i) the generation of coherent phonons by the pump beam; and (ii) the scattering of the probe pulse by the lattice vibrations. The excitation of a coherent optical phonon (COP) with amplitude $Q(\mathbf{r},t)$ by the pump electric field **E**, through the process of conventional impulsive stimulated Raman scattering (ISRS), is described by the equation of motion

$$\ddot{Q}(\mathbf{r},t)+\Gamma\dot{Q}(\mathbf{r},t)+\frac{1}{8\pi^3}\int\Omega_{\mathbf{q}}^2 e^{-i\mathbf{q}\cdot(\mathbf{r}-\mathbf{r}')}Q(\mathbf{r}',t)d^3r'd^3q=\frac{1}{2}\sum_{mp}\left(\frac{\partial\chi_{mp}^{i}}{\partial Q}Q_i E_m E_p\right), \qquad \text{----------(4.2)}$$

in which **q** is the phonon wavevector, $\Omega_{\mathbf{q}}$ is the phonon frequency, and Γ is the phonon damping parameter. The driving force is seen to contain the 2nd rank Raman tensor $R=\frac{\partial\chi_{mp}^{i}}{\partial Q}Q_i$ and the components of the pump electric field E_m and E_p. The Raman tensor is represented by a matrix and is defined as the derivative of the susceptibility (3rd rank tensor) contracted with the atomic displacement vector (a tensor of rank 1). The solution of Equ (4.2) yields

$$Q\propto\sum_{mp}\left(\frac{\partial\chi_{mp}}{\partial Q}\cos(\alpha_m)\cos(\alpha_p)\right) \qquad \text{----------(4.3)}$$

in which $\cos(\alpha_i)$ are the direction cosines of the pump electric field.

Alternatively, if the phonon is instead excited by an optically generated surface space-charge (SSC) field, then it is the SSC field that appears on the right hand side of Equ (4.2) and Q is independent of the pump beam polarization.

By solving the wave equation for the probe electric field in the sample medium, with the electric susceptibility modified by the presence of the phonon, the transient reflectance $\Delta R/R$ detected by the probe is found to be proportional to the phonon amplitude Q and an additional factor

$$\sum_{kl}\left(\frac{\partial\chi_{kl}}{\partial Q}\cos(\beta_k)\cos(\beta_l)\right)$$

----------(4.4)

in which $\cos(\beta_i)$ are the direction cosines of the probe beam. If the phonon is excited by a combination of ISRS and the action of a SSC field, then

$$\Delta R/R \sim \left[C+\sum_{mp}\left(\frac{\partial\chi_{mp}}{\partial Q}\cos(\alpha_m)\cos(\alpha_p)\right)\right]\sum_{kl}\left(\frac{\partial\chi_{kl}}{\partial Q}\cos(\beta_k)\cos(\beta_l)\right)$$

----------(4.5)

where the constant C represents the effect of the SSC field and must be complex to describe both the amplitude and phase of the transient reflectance signal.

Next, it is necessary to consider the measurement geometry and operation of the detector. While the pump beam is incident at near-normal incidence, it is convenient to use a larger angle of incidence for the probe beam so that the beams are spatially separated and can be controlled independently. However, strong refraction occurs at the air-sample interface (the refractive indices of GaSb and GST are 4.4+0.38i [87] and 4.6+4.3i [88], respectively for 800 nm wavelength) so that both beams can be considered as propagating roughly parallel to the [001] axis within the medium. In addition s-polarization is chosen for the probe. Therefore, both pump and probe electric fields can be assumed to lie within the (001) plane parallel to the $(\cos\varphi,\sin\varphi,0)$ and $(\cos\theta,\sin\theta,0)$ directions, assuming the coordinate system of Figure 4.2(b).

The polarizing bridge detector is balanced for the DC probe signal. Therefore, the beams entering the two photodiode detectors within the bridge have their electric field parallel to the $\left(\cos\left(\theta+\pi/4\right),\sin\left(\theta+\pi/4\right),0\right)$ and $\left(\cos\left(\theta-\pi/4\right),\sin\left(\theta-\pi/4\right),0\right)$ directions. The transient R and AR response measured with the bridge detector is then equal to the sum and difference of the two photo-diode outputs.

The transient reflectance $(\Delta R/R)_i$ from the two diodes may be written as

$$\left(\Delta R/R\right)_1 \propto \left(\cos\left(\theta+\pi/4\right),\sin\left(\theta+\pi/4\right),0\right)\mathrm{M}\begin{pmatrix}\cos\left(\theta+\pi/4\right)\\ \sin\left(\theta+\pi/4\right)\\ 0\end{pmatrix}$$

----------(4.6)

$$\left(\Delta R/R\right)_2 \propto \left(\cos\left(\theta-\pi/4\right),\sin\left(\theta-\pi/4\right),0\right)\mathrm{M}\begin{pmatrix}\cos\left(\theta-\pi/4\right)\\ \sin\left(\theta-\pi/4\right)\\ 0\end{pmatrix}$$

----------(4.7)

in which M is the matrix representing the Raman tensor for the particular phonon mode within the coordinate system defined by the crystallographic axes of the sample. The detector electronics outputs the signals

$$S_R = \left(\Delta R/R\right)_1 + \left(\Delta R/R\right)_2, \quad \text{and} \quad S_{AR} = \left(\Delta R/R\right)_1 - \left(\Delta R/R\right)_2,$$

----------(4.8)

which correspond to the transient reflectance and rotation, respectively.

The T_d and O_h space groups have 5 irreducible representations A_1, A_2, E, T_1 and T_2 with the following matrix representations of the Raman tensor

$$A \begin{pmatrix} a & 0 & 0 \\ 0 & a & 0 \\ 0 & 0 & a \end{pmatrix}; \quad E \begin{pmatrix} b & 0 & 0 \\ 0 & b & 0 \\ 0 & 0 & b \end{pmatrix};$$

$$T_x \begin{pmatrix} 0 & 0 & 0 \\ 0 & 0 & d \\ 0 & d & 0 \end{pmatrix}; \quad T_y \begin{pmatrix} 0 & 0 & d \\ 0 & 0 & 0 \\ d & 0 & 0 \end{pmatrix}; \quad T_z \begin{pmatrix} 0 & d & 0 \\ d & 0 & 0 \\ 0 & 0 & 0 \end{pmatrix}.$$

----------(4.9)

Finally, it remains only to combine equations (4.5) to (4.9) and calculate the R and AR signals for each mode. For the A and E modes, S_R has a constant value proportional to a and b respectively, while S_{AR} vanishes. For T_x and T_y both S_R and S_{AR} vanish, but for T_z, S_R vanishes while

$$S_{AR} \propto (C + \sin 2\varphi)\cos 2\theta .$$

----------(4.10)

The form of Equ (4.10), where the transient AR signal exhibits a $\sin 2\varphi$ dependence on pump polarization and a $\cos 2\theta$ dependence on probe polarization, and the predicted absence of phonons in the R signal, fully describes the experimental results presented in fig 4.2.

4.3.5 A microscopic model for the response of GaSb(001)

A similar expression may be obtained from a simple model that considers the orientation of the pump and probe electric fields relative to inequivalent bonds within the zincblende structure.

The zincblende crystal structure of GaSb is shown in Fig 4.4. GaSb lacks inversion symmetry, and is both polar and piezoelectric. While all atoms have tetrahedral coordination, the yellow and blue bonds lie in orthogonal planes and are inequivalent. When the electric field of the pump lies along the [110] direction, it describes angles of 35^0

and 90^0 with the blue and yellow bonds, respectively. Assuming that the excitation of the bond varies as the scalar product of the electric field and a unit vector parallel to the bond, then the blue bonds are excited more strongly. The Ga and Sb atoms experience unequal forces from the blue and yellow bonds, causing them to move in opposite directions parallel to the [001] axis. This is exactly the displacement of basis atoms associated with the T_{2z} optical phonon. If the pump electric field instead lies parallel to the $[1\bar{1}0]$ direction, then the role of the blue and yellow bonds is reversed and the direction of displacement of the two basis atoms is interchanged. The phase of the phonon excited by the pump will therefore change by π radians as the pump electric field is rotated from [110] to $[1\bar{1}0]$ [81]. The optically-induced difference in bond strength is short-lived. However, once the T_{2z} mode has been excited, the oscillatory displacement of the basis atoms causes the yellow and blue bonds to be alternately stretched and compressed. This leads to an optical birefringence that produces maximum (zero) optical rotation when the probe electric field lies along the <100> (<110>) axes. The generation (and detection) of the COP observed in the AR data is hence understood in terms of selective bond excitation.

Consider the green atom with coordinates (1/4,1/4,1/4) within the conventional unit cell shown in Fig 4.4(a). The red nearest neighbours at A (0,0,0), B (1/2,1/2,0), C (1/2,0,1/2) and D (0,1/2,1/2) give rise to bonds that lie parallel to the $[\bar{1}\bar{1}\bar{1}]$, $[11\bar{1}]$, $[1\bar{1}1]$ and $[\bar{1}11]$ directions, respectively. Let us assume that the extent of excitation of each type of bond (i.e. the number of bonding to anti-bonding transitions that occur) is proportional to $\left(\mathbf{E}\cdot\hat{\mathbf{u}}\right)^2$, where $\mathbf{E}$ is the electric field of the pump beam and $\hat{\mathbf{u}}$ is a unit vector parallel to the length of the bond, as expected for an electric-dipole transition. If $\mathbf{E} = E_{0,pump}\left(\cos\varphi, \sin\varphi, 0\right)$, then the net force on the green atom is proportional to

$$\left(\mathbf{E}\cdot\hat{\mathbf{u}}\right)_A^2 + \left(\mathbf{E}\cdot\hat{\mathbf{u}}\right)_B^2 - \left(\mathbf{E}\cdot\hat{\mathbf{u}}\right)_C^2 - \left(\mathbf{E}\cdot\hat{\mathbf{u}}\right)_D^2 = 4E_{0,pump}^2 \sin\left(2\varphi\right)$$

----------(4.11)

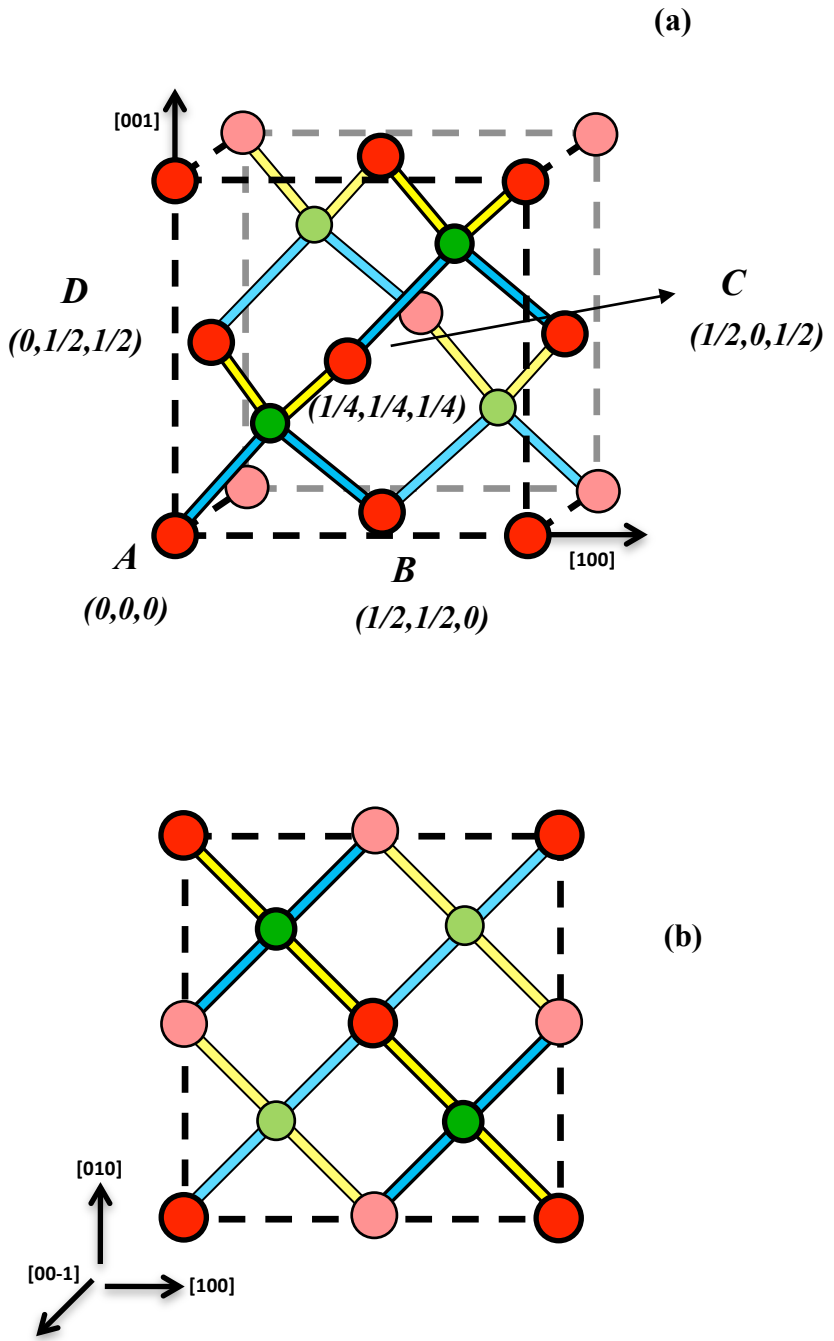

Figure 4.4: Zincblende crystal structure of GaSb in (a) 3 dimensions, and (b) viewed along the [001] axis. The green and red spheres indicate the 2 sub-lattices, while inequivalent bonds are shaded in yellow and blue.

The difference in bond strength and orientation associated with the optical pumping and the displacement of the atoms leads to inequivalent reflection coefficients of $(r+\delta r/2)$ and $(r-\delta r/2)$ when the electric field of the probe beam is polarized parallel to the $[110]$ and $[\bar{1}10]$ directions, respectively. If the incident probe electric field has the form $\mathbf{E}_i = E_{0,probe}(\cos\theta, \sin\theta, 0)$, then the AR signal ($S_{AR}$) is equal to the difference in reflected intensity of incident beams with electric field $\mathbf{E}_1 = \frac{E_{0,probe}}{\sqrt{2}}\left(\cos\left(\theta+\frac{\pi}{4}\right), \sin\left(\theta+\frac{\pi}{4}\right), 0\right)$ and $\mathbf{E}_2 = \frac{E_{0,probe}}{\sqrt{2}}\left(\cos\left(\theta-\frac{\pi}{4}\right), \sin\left(\theta-\frac{\pi}{4}\right), 0\right)$. The reflected electric field amplitudes may be written as

$$\mathbf{E}_{r1} = \frac{E_{0,probe}}{2}\begin{pmatrix} (r+\delta r/2)\left[\cos\left(\theta+\frac{\pi}{4}\right)+\sin\left(\theta+\frac{\pi}{4}\right)\right] \\ (r-\delta r/2)\left[-\cos\left(\theta+\frac{\pi}{4}\right)+\sin\left(\theta+\frac{\pi}{4}\right)\right] \\ 0 \end{pmatrix} = \frac{E_{0,probe}}{\sqrt{2}}\begin{pmatrix} (r+\delta r/2)\cos\theta \\ (r-\delta r/2)\sin\theta \\ 0 \end{pmatrix}$$

$$\mathbf{E}_{r2} = \frac{E_{0,probe}}{2}\begin{pmatrix} (r+\delta r/2)\left[\cos\left(\theta-\frac{\pi}{4}\right)+\sin\left(\theta-\frac{\pi}{4}\right)\right] \\ (r-\delta r/2)\left[-\cos\left(\theta-\frac{\pi}{4}\right)+\sin\left(\theta-\frac{\pi}{4}\right)\right] \\ 0 \end{pmatrix} = \frac{E_{0,probe}}{\sqrt{2}}\begin{pmatrix} (r+\delta r/2)\sin\theta \\ -(r-\delta r/2)\cos\theta \\ 0 \end{pmatrix}$$

----------(4.12)

So that

$$S_{AR} \propto E_{r1}^2 - E_{r2}^2 = \frac{E_{0,probe}^2}{2}\left\{\begin{matrix}\left[(r+\delta r/2)\cos\theta\right]^2 + \left[(r-\delta r/2)\sin\theta\right]^2 \\ -\left[(r+\delta r/2)\sin\theta\right]^2 - \left[-(r-\delta r/2)\cos\theta\right]^2\end{matrix}\right\}$$
$$= E_{0,probe}^2\cos(2\theta) r\delta r$$

----------(4.13)

Since $\delta r \propto \sin(2\varphi)$, we hence find that $S_{AR} \propto \sin(2\varphi)\cos(2\theta)$. Hence the simple model yields the same dependence of the AR signal upon the pump and probe polarizations as predicted by the Raman tensor description of ISRS presented in section 4.3.4.

Longer-lived slow transient response (tail) in the AR signal

While the $\cos(2\theta)\sin(2\varphi)$ form describes the observations of the T_{2z} COP in Ge(001) [81], it does not fully account for the dependence on pump polarization observed in Fig 4.2(b-c) and fig 4.3 (d). Studies of COPs in GaAs [74,82] have shown that the T_{2z} mode may also be excited by an optically-induced SSC field. This simple model can also be extended to describe the effect of a SSC field parallel to the [001] axis. Here, photo-excited electron-hole pairs drift in opposite directions under the influence of the built-in electric field near an interface, generating an additional space-charge field on sub-ps timescales. In a polar compound such as GaSb, the oppositely charged basis ions (Ga and Sb) experience an impulse in opposite directions normal to the plane of the film. This leads to an oscillatory motion of T_{2z} character superimposed upon an offset of the basis atom positions that gives rise to the long-lived transient within the AR response. The amplitude of the T_{2z} COP excited by the SSC field again exhibits a $\cos(2\theta)$ dependence upon the probe polarization but is independent of the pump polarization.

4.3.5 Fitting the dependence of the phonon amplitude and phase upon the pump polarization

ISRS and the SSC field are expected to excite COPs of different phases. In ISRS, the pump selectively excites bonds of different orientations, providing the driving force for the T_{2z} mode and leading to an electron-hole distribution that is anisotropic in k-space. While the bonding will be weakened on the timescale of the electron-hole recombination time (> 100 ps), the electron and hole momentum distributions, and hence the inequivalent strength of bonds of different orientation, relax on fs timescales. The driving force for the T_{2z} phonon will therefore be very short-lived and "impulsive" in character. The rise of the SSC field is limited by the drift of carriers within the built-in potential, and so the excitation of the COP will be delayed. The form of the data plotted in the Argand plane in Figure 4.3(b) can now be understood. When $\varphi = 0$ and 90°, the amplitude of the COP excited by ISRS is expected to vanish, revealing the amplitude and phase of excitation due to the SSC field, which is represented by the vector $\mathbf{S}_{SSC}$. As φ is varied, the amplitude of the phonon excited by ISRS varies, but with constant phase, tracing out a straight line that passes through the origin. The net effect of ISRS and SSC field excitation is a straight line, offset from the origin. It is straightforward to fit a straight line to the data within the Argand plane as explained below, and hence generate the curves shown in Figure 4.2(b-c).

A more quantitative description of the variation within the Argand plane will now be given. When ISRS and a SSC field act simultaneously, the displacement of an ion associated with the resulting COP, and also the time-resolved anisotropic reflectance (AR), may be represented by an oscillatory function of the form

$$\mathrm{Re}\left[Ae^{(i\omega t+\varepsilon)}\right] = \cos(2\theta)\,\mathrm{Re}\left[A_1 \sin(2\varphi) e^{(i\omega t+\varepsilon_1)} + A_2 e^{(i\omega t+\varepsilon_2)}\right]$$

----------(4.14)

where A_1 and ε_1 are the amplitude and phase associated with ISRS, A_2, and ε_2 are associated with the SSC field, and A and ε are the net amplitude and phase.

The signal amplitude is maximum when the probe electric field is applied parallel to a <100> axis. If the pump polarization is then varied, the complex signal $z = Ae^{i\varepsilon}$ traces out a straight line segment in the Argand plane of the form

$$z = z_0 + \lambda(z_1 - z_0) = Ae^{i\varepsilon}$$

----------(4.15)

with end points corresponding to λ = sin (2φ) = +/-1. The values of z_0 and z_1 may be obtained immediately by fitting a straight line to the data within the Argand plane as shown in Fig. 4.3(d). The dependence of the amplitude and phase of the AR signal upon the pump polarization then follows immediately. The square of the amplitude is given by:

$$A^2 = \{z_0{}^* + \lambda(z_1{}^* - z_0{}^*)\}\{z_0 + \lambda(z_1 - z_0)\} = P + Q\sin 2\varphi + R\sin^2 2\varphi$$

----------(4.16)

where

$$P = x_0^2 + y_0^2;\ Q = [x_0(x_1 - x_0) + y_0(y_1 - y_0)];\ R = [(x_1 - x_0)^2 + (y_1 - y_0)^2]$$

----------(4.17)

The tangent of the phase

$$\tan\varepsilon = \frac{Im\ (z)}{Re\ (z)} = \frac{y_0 + H\sin 2\varphi}{x_0 + K\sin 2\varphi}$$

----------(4.18)

where $H = y_1 - y_0$ and $K = x_1 - x_0$. The expressions in equs. (4.16) to (4.18) are then used to generate the curves for the dependence of phase and amplitude upon pump polarization shown in Figs 4.2(b) and 4.2(c) respectively.

4.3.7 Phonon characterization in GST /GaSb(001)

The COPs observed in the transient AR response of GST/GaSb(001) were analyzed in a similar manner. Measurements were made in two sets where firstly, only the pump polarization was changed, and secondly, where the pump polarization and sample orientation were changed together so that effectively the probe electric field was being rotated relative to the electric field of the pump and the crystallographic axes of the sample. Fitting yielded two oscillatory components superimposed on a complicated background within the AR signal from the GST/GaSb(001) sample, there being some small variation in the precise values obtained from the two sets of measurements.

The frequency and relaxation time of the first COP of larger amplitude were 3.4 ± 0.1 THz and 0.5 ps respectively, and 6.79 ± 0.02 THz and 3.0 ps respectively for the second COP. The 6.79 THz COP can again be attributed to the zone centre TO phonon of the GaSb homoepitaxial layer and substrate, while the 3.4 THz COP originates in the GST layer. Fig 4.5(a) and 4.5(b) show the dependence of the amplitude of the 3.4 THz COP upon the probe and pump polarization respectively. While the dependence upon probe polarization is similar to that observed in Fig 4.2(f), there is only a weak dependence upon pump polarization. The data are plotted in the Argand plane in Figure 4.5(c). The clustering of data points close to the horizontal axis indicates that the phase of the COP is also insensitive to the pump polarization.

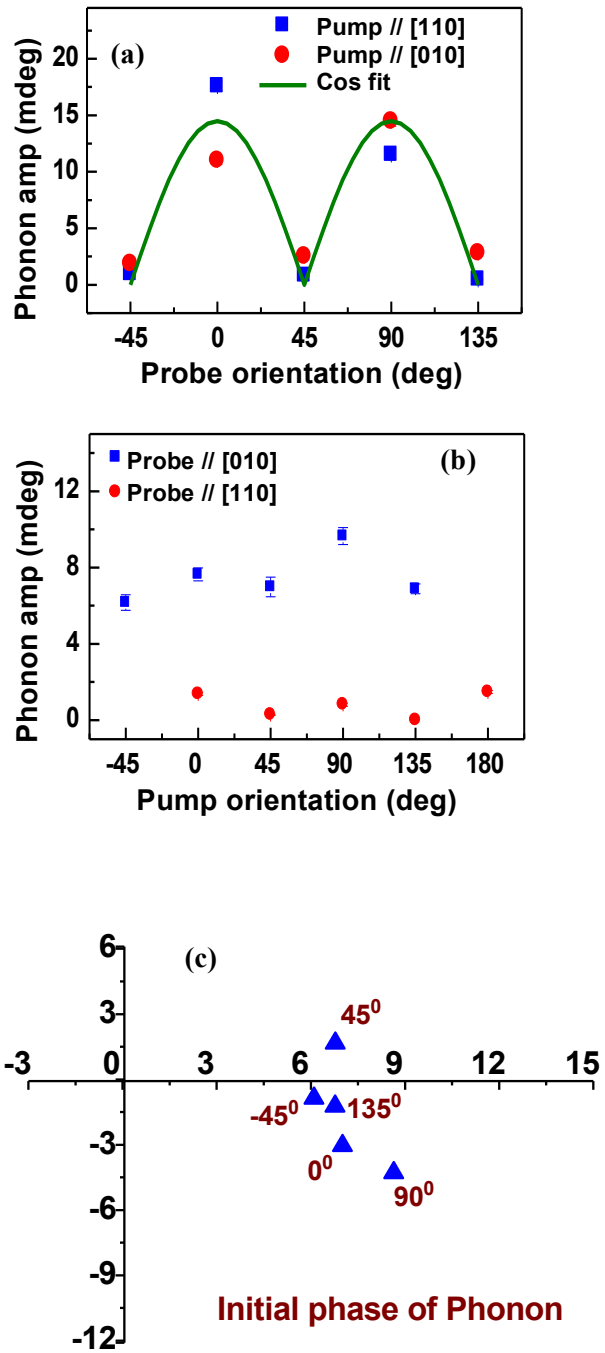

Figure 4.5: Dependence of the amplitude and phase of the 3.4 THz mode observed in GST/GaSb(001) upon: (a) probe and (b) pump polarization. (c) The dependence of amplitude and phase upon the pump polarization are plotted in the Argand plane.

Further plots of the phase of the 3.4 THz COP, and the amplitude of the 6.79 THz COP and the longer-lived transient in the AR signal are presented in Figure 4.6. From panels (a) and (b), the frequency of the first phonon mode is seen to be essentially independent of pump and probe polarization within experimental error. From Fig 4.6(a) the initial phase of the 3.4 THz mode is seen to vary by only 0.7 rads, and has no clear dependence upon pump polarization, when the probe electric field was parallel to the [010] axis. In Fig 4.6(b) the initial phase of the 3.4 THz phonon oscillation appears to roughly alternate between two values different by π rad when the probe polarization is rotated from 0 to 90 degree and the pump polarization is kept fixed along [110], in agreement with the TSRS theory and the microscopic model (section 4.3.4 and 4.3.5). The dependence of the amplitude of the slow transient response (the quantity B_4 within section 4.3.2) on pump and probe orientation is displayed in Fig 4.6(c) and (d) respectively, and is similar to that observed for the GaSb(001) sample. Interestingly, the amplitude of this slow transient is some 3 times larger for the GST/GaSb(001) sample. Panels (e) and (f) show the pump and probe polarization dependence of the amplitude and frequency of the second phonon mode. The frequency remains constant within experimental error, while the dependence of the amplitude upon pump and probe polarization is similar to that observed for GaSb(001) and hence is in full agreement with the models of section 4.3.4 and 4.3.5. Since the amplitude of the 6.79 THz mode was an order of magnitude smaller than that of the 3.4 THz mode, there is greater uncertainty in the extracted amplitude of the 6.79 THz mode, while its initial phase could not be extracted reliably and so has not been presented.

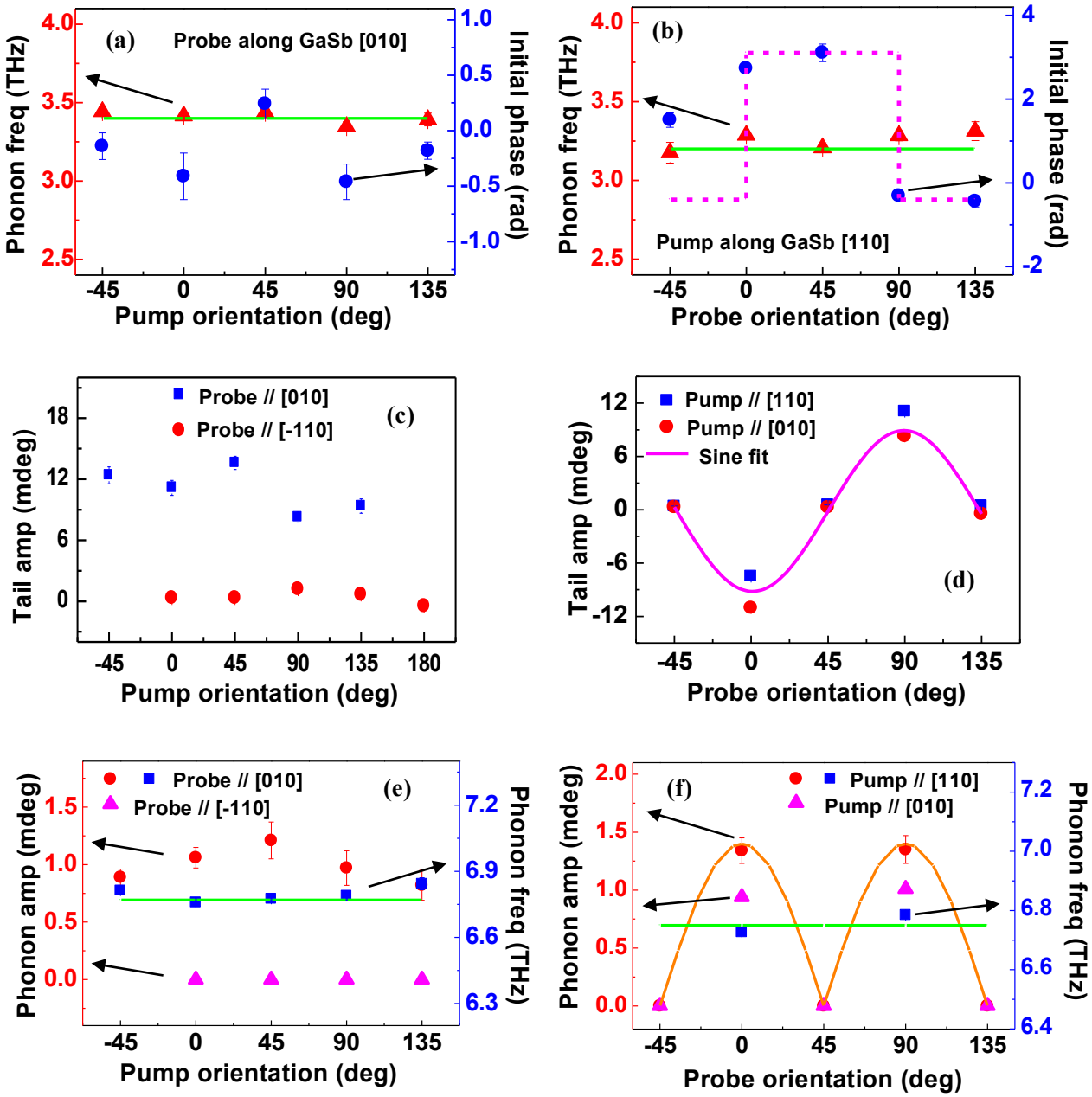

Figure 4.6**:** Variation of features of the AR signal from the GST/GaSb(001) sample as either the pump polarization was varied, in (a), (c) and (e), or the pump polarization and sample were rotated together so that the probe electric field was effectively rotated, in (b), (d) and (e). (a) and (b) show the dependence of the frequency and phase of the lower frequency phonon mode on pump and probe polarization respectively. (c) and (d) show the dependence of the amplitude of the slow transient response (tail) on pump and probe polarization. (e) and (f) show the dependence of amplitude and frequency of the higher frequency mode upon pump and probe polarization.

Dependence of transient response of GST/GaSb(001) on sample orientation

Additional polarization dependence measurements were carried out to investigate the influence of sample orientation upon the transient signals. Rotating the sample while keeping pump and probe polarization unchanged is simply equivalent to collectively rotating the pump and probe polarizations relative to the crystallographic axes of the sample. The dependence of the optical phonons (3.4 THz) upon the sample rotation should therefore reflect a combination of the dependence upon pump and probe polarization. However, since the generation of optical phonons was found to be almost independent of (or weakly dependent on) pump polarization, the orientation of the probe polarization relative to the crystallographic axis should determine whether optical phonons are observed. Three sets of pump-probe measurements were made, in which the angle between the pump and probe polarization was kept at ± 45° and and 90° while rotating the sample. The results shown in Fig 4.7 are identical to the results obtained when pump and probe polarization were varied independently. Clear optical phonons (3.4 THz) were observed only when the sample was rotated to positions where the probe polarization was parallel to the cubic axes, whereas no or only very weak phonons appeared when the probe polarization was along the face diagonals. Fig 4.7(a) and (b) show the oscillatory components of the transient AR signal observed for GST/GaSb(001) for various orientations of pump and probe polarizations. The amplitude and frequency of these phonons are plotted in Fig 4.7(c) and (d) respectively. The large variation of phonon amplitude between the three pump-probe configurations with the probe polarization parallel to the GaSb[100] and [010] axes may arise from inhomogeneity of the sample and uncertainty in the measurement conditions, such as the pump power and extent of overlap of the pump and probe spots. The frequency of the phonons remains constant with changing probe polarization. The initial phase of the optical phonon oscillations, plotted in Fig 4.7(e), was found to be independent of pump polarization, while showing a 180° phase change when the probe polarization was rotated from the GaSb[010] axis to the GaSb[100] axis. The long-lived tail in the GST/GaSb(001) sample was only dependent upon the orientation of probe polarization as presented in Fig 4.7(f).

The dependence of the amplitude and frequency of the 6.7 THz mode in GST/GaSb(001) upon probe orientation is presented in Figs 4.7(g) and (h), respectively.

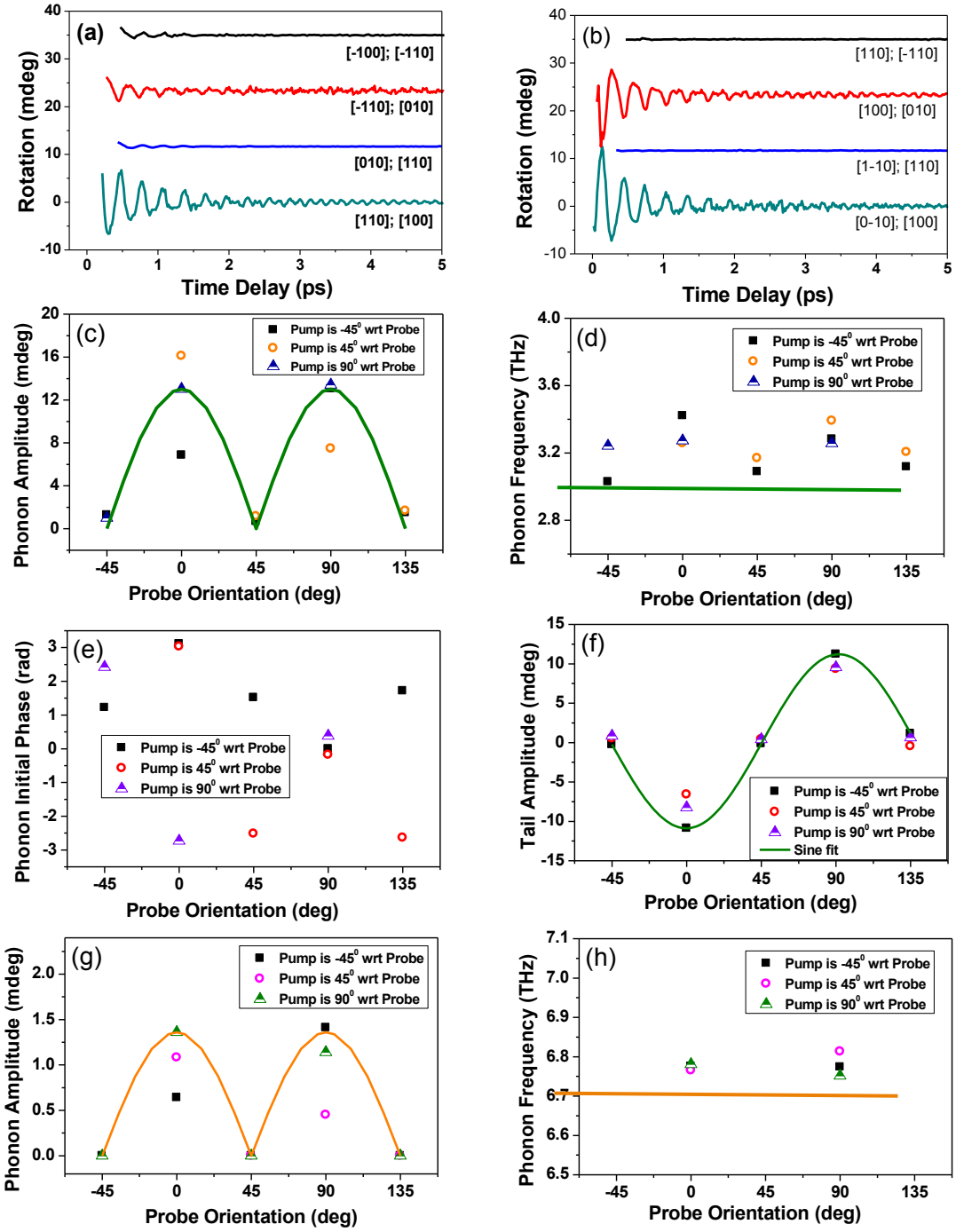

Figure 4.7**: The dependence of transient AR signal upon orientation of the GST/GaSb(001) sample:** (a) and (b) are the oscillatory components of AR signals for various orientations of the sample with pump and probe polarizations fixed relative to each other, at 45° and 90° respectively; (c), (d), and (e) show respectively the amplitude, frequency, and initial phase of optical phonons generated in the GST/GaSb(001) sample; (f) the amplitude of the long-lived tail; (g) and (h) show respectively the amplitude and frequency of optical phonons generated in the GaSb underlayer.

The epitaxial GST film exhibits a distorted rock-salt structure with about 20% of the Ge/Sb atomic sites being vacant. The ideal rock-salt structure has O_h symmetry with five irreducible representations, usually denoted as A_{1g}, A_{2g}, E_g, T_{1g} and T_{2g} [29,84], but none of the associated phonon modes are Raman active [29]. As for zincblende, the threefold degenerate T_2 mode is split into a LO phonon and doubly degenerate TO phonons at the zone centre, the LO mode having a slightly higher frequency [89]. The Raman tensor for the T_2 mode has the same form for structures of both O_h and T_d symmetry. However, the structure of GST is only 'rock-salt like'. Ordering of vacancies and the displacement of ions from their positions in the ideal rock salt structure may remove the inversion symmetry, allowing 1st order Raman scattering and also excitation of COPs by a SSC field. Indeed the character of the allowed phonon modes may be modified. For example, the zone-center T_2 mode might be transformed into 1-D A and 2-D E modes if the symmetry of the crystal is reduced.

In previous studies of amorphous and polycrystalline GST films, a 3.4 THz mode observed in the R signal was assigned A_{1g} character [68-71]. However, Merlin's theory (described in section 4.3.4) predicts that the A and E modes should be observed only within the R signal, with no dependence on pump or probe polarization, while being absent from the AR signal. The weak oscillations at 4.2 – 4.5 THz in the R signal in Fig 4.1(a) have a frequency close to those observed previously [19,68,69] and are attributed to an A mode. However, the observation of the 3.4 THz mode in the AR signal, and its $\cos 2\theta$ dependence on probe polarization, point to T_2-like character. Its frequency suggests that Sb-Te bonds play an important role [68]. In contrast to the 6.77 THz T_{2z} mode of GaSb, the amplitude and phase of the T_2-like mode in GST have only a weak and unclear dependence on the pump polarization. This suggests that the COP is excited by a SSC field, with negligible contribution from ISRS. Excitation may occur within the GST if broken inversion symmetry causes the GST to become piezoelectric. Alternatively, the response of the GaSb to a SSC field may generate impulsive excitation of the GST at the GaSb/GST interface.

Microscopic model

Let us attempt to understand the microscopic origin of T_{2z} excitation in the GST film. In the rock-salt structure there are two basis atoms in the unit cell. The rock-salt structure contains six-fold coordinated atoms rather than tetrahedral bonds like in zincblende.

An incident ultrafast laser pulse excites coherent phonons in the crystal by forcing atoms to vibrate in certain directions. The atomic displacement pattern is an inherent property of any material that depends on its crystal structure. According to Heine, a phonon is said to be participating in a particular Raman mode if the symmetry of the displacement pattern (Q_i) matches the symmetry of one of the representations of the polarizability (or susceptibility) tensor $\left(\frac{\partial \chi_{kl}^{i}}{\partial Q}\right)$ [90]. Unlike for the zincblende structure, the allowed lattice vibrations in an ideal rock-salt structure involve motion with components parallel to all three cubic axes as given below:

$$
\begin{aligned}
d_1 &: (u_1, -v_1, -w_1); (-u_2, v_2, w_2) \\
d_2 &: (-u_1, -v_1, w_1); (u_2, v_2, -w_2) \\
d_3 &: (-u_1, v_1, -w_1); (u_2, -v_2, w_2)
\end{aligned}
$$

----------(4.19)

where d_i represents the allowed mode and u_i, v_i, w_i are the displacement amplitudes in the x, y and z directions, respectively, for the ith basis atom (i = 1, 2). The amplitude of vibration along the x-axis (expressed as u_i) is very small and can be neglected.

Fig 4.8(a) represents the unit cell of the ideal rock-salt where green circles indicate the positions of Te atoms and blue circles describe the positions of Ge, Sb and vacancies. When an optical pump pulse is applied to initiate a disturbance in the material, the basis atoms start to oscillate along three axes as described in equ (4.19). The green and blue atoms oscillate in opposite directions as shown by the blue arrows in fig 4.8(b), which represents a top view of the rock-salt structure. The displacement pattern for the T_{2z} phonon sees the [110] and [-110] directions being inequivalent, leading to a $\cos 2\theta$ probe polarization dependence, as explained by ISRS theory. However, the microscopic picture does not explain the dependence of amplitude upon pump polarization. An improved

understanding of the $Ge_2Sb_2Te_5$ crystal structure is required to understand the microscopic origin of the phonon modes.

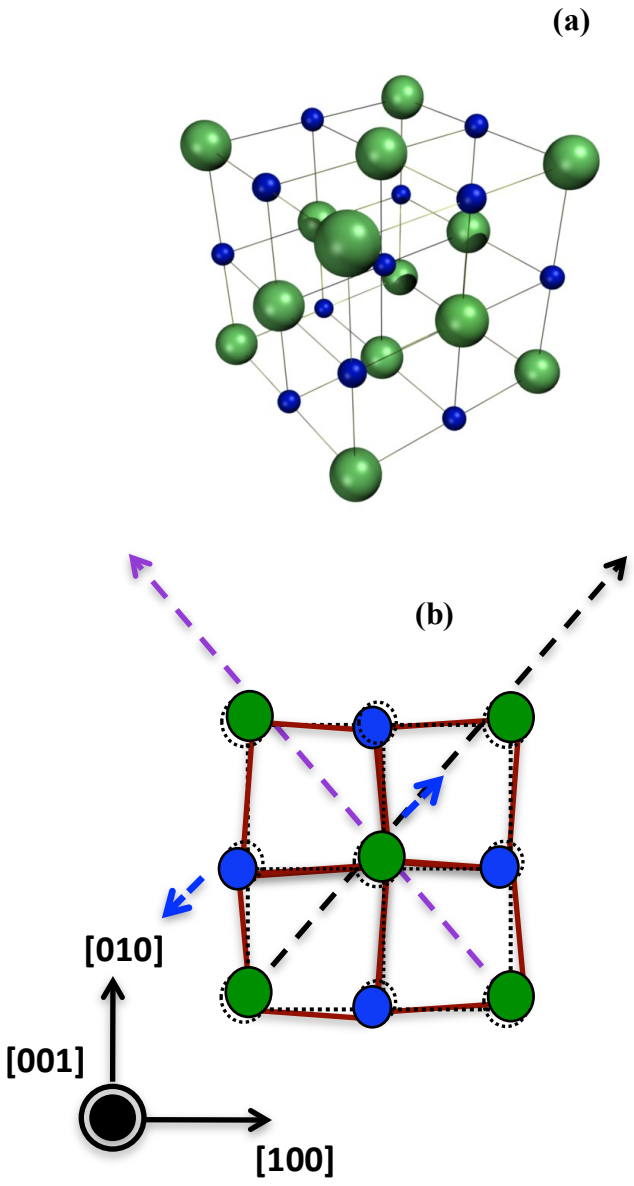

Figure 4.8**:** (a) Unit cell of the ideal rock-salt structure to understand the origin of phonons in GST. GST has a distorted rock-salt structure having 20% randomly distributed vacancies in the unit cell. Top-view and allowed vibrations are represented in (b). Green circles indicate the positions of Te atoms in GST whereas blue circles describe the position of Ge, Sb and vacancies.

4.3.8 Effect of elevated pump fluence and phase transition

Previous studies [91,92,93] have shown that structural phase transitions can be induced in GST by single or multiple fs optical pulses. Here, the dependence of the R and AR signals and the associated COP upon pump fluence was investigated with pump and probe electric fields parallel to the [110] and [100] axes, respectively. A measurement was made on as-deposited material at elevated pump fluence and then immediately repeated with a reduced fluence of 0.42 mJ/cm^2.

The power spectra of AR and R signals calculated from the repeated scans on GST/GaSb is shown in Figs 4.9(a) and (b). The FFT power of AR and R signals from repeated scans on GaSb is presented in Figs 4.9(c) and (d) for comparison.

At low fluence, the COPs with 3.4 and 6.77 THz frequency are observed only in the transient AR response of the GST/GaSb and GaSb samples respectively. The repeated scans at 0.42 mJ/cm^2 fluence show that the 3.4 THz mode in GST/GaSb vanished after exposure to a fluence of 1.70 mJ/cm^2, while the 6.77 THz mode vanished after exposure to a fluence of 2.12 mJ/cm^2 in both samples. COPs instead appeared in the AR signal at frequencies of 4.2 THz in both samples and at 3.1 THz for the GST/GaSb sample. The 4.2 THz mode also appeared with large amplitude in the transient R signal of both samples. The 4.2 and 3.1 THz COPs may be attributed to the A_{1g} and E_g modes of elemental Sb, that segregates at the elevated temperatures induced by the pump [75]. The frequencies observed in the present study are about 0.4 THz lower and hence distinct from those commonly observed by others in the R signal from amorphous and polycrystalline GST [79,94].

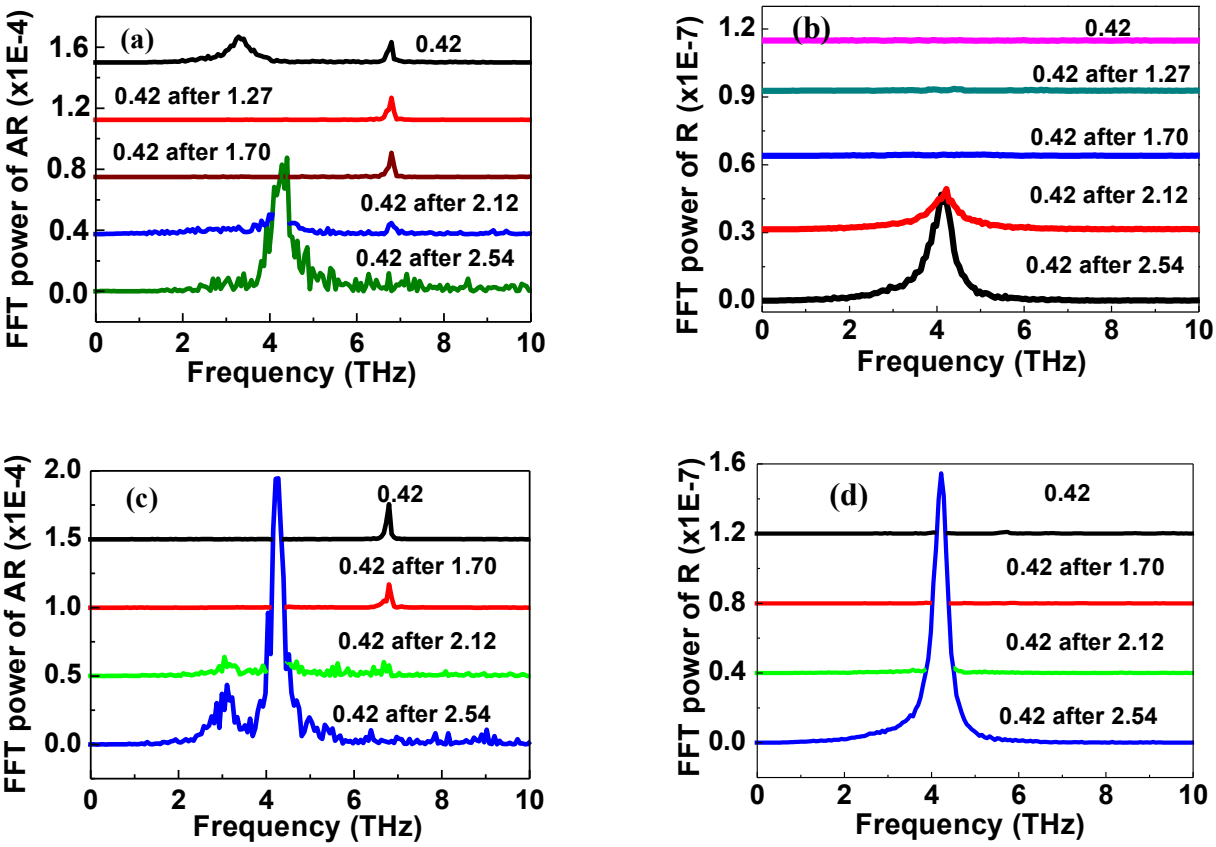

Figure 4.9: Power spectra obtained from AR and R signals measured with a pump fluence of 0.42 mJ/cm^2, after exposure of as-deposited (a-b) GST/GaSb and (c-d) GaSb samples to the higher pump fluences indicated in the plot

Fig 4.10 (a) and (b) respectively show the transient AR and R signals obtained from GaSb(001) with an elevated pump fluence. The oscillatory components of the transient AR and R signals obtained from the repeated measurement at a reduced fluence of 0.42 mJ/cm^2 are shown in 4.10 (c) and (d). The corresponding power spectra are already presented in 4.9 (c) and (d) for comparison.

The amplitude of the oscillatory component (not shown) measured at elevated fluences up to 1.70 mJ/cm^2 was found to have a sub-linear dependence on fluence, as shown in panel (e). The frequency, also shown in panel (e), decreased with increasing pump fluence. The

relaxation time of the oscillations decreased from 5.0 ps to 3.5 ps as the fluence increased from 0.42 to 1.70 mJ/cm^2.

This result is consistent with theoretical calculations of the decay of non-equilibrium phonons into lower frequency phonons [95]. The anharmonic decay of the zone center LO and TO phonon modes in a material with the zincblende structure follows the rules of energy and momentum conservation. A long-wavelength phonon mode can decay into lower energy optical and acoustic modes via either Ridley, Klemen or Vollee-Bogani channels [95]. Klemen described the decay of a zone-center optical phonon into two acoustic phonons with equal and opposite wave vectors. Considering the various possibilities for TO phonon decay in GaSb, it is found that the hot zone-centre phonons excited by the optical pump decay into two (or more) phonon modes via a Klemen channel Γ(TO) -> TA + LA. Unlike the TO mode, the LO mode can decay to lower frequency phonons via all three channels..

The results of measurements made upon GST/GaSb(001) are shown in Fig 4.11. Panels (a) and (b) respectively show the transient AR and R data obtained at elevated fluence. The oscillatory components of the transient AR and R signals extracted from repeated scans at low fluence are shown in (c) and (d), while their respective power spectra are shown in Figs 4.9 (a) and (b). The peak heights of the AR and R signals in Figs 4.11 (a) and (b) are plotted in (f), and are seen to exhibit a linear dependence upon the pump fluence. Clear oscillatory components (not shown) with a frequency of about 3.4 THz were observed in measurements made at elevated pump fluences in the range 0.42 to 1.06 mJ/cm^2. Panel (e) shows how the amplitude increased linearly above a threshold fluence of about 0.4 mJ/cm^2 and the frequency decreased linearly with increasing fluence. The phonon relaxation time (parameter τ_2 of section 4.3.2) was found to decrease from 660 fs at 0.42 mJ/cm^2 to 470 fs at 1.06 mJ/cm^2.

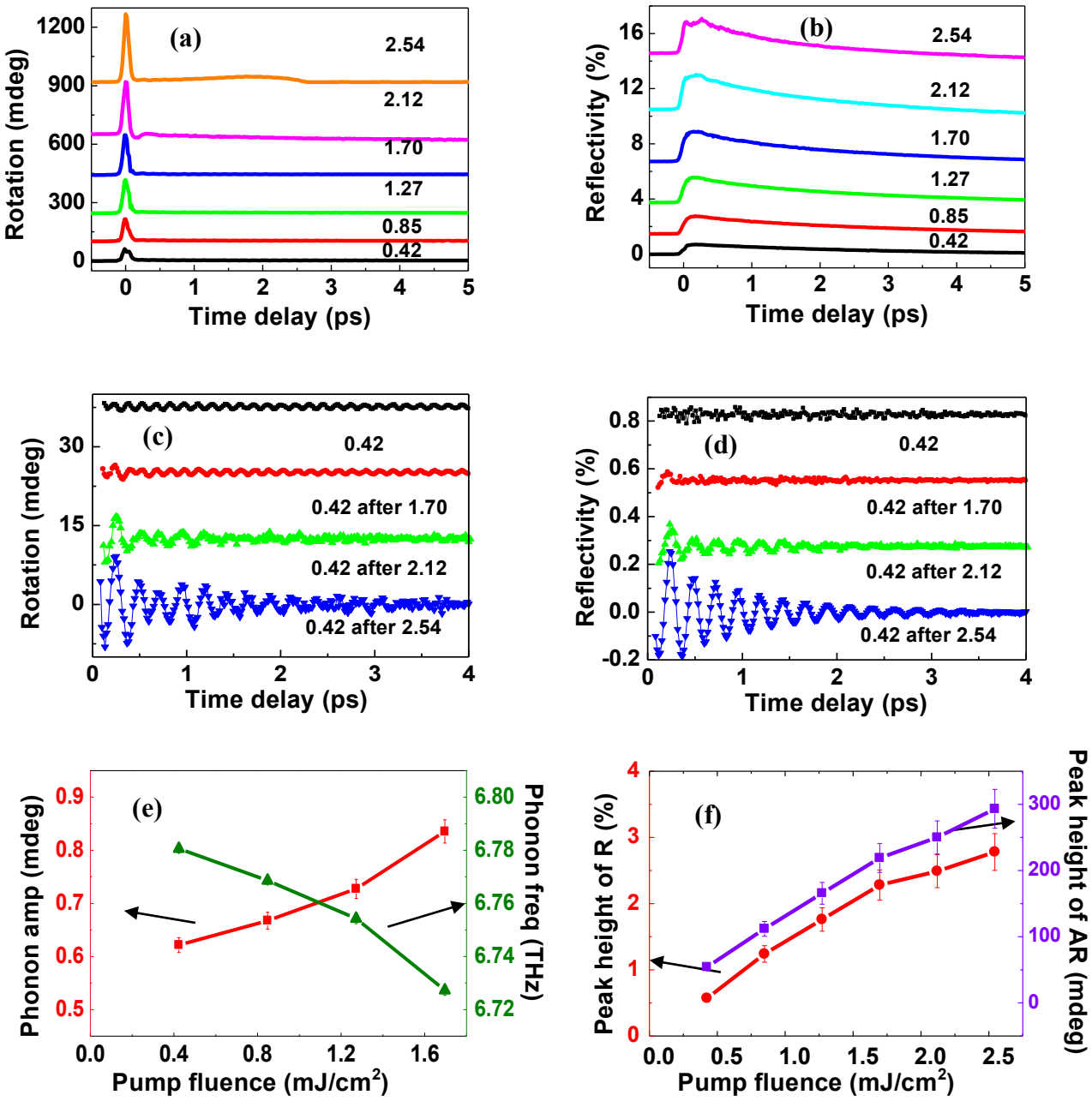

Figure 4.10**:** Effect of elevated pump fluence upon the transient R and AR signals obtained from GaSb(001). (a) and (b) transient AR and R signals respectively, obtained at the values of the elevated fluence indicated in the figure. (c) and (d) oscillatory components of the AR and R signals respectively, obtained with 0.42 mJ/cm^2 pump fluence after exposure to higher pump fluence. (e) dependence of the phonon amplitude and frequency during measurement at the elevated pump fluence. (f) height of the initial peaks in the R and AR signals in (a) and (b) are plotted against pump fluence.

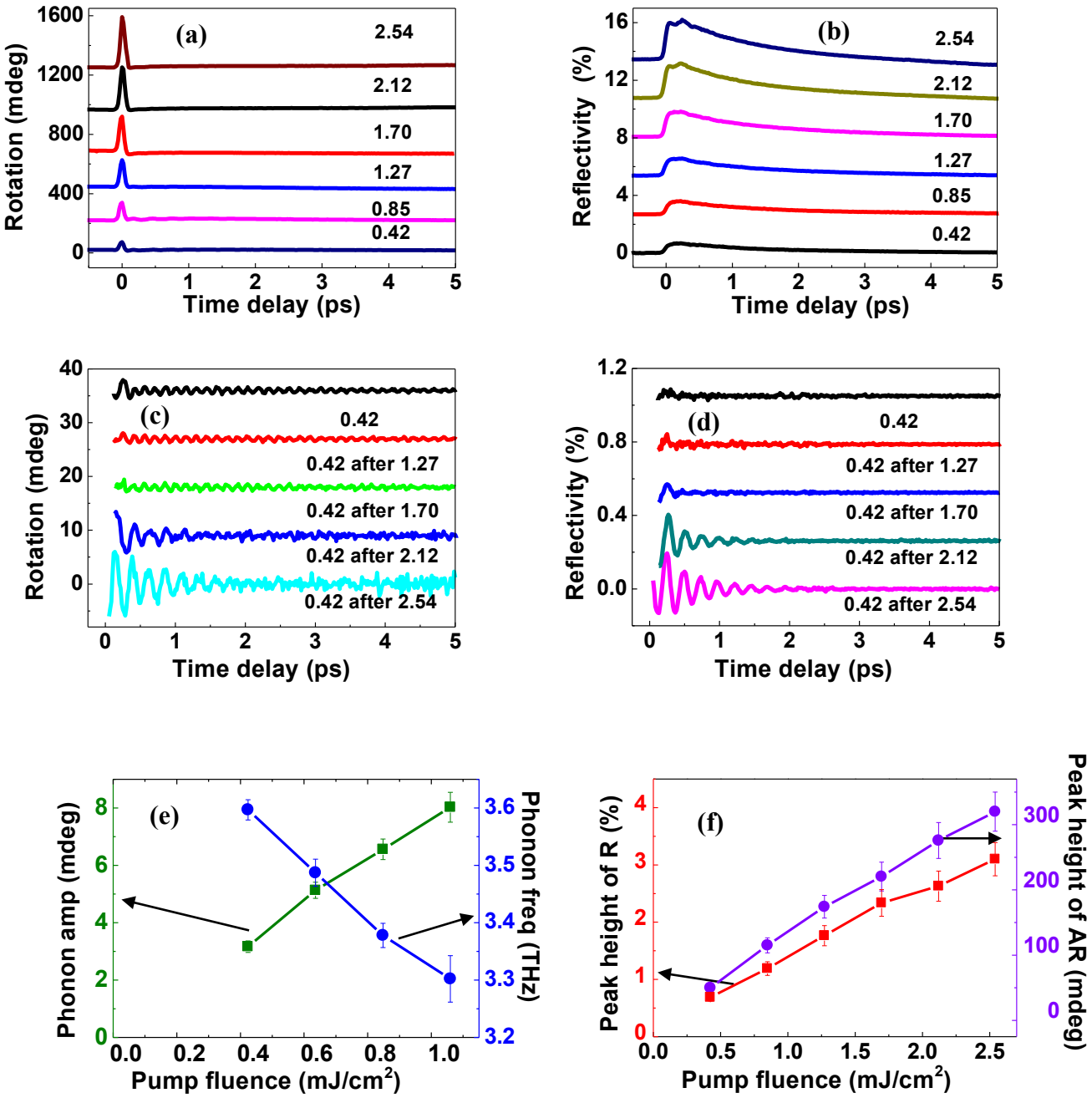

Figure 4.11: Effect of elevated pump fluence upon the transient R and AR signals obtained from GST/GaSb(001). (a) and (b) AR and R signals obtained at elevated pump fluence. (c) and (d) oscillatory AR and R signals obtained from repeated measurements at 0.42 mJ/cm^2 pump fluence. The variation of the phonon amplitude and frequency is shown in (e), while the height of the initial peak in the R and AR signals, from (a) and (b), is plotted against pump fluence in (f).

4.4 Conclusions

In summary, comprehensive time-resolved reflectance and anisotropic reflectance measurements have been performed upon epitaxial GST/GaSb(001) and GaSb(001) samples. The orientation of pump and probe electric fields have been varied relative to the crystallographic axes. The AR measurements are richly featured and yield relaxation times that can be ascribed to the interaction of the different populations of electron and phonons. GaSb(001) is an exemplar in which the observation of the T_2 transverse optical phonon has been shown to result from a combination of ISRS and the action of a SSC field. The results can be fully understood, both in terms of a theory based upon use of the Raman tensor, and also from a microscopic model of selective optical bond excitation. Epitaxial GST/GaSb(100) exhibits both the T_2 mode supported by the substrate and also a T_2-like mode associated with the GST. The insensitivity to the pump polarization suggests that the T_2-like mode is excited by a SSC field, either in the GST if the distorted rock-salt structure lacks inversion symmetry, or by a SSC field in the GaSb leading to impulsive excitation of the GST at the GST/GaSb interface. The observation of the T_2-like mode provides confirmation that the GST is essentially cubic and challenges mode assignments made in previous studies. The SSC field also generates lateral stress in the lattice that leads to a long-lived transient AR response. This may be important for the generation of surface acoustic waves (SAWs) that can be steered by means of the optical polarization, without the need for an overlaid grating. Finally, the formation of a new phase after exposure to large pump fluence was observed in both GST and GST/GaSb. The observed frequencies suggest segregation of Sb, while increased disorder in the GaSb and GST leads to the disappearance of the T_2 and T_2-like modes from the AR signal.

Chapter 5

Coherent Phonons of Crystalline and Amorphous $Ge_2Sb_2Te_5$ thin films: a fingerprint of structure and bonding

5.1 Introduction

$Ge_2Sb_2Te_5$ is widely used in storage media and has the potential to replace semiconductor memories. As described earlier in the thesis, its use in optical storage is based on the large difference in optical properties between its crystalline and amorphous states. Therefore it is important to understand the optical properties of all three states (epitaxial, polycrystalline and amorphous) of $Ge_2Sb_2Te_5$. In this chapter, I investigate the transient reflectivity (R) and anisotropic reflectivity (AR) response of the polycrystalline and amorphous phases of thin-film GST to intense femtosecond laser pulses using a time-resolved optical pump-probe technique. The results are compared to the R and AR response of an epitaxial sample. A detailed study of the reflectance and rotation of epitaxial $Ge_2Sb_2Te_5$ is provided in chapter 4. THz optical vibrations of different frequencies have been observed in the three different phases. Additional Raman microscope measurements confirmed the presence of the modes observed in the pump-probe measurements. These vibrational frequencies help us to understand the crystal structure and phase-transition mechanism in the GST phase-change alloy. As for epitaxial GST measurement, the response of polycrystalline and amorphous samples at high pump fluence is also examined.

5.2 Sample details and experimental method

The samples used in this study were as-deposited polycrystalline (37 nm) and amorphous (57 nm) $Ge_2Sb_2Te_5$ (GST) thin films grown on SiO_2(15 nm)/Si(001) substrates. The sample stacks are shown in fig 5.1. R and AR signals from these samples were compared with those from an epitaxial $Ge_2Sb_2Te_5$ layer grown on a GaSb(001) substrate with stack structure (fig 5.1) as follows: $Ge_2Sb_2Te_5$(15 nm)/GaSb(50-100 nm)/GaSb(001). The epitaxial GST film was found to have a predominantly cubic-on-cubic growth behaviour with the GST[100] axis parallel to the GaSb[100] axis [72]. We use the following terminology: e-GST to represent the epitaxial film; p-GST for polycrystalline; and a-GST for amorphous GST material.

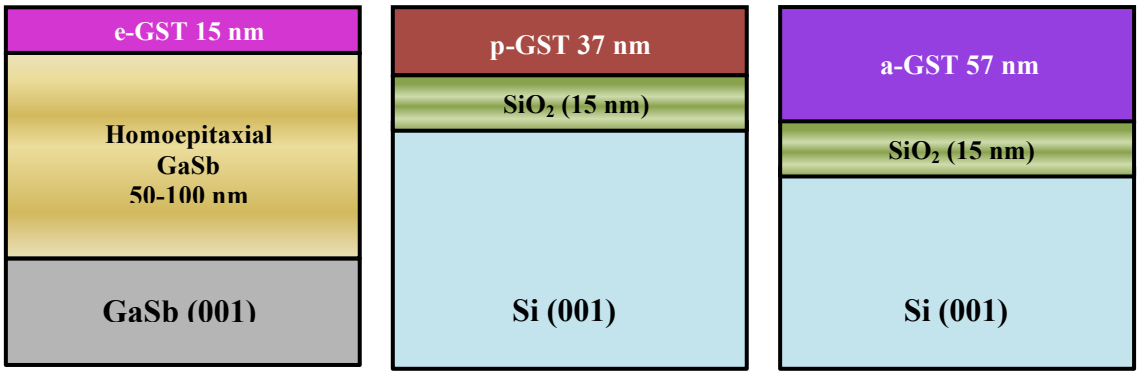

Figure 5.1: **Sample stack**: (a) for epitaxial (b) polycrystalline and (c) amorphous GST films with 225 composition. The films are of various thicknesses and deposited at different temperatures on different substrates. The e-GST film was grown at 200^0 C on homoepitaxial GaSb (001) and found to have cubic growth. The p- and a- GST were grown on Si (001) substrates with a thin SiO_2 underlayer at 200^0 C and at 20^0 C respectively.

Time-resolved optical reflectivity and rotation measurements were conducted upon polycrystalline and amorphous GST thin films in an all-optical pump-probe configuration using femtosecond pulses from a Ti:Sapphire regenerative amplifier. A linearly polarized, 800 nm wavelength, 55 fs pump pulse with a fluence of 0.85 mJ/cm^2 was directed to the

sample at close to normal incidence. An 800 nm wavelength, an s-polarized, 55 fs probe pulse with a fluence of 0.2 mJ/cm^2 incident at 45° was used to monitor the response. The intensity profiles for the pump and probe beams were observed to be Gaussian with 1/e^2 spot sizes of 100 μm × 120 μm and 30 μm × 40 μm respectively. The transient R and AR responses of the sample were measured by detecting the reflected probe beam using a bridge detector. Essentially the experimental conditions for the p/a-GST samples and e-GST were the same. More details about the experiment are provided in chapter 3 (experimental technique) and chapter 4 (epitaxial GST results).

5.3 Results and discussion

5.3.1 Reflectance and Anisotropic Reflectance signal

The transient AR and R responses of all three samples are shown in Fig 5.2 for comparison. Fig 5.2(a)/(b) displays the AR/R response of the e-GST film for the pump polarization along GaSb [110] and the probe polarization along the [100] axis. The pump polarization is set along the face diagonal of the e-GST where the amplitude of oscillations was found to be larger than when the pump polarization is parallel to a cubic axis. Also it is important to notice that the pump polarization makes an angle of 45 deg with the probe polarization. Fig 5.2(c)/(d) present the AR/R response of the p-GST film, and Fig 5.2(e)/(f) show the AR/R response of the a-GST sample when the pump is polarized at 45 deg relative to the probe polarization. The AR signal contains a variety of information on a wide range of different time scales. To extract those various interesting features the response is plotted over ns (main panel) and longer time scales (two insets). The AR signal is plotted on three different timescales to reveal clearly three important features: (i) a large peak on fs time scales with a Gaussian profile within the temporal overlap of the pump and probe pulses; (ii) oscillatory components on the early ps time scale superimposed on a relaxation background; and (iii) a longer-lived tail (ns scale).

It is noticed that all three samples, e-GST, p-GST and a-GST films exhibit a sharp initial peak with maximum amplitude when pump and probe polarizations are ± 45° apart. The peak vanishes when the pump and probe polarizations are either parallel or perpendicular

(90 deg to each other). Throughout the measurements, the probe polarization was kept fixed at 90 deg (i.e. s-polarized) and the polarization of the pump, at normal incidence, was rotated from 0 deg to 135 deg to change the angle between pump and probe polarizations. This initial peak is associated with optical modification of the electron momentum distribution. The linearly polarized pump beam transfers linear momentum to electrons in the surface of the sample, and leads to a transient linear birefringence known as the specular optical Kerr effect (SOKE). The width of the SOKE peak is close to 100 fs in all three samples, and appears similar to an autocorrelation of the pulse in most materials. In fact, the precise form of the pump-induced transient polarization signal contains information about the rate of relaxation of the linear momentum of the excited electrons [96].

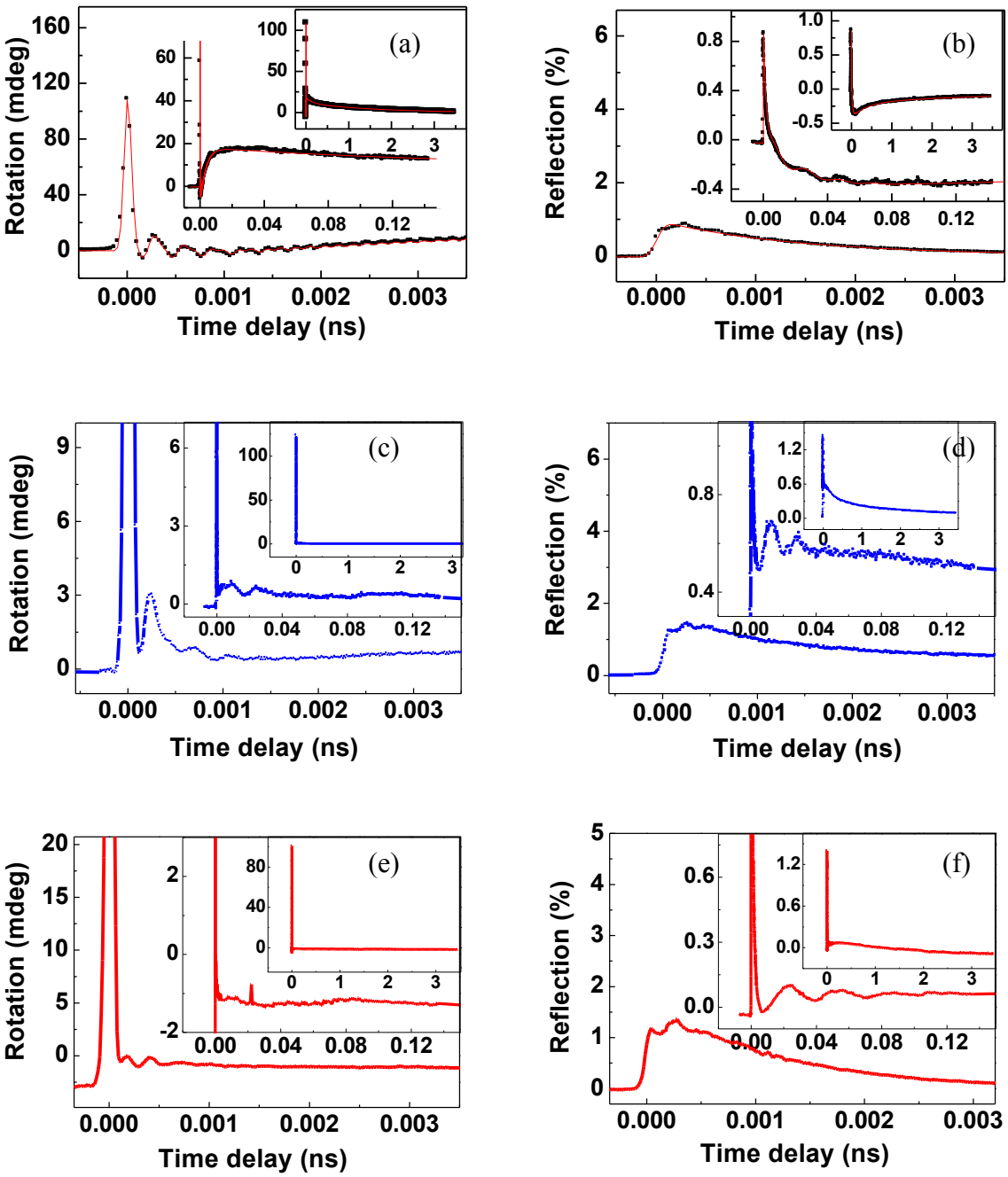

Figure 5.2: **Typical pump probe signals**: (a)/(b) presents the AR/R response of the e-GST film for pump polarization along the GaSb [110] axis and probe polarization along the [100] axis, and (c)/(d) presents the AR/R response of the p-GST film, while (e)/(f) shows the AR/R response of a-GST when pump and probe polarization make an angle of 45°.

5.3.2 Coherent optical phonons (COP)

Oscillations are observed in the AR and R signals acquired from GST on early ps time scales, superimposed on a background. Compared to e-GST, the AR response of p/a-GST is less complicated. The red line in Fig 5.2(a) shows fitting to the experimental data for the e-GST sample. The fitting function consists of a Gaussian function to describe the initial peak, a series of Gaussian error functions to describe the multi-exponential background and a cosine function to describe the oscillatory response. The form of the fitting function is given in chapter 4 with its derivation in appendix 1. Fitting the e-GST rotation signal yields two strong phonon modes and various relaxation times corresponding to the complicated background. These relaxation times are carefully assigned to carrier-carrier and carrier-phonon interaction processes in chapter 4.

The anisotropic reflectance signal of p/a-GST contains a rather simple background with fewer phonons of comparatively smaller amplitude. Therefore only the oscillatory signal was analyzed by taking a fast Fourier transform of the time-domain signal (FFT). Fitting provides the frequency of the COP in the p/a-GST samples, which was then compared to the frequencies of the phonon modes of e-GST.

Clear oscillations with a 3.4 THz frequency were obtained in the transient AR response of the e-GST film with a four-fold dependence on probe polarization. The phonons have weak or no dependence upon the orientation of the pump polarization. Additionally, this mode did not appear in the transient R response. Another weak phonon mode of much smaller amplitude with a frequency close to 4.5 THz was observed only in the transient reflectivity channel. On the other hand, only a few phonon oscillations of close to 4.5 THz frequency, with no pump and probe polarization dependence, were observed in both the transient R and AR response of the p-GST film. An additional frequency of 2.3 THz was also observed in the transient AR signal of the p-GST sample, but only when the probe was polarized parallel to the cube edge of the Si substrate. Phonons with an almost similar 4.5 THz frequency were observed in the transient AR and R response of a-GST. It is also important to mention that the phonons have a much larger amplitude (approx 20 mdeg) and longer relaxation times in the AR response of the e-GST film, whereas phonons with considerably

smaller amplitude and shorter relaxation time were found in the R and AR response of the p/a-GST films.

No long-lived transient birefringence (”tail”) was noticed in p-/a- GST films. The large amplitude tail in the e-GST rotation signal results from strain associated with an optically-induced space-charge in the GaSb substrate.

Micro-Raman measurements were performed on all three samples to check for the presence of the modes observed in the pump-probe measurements, and to gather more information about other modes within GST. A laser beam of 785 nm wavelength was incident at normal incidence to the sample. The spot size of the beam was $20 \times 20\ \mu m$. The reflected beam contains both elastically and inelastically scattered light, which was separated using a filter. The inelastically scattered light then reaches the detector with the help of a diffraction grating. The system was equipped with an optical microscope, which can image the sample area being investigated with the Raman probe. The optical path for the incident beam also contains a waveplate that can be used to change the polarization of the incident beam. By placing a second polarizer (analyzer) in the path of the scattered light, measurements can be made with the incident and scattered polarizations being either parallel or crossed. The inelastically scattered light intensity count was plotted against the wavenumber (cm^{-1}). A calibration on a Si sample was performed before making the measurements on an actual sample. A peak is observed at 520 cm^{-1}, which is a characteristic wavenumber for Si. The Raman spectra for all three samples are presented in fig 5.3 for comparison. Generally all three samples display similar behaviour with stronger intensity peaks at lower wavenumbers. Unlike e-GST, polycrystalline and amorphous sample show a simpler spectrum at higher wavenumber. The additional peak at 236 cm^{-1} (7.08 THz) in the e-GST sample belongs to the e-GaSb substrate. This was confirmed by obtaining the Raman spectrum of the e-GaSb alone. As discussed in chapter 4, the pump-probe measurement of e-GaSb also confirms the presence of optical phonons at 6.77 THz. The different frequency detected by Raman measurements in the e-GaSb sample can be associated with the zone centre LO phonon, whereas the TO phonon is detected in pump-probe measurements. The broad band at smaller wavenumber was fitted by using multi-peak fitting feature in the Origin software package, which gives the frequencies as shown in table 5.1.

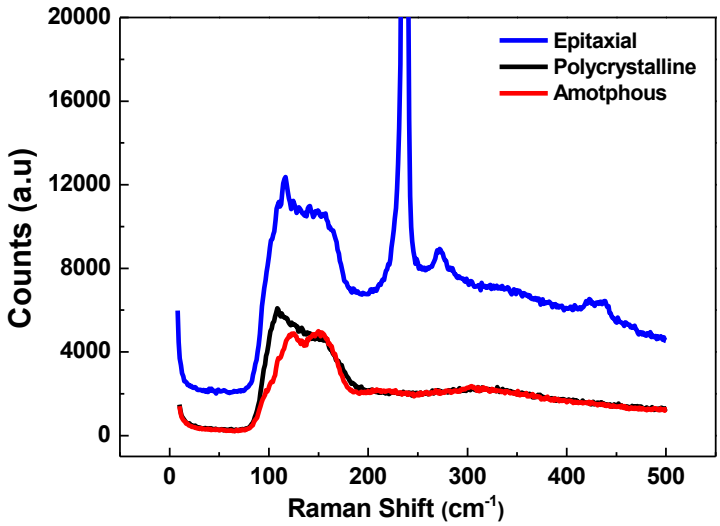

Figure 5.3: Raman spectra for e-/p-/a-GST samples

GST		Epitaxial (THz)	Polycrystalline (THz)	Amorphous (THz)
Pump-probe frequency	AR	3.4 ± 0.1	4.4 ± 0.3	4.5 ± 0.3
	R	4.5 ± 0.3	4.5 ± 0.3	4.5 ± 0.3
Raman frequency		3.37 ± 0.04	3.24 ± 0.04	3.60 ± 0.02
		4.42 ± 0.06	4.31 ± 0.03	4.62 ± 0.02
After high fluence	AR/R	4.21 ± 0.01	3.54 ± 0.01	3.61 ± 0.01

Table 5.1: Comparison of pump-probe and Raman frequencies. Pump-probe frequencies were obtained by directly fitting the time-domain data for e-GST and from the FFT power spectrum of the time-domain data in p/a-GST, while multipeak fitting was applied to the Raman spectra of all three samples.

Table 5.1 displays the GST mode frequencies observed in pump-probe and Raman measurements for comparison. The frequencies were found to change when high pump fluence was applied as described in the next section. The Raman spectra of all three samples display a broad band between 80 and 180 cm^{-1} wavenumber with two strong peaks, one close to 110 cm^{-1} (3.3 THz) and the other around 150 cm^{-1}(4.5 THz). The lower frequency for the p/a-GST sample was not observed in the pump-probe configuration. However, both the Raman frequencies of the e-GST sample are seen in the pump-probe experiment, with the strong 3.4 THz mode seen in the anisotropic reflectance signal and the weak 4.5 THz mode seen in the reflectance signal. The frequencies obtained from Raman and pump-probe measurements agree within experimental error for all three samples.

The pump-probe frequencies for p/a-GST were obtained by peak fitting to the FFT power spectra of their AR and R signals. Fig 5.4 shows a Lorentzian fit to the FFT power spectrum of the AR signal for the polycrystalline sample. The fitting provides a frequency of 4.5 THz with an error of ± 0.3 THz.

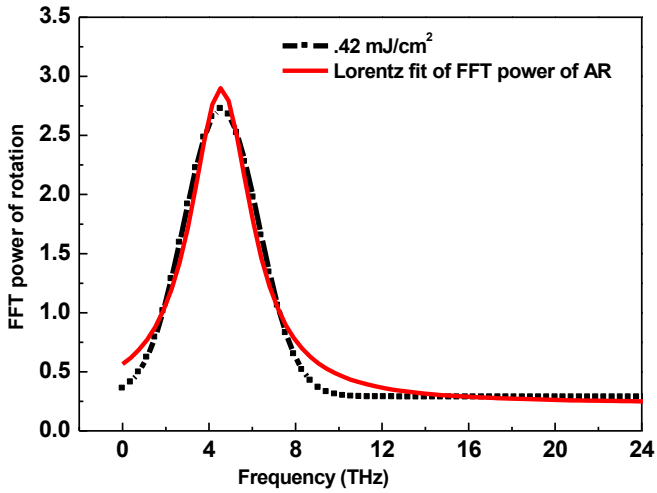

Figure 5.4: The peak fitting of the FFT power spectrum of the AR signal for the polycrystalline GST sample

Fig 5.5 shows how multipeak fitting with the Origin software was used to extract the frequencies from the Raman spectrum. The fitting procedure is as follows: First the

baseline/background of a spectrum was removed. The peak centres were manually located by using the peak analyzer preview function and then these peaks were fitted by a multipeak fit tool. The fitted Raman spectrum of the e-GST sample is shown in Fig 5.5. The green line shows the fitting of three individual peaks while the red line shows the superposition of all individual modes. All the Raman frequencies in table 5.1 were extracted in the same way.

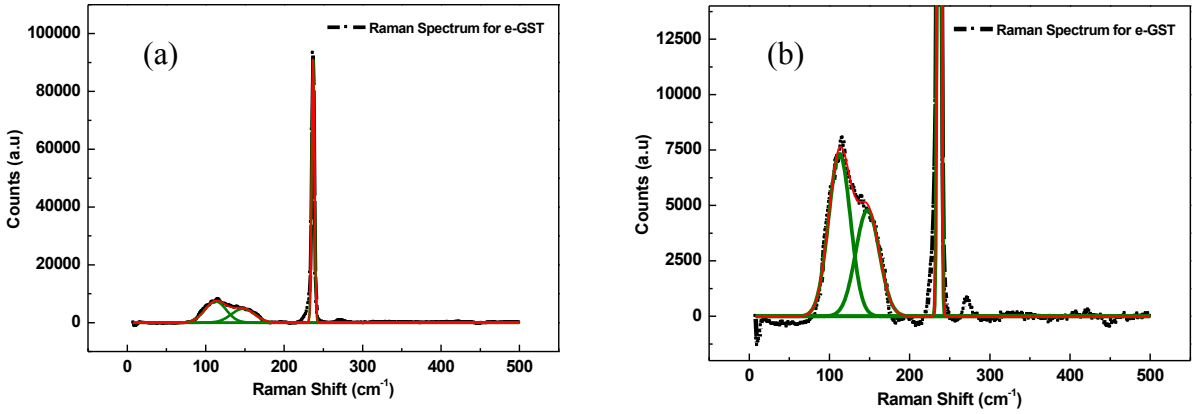

Figure 5.5: (a) The multipeak fitting of the Raman spectrum of the e-GST/GaSb(001) sample. (b) The spectrum in panel (a) is zoomed in to show the fitting of the GST signal at lower wavenumbers.

The differences in the frequencies observed from the different samples are quite small. This suggests the presence of similar bonds that are modified to some extent by the different structural environment found within each sample. It should be noted also that the three samples have different thickness and substrates. e-GST and p/a-GST were deposited on GaSb and Si substrates, respectively. Yet the presence of similar frequencies in the pump-probe and Raman experiments indicate that 3.4 and 4.5 THz are signature frequencies of GST. The Raman spectra for the e-/p-/a-GST samples also agree with those found within the literature [75, 100, 101]. The characteristic modes of the crystalline and amorphous phases of GST detected by a time-resolved pump-probe set up were reported in the literature [71, 72] with a small difference in their frequencies.

Comparing our results with those found in the literature, we can tentatively assign the higher frequency to an A_1 mode of the Te-Te chains or an A_{1g} mode of a Sb_2Te_3 sub-unit in which there is symmetric vibration of Sb and Te layer along the c-axis. However, the assignment of A_1 character to this higher frequency mode is not consistent with Merlin's theory, which predicts that such modes should be observed in both the R and AR channels.

Another mode of 2.3 THz frequency was observed in the AR signal from the p-GST sample for specific settings of the pump and probe polarization. The origin of this mode is unknown.

5.3.3 Effect of high pump fluence

As for the epitaxial GST study presented in Chapter 4, the effect of high pump fluence on the transient R and AR signals and the associated COP was also investigated in p/a-GST films. The transient R and AR signals were collected for both p/a-GST samples from low fluence rescans on the same spot after exposure to the high pump fluence, which takes about 40 minutes. By analysing these signals, the effect of pump fluence upon the height of the peak in the rotation signal, the peak reflectivity signal, and the amplitude and frequency of the coherent optical phonons can be determined. This measurement procedure should allow the repeated low pump fluence scans to reveal the signature of any structural transition that might occur during the scans with high pump fluence.

Figure 5.6(a)/(b) show the effect of pump fluence on the peak height of the transient AR/R signals for p-GST sample. Figure 5.7(a)/(b) shows the effect of pump fluence for the amorphous sample. The polycrystalline and amorphous GST films exhibit quite similar behaviour at low pump fluence (< 2.12 mJ/cm^2) to that observed for e-GST. Firstly, the peak heights of the transient R and AR signals were observed to increase linearly with the pump fluence for the whole range of pump fluences studied. Secondly, only a few period of oscillations of 4.5 THz frequency were observed for the low pump fluence before any structural transitions induced by high pump fluence. Fig 5.6(c)/(d) and 5.6(c)/(d) show the oscillatory components in the transient AR/R signals obtained from the p-GST and a-GST samples, respectively, with a low pump fluence (0.42 mJ/cm^2) after illumination with a high pump fluence. For low pump fluence rescans after exposure to fluences in excess of 2.12 mJ/cm^2, the COP of frequency 4.5 THz in p/a-GST became weak and eventually

disappeared. Instead, a COP was observed with frequency of 3.54 ± 0.01 THz in p-GST and 3.61 ± 0.01 THz in a-GST. These frequencies were obtained by fitting the FFT power spectra of the p/a-GST signals. Fig 5.8 shows the Lorentzian fitting to the power spectrum of the reflection signal for a-GST sample when the sample was rescanned using a low pump fluence of 0.42 mJ/cm^2 after exposure to 2.54 mJ/cm^2. The frequencies obtained from the AR and R signal of p-GST sample were extracted in the same way.

Fig 5.6(e)/(f) and 5.7(e)/(f) show the FFT spectra of the transient AR/R signal for the p-GST and a-GST samples, respectively. A sharp peak at 3.54 (or 3.61) THz in the p- (or a-) GST is suggestive of the degenerate E_g mode of crystalline Sb_2Te_3, for which atoms in the outer Sb and Te layers vibrate perpendicular to the c-axis [68]. This mode can also be associated with the E_g modes of crystalline Sb, which may form locally where high pump fluence has been applied. Comparing the three samples, it is observed that the polycrystalline (amorphous) film has a mode with frequency of 3.54 (3.61) THz after the application of high fluence, which is close to the frequency of the phonon mode observed in e-GST at lower fluence.

While the mode observed in p/a-GST from a low fluence rescan after the application of high fluence is shifted to lower frequency, e-GST shows completely the opposite behaviour. As described in chapter 4, the 3.4 THz mode in e-GST disappeared and a new mode at 4.2 THz due to Sb segregation was obtained from a low fluence rescan after exposure to fluence ≥ 2.12 mJ/cm^2. The sample structure could play an important role in explaining the different frequencies observed after exposure to high fluence. In addition, it is understood from the study of crystallization of GST by fs pulses that will be presented in chapter 6 that these experiments are very sensitive to the details of the sample stack. The presence of a capping layer or underlayer or a difference in sample thickness, can significantly modify the heat flow within the sample, leading to large differences in the structural changes induced by exposure to an elevated pump fluence. The crystallization of GST material depends upon the time-dependent temperature profile. The GST material transforms to the polycrystalline rock-salt structure at temperature between 120 and 150^{0}C. If the material is further heated to higher temperature (above 200^{0}C) then it could crystallize to a hexagonal phase [68]. Given that p/a-GST have different thicknesses, exposure to high fluence could in principle lead to the formation of amorphous, poly rock-salt like, or poly hexagonal GST.

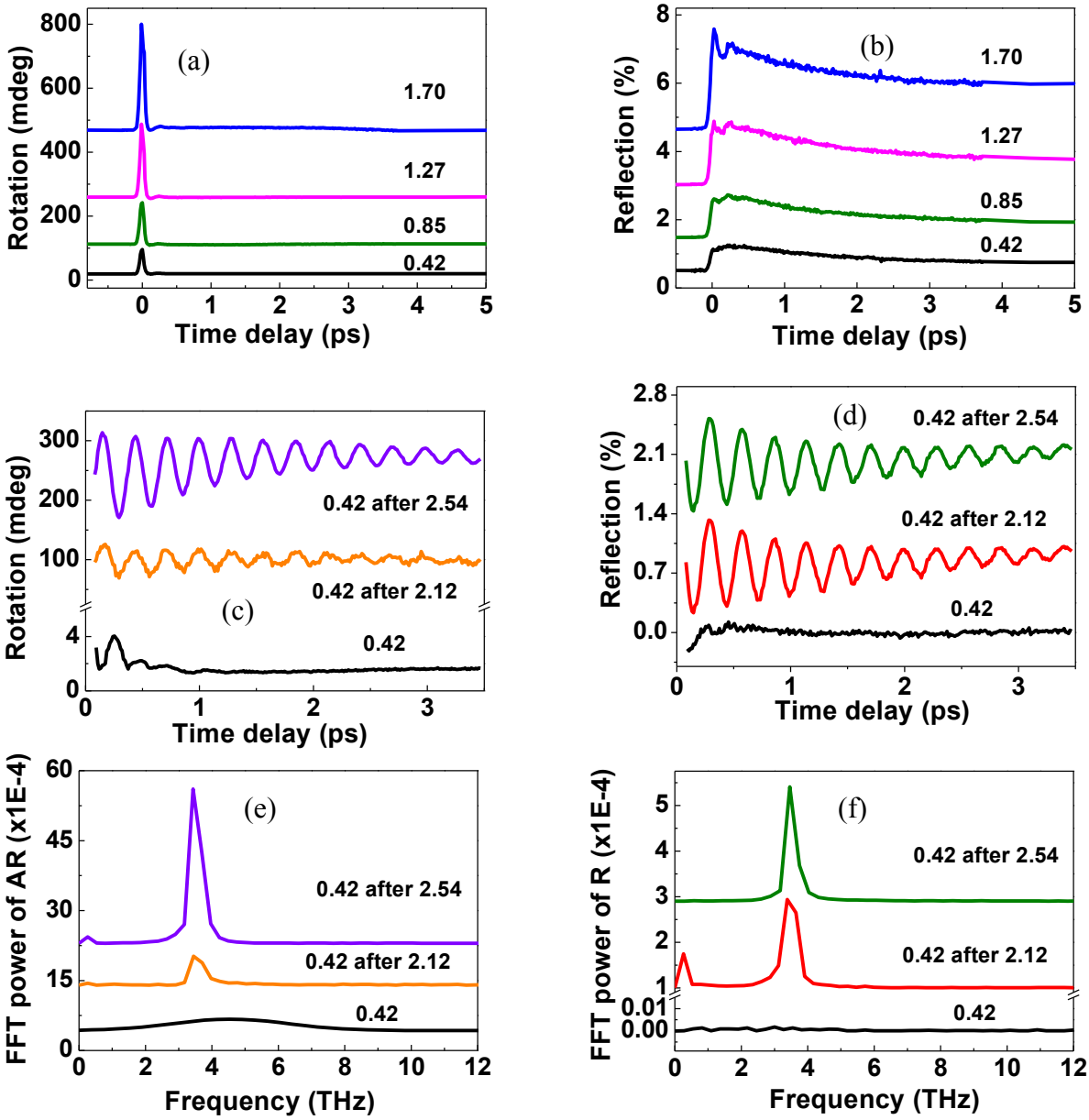

Figure 5.6: **Effect of pump fluence on transient AR and R signals in p-GST:** (a) and (b) display the dependence of peak AR and R signal upon the pump fluence. The oscillatory components of the AR signals obtained with a pump fluence of 0.42 mJ/cm^2 after exposure to a high pump fluence are presented in (c). (d) shows the oscillatory components of R signals obtained with pump power of 0.42 mJ/cm^2 after exposure to high pump fluence. (e) and (f) are the corresponding FFT power spectra of the AR and R signals, respectively.

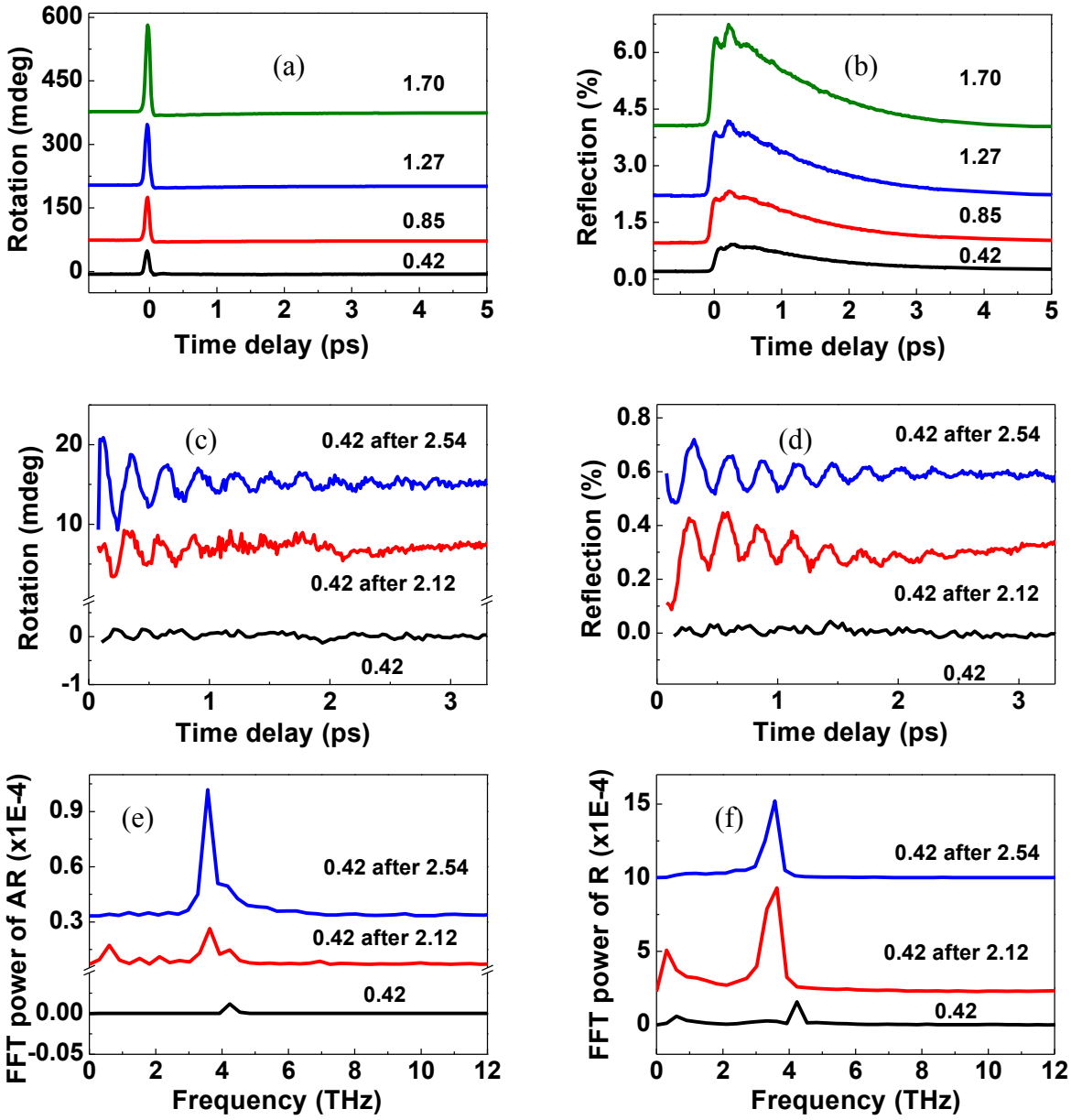

Figure 5.7: **Effect of high pump fluence on transient AR and R signals in a-GST:** The dependence of peak height of AR and R signal upon the pump fluence is displayed in panel (a) and (b). The oscillatory components of AR and R signals obtained with a low pump fluence after exposure to a high pump fluence are presented in (c) and (d) respectively. (e) and (f) display the corresponding FFT power spectra of oscillations in (a) and (b).

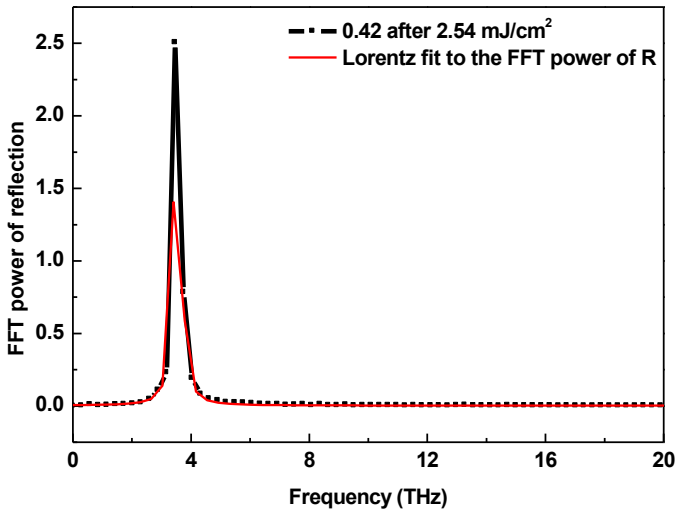

Figure 5.8: The peak fitting of the FFT power spectrum of the R signal obtained after exposure of the a-GST sample to higher fluence and rescanning at low pump fluence

5.4 Conclusion

Comprehensive time-resolved measurements of three samples containing different structural phases of $Ge_2Sb_2Te_5$ were performed. The experimental conditions were similar in each case to allow comparison of the characteristic features of the different phases. The time-resolved transient R and AR responses of the p/a-GST samples are much simpler than those of the e-GST film. Coherent optical phonons of different frequency were observed in all three samples. e-GST exhibits modes of 3.4 THz frequency that appear only in the transient AR response. The dependence of the amplitude of this mode upon the pump and probe polarization suggests it has T_2-like character. The reflectance signal contained oscillations with a frequency close to the 4.5 THz mode. A mode with similar frequency was also observed in the transient R and AR response of the p/a-GST samples. Comparing the frequency with those reported in the literature, we can tentatively assign these modes with frequency of about 4.5 THz to the A_1 mode of Te-Te chains. Exposure to higher pump fluences causes the 4.5 THz vibrations to disappear and a new mode with 3.5 (and 3.6)

THz frequency to appear in the polycrystalline (and amorphous) films respectively. These modes could be associated with the degenerate E_g mode of c-Sb_2Te_3 or the E_g mode of crystalline Sb. Raman spectra obtained from p/a-GST reveal the modes observed in the pump-probe measurements, as well as other modes which were not seen in the pump-probe experiments. The difference in the frequencies observed for the polycrystalline and amorphous samples after exposure to high fluence may result from differences in the sample stack that affect the time-dependent temperature profile within each sample. For all phases there are modes found within the range of 3.2 to 3.6 THz and 4.3 to 4.7 THz. However the frequencies for all three phases are different within the experimental error, which indicates that the structure has a significant effect upon the frequencies.

Chapter 6

Crystallization of $Ge_2Sb_2Te_5$ films by amplified femtosecond optical pulses

In this chapter, we present an experimental study of the phase transition between the amorphous and crystalline states of $Ge_2Sb_2Te_5$ (GST) by exposure of thin films to a series of 60 femtosecond (fs) amplified laser pulses of varying pump fluences. We describe the variation of the area and reflectivity of the crystalline mark with respect to the pump fluence and support our results with a simple algebraic model which provides strong evidence that thermal transport within the sample is vertical (one-dimensional). A theoretical model is presented in which consideration of the optical absorption, thermal transport and thermally activated crystallization leads to simulations of the evolution of the optical reflectivity and mark area that are in good quantitative agreement with the experimental data. Finally, the growth velocity of the crystalline region from the amorphous GST phase is estimated to be in the range 7 – 9 m/s.

Dr Yanwei Liu set up the experiment while Dr Liu and I carried out the measurements in which the pump fluence and number of pulses was varied. A simple form of the theoretical model yielding analytical results was developed by Prof. R. J. Hicken and then further developed by Dr Mustafa Aziz for comparison with our experimental results.

6.1 Introduction

$Ge_2Sb_2Te_5$ can be reversibly switched between the two phases on a short time scale by applying optical or electrical pulses. Despite of lot of research to establish the optimum

parameters for phase switching between two states [99-104], discrepancies still remain in the literature, such as disagreement about the minimum pulse duration and optimum pump fluence required to induce the phase transition. Similarly, it is still debatable if crystallization can be induced by the application of a single femtosecond optical pulse.

We study the phase transition in GST sample by multiple fs pulses generated from a regenerative laser amplifier system for a continuous range of pump fluences and pulse numbers.

6.2 Experimental Method

6.2.1 Sample detail

Amorphous GST thin films of 20 nm thickness were deposited at room temperature by sputtering upon Si(001) substrates coated with a ZnS-SiO_2 underlayer of 310 nm thickness. The sample stack is shown in fig 6.1. The ZnS-SiO_2 dielectric layer provides a means of controlling the thermal conductivity to optimize the optically-induced phase transition process. The films were capped with 30 nm of ZnS-SiO_2, which acts as a protective layer against oxidation. It is important to precisely adjust the thickness of the underlayer and capping layer to obtain the maximum reflectivity contrast between the crystalline and amorphous phases [105].

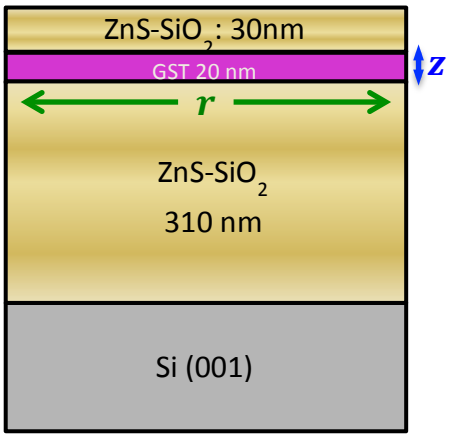

Figure 6.1: **Sample stack**: GST 20 nm sputter deposited on a Si substrate with different thicknesses of ZnS-SiO_2 for the underlayer and capping layer.

6.2.2 Optical pump probe configuration for mark writing

In order to experimentally investigate the phase transition in GST, the measurements were conducted in an optical pump-probe configuration within an optical microscope. The experimental technique is shown in fig 6.2. The 800 nm s-polarised pump pulses of 60 fs duration, energy of up to 8 µJ, and a repetition rate ranging from 300 kHz to single shot were generated from a coherent regenerative amplified Ti-Sapphire laser (RegA). The pulse duration was determined from the intensity autocorrelation width of 85 fs, assuming a Gaussian time profile. A continuous wave He-Ne laser of 633 nm wavelength with s-polarization was used as a probe to record the sample reflectivity during excitation. The pump and probe beams were overlapped and focused onto the sample surface within the focal plane of the optical microscope which was equipped with a 20x objective lens and a 632/25nm bandpass filter so that reflectivity changes measured with the microscope and with the probe beam could be directly compared.

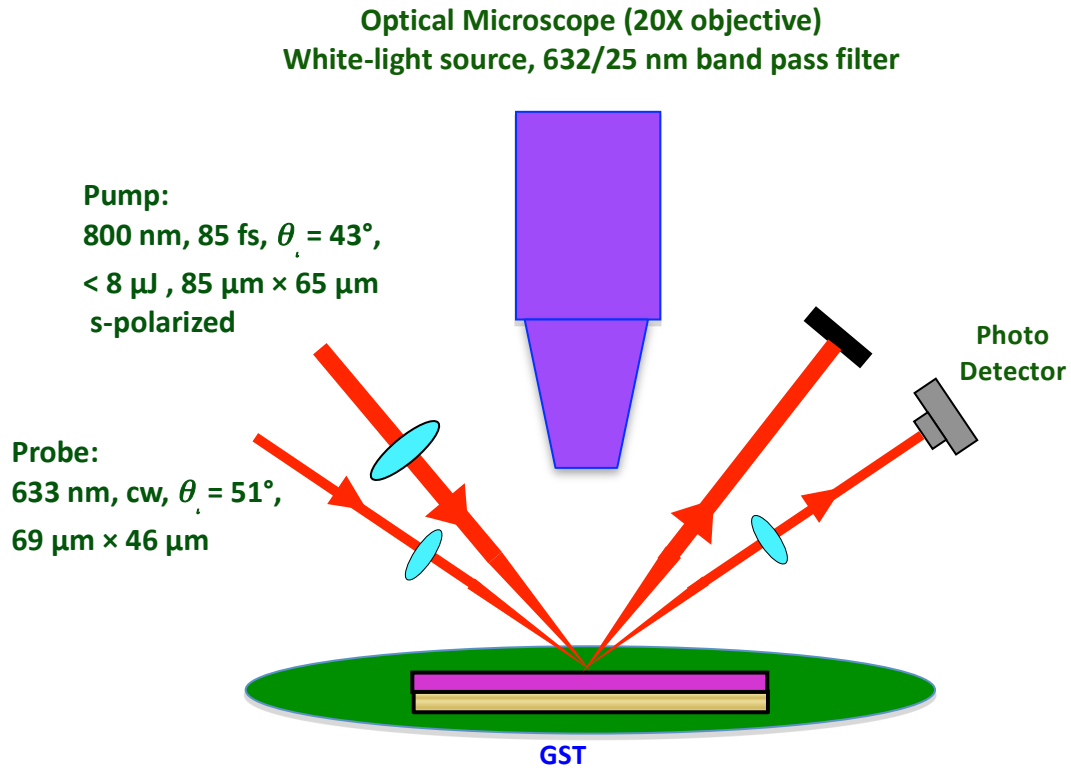

Figure 6.2: **Experimental set up**: the pump-probe configuration is shown. Pump and probe beams are focused onto the sample in the focal plane of the optical microscope

A DataRay WinCamD-UCD12 beam profiler with 4.65 μm pixel size was first inserted in place of the sample to obtain optimum maximum overlap of the pump and probe spots. The intensity profiles of the spots along their principal axes were Gaussian. The s-polarized pump beam was incident at an angle of 43° with a 85 μm × 65 μm elliptical spot size, while the s-polarized probe beam had an angle of incidence of 51° and a spot size of 69 μm × 46 μm. The spot size is defined by the distance between the $1/e^2$ points along the principal axes of the spot. The pulse width was varied continuously between 60 fs and 1.4 ps by adjusting the compressor stage of the regenerative amplifier and monitoring the pulse width with an autocorrelator, while the pulse repetition rate was adjusted from 4 to 300 kHz by controlling the rate of injection of seed pulses to the amplifier cavity. A Labview-controlled Keithley 3390 arbitrary waveform generator was used to trigger the regenerative amplifier and hence to generate a series of pump pulses of variable number and repetition rate. Images of the crystallized marks written by the optical pulses on the amorphous $Ge_2Sb_2Te_5$ films were acquired from the optical microscope using an intensity calibrated Leica DFC295 CCD camera. From the images, we obtain contour and line profiles from the marks, which show the relative change of the reflectivity compared to the amorphous background.

6.2.3 Generation of longer pulses

Longer laser pulses were required to induce crystallization in amorphous GST films. The single laser pulses of fs and ps duration were not able to switch the material from the amorphous to the crystalline state. It was difficult to stretch the pulse duration beyond 1 ns using our existing pulsed laser system. Therefore to obtain ns pulses, we used an electro-optic modulator along with two polarizers. The modulator used in our experiment needs two input signals: a DC bias voltage to compensate the intrinsic birefringence of the crystal and an AC signal to control the phase retardation to modulate the polarization states of the beam. Fig 6.3 shows the experimental setup used to generate the longer pulses. The pump beam had 532 nm wavelength. A polarizer was placed in the middle to align the incident pump beam along one of the optical axes of the crystal. A digitized arbitrary waveform containing a single pulse or a series of pulses was generated by a signal generator, which were then sent to the amplifier driving the modulator. A modulated pulse of 200 ns minimum duration was achieved using this set up.

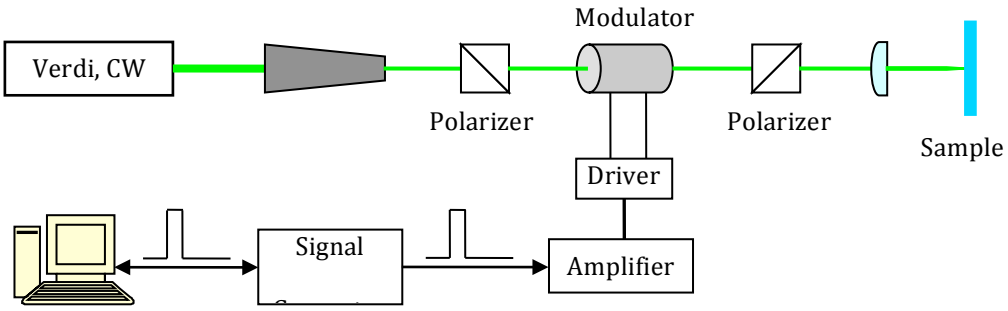

Figure 6.3: Set up using an electro-optic modulator to generate ns pulses

6.3 Results and Discussion

6.3.1 Experimental Results

First, a single pulse of duration 60 fs was used to write micron sized marks on the GST thin film. Microscopic images of the laser-induced marks with increasing pump fluence are shown in figure 6.4.

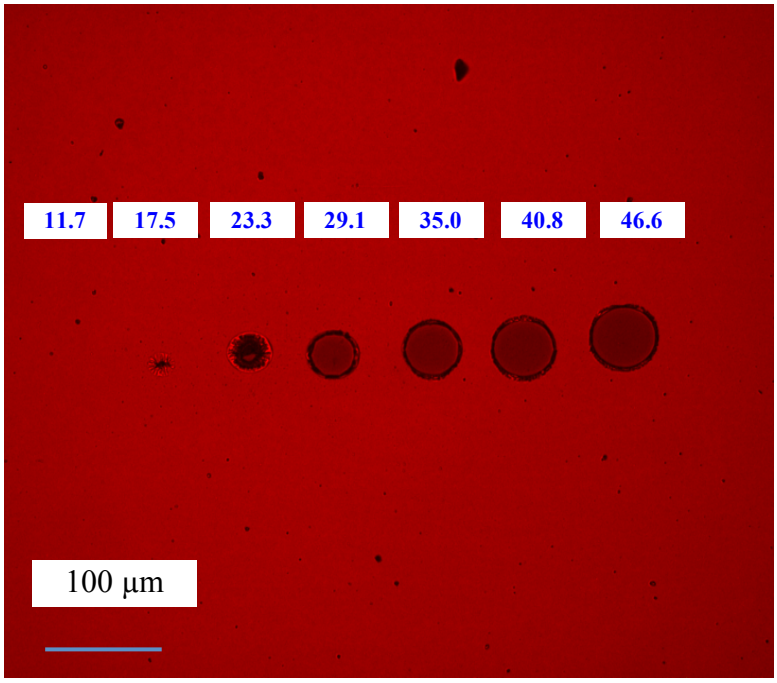

Figure 6.4: **Single pulse excitation:** Microscopic images obtained after excitation by a 60 fs pulse for different pump fluences. The value of the average fluence (mJ/cm^2) is shown for each mark.

It is clear that a single femtosecond pulse cannot crystallize the film. Instead permanent damage occurs if the average pump fluence (F_{avg}) is greater than or equal to 17.5 mJ/cm^2, with the damaged area increasing with F_{avg}. The average fluence F_{avg} (mJ/cm^2) is calculated as the applied pulse energy divided by the 1/e^2 area of the spot. Our results significantly differ from Huang's work [104], where they reported that a single

femtosecond pulse could induce crystallization of amorphous $Ge_1Sb_2Te_4$ films grown on polycarbonate substrates. However, in the present work, it was observed that crystallization could be achieved by a single pulse with duration of larger than 200 ns (not shown).

Although a single femtosecond pulse with small fluence did not produce any visible effects it may well influence the size distribution of nanometer-scale crystalline nuclei that can grow and then coalesce during the crystallization process [106]. To further address this issue, we conducted a comprehensive investigation of crystallization using multiple optical pulses of different fluence.

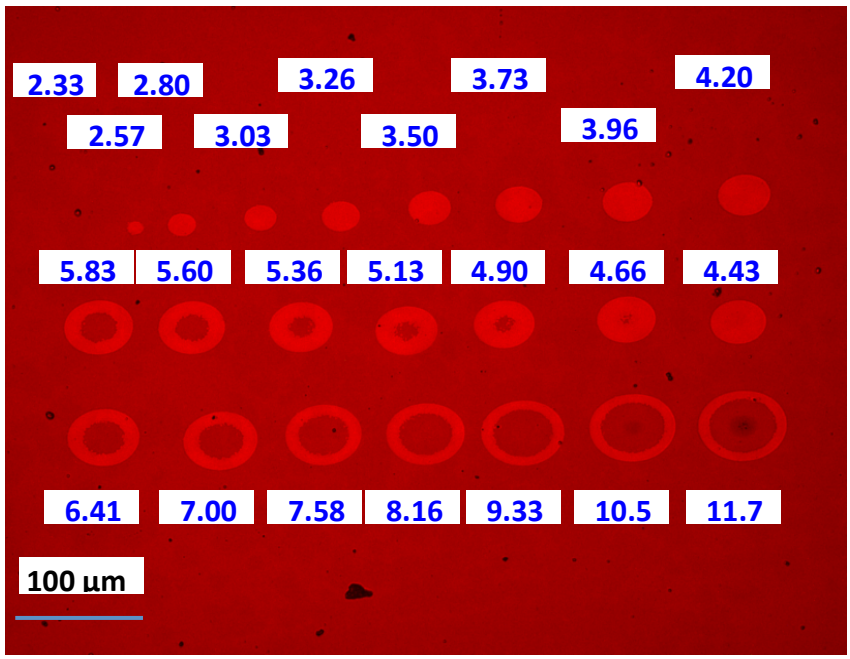

Figure 6.5: **2000 pulse excitation:** Microscopic images obtained after excitation by 2000 pulses of 60 fs duration. The value of the average fluence (mJ/cm^2) is shown in each case.

Fig. 6.5 shows the microscope image of the crystallized marks generated by using 2000 pulses of 60 fs duration of variable fluence, and reveals a clear dependence of crystallization upon the pulse fluence. There are clearly four different regions: (i) for F_{avg} less than 2.57 mJ/cm^2, no change in the reflectivity is observed, which implies that even

2000 pulses of 60 fs duration with a fluence of 2.57 mJ/cm^2 were unable to crystallize the film; (ii) for F_{avg} between 2.57 and 4.43 mJ/cm^2, homogeneous elliptical marks with a reflectivity higher than the amorphous film were obtained; (iii) for F_{avg} between 4.66 and 9.33 mJ/cm^2, annular marks were obtained where the reflectivity within the annulus is higher than that of the surrounding amorphous region. However, the reflectivity in the central enclosed region is observed to be the same as for the amorphous background; (iv) for F_{avg} greater than 10.5 mJ/cm^2, annular nuclei were obtained, but with the reflectivity of the enclosed region being smaller than that of the amorphous background, which indicates that the central region has suffered permanent damage.

Fig. 6.6 shows how the 2000 pulses of variable fluence affect the formation of the crystallized marks. The line profiles through the crystallized marks from region (ii), F_{avg} = 3.50 mJ/cm^2, and region (iii), F_{avg} = 5.83 mJ/cm^2, are shown in Figs. 6.6(a) and 6.6(b), respectively. The reflectivity shows a sharp change at the boundary between the crystalline and amorphous regions. In fig 6.6(a), there is one such boundary and the reflectivity at the center of the mark is slightly lower than the rest of the crystalline area. In fig 6.6(b), the line scan reflectivity profile reveals a clear ring structure with two sharp boundaries. The reflectivity of the inner (or central) region has the same value as the amorphous background, which implies that the local fluence at the center of the mark is sufficiently large that the GST melts before being rapidly quenched back to the amorphous state. Figure 6.6(c) shows that the area of the crystalline region increases linearly with F_{avg} until F_{avg} = 4.43 mJ/cm^2, after which it saturates at a value of 1200 (μm^2). In other words, the area of the high reflectivity region increases until the formation of the ring structure. With further increase of fluence, the width of the annular region decreases as its outer perimeter increases so as to leave its area constant.

The reflectivity values of the crystallized and amorphous regions were determined by (1) taking line scans along the major axes of the crystalline marks obtained from the optical microscope, and (2) recording the reflectivity response with the probe beam. The respective scans are plotted in fig 6.6(d) for comparison.

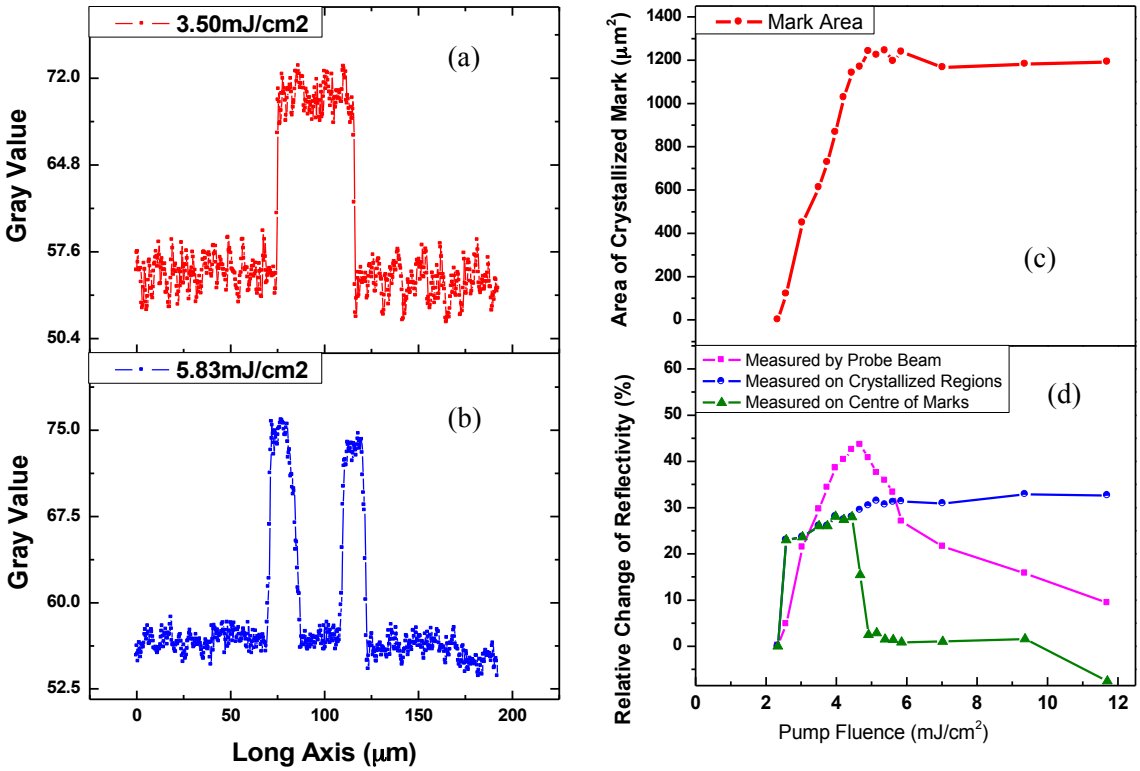

Figure 6.6: **Reflectivity and area of crystalline mark:** (a) and (b) show line scans from a microscopic image of a high reflectivity region obtained by exposure of 2000 pulses of fluence 3.83 mJ/cm^2 and 5.83 mJ/cm^2 respectively. The effect of pump fluence on the area of the crystalline mark is plotted in (c). (d) shows the measured variation of reflectance extracted from line scans at the center of the mark (green triangle) and within the annuli (blue circle), and measured by the probe beam (magenta square). The change in reflectance is defined as $(R - R_{am})/R_{am}$, where R is the measured reflectance and R_{am} is the reflectance of the amorphous background.

The green line represents the reflectivity value at the center of the crystallized mark while the blue line shows the reflectivity at the center of the annular region, obtained by line scans of microscopic images. A large change of almost 23% in the reflectivity was observed when the film crystallizes for the first time. The reflectivity is increased to 28% with increasing fluence. When F_{avg} reaches a value of 4.66 mJ/cm^2, the reflectivity at the center of the mark falls to that of the amorphous material. At this fluence, the annulus is first observed. The reflectivity at the center of the annular region increases with fluence

and finally saturates at a value of 32 % when F_{avg} exceeds 5.13 mJ/cm^2. This increased reflectance at the outer perimeter of the crystalline marks may indicate the formation of the hexagonal crystalline phase in this region, as will be discussed later. The magenta line represents the reflectivity measured by the probe beam. It is observed that the reflectivity starts to increase when the sample first crystallizes as seen in the microscope image line scans, but the relative change of reflectivity is not the same in the two measurements. This can be understood because the spot size of the probe beam (69 μm × 46 μm) is significantly larger than the size of the crystallized marks, and because of the different angles of incidence for the probe beam and microscope illumination. Therefore, the reflectivity signal contains contributions from both the crystalline and amorphous regions. The change in the reflectivity increases until the annulus is formed and then it decreases as the region of high reflectance within the annulus moves outwards from the region of maximum probe beam intensity. The maximum value of the relative change of reflectivity obtained with the probe beam is larger than the value obtained using the optical microscope, due to the different angles of incidence for the probe beam (51^0) and microscope illumination (90^0).

Clearly the total fluence delivered to the film may be controlled via either the fluence of an individual pulse or the number of pulses used. Fig. 6.7 shows the effect of using different numbers of pulses of variable pump fluence upon the crystallization of the $Ge_2Sb_2Te_5$ film. The average pump fluence was kept constant in each row and the number of pulses was increased by 50 for each successive mark, starting from 200 (far left) until 600 (far right).

For the region of fluence 3.26 – 4.43 mJ/cm^2 shown in Fig. 6.7, the minimum number of optical pulses required for the appearance of crystallization is nearly the same, between 200 and 250. For small F_{avg}, the crystallization is first observed at the center of the spot, but as F_{avg} is increased, the temperature at the center exceeds the melting temperature and therefore, crystallization first begins at a finite distance from the center spot, where the temperature is less than the melting temperature. At the center, a low reflectivity occurs because the GST melts and is rapidly quenched to the amorphous state. Once the annulus has formed, further increase of the fluence results in an increase of the outer perimeter and a decrease of the inner perimeter. The closure of the rings with increasing pulses is explained in the discussion section by applying a theoretical model that considers the heat flow and crystallization kinetics.

Compared to the crystallized marks obtained using 2000 pulses shown in Fig. 6.5, the marks in Fig 6.7 can be used to define more precisely the critical value of the pump fluence above which the temperature at the center of mark is higher than the melting temperature. This critical fluence of 3.73 mJ/cm^2 is the value at which the inner perimeter first appears for 250 pulses. Figs. 6.8(a) and (b) show respectively the dependence of the area of the crystallized marks and the relative change of reflectivity upon the number of pulses when the fluence is less than the value required for melting. As observed in fig 6.8(a), for a given number of pulses, the area of the crystallized mark is strongly dependent on the pulse fluence when F_{avg} is small. For larger F_{avg} values, the area of the crystalline mark saturates.

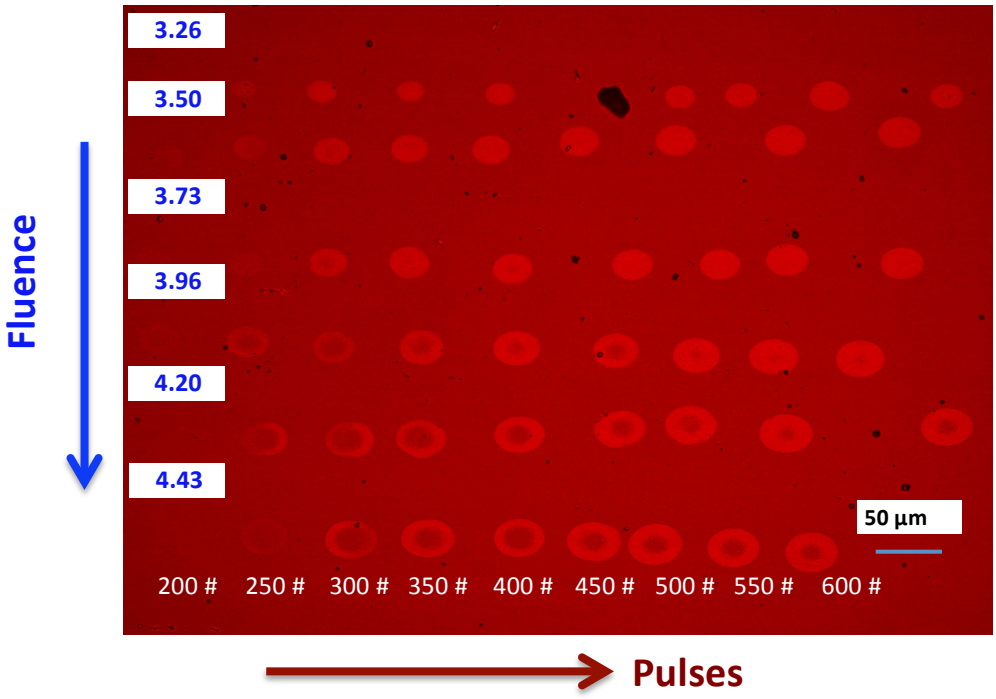

Figure 6.7: **Microscope images for variable number of pulses and** F_{avg} obtained after excitation by 200 pulses (far left) of 60 fs duration with an increment of 50 pulses for each successive mark until 600 pulses (far right). F_{avg} is fixed in each row (as labeled).

The change of reflectivity is relatively insensitive to the application of further pulses once the crystalline state is formed, as seen in fig 6.8(b). However, the minimum number of pulses required for the transition to high reflectivity decreases with increasing fluence. This

is due to the increased temperature in the GST at higher fluence, which increases the nucleation rate and reduces the incubation time. When the fluence was further reduced below 3.26 mJ/cm^2 (not shown here), the number of pulses required to induce crystallization increased significantly. About 1000 pulses were required to crystallize the film for F_{avg} = 2.57 mJ/cm^2, whereas 2000 pulses were insufficient to increase the reflectivity when F_{avg} = 2.33 mJ/cm^2.

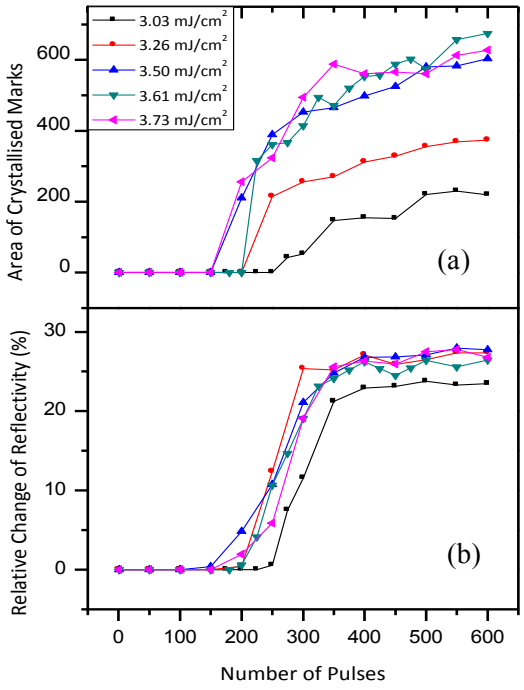

Figure 6.8: **Reflectivity and area of crystalline mark:** (a) and (b) represent the dependence of the area of the crystallized mark and reflectivity respectively upon the number of pulses.

Further investigations of the crystallization process using different pulse durations and repetition rates were also carried out. The pulse width was varied between 60 fs and 1.4 ps by adjusting the compressor stage and monitoring the pulse duration with an autocorrelator. The pulse repetition rate was adjusted from 4 to 300 kHz by controlling the rate of injection of the seed pulses into the amplifier cavity. There was no noticeable dependence of the mark profile upon the pulse duration and repetition rate. This is expected since lateral heat diffusion is limited at these non-equilibrium short time scales (< 5 ps for

$Ge_2Sb_2T_5$) [107] and the slow repetition rates ensure negligible heat storage (compared to the nanosecond relaxation time of the temperature after the application of a laser pulse).

The results above have clearly demonstrated that the crystallization of amorphous $Ge_2Sb_2Te_5$ films can be induced using multiple ultrafast optical pulses. However, in order to make the sub-picosecond laser pulses applicable to erasable optical storage applications, the possibility of a reversible phase transition between amorphous and crystalline states has to be investigated. We therefore made further measurements to explore the conditions for amorphization by femtosecond laser pulses. Fig. 6.9(a) shows a crystallized mark made by using 2000 pulses of 60 fs duration with an average fluence of 3.50 mJ/cm^2. Fig. 6.9(b) shows that the mark was completely reamorphized by a single pulse with F_{avg} = 9.33 mJ/cm^2. In fact, single pulse amorphization could be achieved using fluences from 7.6 to 11.7 mJ/cm^2. Damage occurred for fluences greater than 11.7 mJ/cm^2. Five cycles of crystallization and reamorphization were successively achieved for the mark in Fig. 6.9 and we expect that many thousands of cycles are possible before material suffers permanent damage.

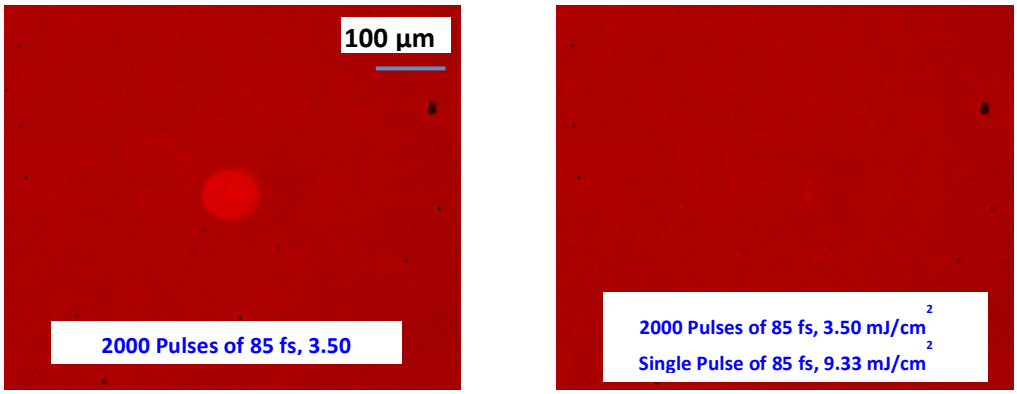

Figure 6.9: **Reversible transition:** (a) Microscope image of a crystallised mark obtained using 2000 pulses of 60 fs duration with F_{avg} = 3.50 mJ/cm^2. (b) Microscope image after re-amorphization using a single 60 fs pulse with F_{avg} = 9.33 mJ/cm^2.

Discussion

6.3.2 Mark area and laser-fluence relation

We have observed that applying multiple pulses results in a crystalline mark, which is characterised by an increased reflectivity. These marks have features which depend on the fluence and number of applied pulses. For now, we keep the number of pulses constant and derive a relation between the area of the crystalline mark and the average fluence applied. As observed in fig 6.6(c), for a fixed number (2000) of pulses, the area of the crystallized region initially increases with fluence until it becomes saturated at a value close to 1200 μm^2 with the formation of the annular region. The area of the annulus remains constant with increasing fluence.

Let the position dependent fluence within the focused pump spot have the form

$$I(x,y) = I_0 \exp\left\{-\left[\left(\frac{x}{a}\right)^2 + \left(\frac{y}{b}\right)^2\right]\right\}$$

----------(6.1)

where I_0 is the maximum pump fluence at the center of the spot, a and b are radii along the x and y-axis of the elliptically shaped shot. The locus of points of equal intensity is defined by a parameter r such that

$$\left(\frac{x}{a}\right)^2 + \left(\frac{y}{b}\right)^2 = r^2$$

----------(6.2)

which corresponds to an ellipse with semi-principal axes of length $\boldsymbol{ra}$ and $\boldsymbol{r}$ with area $A = \pi abr^2$. The average fluence is defined as the pulse energy divided by the spot size. The pulse energy is calculated by integrating equ (6.1) within the *xy* plane. The spot size is measured as $1/e^2$ fullwidth point of Gaussian peak measured by the beam profiler. Therefore,

$$\left(\frac{x}{a}\right)^2 + \left(\frac{y}{b}\right)^2 = 2,$$

$$\left(\frac{x}{a\sqrt{2}}\right)^2+\left(\frac{y}{b\sqrt{2}}\right)^2=1,$$

----------(6.3)

so that $a\sqrt{2}$ and $b\sqrt{2}$ are the lengths of the semi-major axes of the $1/e^2$ elliptical spot with an area equal to $2\pi ab$. Therefore,

$$F_{avg}=\frac{\left(Pulse\,energy\right)}{\left(1/e^2\,area\right)}=\frac{(\pi ab)I_0}{2\pi ab}=\frac{I_0}{2},$$

----------(6.4)

and the peak fluence is $I_0 = 2F_{avg}$.

If transport of heat within the sample is one-dimensional, then each value of r corresponds to a distinct fluence and temperature. Let r_m correspond to I_m at which T_{max} is equal to the melting temperature (T_m), and r_c corresponds to an fluence I_c where T_{max} is just sufficient for crystallization (T_c) for 2000 pulses.

For $I_0 < I_c$, there is no crystallization at any value of r, but for $I_c < I_0 < I_m$ an elliptical mark is obtained with area

$$A=\pi abr_c^2=\pi ab\left[\ln(I_0)-\ln(I_c)\right]=\pi ab\left[\ln(F_{avg})-\ln(I_c/2)\right]$$

----------(6.5)

Fitting this equation to the rising portion of the data yields $\pi ab = 1730\,\mu m^2$ and I_c = 4.77 mJ/cm^2. Using the values of a = 30 μm and b = 23 μm measured with the beam profiler yields an area of πab = 2168 μm^2. This is 20 percent larger than that calculated from the fit to Fig. 6.6(c), but corresponds to only a 10 percent discrepancy in the determination of the linear dimensions of the ellipse.

Once an annular mark has formed, its area A may be written as:

$$A=\pi ab\left[r_c^2-r_m^2\right]=\pi ab\left[\ln(I_0/I_c)-\ln(I_0/I_m)\right]=\pi ab\ln(I_m/I_c)$$

----------(6.6)

which is independent of the pump intensity I_0, or equivalently F_{avg}, in agreement with the saturated part of the experimental curve in Fig. 6.6(c). Taking this area to be equal to A ~ 1200 μm^2 from Fig. 6.6(c) and using I_c = 4.77 mJ/cm^2 from the previous fitting, we calculate from equ (6.6) that the local threshold fluence required for melting is I_m = 9.54 mJ/cm^2 (or F_{avg} = 4.77 mJ/cm^2) which is in good agreement with the experimental melt threshold (4.66 mJ/cm^2) and the value predicted by modelling, as will be later shown.

Equations (6.5) and (6.6) provide a very good description of the data within Fig. 6.6(c), supporting the assumption of 1D thermal transport which is expected, given the large aspect ratio of the optically pumped region of the GST film.

6.3.3 Dependence of reflectance upon the fluence and number of pulses: Theoretical Model

The following models were employed to explain the experimental results.

(1) A simple model

(2) Heat flow and crystallization model (Analytical model)

The first model assumes that the onset of crystallization is sufficiently rapid that the area occupied by partially crystallized material is negligible. But there is a range of pump fluence and number of pulses where the reflectivity varies continuously between the amorphous and fully crystallized values. To reproduce these variations, a more complicated model is needed.

(3) Finite-element (Comsol Multiphysics calculations)

Further calculations by a finite-element method support the validity of the analytical model.

In this chapter, only the first model is presented in detail. Dr Mustafa Aziz developed the other two models, which solve the heat diffusion equation. These latter models will be briefly introduced and then used to explain the experimental results. Further details may be found in reference [91].

(1) A simple model

Let us begin by considering the simplest possible extension of the model used to explain the dependence of the mark area upon fluence. It will be assumed that crystallization occurs when the accumulated local fluence $J = NI(r)$ reaches a threshold value of J_x. If $I_0 < I_m$ then the area of the written mark may be written as

$$A = \pi abr^2 = \pi ab\left[\ln(N) + \ln(I_0) - \ln(J_x)\right]$$

----------(6.7)

Equation (6.7) has been used to generate the family of curves in Figure 6.10 that correspond to the fluences used in the experiments. The curves assume the value of

$\pi ab = 1730\,\mu m^2$ deduced previously, while the value J_x = 1330 mJ/cm^2 was chosen so as to approximately reproduce the number of pulses at which crystallization first occurs (between 170 and 250, depending upon the fluence). The curves greatly overestimate the areas of the written marks and fail to reproduce the strong variation of area with fluence above the threshold value. This is unsurprising since crystallization is known to be thermally activated, so that for a given accumulated fluence one would expect a smaller number of pulses of larger fluence to be more effective in inducing crystallization.

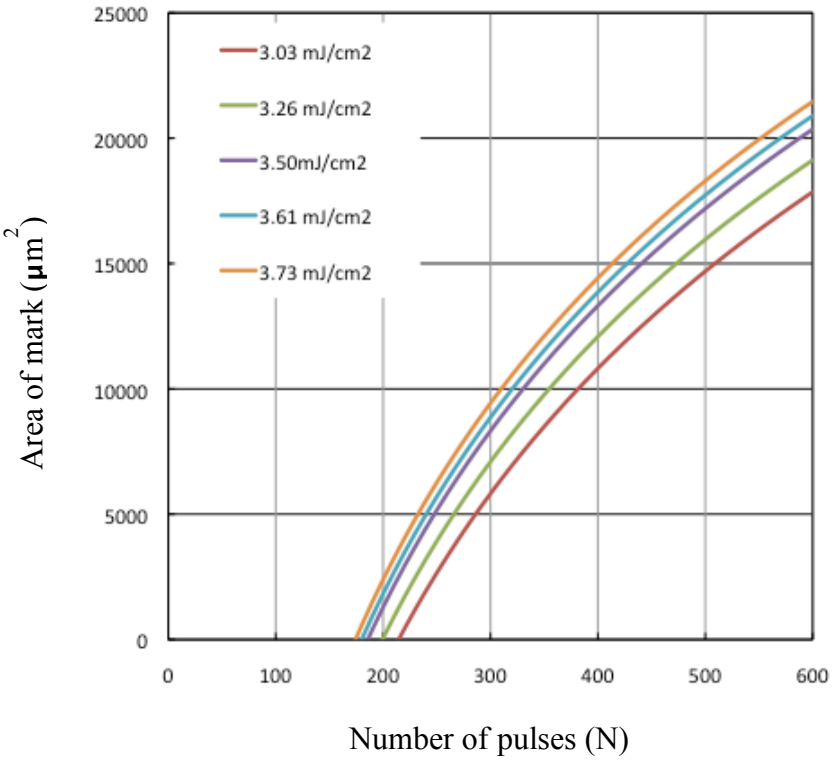

Figure 6.10: Equation (6.7) has been used to calculate the dependence of the mark area upon the number of pulses for different fluences used within the experiments.

Let us assume instead that the rate of fractional crystallization R is described by a relation of the form

$$R = R_0 \exp\left(-E_b / k_B T\right)$$

----------(6.8)

where R_0 is an attempt rate and E_b is an energy barrier. If each pulse raises the temperature of the film from the ambient value T_0 to $T = T_0 + cI$ for time Δt then crystallization is achieved when

$$R(T)N\Delta t = R_0 \exp\left(-\frac{E_b}{k_B(T_0 + cI)}\right)N\Delta t = 1$$

----------(6.9)

Again the local intensity I has a unique correspondence with an ellipse represented by the value of r. Assuming that $I_0 < I_m$, so that there is no melting at the centre of the mark, then its area is given by

$$A = \pi abr_x^2 = \pi ab\ln(I_0/I) = -\pi ab\ln\left\{\frac{1}{cI_0}\left[\frac{E_b}{k_B\ln(R_0N\Delta t)} - T_0\right]\right\}$$

----------(6.10)

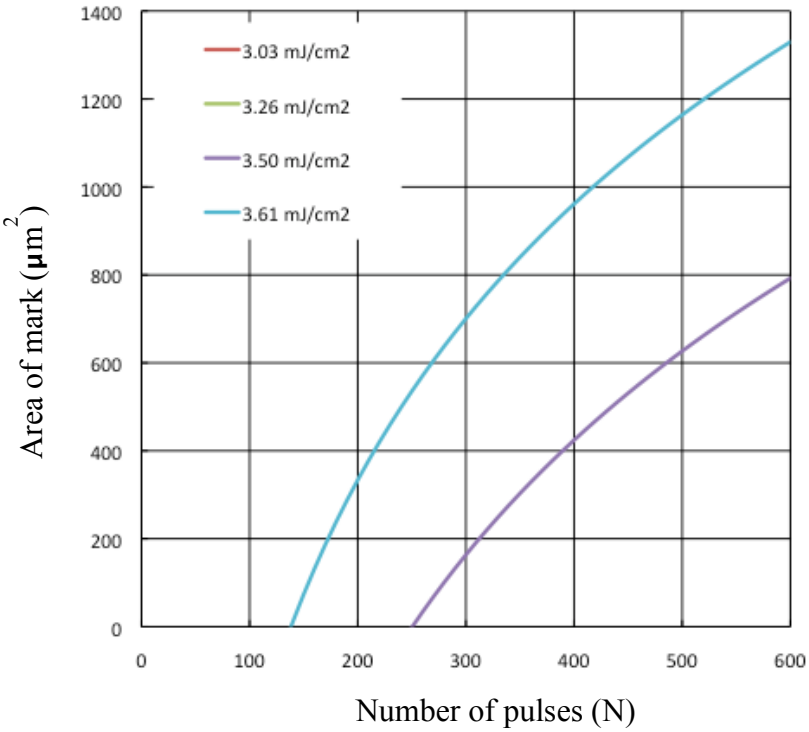

Figure 6.11: The dependence of mark area upon number of pulses has been calculated from equation (6.10) for different fluences used within the experiments. Crystallization is not achieved for the two smaller values of the fluence, i.e. the calculated area is always negative.

Since we found that $I = I_m$ = 9.54 mJ/cm^2 was required to reach the melting temperature of 650 K from an ambient temperature T_0 = 300 K, the value of the constant c is estimated to be 36 K cm^2/mJ. We assume the commonly used values of $R_0 = 10^{25}$ THz, E_b = 2 eV and have chosen Δt = 700 ps so that the onset of crystallization again occurs after approximately the correct number of pulses for a fluence of 3.61 mJ/cm^2. The mark area predicted by equation (6.10) has been plotted in Figure 6.11 for different fluences used within the experiments. Compared to Figure 6.10, the calculated area is now much more sensitive to the precise value of the fluence, in fact more so than within the experiments of Figure 6.8(a), and the values of the area are much closer to the experimental values. Clearly the assumption of a constant elevated temperature during the time interval Δt is a poor approximation to the expected exponential relaxation of the temperature but this simple model illustrates how thermal relaxation accentuates the sensitivity to the pulse fluence. A better description requires a more sophisticated rate equation model that takes into account both the nucleation and growth of a size distribution of crystallites [106].

(2) Heat flow and crystallization model

From fig 6.6(d) and 6.8(b) it is clear that there are ranges of values of pump fluence and number of pulses for which the value of the reflectivity lies between that of the crystalline and amorphous states. These variations are reproduced by considering the heat flow equation in the following way:

- ✧ Heat Flow: calculate the temperature profile T(r, z; t) induced within the film by each successive laser pulse by including the spatial and temporal variation of the optical power density within the heat diffusion equation.
- ✧ Crystallization Kinetics: calculate the increase of the crystalline fraction using a first-order rate equation.
- ✧ Effective Medium Theory: Recalculate the optical constants after increasing the crystalline fraction
- ✧ Feed back the new optical parameters to calculate the power absorbed from the next pulse

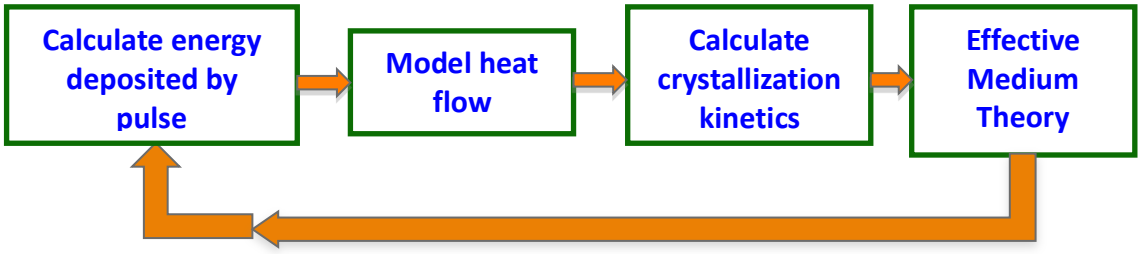

Figure 6.12: **Flow chart for the crystallization model**: representing the process of calculating the optical parameters after every successive laser pulse

The material parameters are assumed to be constant during the arrival of a particular pulse, due to the very small change in crystalline fraction induced by an individual short laser pulse. The simplified analytical models provide a method for quickly calculating the temperature and crystalline volume fraction in the GST layer due to the application of hundreds and thousands of laser pulses.

The transient temperature evolution $T(r,z,t)$ within the GST film due to the application of the pump laser pulse will be described by the one-dimensional heat diffusion equation, ignoring lateral heat diffusion:

$$\frac{1}{D}\frac{\partial T}{\partial t} = \frac{\partial^2 T}{\partial z^2} + \frac{g(r,z,t)}{k} \qquad \text{----------(6.11)}$$

where z is the depth within the film (z=0 refers to the interface between the GST and the capping layer) and r is the radius that define the radial distribution of laser fluence (shown in fig 6.1).

The solution of equation (6.11) is valid only for temperatures less than the melting temperature of 894 K for GST [108], and assumes that the optical and thermal parameters of the GST material do not vary with depth. Figures 6.13(a) and 6.13(b) show the calculated temperature distribution through the fully amorphous and crystalline phase-change layer at different times using F_{avg} = 2.33 mJ/cm^2. It is observed that the temperature is maximum immediately after the optical excitation (within 1 ps) at the upper surface of the GST layer (z = 0 nm), before heat diffuses towards the substrate. Therefore

crystallization is expected to occur first through heterogeneous nucleation at the GST/ZnS:SiO_2 capping interface [109]. The remaining 20 nm of the GST film can then crystallize by growth from the upper surface of the film with increasing laser pulse number. Nucleation and growth deeper within the GST layer is also expected to occur with each subsequent pulse. As time proceeds, the maximum temperature tends to be found more towards the center of the layer.

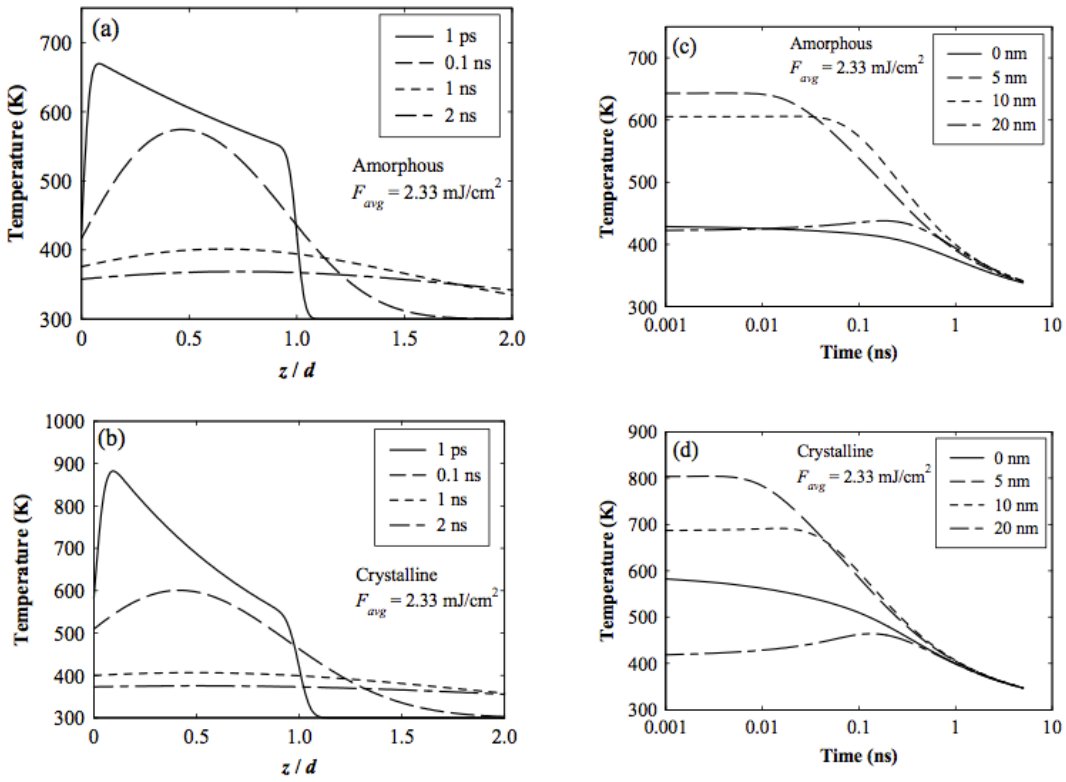

Figure 6.13: **Transient temperature distributions:** calculated using the analytical model for F_{avg} = 2.33 mJ/cm^2 and a pulse duration of 60 fs. (a) and (b) show the temperature distribution at different times when the GST layer is fully amorphous and fully crystalline respectively. (c) and (d) show the transient temperature at different points through the 20 nm fully amorphous and fully crystalline GST layer respectively.

The amorphous region starts to crystallize with each pulse, which leads to an increase in optical absorption and therefore results in a high surface temperature, as illustrated in fig 6.13(b) with a large temperature gradient through the layer thickness.

The transient temperature calculated at different depths for the amorphous and crystalline phases is shown in fig 6.13(c) and 6.13 (d), respectively. The thermal contact between the GST layer and the $ZnS:SiO_2$ capping/underlayer leads to immediate heat extraction and therefore lower temperatures near these interfaces with the maximum temperature occurring in the center of the medium as time progresses.

The temperature in the middle of the phase-change layer (z = 10 nm) is used as an averaged transient temperature through the thickness of the phase-change layer, producing a depth averaged estimate of the crystalline fraction. The medium is initially amorphous at the start of the calculations with a crystalline fraction of zero that updates after every subsequent pulse. Evaluating the crystalline fraction using the calculated average temperature for a single 60 fs laser pulse confirmed that it is not possible to crystallize the heated region with a single fs laser pulse in agreement with experiment. Applying successive fs laser pulses at increasing fluence increases the calculated crystalline fraction and corresponding reflectance.

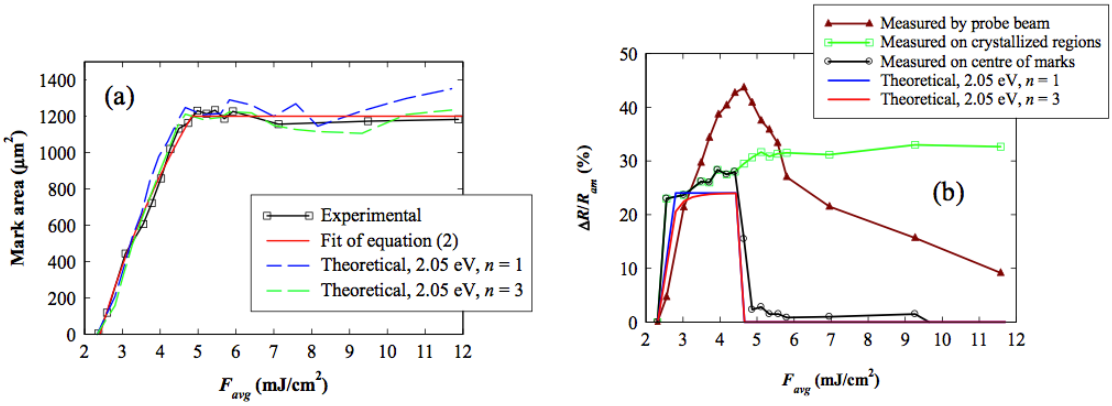

Figure 6.14: Area (a) and reflectivity (b) of crystallize mark calculated using the analytical model for increasing fluence. The simulations agree well with the experimental data of Figure 6.6(c) and 6.6(d).

Fig 6.14(a) represents the reflectivity of the crystallized mark calculated using the theory discussed above. It shows a sudden increase in reflectance reaching a maximum of 24% at

an average fluence of 2.8 mJ/cm^2, in good agreement with the experimental curve measured at the centre of the crystalline mark. When the temperature of the layer at z = 10 nm reaches the melting threshold there is a sudden drop in the calculated change in reflectivity from 24% to 0%. This occurred at 4.66 mJ/cm^2, which is in close agreement with the experimental values. This value also agrees with the value deduced (4.77 mJ/cm^2) from the appearance of the annular spot shape in Fig 6.5. The area calculated by the theoretical model is plotted as a function of increasing average fluence after 2000 pulses in Figure 6.14(b) (dashed lines). The calculated areas are in excellent agreement with the measurements and fitting to the laser beam profile in equ (6.5), predicting accurately the measured melting threshold average fluence of ~ 4.66 mJ/cm^2.

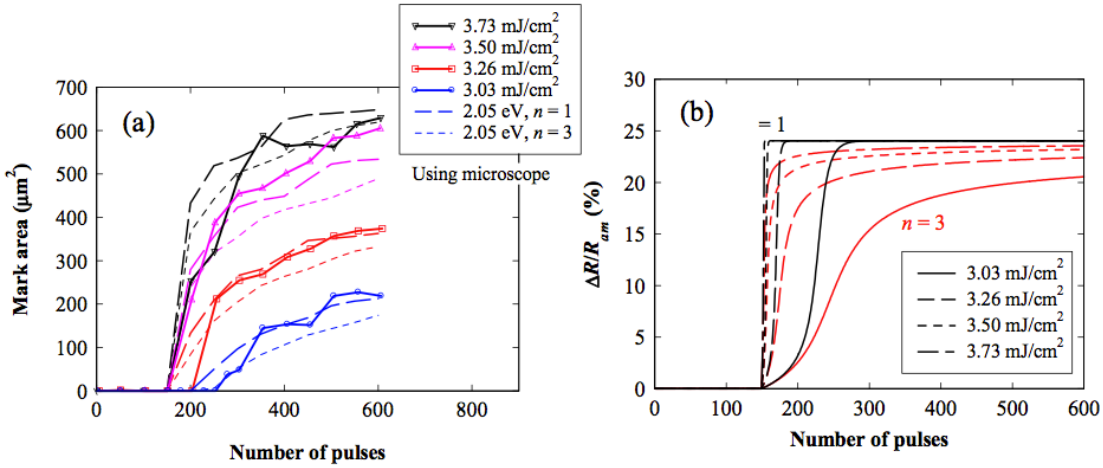

Figure 6.15: Area (a) and reflectivity (b) of the crystallized mark calculated using the analytical model for increasing number of pulses applied. The simulations with reaction order 1 and 3 are seen to reproduce the experimental data of Figure 6.8(a) and 6.8(b).

The calculated area for a fixed fluence (below the melting threshold) as a function of pulse number is shown in Figure 6.15(a), and follows closely the experimental increase in area with increasing pulse number, which further supports the one-dimensional (vertical) heat flow model proposed in this chapter.

Figure 6.8(b) showed that the change in reflectance of the irradiated region as a function of pulse number, and in particular the slope of this curve (and hence the crystallization rate), is less sensitive to the applied fluence. This behaviour was also observed in transient reflectivity measurements of a 200 nm thick GST film irradiated with isolated picosecond laser pulses of increasing fluence [110]. The crystallization rate depends upon the peak temperature in the medium (and hence the peak laser fluence), the cooling rate, the activation energy for crystallization and the crystallization mechanism (which may be described by the reaction order of the system).

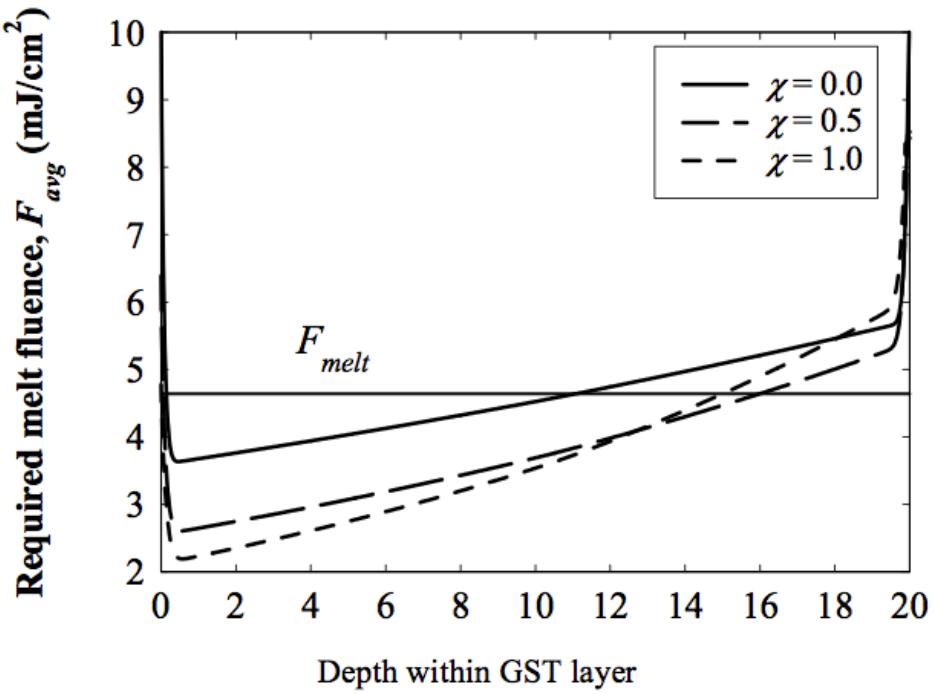

Figure 6.16: Calculated average fluence F_{avg} (for a single laser pulse) required to induce melting at the centre of the irradiated region at increasing depths within the GST layer for different crystalline volume fractions. The dashed line indicates the threshold fluence for melting at F_{avg} = 4.66 mJ/cm^2 observed from measurements and calculations in Figures 6.6 (c) and 6.6(d). z=0 nm corresponds to the upper surface of GST layer.

Fig 6.16 shows the dependence of the fluence required for melting upon the crystalline fraction at different depths within the GST layer. The theoretical model predicts that there is no melting at low fluence in the amorphous starting phase ($\chi = 0$), which confirms the formation of fully crystalline elliptical marks. Further increasing F_{avg} to ~ 3.7 mJ/cm^2

increases the temperature at the surface ($z = 0$) of the GST layer at the center ($r = 0$) of the irradiated region causing melting of the amorphous material ($\chi = 0$), as shown in Figure 6.16. Direct contact of the molten GST with the ZnS-SiO_2 capping layer results in heat extraction and fast quenching to the amorphous state. The annular crystalline rings are clearly observed for fluences ≥ 3.50 mJ/cm^2 in Figure 6.7, which is in close agreement with the value 3.7 mJ/cm^2 predicted by the theoretical model (Figure 6.16) for the beginning of surface melting in amorphous GST. When the fluence is further increased, surface melting takes place with an increasing crystalline fraction ($\chi > 0$) at moderately low fluence due to an increase in optical absorption. However regions at a finite distance from the center experience lower temperatures and hence crystallize forming the annular ring as seen in fig 6.7.

Fig 6.17 shows the reflectance line scans of marks written at fluence 4.2 mJ/cm^2 from fig 6.7. It explains the closure of rings with increasing number of pulses supporting the recrystallization model. When further pulses are applied to the annular area, the crystalline material starts to grow from the inner perimeter and from the surrounding crystalline area within GST layer [111]. This results in the closure of crystalline annular rings, either directly from the melt, or more likely when the material has solidified and the temperature remains above the glass transition temperature. The release of heat of fusion during solidification of the melt at the interface between the GST and the capping layer may also reduce the cooling rate and promote re-crystallization of the melt [112].

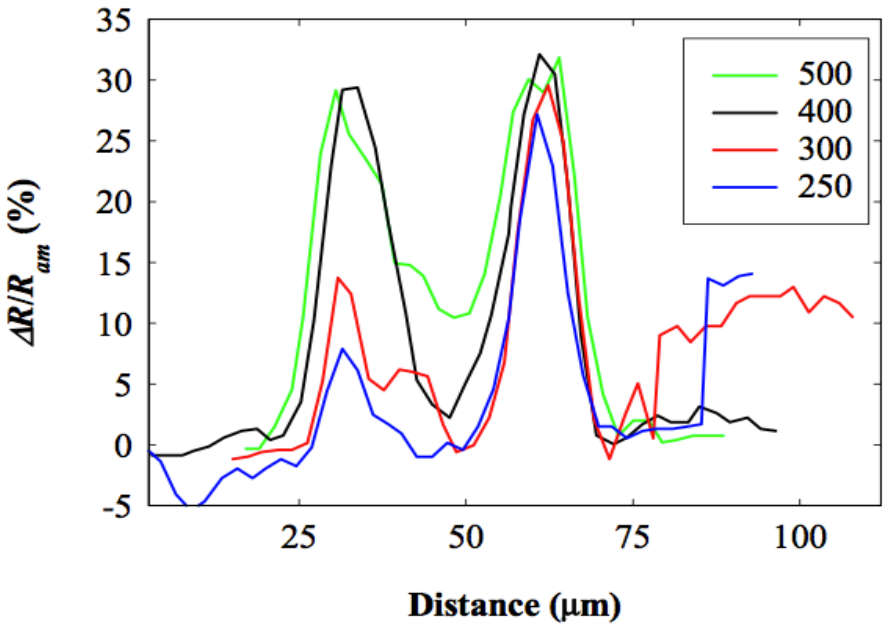

Figure 6.17: Reflectance line scans along the major axis of the marks shown in Figure 6.7 produced using different numbers of 60 fs pulses at F_{avg} = 4.20 mJ/cm^2, showing the growth of the crystalline material from the inner perimeter and central region of the annular rings with increasing pulse number.

As shown in figs 6.6(a) and 6.6(b), the line scans of the microscopic images show a sharp reflectivity contrast between crystalline mark and amorphous background. However, the outer perimeter shows a greater increase in reflectance than the rest of the crystalline area. This indicates the formation of the hexagonal phase starting from the high temperature experienced in the outer region. This is supported by calculations of the reflection coefficient derived from the analytical model (not shown here) yielding changes in reflectance of 24% and 32% for the fcc and hcp crystalline phases, respectively. This is in complete agreement with the microscope reflectivity measurements presented in fig 6.6(d). The existence of the hexagonal phase in the surrounding crystalline area may also increase the recrystallization of the melt-quenched central region, where surface melting occurs, to the fcc crystalline phase [113].

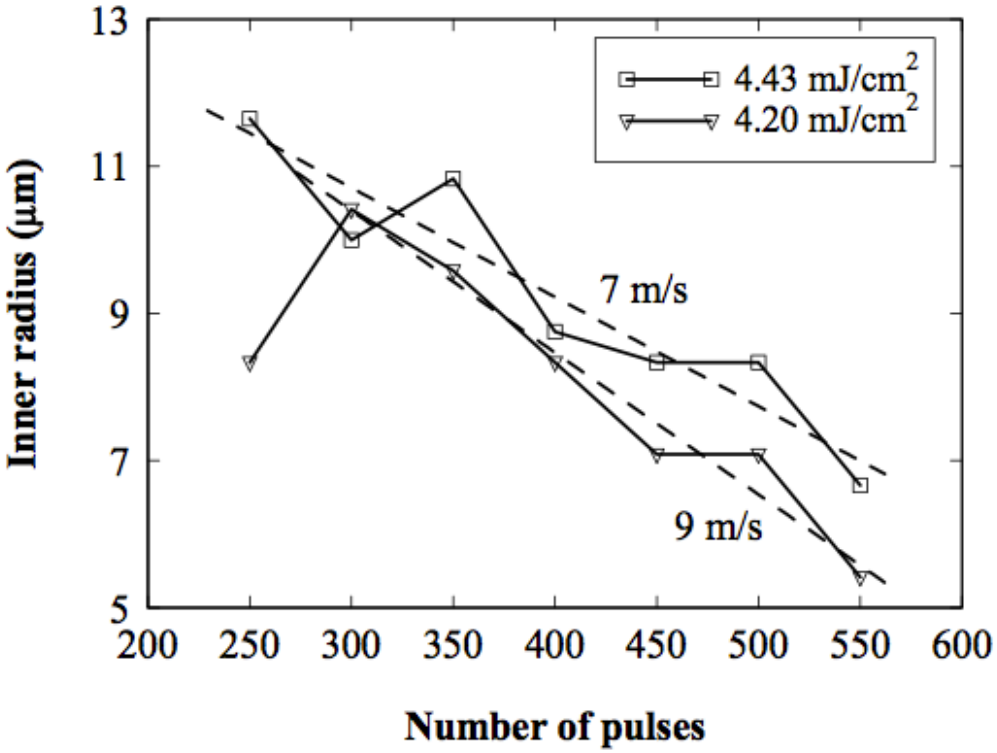

Figure 6.18: Measurements of the inner diameters of the annuli in Figure 6.7 for two fluences as functions of increasing laser pulse number. The straight lines fits yield an estimate of the elevated temperature growth velocity assuming that the growth occurs over a 2 ns period from the application of a laser pulse.

The reduction of the inner perimeter of the marks in Figure 6.7 for fluences 4.20 mJ/cm^2 and 4.43 mJ/cm^2 is plotted in Figure 6.18 against pulse number. The straight-line fits provide estimated growth velocities in the range 7-9 m/s, assuming that crystal growth after each fs pulse occurs within 2 ns, estimated from the time taken for the calculated temperature to decrease from the melting point to the glass transition temperature (assuming that crystal growth follows heat diffusion). There was negligible change in the outer diameters of the marks at these fluences. While there is potential for further refinement of this measurement technique, this estimate is in good agreement with the value of 10 m/s obtained from low temperature measurements of growth rates extrapolated to high temperatures near the melting point [114].

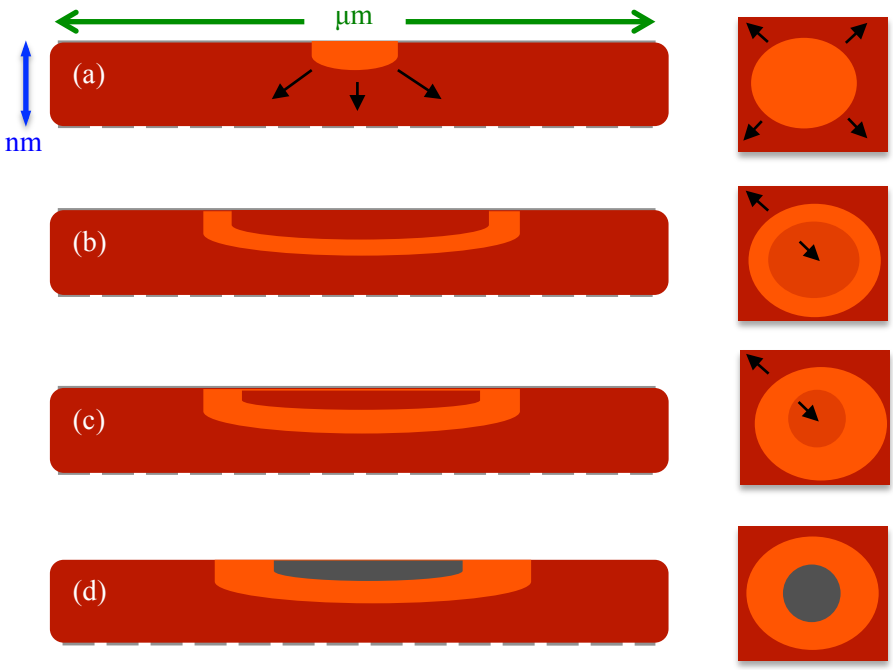

Figure 6.19: **Effect of fluence and number of pulses on crystalline area**: (a) The formation of the high reflectivity region starts from the center for $T > T_x$; (b) The temperature at the center is higher than the melt threshold ($T > T_m$) which causes the central region to go through melting and fast quenching to the amorphous state due to heat extraction by the capping layer; (c) for temperatures greater than the melting threshold ($T > T_m$), further increasing the number of pulses leads to growth of the crystalline fraction from the inner perimeter of the ring, leading to closure of the ring and reproducing the results of fig 6.7; (d) For a fixed number of pulses, increasing fluence results in permanent damage of the central region ($T >> T_m$).

Fig 6.19 explicitly sketches the cross section and top view of the GST layer, demonstrating how increasing fluence and number of pulses controls the formation of the high reflectivity region (by nucleation and growth of the crystalline fraction) at different radial locations and through the thickness of the GST layer.

6.4 Summary

A comprehensive investigation of phase-change switching in GST by the application of amplified pump pulses has been conducted. Crystallization of amorphous marks in GST thin films is achieved by varying the number of pulses and their fluence. It was observed that crystallization could not be achieved using a single pulse. Increasing the fluence of a single pulse led to reamorphization and then permanent damage of the material. A minimum of 200 pulses was required to induce crystallization for fluences less than the damage threshold. The shape of the mark was elliptical for smaller fluences, before changing to an annular ring with increasing fluence as the peak fluence became sufficient to melt the center of the mark region. Using a simple algebraic model, the dependence of the crystalline upon the fluence of a fixed number of pulses has been described, justifying the assumption of one-dimensional heat flow. A detailed theoretical model is also presented in which consideration of thermal transport, optical absorption and crystallization theory leads to simulations that are in good agreement with the experimental results. Finally the growth velocity is estimated to be about 7-9 m/s. The analysis of crystalline marks provides an effective way of understanding the crystallization kinetics of phase change materials.

Chapter 7

Development of an optical set-up using white-light probe

7.1 Introduction: Motivation for a white-light probe

The white-light set-up is an optical pump-probe technique with a white-light probe pulse. The aim of the white-light pump probe set up is to study the time-resolved reflectance spectra of a sample in the visible range (approx 400 – 800 nm). Knowing the wavelength/frequency which shows the largest response for a particular sample, one can set up a pump probe technique to study the sample further at that particular probe wavelength. Time-resolved optical spectra also provide a fingerprint of the physical structure of the material at different time delays.

In this chapter, I explain the process of alignment and testing of pump-probe measurements in which the probe is a white-light pulse. The operation of the measurement system was verified by making measurements on samples with a well-known response. My study confirms that the set up can be used to study phase-change samples in the future.

7.2 Jobin Yvon Spectrometer System

The measurement system is equipped with a fully automated Jobin Yvon iHR320 imaging spectrometer. It is a triple grating spectrometer operating over a wavelength range from 150 nm to 15 μm. The spectrograph is capable of providing better than 0.06 nm wavelength

resolution for a grating with 1200 grooves/mm. It also possesses high accuracy automated slits, a stepper drive to control the grating turret, and a USB interface.

Spectrograph Operation

The iHR320 unit is shown in fig 7.1. It consists of one entrance and two (front and side) exit slits with a CCD detector connected at the front exit. The measurement is based on the diffraction of light by a grating and its spatial dispersion across the exit focal plane. The array detector at the exit captures a snapshot of a range of wavelengths. The data can be presented as an image, or else the pixels in each vertical column are summed to yield a spectrum. The iHR320 allows the user to select the central wavelength that identifies the grating position. The spectrograph can also function as a monochromator to select a single wavelength of light. The output is instead directed to the side exit using a computer-controlled swing mirror. The spectrograph consists of an automatic shutter placed at the front entrance. The grating turret supports the gratings and their rotation during scanning. The grating can be selected via software, with about 30 seconds being required to rotate the turret to a new grating position. The iHR320 has fully automated slits that can be controlled via a LabView program. The slit width controls the throughput and wavelength resolution of the system. The slit width is continuously adjustable from 0 mm to 2 mm.

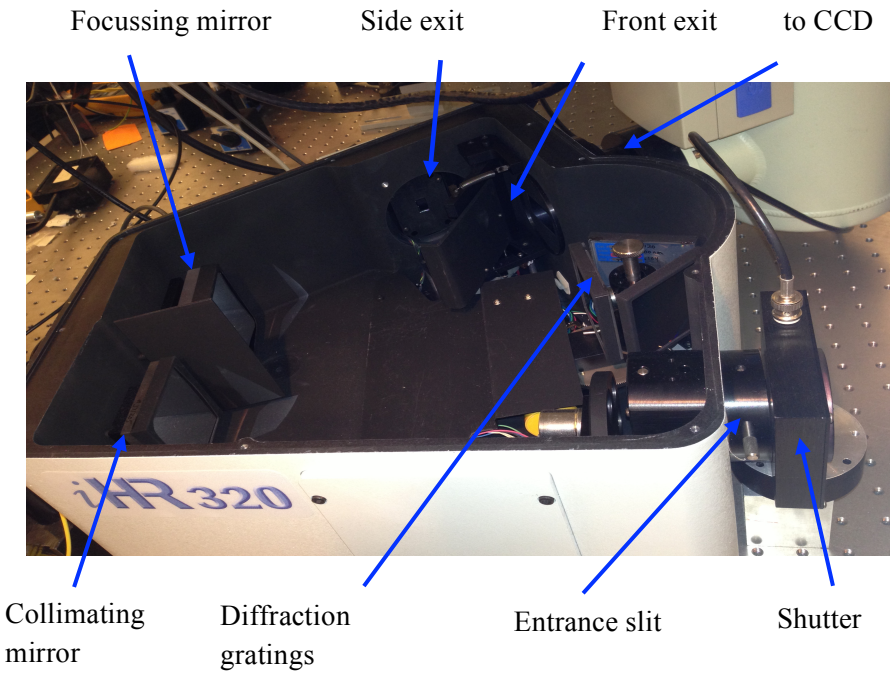

Figure 7.1: Optical design of the iHR 320

There are various data acquisition modes allowed for the Symphony CCD detector. The correct acquisition mode will depend upon the experiment being performed and the format required by the user. Data acquisition modes and experimental parameters are selected by the end-user via the SynerJY software. The data can be recorded in image mode and spectral mode, as discussed in the measurement procedure section.

7.3 Laser System

The Coherent Mira and RegA regenerative amplifier system provides a 800 nm wavelength near-infrared beam with pulse duration as short as 55 fs. The RegA amplifies the nJ femtosecond pulses generated by the Mira seed laser to pulses of micro-Joule energy. In order to obtain a white-light beam, the amplified pulses are focused into a sapphire crystal that is used within the Coherent optical parametric amplifier (OPA). The white-light continuum requires only 25% of the RegA output. The OPA generally provides four outputs: a tunable signal in the visible range from 480 nm to 700 nm known as the signal; another tunable signal in the range of 930 nm to 2300 nm called the idler; a clean, low energy white-light continuum output which serves as the probe beam in the present experiment set up; and the residual second-harmonic generation (SHG) from the pump beam which can serve as the second beam in a two-color time-resolved pump-probe set up. All four outputs are well synchronized in time because they are generated from the same high energy RegA pulses.

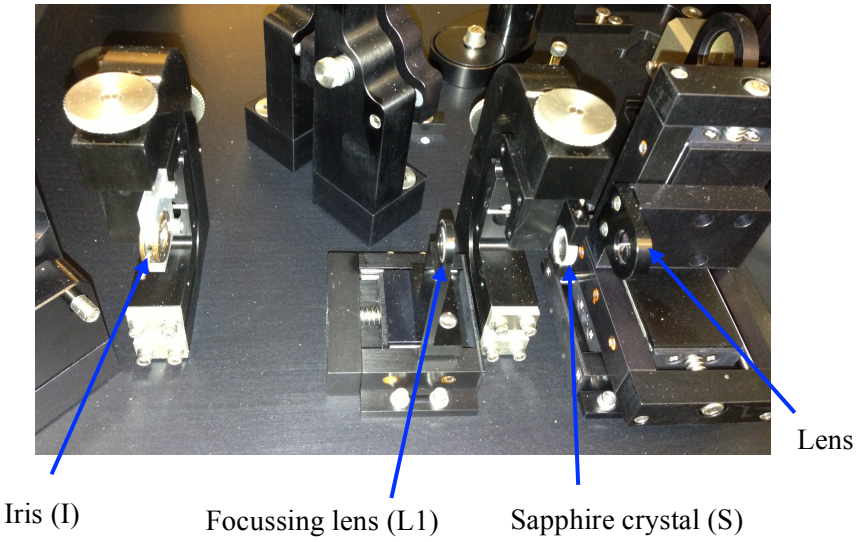

Figure 7.2: White-light generator assembly

The white-light generator assembly consists of an iris (I), focussing lens (L1), sapphire crystal (S), and lens L2, as shown in fig 7.2. L1 focuses the incoming high energy 800 nm pulse onto the sapphire crystal (S) that generates the white-light by self focussing (SF) and self phase modulation (SPM) based on a Kerr non-linearity. L2 then collimates the white-light output [115].

7.4 Measurement Procedure

The measurement procedure requires the following steps:

(i) Monochromator power up/Initialization

The monochromator must first be initialized by using a LabView program called "JY Mono Example.vi" to gear up the grating turret. The LabView panel, as shown in fig 7.3, contains information about the monochromator id, its initialization on the left hand side, and control of the grating and slits on the right hand side. Once the monochromator is initialized, the rest of the LabView panel becomes active, allowing the user to select the central wavelength and the grating. The user can also select the entrance slit width, the front or side exit, and its width using the same panel.

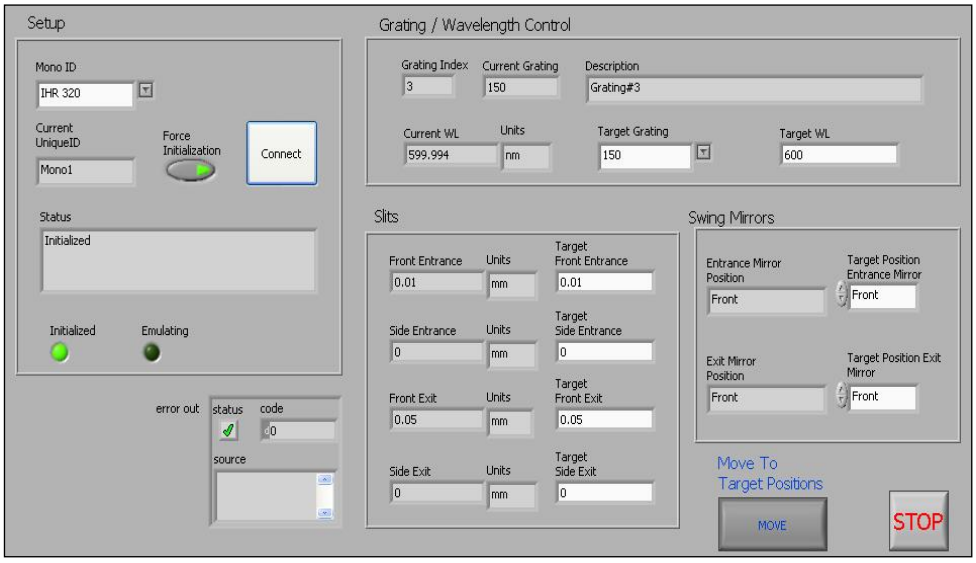

Figure 7.3: LabView panel for the initialization of the monochromator

(ii) Image Acquisition

After the imaging spectrograph is powered up and appropriate settings selected, the user can fine-tune the alignment to obtain a signal. In an imaging experiment, the signal is recorded from every pixel. The output data are therefore a 2-dimensional plot of intensity as a function of pixel position. The horizontal axis can be converted to wavelength or frequency as required. The image acquisition is software controlled. The images, as shown in fig 7.4, are captured using the "Image Acquisition demo.vi" LabView program.

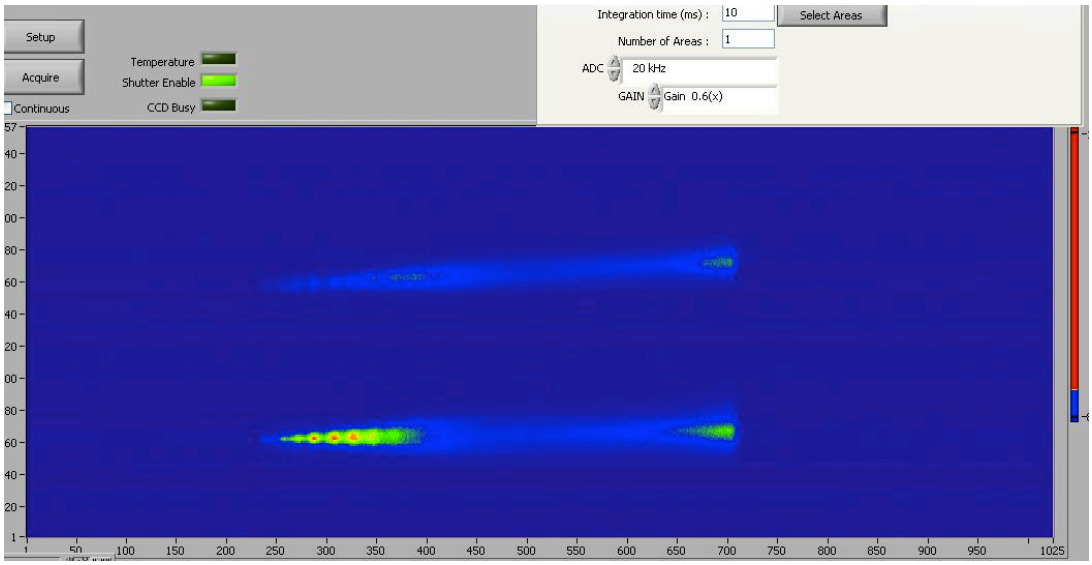

Figure 7.4: Image acquisition of reflected probe beams

(iii) Spectral Acquisition

Another LabView program called "Spectral Acquisition demo.vi" is used to plot the spectral intensity against pixels. As shown in fig 7.5, data are recorded for each individual pixel, and the pixel values in each column are summed to generate a spectrum. The spectrum data can be saved in a .dat file and used for further analysis, such as intensity comparison.

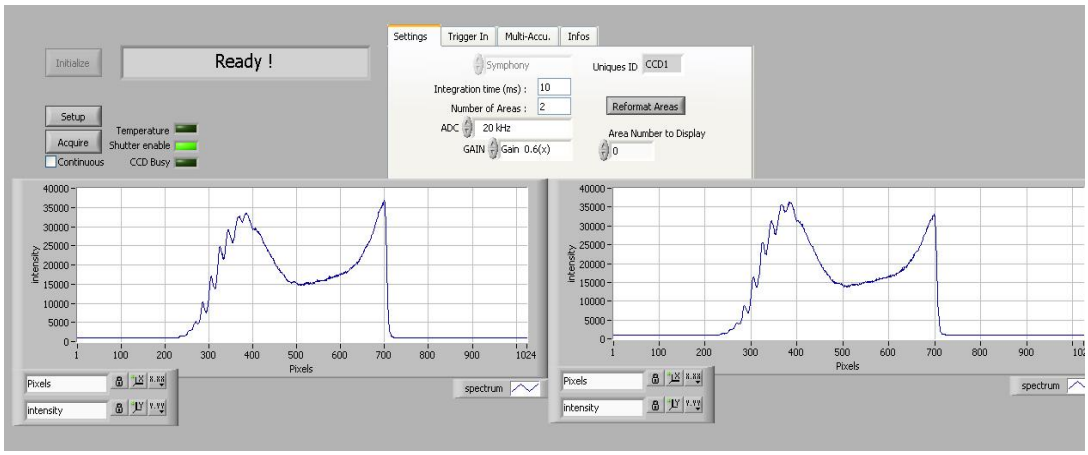

Figure 7.5: Spectral acquisition of reflected probe beams using LabView program

7.5 Alignment

To study the time-resolved reflectance spectrum response of a sample in the visible range on timescales down to 100 fs, a time-resolved optical measurement technique is employed.

In the following section, the alignment of the probe beam is explained. Initial results are also presented that verify the functionality of the system. The set up can be further extended to carry out time-resolved pump probe measurements with an 800 nm pump pulse and a white-light probe pulse.

The experimental set up is shown in fig 7.6. The white-light probe pulse from the OPA is directed to the sample by two silver mirrors M1 and M2. The reflected beam from M2 is equally divided into two orthogonal beams by a 50:50 beam splitter (BS1). The first beam is incident on the sample to probe its state after pump pulse excitation. The second beam in the orthogonal arm probes the state of a reference (silver) mirror. Both reflected probe beams are collected by another 50:50 beam splitter (BS2) and focussed onto the entrance slit of the imaging spectrograph using a focussing lens L1. The probe beams should be aligned in such a way that they completely pass through the entrance slit and image the

spectra from the sample/reference at the center of the lower/upper half of the CCD detector chip. Since the entrance slit width is kept very small (0.01 mm) and there are a number of optics inside the spectrograph (fig 7.1), it becomes difficult to separate precisely the beams at the detector chip. This can be achieved by passing the beams through the entrance slit and simultaneously aligning them inside the spectrograph with the help of collimating mirrors (shown in fig 7.1). Care should be taken so that the beams do not merge or diverge away from the detector chip. A filter with a cut-off wavelength of 700 nm is also introduced into the probe beams path to observe the sample response for wavelengths smaller than 700nm.

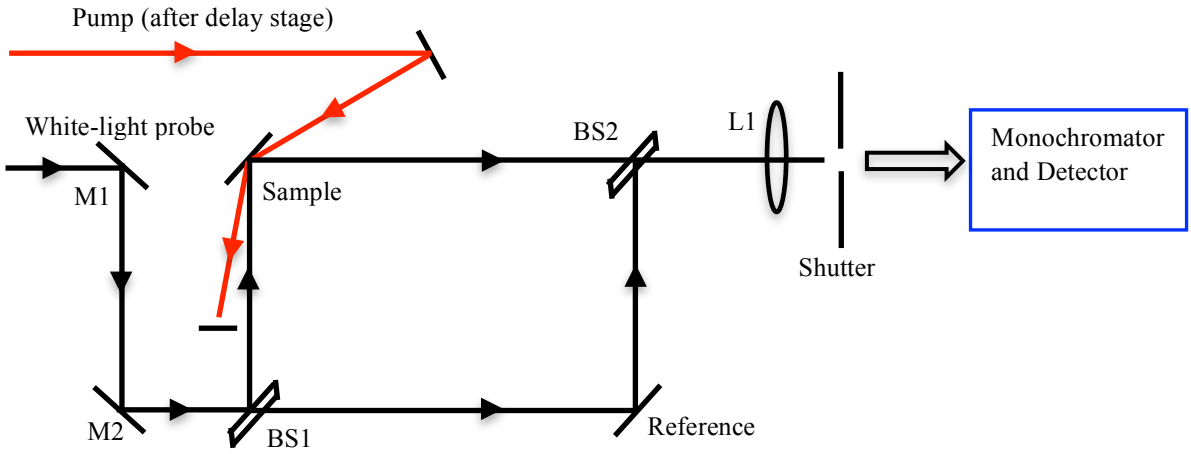

Figure 7. 6: Alignment of white-light probe beam to measure the reflectance spectra of the sample

To test the set up, it is essential to measure well-studied materials first. Therefore, the spectral response of gold and silver mirrors purchased from Thorlab company were obtained with the experimental set up. The reflected intensities were compared with the manufacturer's data sheets and calculated reflectance spectra. The calculations were performed in an Excel spreadsheet using the optical constants of gold and silver obtained from a handbook [116].

The signal and reference spectra were collected and compared at different times. It was observed that any drift in the incident white-light spectrum affects both spectra in a similar manner.

7.6 Results

7.6.1 System Calibration

This system had not been used previously for the simultaneous measurement of two reflected beams. Therefore, it was essential to calibrate the system before beginning measurements.

The detector chip is a 2D array with 1024×256 pixels, which collects the reflected beam and integrates the intensity incident upon each column of pixels to generate a signal spectrum. A mercury lamp was used to calibrate the system by converting the pixel position into an incident laser wavelength. The spectrum of the mercury lamp is well known and contains five major lines in the visible range. These lines are located at 365 nm, 404.6 nm, 435.8 nm, 546.1 nm and 578 nm, as shown in fig 7.7. The monochromator was set to select a grating with 150 gr/mm. The user can select any centre wavelength. The grating is rotated to centre the given special feature on the chip i.e to locate the given centre wavelength half way along the horizontal axis of the CCD chip (at pixel number 512). To calibrate the pixel positions, one of the mercury spectral lines at 435.8 nm was selected as the centre wavelength of the monochromator. The spectrum was collected and the position of each spectral line was identified in terms of the pixel position. It was observed that all five mercury lines fall on a straight line.

Let us consider the grating equation [117],

$$a\,[\sin\theta_i + \sin\theta_m] = m\lambda\,, \qquad \text{----------(7.1)}$$

where θ_i is the angle of incidence, θ_m is the angle of the m^{th} diffracted order from the grating and λ is the wavelength of the incident beam. Since the detector chip is at a large

distance from the grating to its lateral size, the range of diffracted angles incident upon the chip is small.

Let us consider that the angle of diffraction changes by $\Delta\theta_m$ for a change in wavelength ($\Delta\lambda$), then

$$a\,[\sin\theta_i + \sin(\theta_m + \Delta\theta_m)] = m(\lambda + \Delta\lambda).$$

----------(7.2)

If we expand and solve equation (7.2), it can be shown that,

$$\Delta\theta_m \propto \Delta\lambda\,,$$

which indicates that the pixel position on the detector chip is linearly proportional to the change in the wavelength.

Fitting a straight line provides a relation between p and λ.

$$\lambda = 0.53 * p + 160.57\,.$$

----------(7.3)

where p is the number of pixels.

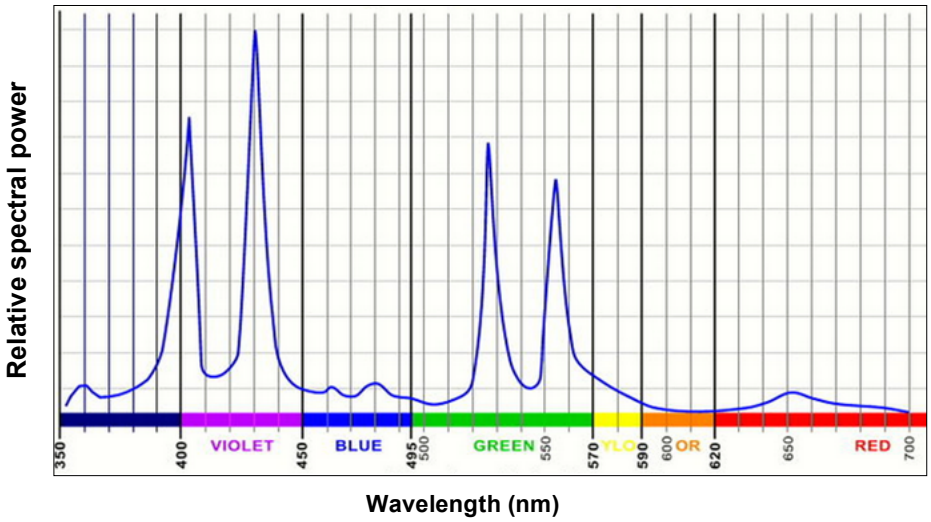

Figure 7. 7: Mercury lamp spectral lines

7.6.2 silver/silver reflectance spectra

In the next step of the calibration, two silver mirrors (PF10-03-P01) obtained from Thorlabs were used as the sample and reference. Among all the metals, silver offers the highest reflectance in the visible part of the spectrum (400 – 700 nm, $R_{avg} > 96\%$), and also the high reflectance in the near-infrared (700 nm – 2 μm, $R_{avg} > 97.5\%$), but it is a poor reflector in the ultraviolet. Therefore silver mirrors were a perfect choice to reflect the light in the 400 nm to 2 μm wavelength range. Since silver is susceptible to oxidation, an overcoat of SiO is used to protect the silver surface.

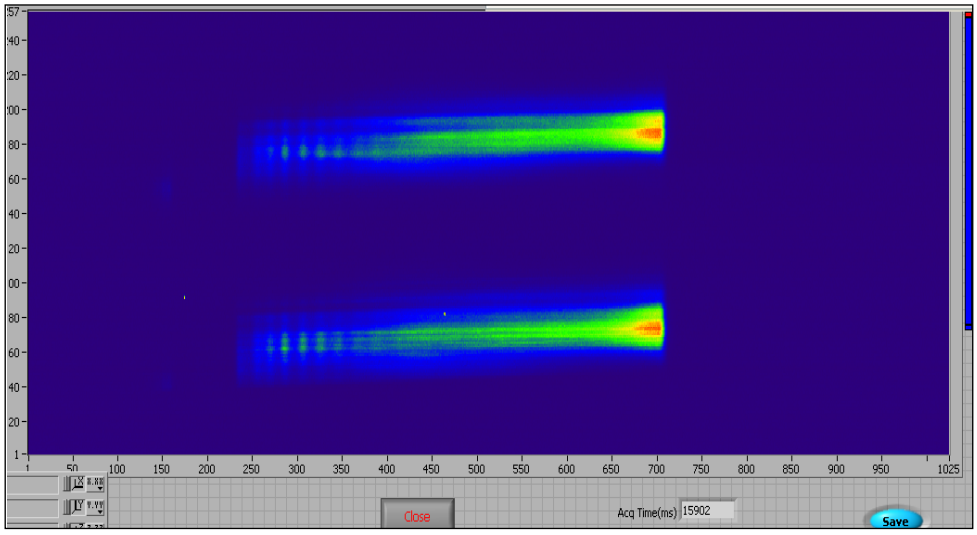

Figure 7. 8: Image acquisition of reflected beams

The reflectance spectrum is collected by the 2D CCD array detector attached at the exit slit. Fig 7.8 shows the reflectance spectral images from the signal and reference mirrors. The associated integrated column spectra are plotted in fig 7.9(a). The LabView program was modified to integrate the upper half and lower half pixels of the chip separately. Both the spectra can be saved within a .dat file. The images shown in 7.8 yield almost similar reflectance spectra for the two mirrors, but with some streaks at lower wavelengths, which correspond to oscillations in the intensity spectra, as shown in 7.9(a). The ratio of the reflectance spectra for the two mirrors is plotted in fig 7.9(b). The ratio is close to unity but

for a few "spikes". The spikes may be the result of *x*-axis mismatch of the individual intensity spectra producing oscillations at a smaller offset to each other. The two beams incident on the grating at slightly different angles and therefore get displaced on the chip. In principle, this could be corrected by changing the steering of the two beams that go into the spectrometer. The sharp fall at the right hand end of the curve in Fig 7.9(a) results from the insertion of the band pass filter, which obstructs wavelengths greater than 700 nm.

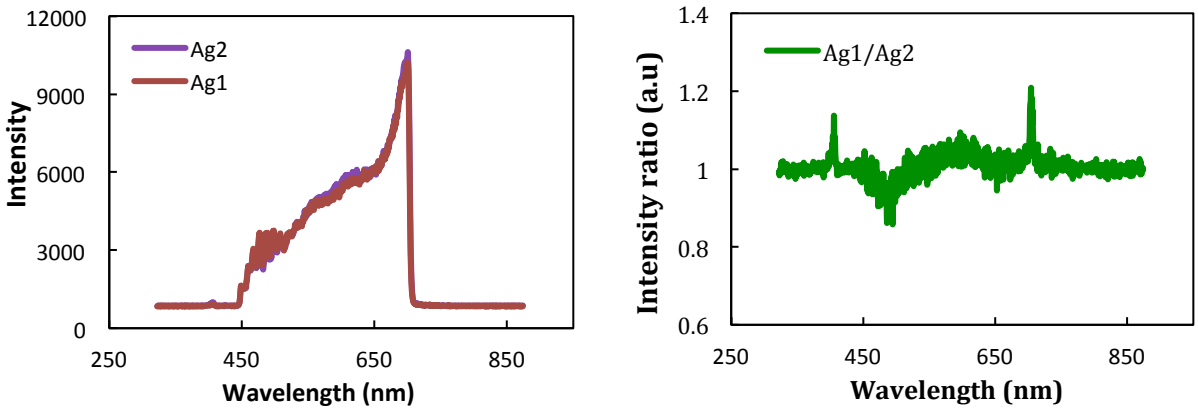

Figure 7.9: (a) Intensity spectra of reflected beams (b) Intensity ratio of two beams

7.6.3 Silver and gold spectra

The first sample to be measured with the white-light probe set-up was a gold mirror (PF10-03-M01) purchased from Thorlabs. A gold mirror was chosen for this experiment because it has a large reflectance over the entire infrared region and its reflectance spectrum is well known. An overcoat was used to protect the gold surface from oxidation. A silver mirror was used as a reference. The sample (gold) and reference (silver mirror) were located in the orthogonal arms of the measurement set up.

The slit width is continuously adjustable from 0 to 2 mm. For the initial alignment, the side exit was selected (fig 7.1). The entrance and exit slits were kept wide open. If the reflected beam can successfully pass through the side exit, then the user can centre the beam position at the entrance slit and minimize the slit widths. The reflected beams are then aligned more

precisely to pass through the 0.1 mm entrance slit and to be incident on the CCD detector chip through the front exit. An internal shutter is placed at the front entrance slit of the spectrograph, which is connected via an electronic connector board. When instructed by the control software, the shutter opens and the CCD detector records the sample image. The automated front slit is also equipped with a height limiter. It controls the slight height and has three primary settings: closed slits, 1 mm open and full open.

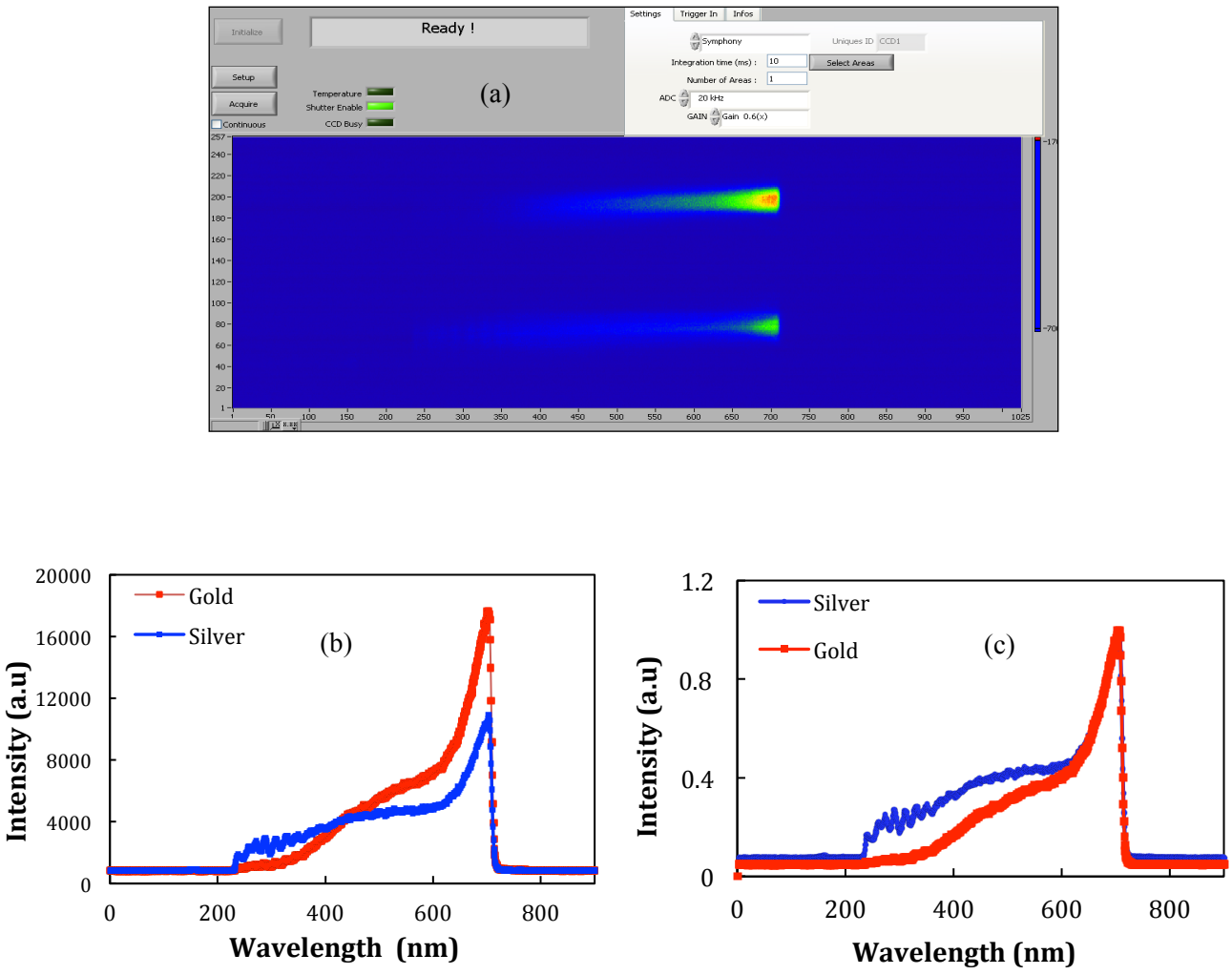

Figure 7.10: (a): Image acquisition for gold and silver mirrors (gold reflection image is at upper half). Intensity spectra - for silver and gold (b), and normalized to unity (c)

Fig 7.10(a) presents the images of the gold reflectance spectrum on the upper half and the silver spectrum on the lower half of the chip. The spectral intensity is plotted in fig 7.10(b) and again exhibits oscillations at shorter wavelengths. Streaks are not visible in the image spectrum due to the large difference in intensity between shorter and longer wavelengths. However the oscillations are clearly seen within the intensity spectra. The oscillation amplitude is significantly larger for the silver spectrum. The maximum intensity of both spectra is normalized to 1 in order to compare the fine features at all wavelengths. The spectra show good agreement with the manufacturer's reflectance data.

7.6.4 White-light spectra Calibration: Gold/Silver (theory)

When light moves from one medium to another, both reflection and refraction of the light may occur at the interface. As shown in Fig 3.1, if n_1, n_2 are the indices of refraction and θ_1, θ_2 are the angle of incidence and refraction respectively, then the reflection coefficient can be written as

$$r_{ss} = \frac{\hat{n}_1 \cos\theta_1 - \hat{n}_2 \cos\ \theta_2}{\hat{n}_1 \cos\theta_1 + \hat{n}_2 \cos\ \theta_2},$$

----------(7.4)

for light polarised with its electric field perpendicular to the plane of incidence (*s*-polarised)

and

$$r_{pp} = \frac{\hat{n}_1 \cos\theta_2 - n_2 \cos\theta_1}{\hat{n}_1 \cos\theta_2 + \hat{n}_2 \cos\theta_1},$$

----------(7.5)

when the incident light is polarised in the plane of incidence (*p*-polarised).

The complex index of refraction can be defined as

$$\tilde{n} = n + ik\,,$$

----------(7.6)

where the imaginary part k defines the absorption loss and is commonly known as the extinction coefficient. Both n and k are a function of the frequency (wavelength).

Since the white-light continuum output from the OPA is s-polarized, the calculations are carried out using equation 7.4. The refractive index of the first medium and angle of incidence are known:

$$\hat{n}_1 = 1\,,$$

$$\theta_1 = 45^0\,.$$

----------(7.7)

For the second medium (gold and silver respectively) the value of the refractive index and extinction coefficient at each wavelength are obtained from a handbook [116].

$$\tilde{n}_2 = n + ik\,,$$

Using Snell's law, the angle of refraction can be expressed as

$$\sin\theta_2 = \frac{\hat{n}_1}{\hat{n}_2}\sin\theta_1 = \frac{1}{(n+ik)\sqrt{2}}\,,$$

$$\sin\theta_2 = \frac{(n-ik)}{\sqrt{2}(n^2+k^2)}\,.$$

----------(7.8)

Combining equation (7.4) and (7.8), the reflection coefficient can be expressed as

$$r_{ss} = \frac{\frac{1}{\sqrt{2}} - (n+ik)\sqrt{1-\left(\frac{(n-ik)}{\sqrt{2}(n^2+k^2)}\right)^2}}{\frac{1}{\sqrt{2}} + (n+ik)\sqrt{1-\left(\frac{(n-ik)}{\sqrt{2}(n^2+k^2)}\right)^2}}\,.$$

----------(7.9)

Therefore the intensity for s-polarized white-light is

$$I = (r_{ss})^2\,.$$

----------(7.10)

The calculations were performed in an Excel spreadsheet using its built-in complex number algebra. For example, $\sin\theta_2$ and $\cos\theta_2$ can be calculated as follows:

$$\sin\theta_2 = \text{complex}\left[\frac{\text{n}}{\sqrt{2}(n^2+k^2)}, -\frac{\text{k}}{\sqrt{2}(n^2+k^2)}\right],$$

----------(7.11)

$$\cos\theta_2 = \text{Imsqrt}\left[\text{Imsub}\left\{1, \text{Improduct}\left(\begin{matrix}\text{complex}\left[\frac{\text{n}}{\sqrt{2}(n^2+k^2)}, -\frac{\text{k}}{\sqrt{2}(n^2+k^2)}\right], \\ \text{complex}\left[\frac{\text{n}}{\sqrt{2}(n^2+k^2)}, -\frac{\text{k}}{\sqrt{2}(n^2+k^2)}\right]\end{matrix}\right)\right\}\right].$$

----------(7.12)

The intensity for Au and Ag is calculated using equ 7.10 and the ratio is plotted against wavelength in fig 7.11. The calculated intensity is compared with the experimental values and the values from the Thorlabs data sheet. The experimental values are in good agreement with the calculation (for s-polarized white-light) and the manufacturer's data. The set up can then be extended to measure unknown samples.

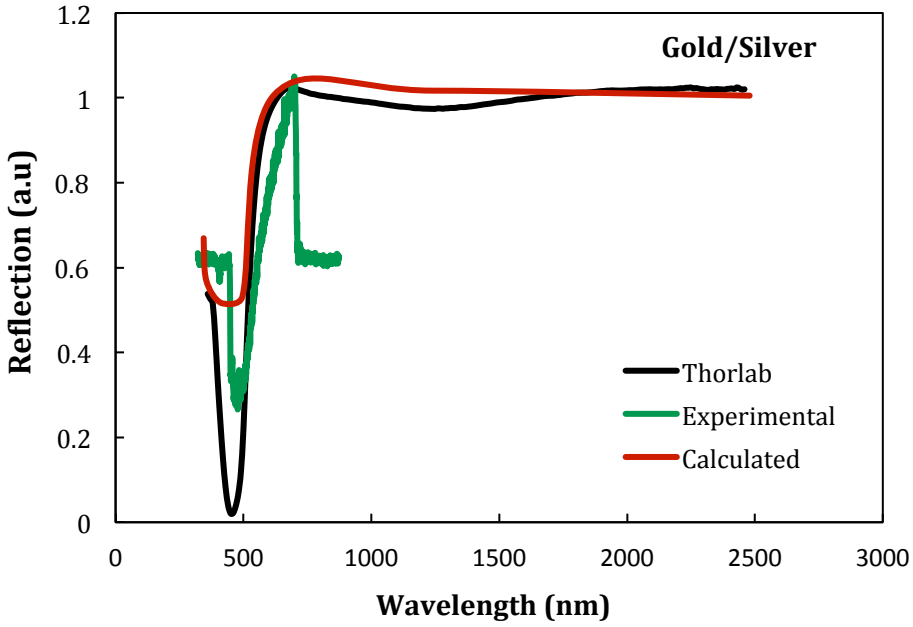

Figure 7.11: Ratio of gold/silver reflectance spectra obtained from the experiment, calculations, and manufacturer's data

7.6.5 GST Spectra

Image and intensity spectra were obtained from the epitaxial GST sample grown on a GaSb[100] substrate that was discussed previously in chapter 4. The gold mirror was replaced by the GST sample, keeping the same silver reference mirror. No pump pulse was used to excite the sample initially. The probe beams reflected from the GST and the reference samples were recorded. The filter was removed to acquire spectra in the visible and IR (400~1000 nm) wavelength range. The entrance and exit slit width was kept at 0.1 mm and a centre wavelength of 800 nm was selected.

The intensity spectra for GST and reference silver mirror are presented in fig 7.12(a)/(b). Since GST shows a strong maximum close to 800 nm, which is also a characteristic peak for the white-light continuum, the GST spectrum normalized to the silver spectrum is

presented in figure 7.13 (a). Figure 7.13 (b) shows the image acquired of the reflected beams from GST and Ag. The normalized GST spectrum in figure 7.13 (a) does not seem to provide any conclusive information. The peak is probably an artefact resulting from imperfect normalization. Further refinement of the normalization technique is required.

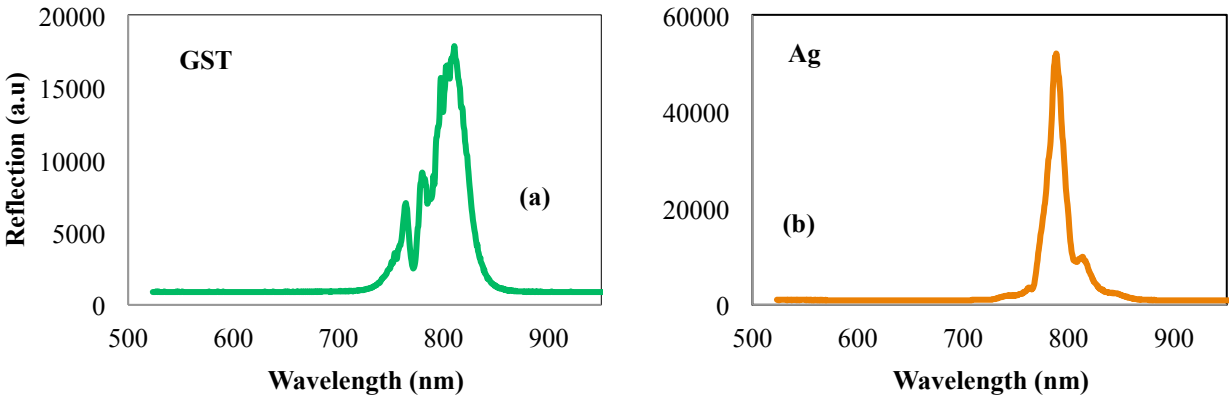

Figure 7.12: Intensity spectra for (a) GST and (b) Silver mirror

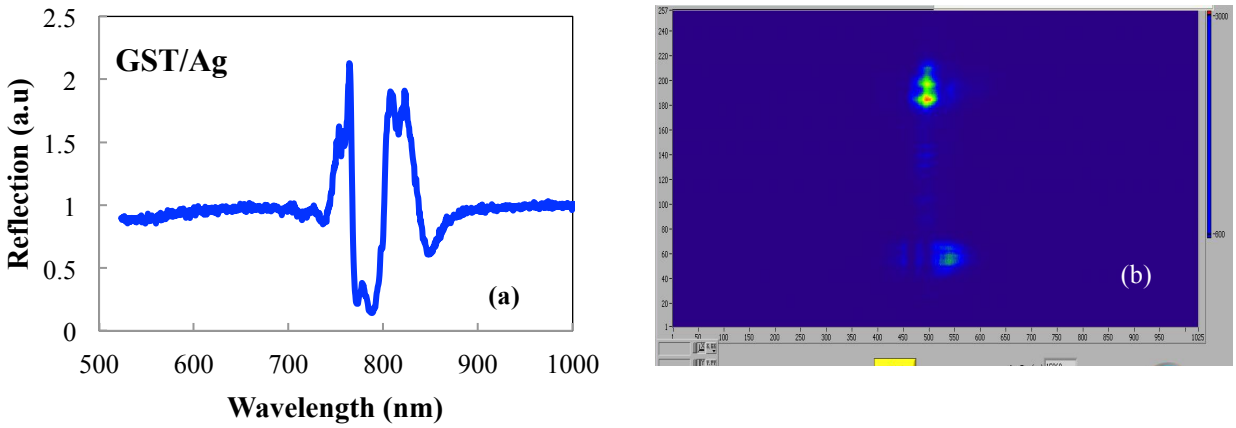

Figure 7.13: (a) Normalized reflactance spectra of GST and (b) Image acquisition for GST and the silver mirror

7.6 Conclusion

A white-light spectroscopy system was set up and tested on materials with known reflectance spectra. The results were in good agreement with the calculated reflection coefficients. A spectrum was obtained from GST confirming its high reflectance at a wavelength close to 800 nm. However this peak seems like an artefact from the normalization process. A more detailed study of GST sample is required. This system will then be ready for time-resolved pump probe measurements using a high energy pump pulse and a white-light probe.

Chapter 8

Electrical testing of $Ge_2Sb_2Te_5$ vertical cells

8.1 Introduction

Phase-change materials (PCM) show fast and reversible switching between two solid states that have significant optical and electrical contrast. The amorphous (RESET) state of the PCM has a resistance that is several orders of magnitude larger than that of its crystalline (SET) state. The electrical switching is different to optical switching because it shows two types of reversible phenomena: threshold and memory switching. These materials can be easily integrated with MEMS and CMOS technologies, which makes them an attractive candidate for electronic memories and ohmic switches.

PCM memory requires electronic pulses to heat and switch the material between two solid states. Small voltages are then used to read the resistance of the state and hence the information stored in the device. The design of the memory cells is important in order to generate a high current density and the temperature necessary to switch between the states.

The devices were fabricated at the Optoelectronics Research Centre in Southampton with the help of Dr. Behrad Gholipur. The electrical testing of devices was performed at the University of Exeter. Discussions with Martin Simpson from the Engineering Department were a great help.

8.2 Sample fabrication

8.2.1 Phase-change memory cell

Generally there are two types of cell structure: the mushroom cell [118] and the line-cell [40]. Both concepts use the Joule heating of an electrical pulse to induce the phase change in a small nanometer sized volume. This chapter focuses on the fabrication and electrical testing of a $Ge_2Sb_2Te_5$ (GST) vertical memory cell. The cell structure of the GST phase change memory cell is shown in fig. 8.1. The vertical line cell is sandwiched between a top and bottom electrode made of TiW. ITO is also a good choice for the bottom electrode. The top electrode is shaped to form a T (fig. 8.1) with a contact pad onto which a 2-pin electrical probe can be landed. The bottom electrode is common for all devices and also works as a contact pad.

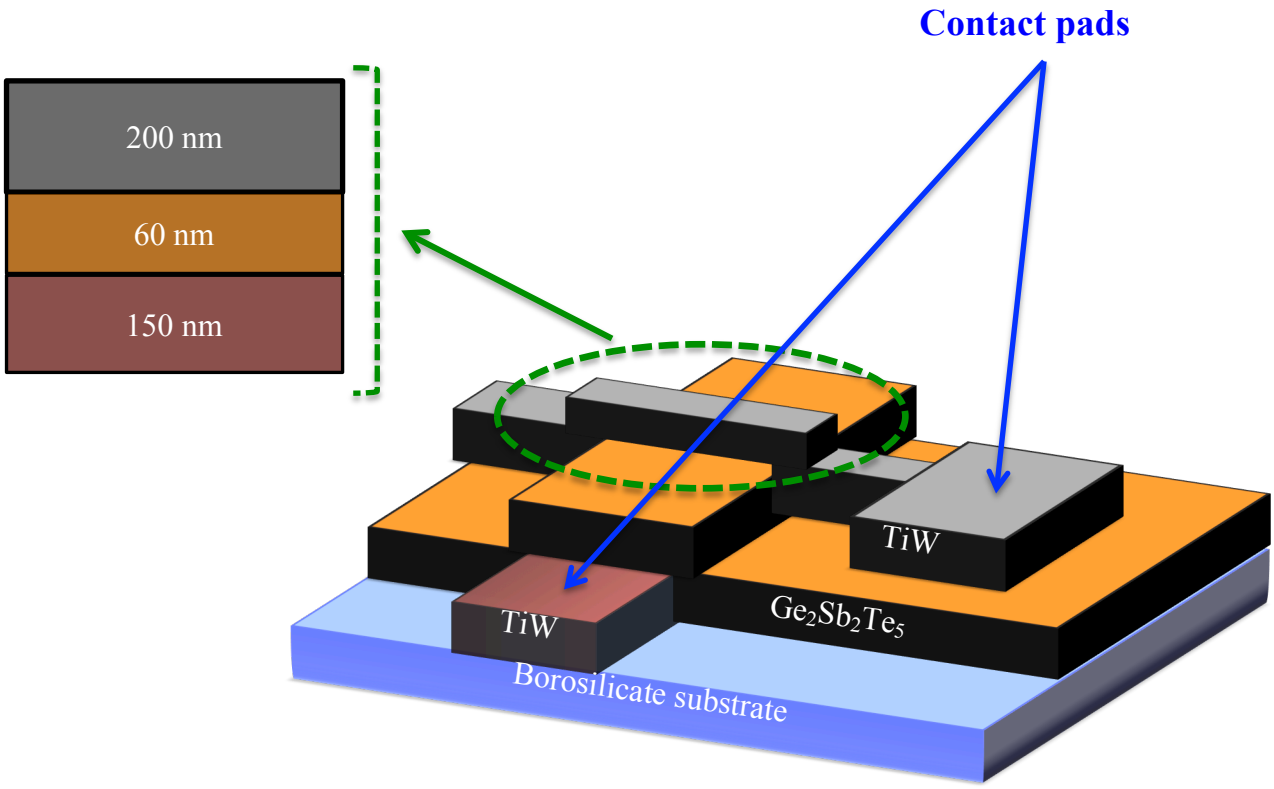

Figure 8.1: Structure of a GST memory cell. The vertical line cell is sandwiched between a TiW top and bottom electrode.

8.2.2 Device fabrication

The GST memory cells were fabricated using high-end optical lithography tools in the strictly controlled cleanroom environment of the Optoelectronics Research Center (ORC) at the University of Southampton. The vertical cells were made on a 5 cm × 5 cm glass substrate. There were more than 1000 devices on one glass plate. The final structure of the cell is shown in fig 8.1. Each memory cell consists of one top and bottom electrode with the GST cell deposited in the middle. The contact pad of the top T-shaped electrode (as shown in right side of figure) is a 40 μm × 40 μm square. The bottom contact pad is a 120 μm × 120 μm square. The device size is 5 μm × 5 μm, which corresponds to the intersection of the two contact pads in contact with the GST. The GST thickness was measured during deposition and was 60 nm. The thicknesses of the top and bottom electrode were determined to be 200 nm and 150 nm respectively. The sample fabrication consists of multiple processing steps in which each process follows a series of steps. The fabrications steps are described below.

1. Clean the Borosilicate substrate
2. Spin photoresist (PR)

The Borosilicate substrate was mounted on the vacuum chuck of a spinner. The PR was spun for 60 seconds at 4000 revolutions per minute (rpm). The PR is dispensed onto the substrate through a filter that removes dust from the polymer. The thickness of the PR was almost 5 μm. The substrate was soft baked for 60 seconds on a hot plate to remove any solvent and leave only polymer. Fig 8.2 describes all the steps required for the fabrication of GST cells. The spinning of the PR step is shown in fig. 8.2(i).

3. Create the bottom contact

Optical photolithography (PLG) is a diffraction-limited process, which employs light to transfer a pattern to the PR. Generally PLG is divided into three important categories, one of which is contact lithography. In contact lithography, a photomask is placed in direct contact with the substrate and the unmasked PR is then exposed to UV light. The formation of a bottom contact involves the following steps:

a. Align the mask

A mask of 5 inches by 5 inches was aligned and placed onto the substrate using an optical microscope as shown in fig. 8.2(ii). The mask for the bottom electrode was T-shaped.

b. Expose to UV light

Once the mask was in place, the PR was exposed to UV light with a wavelength of 400 nm light for 8 s as shown in fig 8.2 (iii).

c. Develop the photoresist

The substrate was placed into PR developer for 45 s after exposure and the exposed PR removed. The substrate was cleaned using acetone and the pattern was confirmed using an optical microscope.

d. RF sputter deposition of TiW

The substrate was mounted in the deposition chamber immediately after PR development to ensure minimal contamination of the substrate. The chamber was evacuated for half an hour to a base pressure of 9.8×10^{-5} Torr and then backfilled with Argon gas. Subsequently the deposition process was initiated by igniting an argon plasma with an ac voltage. Argon ions bombarded the TiW target to displace atoms, which were then deposited on the substrate until a thickness of 150 nm was achieved.

e. Use of lift-off technique to remove unwanted TiW

The lift-off process as shown in 8.2 (v) was performed in an ultrasonic bath of acetone for 2 minutes to remove unexposed PR along with the TiW. The pattern was confirmed using an optical microscope.

f. Reactive ion etching (RIE)

RIE is used at the end of every layer deposition to remove any polymer, which has remained after the developing process. RIE was done in an oxygen plasma for almost a minute. This process is generally known as Ashing.

4. RF sputtering to deposit GST

The phase-change layer in the as-deposited amorphous state was deposited in the same sputtering machine at a deposition rate of 1.31 Å/s. The sputtering was performed for 7 to 8 minutes to deposit 60 nm thick GST.

5. Pattern transfer for the top electrode

To create the top contact, the same procedure as described for the bottom contact in step 3 (above) was followed. The feature on the photomask was aligned with the GST layer and substrate with the help of alignment marks. As for the bottom contact, the top contact was also T-shaped.

These devices can only switch from the amorphous to the crystalline state. To perform the reverse process a layer of $ZnS:SiO_2$ is required to (i) support the GST melt and (ii) provide high heat extraction to quench the GST crystalline cells and allow the amorphous state to form.

An optical microscope image of the bottom electrode is shown in fig 8.3(a). Fig 8.3 (b) and (c) show reflection and transmission microscopy images of the top electrode.

(i) PR Coating

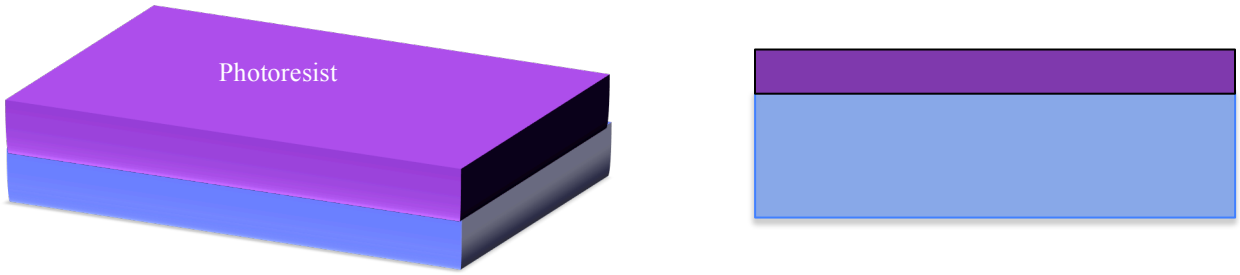

(ii) Mask alignment

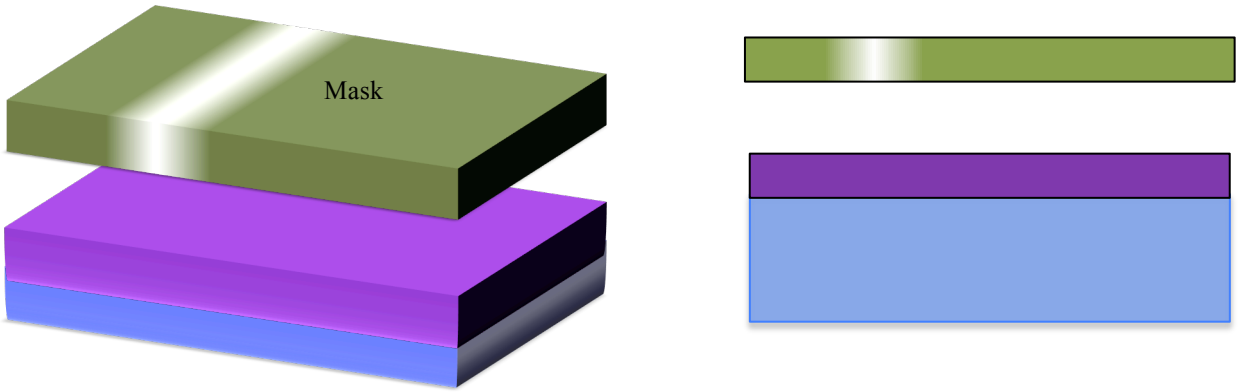

(iii) Optical PLG

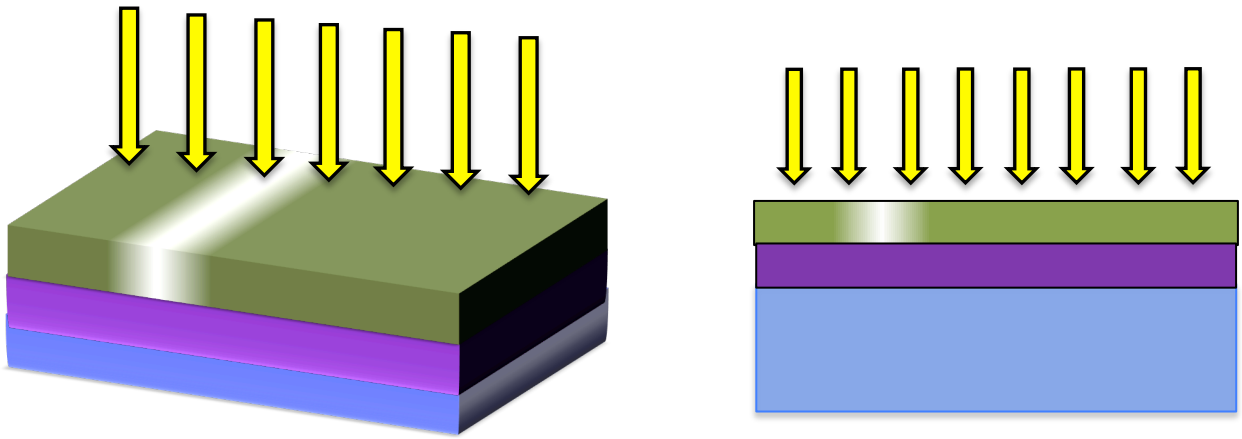

(iv) Developing PR

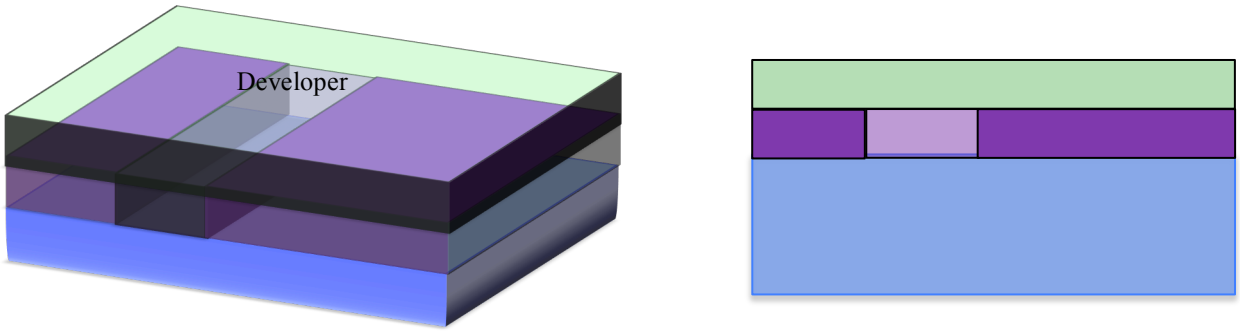

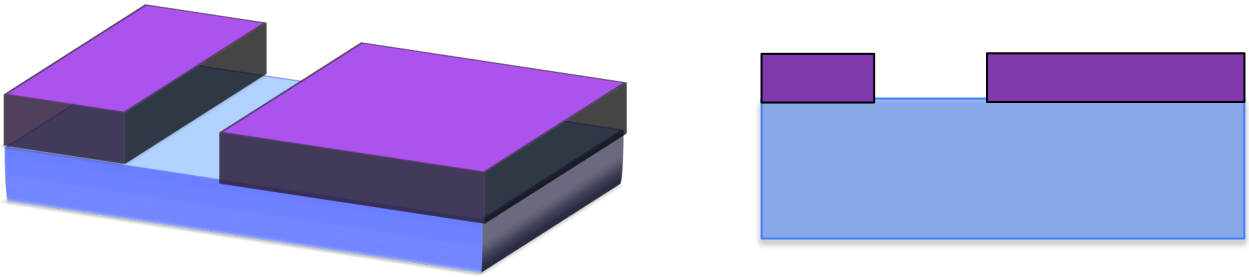

(v) TiW layer deposition

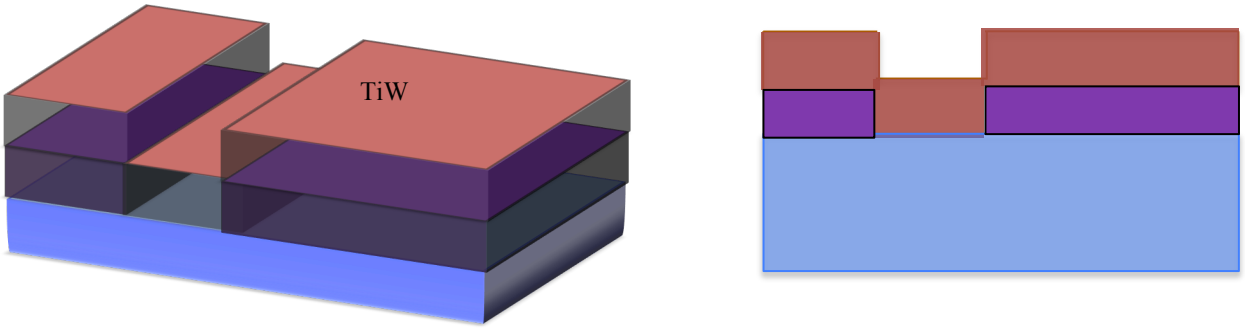

(vi) Lift-off

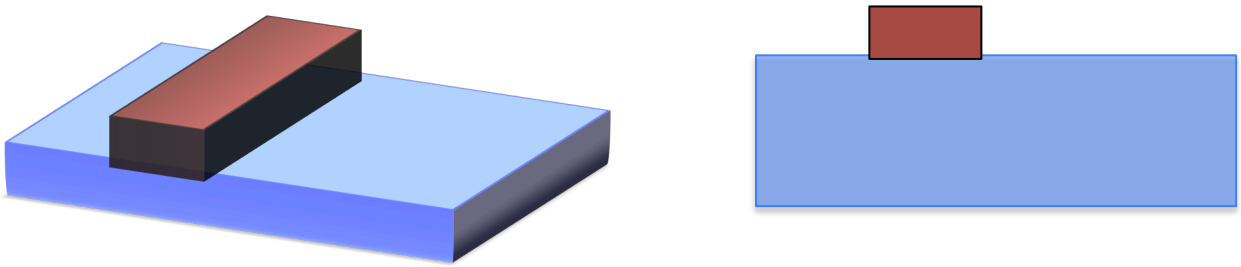

(vii) Phase-change layer deposition

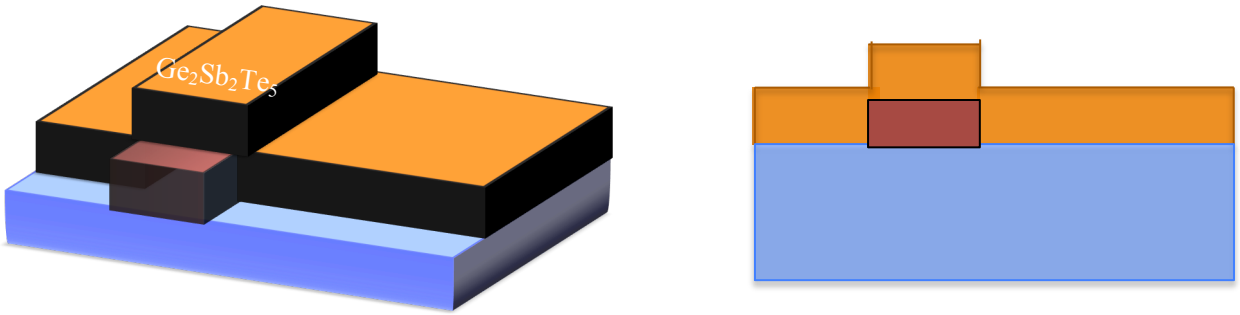

(viii) Formation of top contact (TiW)

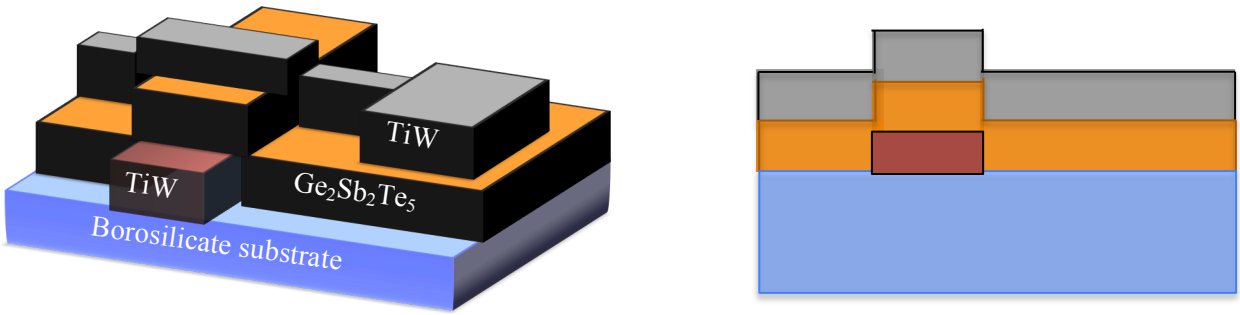

Figure 8.2**:** The steps for the contact photolithography and lift-off process. Lithography: a photo resist is spin-coated onto the glass substrate (i) and exposed to UV light (iii) using a contact mask aligner (ii); the exposed photo resist is removed by a chemical developer (iv). Lift-off process: a phase-change layer and a titanium nitride top and bottom layer are deposited on the structured photoresist by rf sputtering; dissolving the PR with acetone removes the material which has been deposited on top of the PR (v). The fabrication steps are shown on the left side whereas the right side shows a cross-sectional view.

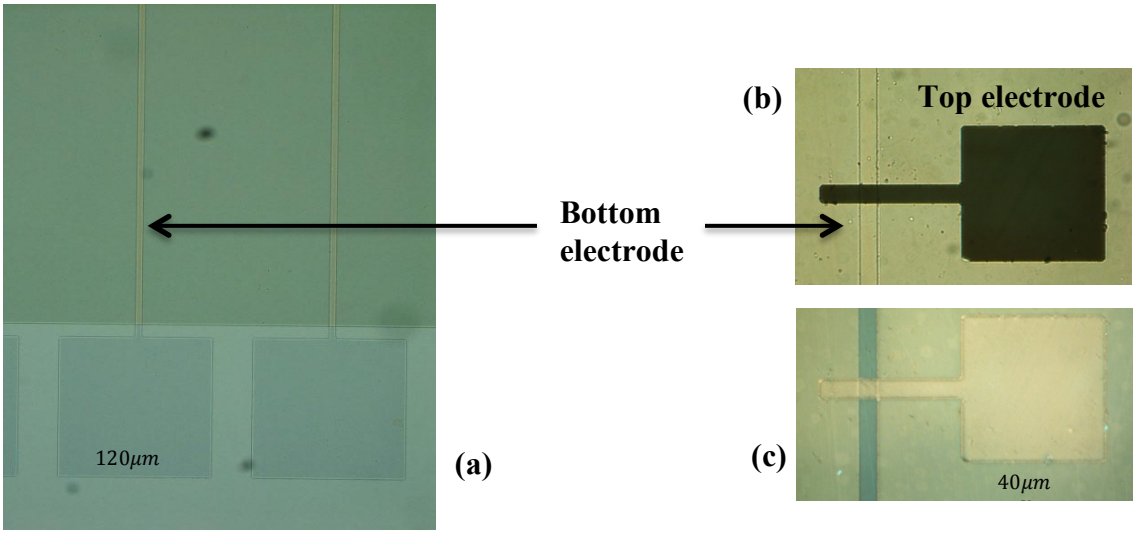

Figure 8.3**:** (a) Optical microscope image of bottom electrode; (b) reflection and (c) transmission microscopy images of the top electrode.

8.3 High frequency measurements: Theory

GST requires nanosecond (high frequency) pulses of electrical current to induce the phase transition between amorphous and crystalline states. Conducting high frequency measurements requires a lot of care and understanding. At high frequency, where the wavelength of the electrical signal is similar to, or shorter than the length of the cables used in the experiments, the cables must be treated as transmission lines. The propagating wave can reflect from any discontinuity, for example the terminating end of the transmission line. The interference associated with such a reflection can lead to an irregular response of the system. Transmission lines can carry alternating current of high frequency with minimum loss or distortion. However, at even higher frequency (above the microwave range), when the wavelength becomes much shorter than the lateral dimensions of the transmission line, a different approach is required which can be referred to as optical engineering [119].

8.3.1 Characteristic impedance of an electrical transmission line

The transmission line can be studied as an electrical circuit in which an electrical signal propagates along a pair of parallel conductors. Consider an ideal transmission line and divide it into sections of length dx characterised by a combination of inductance (L_0) and capacitance (C_0) with zero electrical resistance (Fig 8.4). The capacitance arises due to the electric field between parallel conductors, while the inductance describes the effect of the magnetic field generated by the conductors. The signal velocity and the characteristic impedance of the transmission line can be derived for this electrical circuit.

The time-varying voltage causes the changes in charge stored on conductors given by,

$$\Delta q = - C_0 \Delta x \, V. \qquad \text{----------(8.1)}$$

The change in charge that occurs in a time Δt over distance Δx is

$$\Delta I = \frac{\Delta q}{\Delta t} = -C_0 \Delta x \frac{\Delta V}{\Delta t},$$

----------(8.2)

Dividing the above equation by Δx and taking the limit $\Delta x \to 0$ gives the following differential equation,

$$\frac{\partial I}{\partial x} = -C_0 \frac{\partial V}{\partial t},$$

----------(8.3)

Similarly the voltage drop across the inductor is

$$\Delta V = -L_0 \Delta x \frac{\Delta I}{\Delta t},$$

Therefore,

$$\frac{\partial V}{\partial x} = -L_0 \frac{\partial I}{\partial t}.$$

----------(8.4)

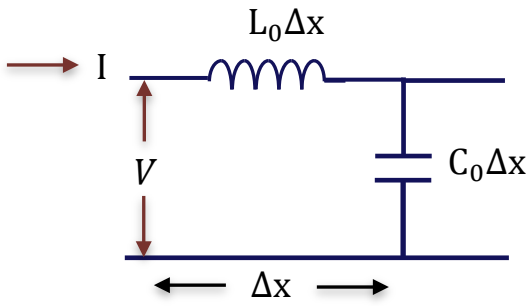

Figure 8.4: Equivalent circuit of a unit length of transmission line.

Equations (8.3) and (8.4) describe the time dependence of the voltage and current within the transmission line. Differentiating these equations with respect to x leads to the wave equations for voltage and current.

$$\frac{\partial^2 I}{\partial x^2} = L_0 C_0 \frac{\partial^2 I}{\partial t^2},$$

----------(8.5)

and,

$$\frac{\partial^2 V}{\partial x^2} = L_0 C_0 \frac{\partial^2 V}{\partial t^2}.$$

----------(8.6)

Therefore the velocity of wave propagation is defined as

$$v^2 = \frac{1}{L_0 C_0}.$$

----------(8.7)

Solving the wave equations (8.5) and (8.6) for I and V and substituting the wave solutions back into equation (8.1) yields,

$$z_0 = \frac{V_i}{I_i} = -\frac{V_r}{I_r},$$

$$Z_0 = \sqrt{\frac{L_0}{C_0}},$$

----------(8.8)

where V_i and V_r are the incident and reflected voltages respectively. Z_0 is defined as the ratio of the voltage and current amplitudes of a wave travelling along the transmission line in the absence of reflection.

8.3.2 The load effect

When a pulse propagating along a transmission line encounters a boundary, a part of the incoming wave is reflected back towards the source. If the wave comes to an open end, then the entire pulse is reflected in the opposite direction, as shown in Fig. 8.5.

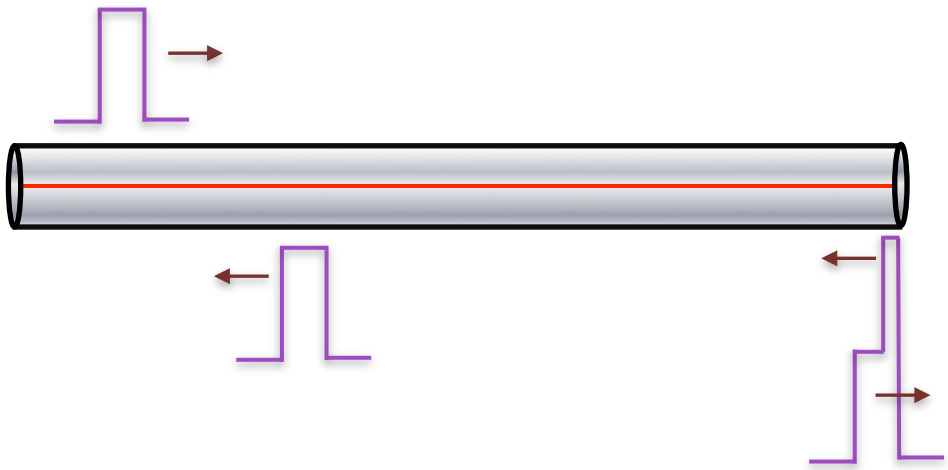

Figure 8.5: Reflection of an electrical pulse from an open circuit.

If the cable is connected to a load of impedance Z_L, then some of the incident pulse is reflected, depending upon the value of Z_L. If the incident and reflected voltages are represented as V_i and V_r, then the boundary condition at Z_L can be written as

$$V = V_i + V_r \,,$$

$$I = I_i + I_r \,.$$

----------(8.9)

The characteristic impedance is

$$z_0 = \frac{V_i}{I_i} = -\frac{V_r}{I_r} \,,$$

----------(8.10)

and the load impedance can be expressed as

$$z_L = \frac{V}{I},$$

----------(8.11)

The reflection coefficient can now be defined as

$$\Gamma = \frac{V_r}{V_i} = \frac{Z_L - Z_0}{Z_L + Z_0}.$$

----------(8.12)

Fig 8.5 refers to the situation when the reflection coefficient is equal to 1. If the load is replaced by zero load resistance (short circuit), then the pulse will reflect with opposite polarity, i.e. $\Gamma = -1$, as shown in fig 8.6.

Figure 8.6: The reflection of an electrical pulse from a short circuit.

If the value of the load impedance is chosen between these two extreme cases then there will be some value for which the reflection coefficient will be zero. This is equivalent to connecting another cable of the same characteristic impedance, and so the value of the load resistance is equal to the characteristic impedance Z_0. For coaxial cables, the value of the characteristic impedance is usually 50 Ω or 75 Ω. In this work, Z_0 was equal to 50 Ω. Impedance matching is usually required to maximize the power transfer and minimize reflection from the load.

8.3.3 Coaxial cable

Coaxial cables were used in the experimental set up. These cables contain an inner or centre conductor, and an outer cylindrical conductor separated by a dielectric material. The cable has a distributed inductance and capacitance that can be thought of as a chain of LC elements of the form shown in fig. 8.4. The outer conductor is usually at ground potential and acts as a shield for the central conductor (signal line). These cables are connected together and to instruments and loads with BNC and SMA connectors (in this experiment), which also have the coaxial cylindrical geometry.

In the microwave regime, the signal is transmitted using waveguides while optical fibers are used in the optical region.

In a coaxial cable, the inductance per unit length can be written as

$$L_0 = \frac{\mu}{2\pi} \ln \frac{r_2}{r_1},$$

----------(8.12)

where r_1 and r_2 are the radii of the inner and outer conductors respectively and μ is the magnetic permeability of the dielectric.

Similarly the capacitance per unit length is

$$C_0 = \frac{2\pi\varepsilon}{\ln \frac{r_2}{r_1}},$$

----------(8.13)

where ε is the permittivity of the dielectric.

Therefore, the velocity v of the electrical signal is given by

$$v^2 = \frac{1}{L_0 C_0} = \frac{1}{\mu\varepsilon}.$$

----------(8.14)

By knowing the inductance and capacitance of a transmission line, the velocity of the signal can be calculated, which can provide information about the time required for an electrical signal to travel a given distance along the cable.

8.4 Building the electrical test set up

There are two basic prerequisites to electrical switching in GST cells. First is the fabrication of phase-change memory cells, which can demonstrate switching between two states. Second is the design of a set up that can provide an interface for electronic devices to communicate with and connect to the sample. The set up should be able to generate electrical pulses of different durations and record the response of the memory cells during/after the pulse.

There are many challenges in building such a system. These are related to the material and its properties in the two structural states. The memory cells exhibit a large resistivity contrast between their amorphous and crystalline states that covers a broad range of memory resistance. In addition, the crystallization in a PCM takes place within a few nanoseconds and so the electronic properties of the material change in similarly short time. Therefore, it is necessary to design an impedance matching network that allows high frequency pulses to be applied and recorded, since the memory device changes its resistance over several orders of magnitude during the application of a pulse.

Parasitic capacitance and inductance are other unavoidable problems, which limit the maximum frequency (or cut-off frequency or f_c) that can be achieved in an electronic circuit. f_c depends on the time constant (τ) of the circuit component.

$$f_c = \frac{1}{2\pi\tau}.$$

----------(8.15)

τ characterizes the time to charge or discharge the capacitor in the circuit. The time constant of an RC circuit is expressed as the product of capacitance and resistance (through which the capacitor charges or discharges) in the circuit.

$$\tau = RC.$$

----------(8.16)

In our set up, we assume that the effect of inductance that limits the rise time of current within a circuit is very small compared to the capacitative effects.

8.4.1 DC set up

To demonstrate that vertical GST memory cells can switch from the amorphous to the crystalline state, a first simple test set up was designed.

The system was built on a transport kit or probe station, which contains two-xyz manipulators to land the probes on the preferred area. Two probes (one on each manipulator) were required to determine the resistance of the memory cell. The probe has two tips, known as signal and ground, separated by a distance of 125 µm. The signal tip of the first probe was landed on the top TiW electrode while the ground tip was left floating. The signal and ground tips of the second probe were both landed on the bottom electrode. The voltage to the device was applied using a DC power supply connected through a multimeter, which measures the device current simultaneously. The set up is shown in fig 8.7.

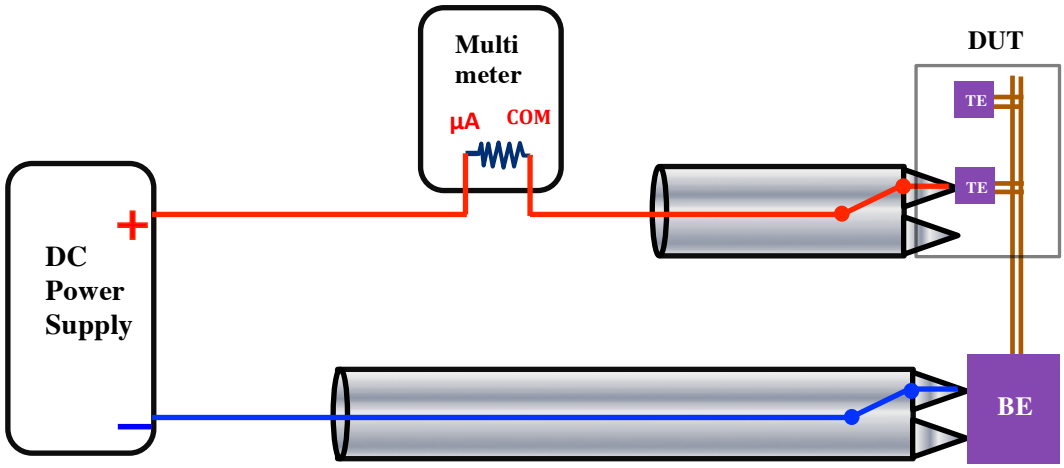

Figure 8.7: DC test set up to switch the memory cells, where DUT stands for device uner test (sample), TE for the top electrode and BE for the bottom electrode.

Care should be taken not to damage the probe while landing on a device. To confirm that the probe is making proper electrical contact with the electrode, the other end of the probe is connected to a multimeter via a BNC cable. Simultaneously, a CCD camera was used to

observe the probe tip movement closer to the sample surface. The multimeter gives a response as soon as the probe comes into contact with the surface.

The GST memory cells are initially in the as-deposited amorphous state. The resistance of the device in the amorphous state was measured to be between 40 and 60 MΩ. The voltage was applied using an external power supply and increased in 0.5 V steps up to 10 V. The multimeter measuring the device current shows a rapid increase as the device is switched from the high-resistance to the low-resistance state. For small voltages, a current in the μA range was observed. With increasing voltage, the device current starts to increase from 0.12 μA to 1 μA maximum before displaying a sudden increase to 15 μA at a voltage close to 4.5 V. The process was repeated for a number of cells, showing that the threshold voltage of the GST memory cells lies between 4.5 to 6 V. The device current for an amorphous GST cell with respect to applied voltage is shown in fig 8.8.

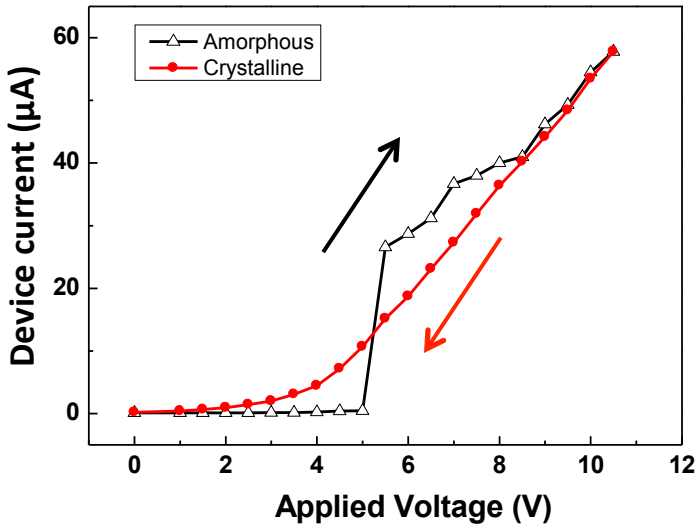

Figure 8.8: The device current is plotted with respect to applied dc voltage

The resistance in the low-resistance state was measured to be 4 MΩ using a multimeter, while the I-V characteristic shows a resistance of 200 to 300 kΩ in the crystalline state. The reason that multimeter reads a higher value for resistance is because it applies a smaller voltage (of 0.5 V) to measure the current flow in the device. After the device switched to a low-resistance state, the voltage was swept back from 10 V to 0 V to measure the device current in the crystalline state.

8.4.2 DC set up with an external resistor

Further progress in the set up was made by inserting an external 219.4 kΩ (R_1) resistance parallel to the GST memory cell. The device current can be precisely determined by observing the voltage drop across the external resistor. Again to keep the set up simple, a multimeter was used to measure the device current. A two-channel Rigol oscilloscope, which calculates the difference of voltage signals at the two ends of the resistor by a simple math function, measured the voltage drop across the external resistor. The oscilloscope was convenient to use for testing; however an ordinary differential voltmeter can work equally well. The set up is shown in fig 8.9.

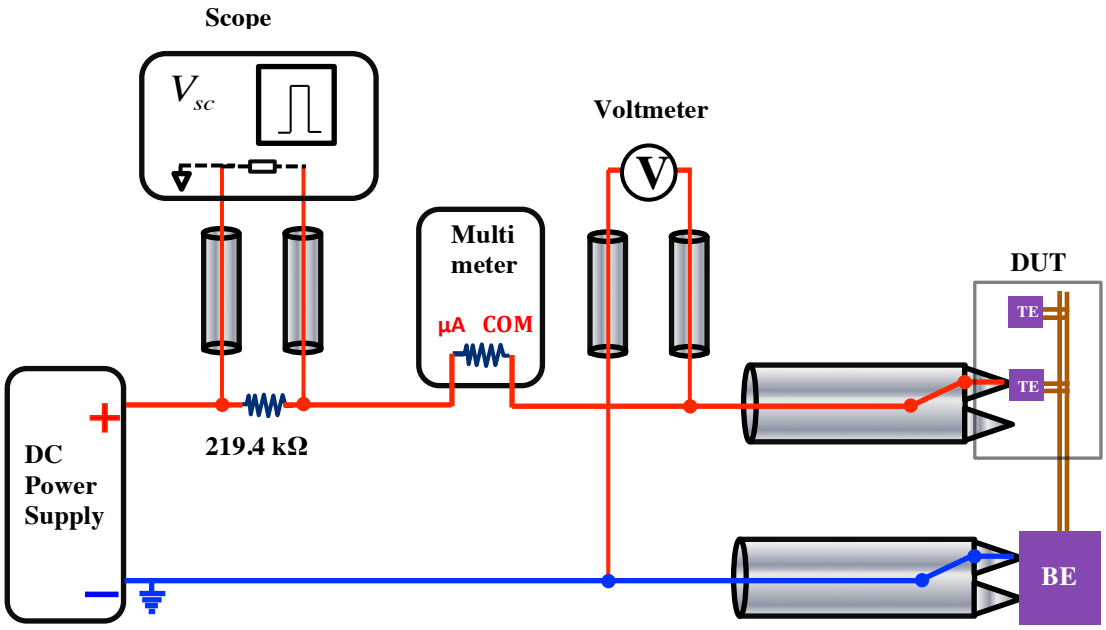

Figure 8.9: DC test set up with an external resistor

The applied voltage was increased up to 18 V in steps of 1 V. When the probes are properly landed, the device current starts to increase slowly up to the 1 µA range for smaller applied voltages. When the device is in the amorphous state, most of the applied

voltage falls across the device. At an applied voltage close to 8 V, the voltage dropped across the device was measured to be 6.5 V. As the applied voltage was increased further, the device voltage showed a rapid decrease. At 8.7 V applied voltage, the device voltage was measured to be 4.3 V, which confirms that the device had switched to a crystalline state with a resistance close to the external resistance (219.4 kΩ). At this voltage, the device current also increases from 1 to 12 μA. As the applied voltage was increased further, the voltage across the device also increased. Fig 8.10 shows the dependence of (a) device current and (b) device voltage upon the applied voltage.

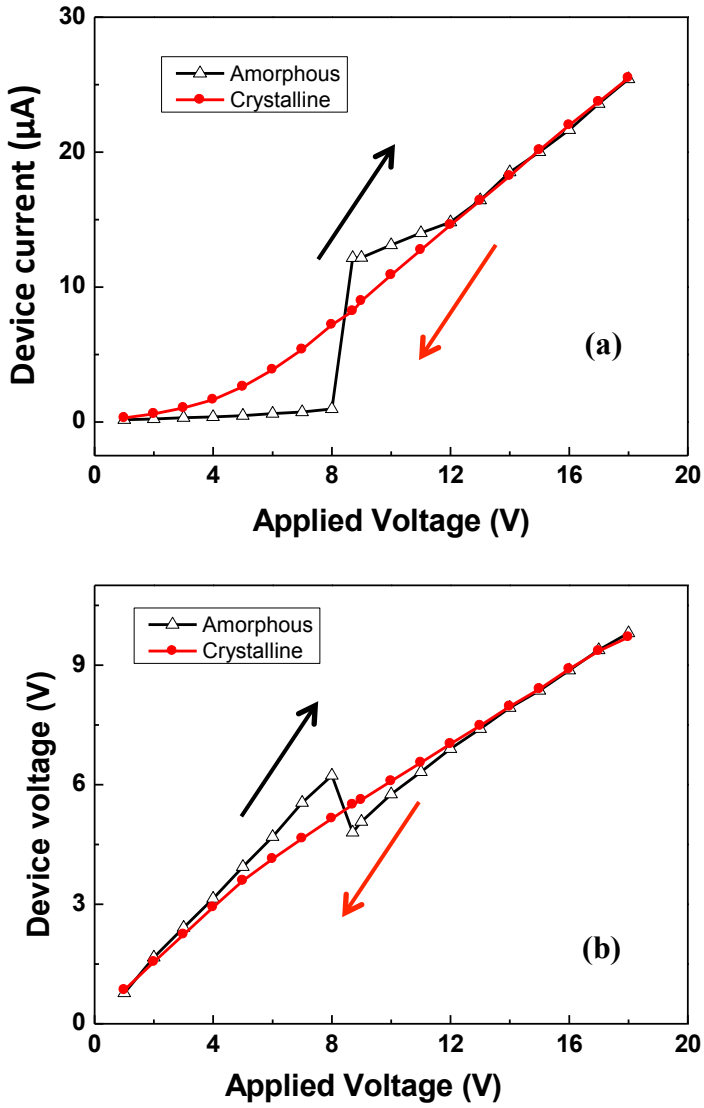

Figure 8.10: (a) plots the device current and (b) device voltage against the applied voltage

8.4.3 Pulsed measurement set up

GST devices were successfully switched to the crystalline state using a DC voltage. However, pulsed measurements are required to record the response of memory cells on nanosecond (ns) time scales. Therefore, efforts were made first to build a set up in which a ns pulse can switch the cells and a AC/DC voltage can measure the resistance of the device during/after the pulse.

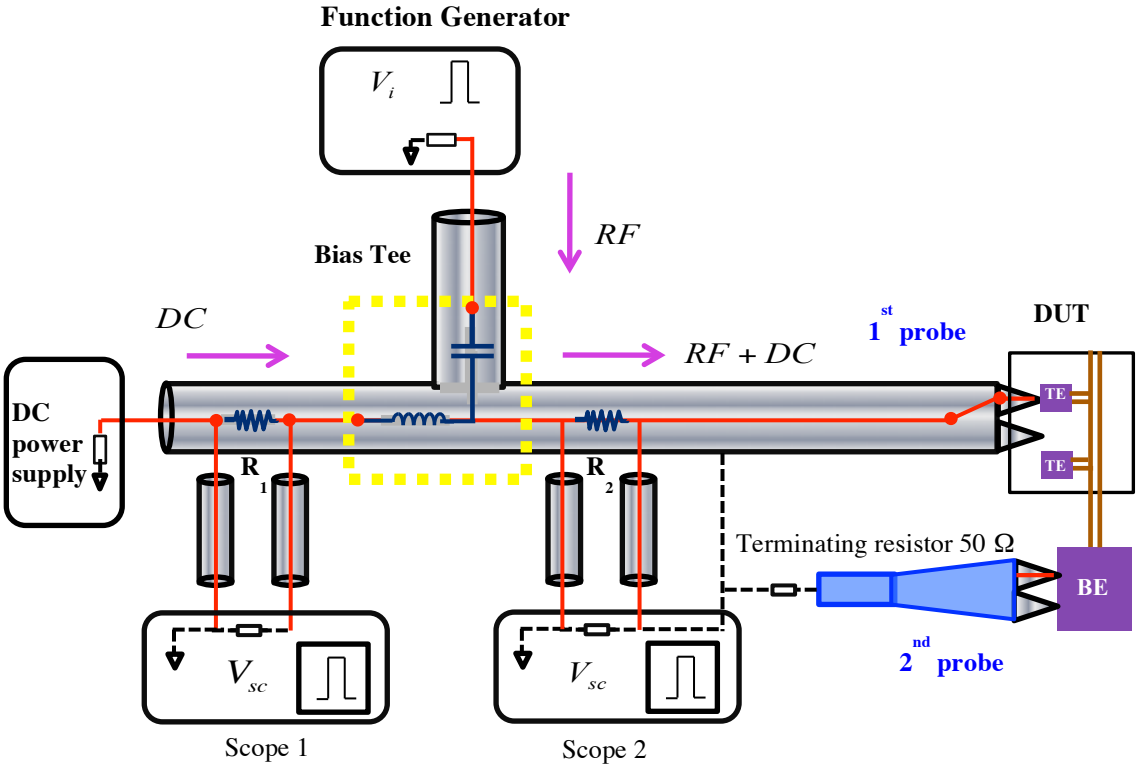

Figure 8.11: Test set up to perform pulsed measurements

The DC set up was extended to carry out pulsed measurements using a function generator, bias-tee and an additional oscilloscope. The function generator was used to produce pulses of short duration, which were sent to the device through an external resistor (R_2). A 4-

channel LeCroy scope was inserted across the external resistor R_2 to measure the device current during a pulse. 50 Ohm tee pieces were used to connect the two inputs of the scope to either side of the resistor. A Bias-tee with its inductive arm connected to the DC signal path and its capacitative arm connected to the AC signal path was used to perform the switching measurements. The first scope measures the resistance after the pulse and confirms that the switching process has occurred, while the second scope is supposed to record the device response during the pulse. The value of R_1 was kept fixed at 219.4 kΩ and R_2 was varied so as to control the programming current. The set up is shown in fig 8.11.

The correct operation of the set-up was verified by observing the response of a gold sputtered film, which has a resistance close to 100 Ω. The value of R_2 was chosen to be 150 Ω (close to the sample resistance) while the scope coupling was set to 50 Ω. The current reflected from the gold sample was -0.33 times the incident current. The superposition of two pulses was clearly observed with the oscilloscope. The impedance matching was not a problem here because the impedance of the cable and scope, and resistance of the external resistor and the sample resistance were all in the same range.

However, the GST device resistance is 100 to 300 kΩ in the crystalline (SET) state and > 40 MΩ in the amorphous (RESET) state, which is much larger than the characteristic impedance of the coaxial cable. Therefore, for an applied pulse, the current is reflected back from the device with a reflection coefficient very close to -1. The oscilloscope connected across the external resistor shows a characteristic spike until the reflected pulse returns from the sample, after which the voltage falls almost to zero as shown in fig 8.12 (a). Since the device takes a few nanoseconds (ns) to change between two different resistance levels, the reflection coefficient will change and the reflected pulse is expected to display a more complicated leading edge. As that leading edge passes through the resistor, the reflected current falls down to a small value. However, the change in voltage on the leading edge due to the changing sample resistance is small compared to the height of the spike. Therefore the signal of interest is small and lies just after the spike and cannot be measured precisely. The equivalent circuit of the set up is shown in fig 8.12 (b).

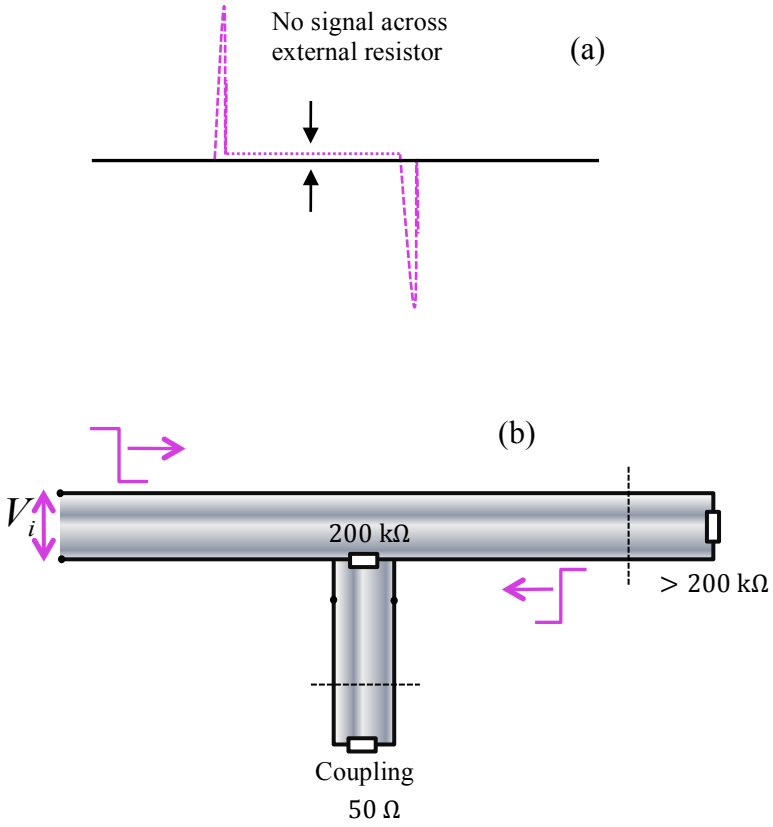

Figure 8.12: (a) Scope response for an applied pulse and (b) Equivalent circuit for a 200 kΩ external resistor

We also used high impedance probes: in a first experiment, two standard 10x probes were connected to either side of the resistor and in a second approach, an active voltage probe (100 kΩ resistance and 70 pF capacitance) and a standard 10x probe were used to connect either side of the resistor to the scope. In these cases, there will be no shunting of the current by the oscilloscope due to the high input impedance of the probes. Ideally, the device current can be calculated by recording two waveforms on either side of the resistor. However, this approach was also unsuccessful and the reasons for this are still being considered.

The device was found to switch when pulses of 300 ns duration and increasing amplitude were applied. The device resistance after the switching was calculated by measuring the voltage drop across the external resistor in the DC arm. However, the device current was not precisely measured during the pulse. The device demonstrated the resistance change for

pulses duration as small as 100 ns.

The oscilloscope also had an alternative high impedance input of 1 MΩ. However, at higher frequency, the RC time constant becomes significant. For 1 MΩ coupling and 16 pF capacitance, the RC time constant of the scope input is

$$\mathrm{RC} = (1\ \mathrm{M\Omega}) \times (16\ \mathrm{pF}) = 16\ \mu\mathrm{s}. \qquad \text{----------(8.17)}$$

The applied pulse duration is much shorter (300 ns) than the RC time constant of the scope. In this case, the input capacitance of the oscilloscope does not have sufficient time to either fully charge or discharge and therefore the measured voltage is much less than the maximum input voltage. The cut-off frequency (f_c) for this set up is calculated from equation (8.11) to be 9.95 kHz. This indicates that the set up could be used up to a maximum frequency of 10 kHz above which the measured signal would be diminished. To obtain the complete signal at higher frequencies, the RC time constant of the oscilloscope would need to be significantly reduced.

8.5 Conclusion

The measurement set up was able to observe successful switching of GST cells from the amorphous to the crystalline state in response to a DC applied voltage. The device was also observed to switch in response to a pulse of 100 ns minimum duration. However the set up was unable to measure the response of the device during the pulse. The use of a more advanced impedance matching network as in reference [120] is required to record the device current during a pulse.

Chapter 9

Summary and Future work

9.1 Summary

Phase-change alloys have received a lot of attention in the memory-device industry these days because of their two very important properties. First, these chalcogenide-based semiconductor materials can be reversibly switched between high- and low-resistance states and second these materials are non-volatile in nature. These materials can be electrically or optically switched with the application of pulses of a few ns duration. In this thesis, the results of a number of experiments performed on $Ge_2Sb_2Te_5$ (GST) samples have been presented.

When a material is excited by ultrashort pulses of duration close to the time scale of its internal dynamics, then it immediately reaches a (transient) non-equilibrium state. Probing the material by ultrashort pulses of similar duration can trace the evolution of carrier dynamics and relaxation processes. Therefore, time-resolved pump-probe measurements were performed on GST and GaSb films to gather information about electronic excitations and the behavior of optical phonons. The dynamic response of the sample provides information about the structural properties and non-thermal nature of the transition process in phase-change materials. The results of a time-resolved optical investigation of e-GST and e-GaSb films were presented in chapter 4, while a comparison of e, p and a-GST was provided in chapter 5.

A thorough investigation of GST material in epitaxial (e), polycrystalline (p) and amorphous (a) phases provides interesting information about their characteristic modes and hence the underlying structure of the material. The transient AR response of all samples was plotted on three different time scales to reveal their important features. Firstly, it was observed that all samples, e-GST, p-GST, a-GST and e-GaSb, exhibit a sharp initial peak at zero time delay with maximum amplitude when pump and probe polarizations lie $\pm$ 45° apart. The peak amplitude reduces to zero when the pump and probe beams are either parallelly or perpendicularly polarized. This peak is related to the specular optical Kerr effect (SOKE) and contains information about the rate of relaxation of the linear momentum of the excited electrons. Secondly, coherent optical phonons (COP) of different frequencies were observed on the early ps time scale superimposed on a relaxation background. The frequencies of these phonon modes were found to be 6.7 THz for e-GaSb, 3.4 and 6.7 THz for e-GST and 4.5 THz for p/a-GST. It was noticed that the COP of e-GaSb and e-GST samples appeared in the AR channel only while the COP of p/a-GST were present in both R and AR channels. These modes were analyzed by applying the transient stimulated Raman scattering (TSRS) theory provided by Merlin. This theory describes the behaviour of A (1D), E (2D) and T (3D) modes and their dependence upon pump and probe polarizations. It was observed that 6.7 THz mode in e-GaSb shows a higher amplitude when the pump is polarized along the face diagonal and the probe is polarized along a cubic axis. The amplitude of phonon is minimum when the pump and probe polarizations are interchanged. This dependence of the GaSb transverse optical mode on pump and probe polarization was described by a $\cos 2\theta \sin 2\varphi$ functional form, where θ and φ are the angles of probe and pump polarizations relative to the [100] axis. This four-fold dependence is characteristic of the T_2 phonons as expected for a crystal with T_d point group symmetry. However, this T_2 mode was found to have significant amplitude when the pump is along the cube edge. It was then realized that a surface space-charge (SSC) field in GaSb also contributes to the excitation. Therefore, the COPs in GaSb are described by a combination of TSRS and SSC excitation. A microscopic model of the optically-induced deformation of GaSb was also provided which was in complete agreement with the symmetry-based Merlin theory. The microscopic model invokes selective optical bond breaking by polarized light and demonstrates how the optical excitation of phonons and phase transitions may possess non-thermal character.

Comparing the AR response of e-GST and e-GaSb shows that the 3.4 THz mode is associated with e-GST. A similar analysis, as for e-GaSb, was applied to the 3.4 THz mode of an e-GST sample. The amplitude of the COP in the AR channel demonstrated a four-fold dependence on probe polarization, which explains the T_2-like character of the transverse optical phonon, as expected for O_h point group symmetry. The COP amplitude was almost independent of, or weakly dependent on, pump polarization. It suggests that the T_2-like 3.4 THz mode in e-GST is initiated by a SSC mechanism either in GST itself, if the distorted rocksalt structure lacks inversion symmetry,or in the GaSb. The observation of a T_2-like mode in e-GST provides confirmation that the underlying structure is cubic. This work questions the interpretation of previous studies where the 3.4 THz mode was assigned to a 1D or 2D mode.

The time-resolved measurements performed on the p/a-GST samples demonstrated the presence of a 4.5 THz mode in R and AR channels. Comparing the frequency of our measurements with the literature, it was realized that the 4.5 THz frequency could be associated with either the A_1 mode of Te-Te chains or an A_{1g} mode of a Sb_2Te_3 sub-unit in which there is symmetric vibration of Sb and Te layer along the c-axis. It is important to note that the amplitude of 3.4 THz phonons in e-GST was almost 10 times larger than the amplitude of the 4.5 THz phonon in p/a-GST. A weak 4.5 THz phonon was also observed in the R channel of e-GST, which could again reflect A or E-like behaviour, as observed in p/a-GST. Additional Raman measurements confirmed the presence of the pump-probe frequencies in all samples, as well as other modes that were not seen in the pump-probe experiments performed on p/a-GST samples.

The phonon modes in the AR response of e-GST and e-GaSb were superimposed on a multi-exponential background. The initial peak, phonons and exponential background were fitted by a phenomenological fitting function, which contains one Gaussian function, a series of Gaussian error functions and oscillatory terms. The fitting parameters yield various relaxation times that can be ascribed to the interaction of the different populations of electron and phonons. Unlike e-GST and e-GaSb, the background for p/a-GST was observed to be relatively simple in both the pump-probe and the Raman experiments.

Finally, the longer time scale AR response exhibits a slow relaxation background in e-GST and e-GaSb samples, which was referred to as the "tail". The tail on the ns scale was generated by the SSC field, which generates a lateral stress in the lattice and that leads to a

long-lived transient AR response. The tail is observed when the probe electric field lies parallel to a <100> axis. The generation of the SSC field is independent of the pump polarization, while the amplitude of the tail has a $\cos 2\theta$ dependence on the probe polarization.

The samples were also exposed to high pump fluence and the same spot was then measured by a low-fluence rescan. The results showed that the old modes in all four samples disappeared and new modes at 4.2 and 3.1 THz in e-GaSb, 4.2 THz in e-GST, 3.5 THz in p-GTS and 3.6 THz in a-GST were observed. The observed frequencies suggest segregation of Sb, while increased disorder in the e-GaSb and e-GST leads to the disappearance of the T_2 and T_2-like modes from the AR signal. The difference in the frequencies for p/a-GST may arise from the difference in the sample stack and temperature profile within the GST.

The optical investigation of phase-change switching by the application of amplified fs pulses was presented in chapter 6. The GST sample was 20 nm thick and sandwiched between a 30 nm $ZnS:SiO_2$ capping layer and a 310 nm $ZnS:SiO_2$ underlayer. Crystallization marks were made in an amorphous GST film by varying the number of pulses and their fluence. We observed that a single pulse of fs duration could not crystallize the film. When the fluence of a single fs pulse was increased to greater than or equal to 17.5 mJ/cm^2, it led to permanent damage of the amorphous GST film. We also conducted measurements with increasing number of pulses and different fluences to study the crystallization process. It was observed that a minimum of 200 pulses was required to induce crystallization with a fluence less than the damage threshold. For smaller fluences the marks were elliptical in shape, but then changed to an annular shape as the fluence was increased. The annular shape was observed because the peak fluence exceeded the melt threshold and therefore melted the center of the mark region. The dependence of the crystalline mark area upon the fluence for a fixed number of pulses was described using a simple algebraic model. This model justifies the assumption that heat flows in a vertical dimension. The annular crystalline regions were observed to close again with increasing number of pulses for a fixed fluence. A detailed theoretical model, which considered the thermal transport and crystallization kinetics, was also presented to explain the experimental results. The simulations from the theoretical model were in good agreement with the experimental results. The closure of crystalline annular rings with successive laser

pulses provides a useful method for estimating the growth velocity of phase-change materials at high temperatures. In our experiments the growth velocity was calculated to be 7-9 m/s.

The alignment and testing of the pump-probe set up using a white-light probe was presented in chapter 7. The set up was designed to have two probe pulses. One is reflected from the sample to probe its dynamics after pump pulse excitation, and the other is reflected from a reference sample. Since the pump and probe beams are originating from the same source, any fluctuations in the pump power will also affect the probe beam reflected from the reference. By comparing these two reflected probe beams, intensity noise can be removed from the signal obtained from the unkown sample. So far only the probe beam part of the experiment has been tested. The reflectance spectrum of the sample was achieved by passing the probe beams through a spectrometer, which then directed them onto the top and bottom half of a CCD chip. The set-up functionality was tested using a silver mirror as a reference. The ratio of the reflectance spectrum of a gold sample to the reference was in good agreement with the manufacturer's data and the reflection coefficients calculated using the value of refractive index and extinction coefficient for an s-polarized probe. The ratio of the reflectance spectrum of the GST sample and the Ag reference was also measured from the experiment. The response of the GST film appear to be submerged within a spectrum characteristic of the white-light pulse and hence this measurement remains inconclusive. A peak in the spectrum is probably an artefact resulting from imperfect normalization and can be corrected by changing the steering of the two beams going into the spectrometer. The system can now be extended to carry out time-resolved pump probe measurements using a white-light probe beam.

The results of electrical testing on GST memory cells were described in chapter 8. Switching of the cells was achieved using a DC voltage from 4.5 to 6 V. An attempt was made to record the response of the cells in pulsed measurements. Although the time-dependent response was not measured due to the impedance mismatch between the different electrical components, we were able to switch the devices using a minimum pulse duration of 100 ns duration. While the use of a 50 Ω oscilloscope shunts an external load resistance, the use of 1 MΩ oscilloscope probe led to reflections between the scope and the external resistor. An active voltage probe and 10x standard probe were also used to check

the response but proved not to be useful. Either more exotic probes or a more advanced impedance matching network are required to record the device response during the pulse.

9.2 Future work

Many experimental techniques and samples were studied during this PhD and a rich variety of data has been presented in this thesis. This section is focused on the details of possible future work which may require either the use of an existing technique described in this thesis to make further measurements or the implementation of new techniques.

9.2.1 Time-resolved pump-probe measurements on an e-GST(111) surface

9.2.1.1 e-GST(111) study

The structure of GST material has been a topic of debate for over several years now. In chapter 4, application of Merlin's theory to the interpretation of our experimental results for an e-GST(001)/GaSb(001) sample indicates that the underlying structure is cubic. The ISRS described by Merlin and SSC proposed by Cho et al. explain the origin of T_2 phonons in GST with displacements along the z axis.

A suggestion for future work could be a time-resolved pump probe study on e-GST(111) film. The calculation of Raman-active modes in e-GST(111) is provided in appendix 2, according to which the three-dimensional T_2 mode with its displacement along all three axes should be observed in both R and AR channels.

9.2.1.2 Using lower fluence for phonon detection in the reflectivity channel

According to the studies presented in chapter 4, weak phonons of 4.5 THz frequency were observed in the reflectivity channel of the e-GST sample. Comparing our reflectivity signal with the literature, it was realized that the fluence applied in our studies was much higher (mJ/cm^2 vs $\mu J/cm^2$). This may in turn induce the huge background in the transient reflectivity channel while the phonon response may become saturated. The study of GST films at lower fluence in future may help increased the amplitude of the phonons relative to the background and the experimental noise. Two-colour studies of GST samples may also provide useful information.

9.2.2 Extension of the white-light probe set up

In chapter 7, the pump-probe measurement set up using a white-light probe was established using materials with well-known reflectance spectra. As suggested in that chapter, the experiments can now be taken one step further by introducing a time-resolved pump beam to extract the dynamics of the sample with a white-light probe.

9.2.3 Electrical testing using an impedance matching network

In chapter 8, the electrical switching of GST cells using a DC set up, and by applying pulses of minimum 100 ns duration was achieved. The use of a more advanced impedance matching network may be required to record the device current during the presence of the pulse. The eventual aim of this strand of work is to perform time-resolved electro-optical measurements. For example, it would then be possible to observe the effect of optical assistance upon threshold switching.

Appendix 1

Fitting the time-resolved reflectance and anisotropic reflectance data

We used the following formula to fit the AR signals obtained from the GST and GaSb films,

$$S \propto A\exp\left(-\frac{(t-t_0)^2}{4w^2}\right) + \frac{B}{2}\exp\left(\frac{w^2}{\tau^2}-\frac{t-t_0}{\tau}\right)\left[1-\operatorname{erf}\left(\frac{w}{\tau}-\frac{t-t_0}{2w}\right)\right] + \frac{C}{2}\exp\left(-\frac{t-t_0}{\tau}\right)\left[1-\operatorname{erf}\left(-\frac{t-t_0}{2w}\right)\cos[\omega(t-t_0)+2\pi\beta(t-t_0)^2+\phi]\right].$$

----------(A.1)

Derivation

The pulse intensity for a Gaussian pump/probe pulse can be written as:

$$I(t) \propto \frac{1}{\sqrt{2\pi}w}\exp\left(-\frac{t^2}{2w^2}\right),$$

----------(A.2)

where w is the rms pulse width.

The rotation of a probe beam as a function of time delay is calculated as the convolution of two Gaussian pump and probe beams. Therefore the signal is proportional to

$$\frac{1}{\sqrt{2\pi}}\int_{-\infty}^{\infty}\exp\left(-\frac{t^2}{2w^2}\right)\exp\left(-\frac{(t'-t)^2}{2w^2}\right)dt,$$

$$=\frac{1}{\sqrt{2\pi}}\int_{-\infty}^{\infty}\exp\left\{-\frac{1}{2w^2}\left(t'^2-2tt'+2t^2\right)\right\}dt,$$

$$=\frac{1}{\sqrt{2\pi}}\int_{-\infty}^{\infty}\exp\left\{-\frac{1}{w^2}\left(\frac{t'}{2}-t\right)^2-\frac{t'^2}{4w^2}\right\}dt,$$

$$=\frac{1}{\sqrt{2\pi}}\exp\left(-\frac{t'^2}{4w^2}\right)\int_{-\infty}^{\infty}\exp\left\{-\frac{1}{w^2}\left(t-\frac{t'}{2}\right)^2\right\}dt,$$

$$=\exp\left(-\frac{t'^2}{4w^2}\right).$$

----------(A.3)

which has the same form as the first term in the fitting formula.

The total signal measured for a time delay t_d is

$$S=\int_{-\infty}^{\infty}S(t)\exp\left\{-\frac{(t-t_d)^2}{2w^2}\right\}dt,$$

----------(A.4)

where $S(t)$ is the total signal at time t. It can be written as

$$S(t)=\int_{-\infty}^{\infty}\exp\left\{-\frac{{t_0}^2}{2w^2}\right\}h(t-t_0)\exp\left(-\frac{t-t_0}{\tau}\right)dt_0,$$

----------(A.5)

where t_d is the zero time delay and $h(t-t_0)$ is the step function defined as

$$h(t-t_0)=\left.\begin{matrix}0, & t_0 > t\\ 1, & t_0 < t\end{matrix}\right\},$$

----------(A.6)

Combining equations (A.4), (A.5) and (A.6), the total signal is

$$S=\int_{-\infty}^{\infty}\int_{-\infty}^{\infty}\exp\left\{-\frac{{t_0}^2}{2w^2}\right\}h(t-t_0)\exp\left(-\frac{t-t_0}{t}\right)dt_0\exp\left\{-\frac{(t-t_d)^2}{2w^2}\right\}dt,$$

$$S=\int_{-\infty}^{\infty}\int_{-\infty}^{t}\exp\left[-\left\{\frac{t^2+t_d^2-2tt_d+t_0^2}{2w}+\frac{t-t_0}{t}\right\}\right]dt_0dt.$$

----------(A.7)

Let us define another variable time $t'=t_0-t$, therefore

$$t_0=t'+t \text{ and } t_0^2=t'^2+t^2+2tt',$$

----------(A.8)

The signal in equation (A.7) becomes,

$$S=\int_{-\infty}^{\infty}\int_{-\infty}^{0}\exp\left[-\left\{\frac{2t^2+t'^2-2tt_d+2tt'+t_d^2}{2w}-\frac{t'}{t}\right\}\right]dt'dt.$$

----------(A.9)

Reversing the order of integration,

$$S=\int_{-\infty}^{\infty}\int_{-\infty}^{\infty}\exp\left[-\left\{\frac{\left\{t-\left(\frac{t_d-t'}{2}\right)\right\}^2-\left(\frac{t_d-t'}{2}\right)^2+\frac{t'^2+{t_d}^2}{2}}{w}-\frac{t'}{t}\right\}\right]dtdt',$$

$$S = \int_{-\infty}^{0} \exp\left[-\left\{ \frac{t'^2}{4} + \frac{t_d t'}{2} + \frac{t_d{}^2}{4} \right\} + \frac{t'}{t} \right] dt' \int_{-\infty}^{\infty} \exp\left[-\frac{\left\{ t - \left(\frac{t_d - t'}{2} \right) \right\}^2}{w} \right] dt,$$

$$S \propto \int_{-\infty}^{0} \exp\left[-\frac{(t'+t_d)^2}{4w} + \frac{t'}{t} \right] dt'.$$

----------(A.10)

To simplify the integration, let us define $t'' = t' + t_d$.

The signal in equation (A.10) becomes,

$$S \propto \int_{-\infty}^{t_d} \exp\left[-\frac{t''^2}{4w} + \frac{t''-t_d}{t} \right] dt'',$$

$$S \propto \exp\left(-\frac{t_d}{t} \right) \int_{-\infty}^{t_d} \exp\left[-\left\{ \frac{t''}{2w} - \frac{w}{t} \right\}^2 + \frac{w^2}{t^2} \right] dt'',$$

----------(A.11)

Again, define $t''' = \frac{t''}{2w} - \frac{w}{t}$ and $dt'' = 2w\,dt'''$,

$$S \propto \exp\left(\frac{w^2}{t^2} - \frac{t_d}{t} \right) \int_{-\infty}^{\left(\frac{t_d}{2w} - \frac{w}{t} \right)} \exp\left[-t'''^2 \right] 2w\,dt''',$$

$$S \propto \exp\left(\frac{w^2}{t^2} - \frac{t_d}{t} \right) \int_{\left(\frac{w}{t} - \frac{t_d}{2w} \right)}^{\infty} \exp\left[-x^2 \right] dx,$$

$$S \propto \exp\left(\frac{w^2}{t^2} - \frac{t_d}{t} \right) \left[1 - erf\left(\frac{w}{t} - \frac{t_d}{2w} \right) \right],$$

$$S \propto \exp\left(\frac{w^2}{t^2} - \frac{t-t_0}{t}\right)\left[1 - erf\left(\frac{w}{t} - \frac{t-t_0}{2w}\right)\right].$$

----------(A.12)

Equations (A.1) and (A.12) are the first two terms used within the fitting formula (A.1). The last oscillatory term is considered to be phenomenological and is not rigorously derived.

Appendix 2

Mode Calculations for epitaxial $Ge_2Sb_2Te_5$(111) surface

If an epitaxial $Ge_2Sb_2Te_5$ sample is grown with a (111) crystal orientation, then $[1\bar{1}0]$ and $[11\bar{2}]$ are mutually orthogonal in-plane axes. Let the z-axis lie along [111] and the x and y axes lie parallel to the $[1\bar{1}0]$ and $[11\bar{2}]$ directions respectively, as shown in fig (A.1).

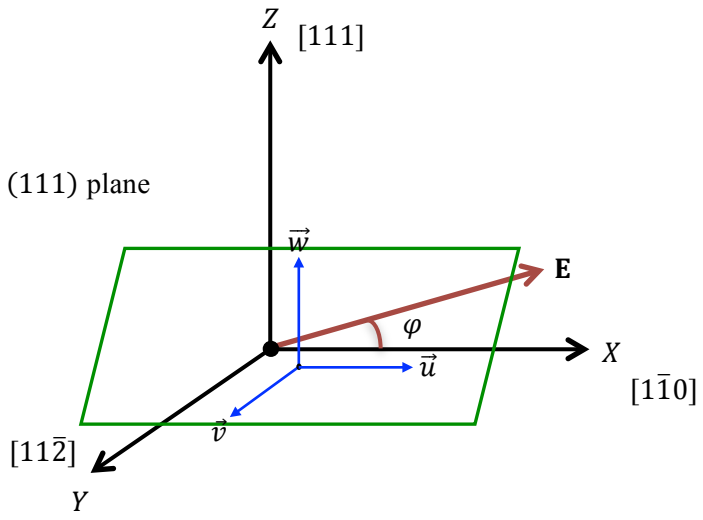

Figure A.1: Crystal directions for an epitaxial GST(111) sample. **E** represents the pump electric field in the (111) plane at an angle φ to the x-axis.

If a pump beam is applied with electric field in the (111) plane at an angle of φ from the x-axis, then a unit vector parallel to the pump electric field is

$$\vec{E} = \cos\varphi\ \hat{u} + \sin\varphi\ \hat{v}\ ,$$

where the unit vectors are

$$\hat{u} = \tfrac{1}{\sqrt{2}}(1\ \bar{1}\ 0) \text{ and } \hat{v} = \tfrac{1}{\sqrt{6}}(1\ 1\ \bar{2})\ ,$$

Therefore, the applied electric field can be written as:

$$\vec{E} = \cos\varphi\ \hat{u} + \sin\varphi\ \hat{v}$$

$$\vec{E} = \cos\varphi\ \frac{1}{\sqrt{2}}(1\ \bar{1}\ 0) + \sin\varphi\ \frac{1}{\sqrt{6}}(1\ 1\ \bar{2})$$

$$\vec{E} = \left(\frac{1}{\sqrt{2}}\cos\varphi + \frac{1}{\sqrt{6}}\sin\varphi\ , -\frac{1}{\sqrt{2}}\cos\varphi + \frac{1}{\sqrt{6}}\sin\varphi\ , -\frac{2}{\sqrt{6}}\sin\varphi\right)$$

----------(A.13)

The reflectivity and anisotropic reflectivity signals are calculated for various crystal-growth orientations by using the respective Raman tensors. The table (A.1) shows a summary of mode calculations, indicating that the T_2 mode is observable in both channels for a rocksalt or zincblende structure of (111) orientation.

Mode	Raman Tensor	(100)		(110)		(111)	
		Reflection	Rotation	Reflection	Rotation	Reflection	Rotation
A	$\begin{bmatrix} a & & \\ & a & \\ & & a \end{bmatrix}$	✓	✗	✓	✗	✓	✗
E_x	$\begin{bmatrix} b & & \\ & b & \\ & & b \end{bmatrix}$	✓	✗	✓	✗	✓	✗
E_y	$\begin{bmatrix} b & & \\ & b & \\ & & b \end{bmatrix}$	✓	✗	✓	✗	✓	✗
T_x	$\begin{bmatrix} & & d \\ & d & \end{bmatrix}$	✗	✗	✗	✓	✓	✓
T_y	$\begin{bmatrix} & & d \\ d & & \end{bmatrix}$	✗	✗	✗	✓	✓	✓
T_z	$\begin{bmatrix} & d & \\ d & & \end{bmatrix}$	✗	✓	✓	✓	✓	✓

Table A.1: Observability of phonon modes for various orientations of crystals of T_d (and O_h) point group symmetry

Bibliography

[1] T. H. Maiman, Nature **187**, 493 (1960).

[2] I. S. Ruddock and D. J. Bradley, Appl. Phys. Lett. **29**, 296 (1976).

[3] D. H. Sutter, G. Steinmeyer, L. Gallmann, N. Matuschek, F. Morier-Genoud, U. Keller, V. Scheuer, G. Angelow, and T. Tschudi, Opt. Lett. **24**, 631 (1999).

[4] J. Shah, "Ultrafast Spectroscopy of Semiconductors and Semiconductor Nanostructures", Springer Verlag, Berlin (1996).

[5] A. H. Zewail, "Femtochemistry: Ultrafast Dynamics of the Chemical Bond", World Scientific, Singapore (1994).

[6] M. Kandyla "Ultrafast dynamics of the laser-induced solid-to-liquid phase transition in aluminum", PhD thesis, Harvard university (2006).

[7] J. P. Callan, "Ultrafast Dynamics and Phase Changes in Solids Excited by Femtosecond Laser Pulses", PhD thesis, Harvard university (2000).

[8] J. A. Kash, J. C. Tsang and J. M. Hvam, Phys. Rev. Lett. **54**, 2151 (1985).

[9] Qin F. Wang, Lu P. Shi, Su M. Huang, Xiang S. Miao, Kai P. Wong and Tow C. Chong, Jpn. J. Appl. Phys. **43**, 5006 (2004).

[10] N. M. Bulgakova, I M. Burakov, Y. P. Meshchryakov, R. Stolan, A. Rosenfeld and I. V. Hertel, Journal of Laser Micro/Nanoengineering **2**, 1, 2007.

[11] C. V. Shank, R. Yen and C. Hirlimann, Phys. Rev. Lett. **50**, 454 (1983).

[12] H. W. K. Tom, G. D. Aumiller and C. H. Brito-Cruz, Phys. Rev. Lett. **60**, 1438 (1988).

[13] K. Sokolowski-Tinten, J. Bialkowski and D. von der Linde, Phys. Rev. B **51**, 14186 (1995).

[14] S. V. Govorkov, T. Schröder, I. L. Shumay and P. Heist, Phys. Rev. B **46**, 6864 (1992).

[15] P. Saeta, J. K. Wang, Y. Siegal, N. Bloembergen and E. Mazur, Phys. Rev. Lett. **67**, 1023 (1991).

[16] I. L. Shumay and U. Höfer, Phys. Rev. B **53**, 15 878 (1996).

[17] C. Guo, G. Rodriguez, A. Lobad and A. J. Taylor, Phys. Rev. Lett. **84**, 4493 (2000).

[18] D. H. Reitze, H. Ahn and M. C. Downer, Phys. Rev. B **45**, 2677 (1992).

[19] J. Hernandez-Rueda, A. Savoia, W. Gawelda, J. Solis, B. Mansart, D. Boschetto, and J. Siegel, Appl. Phys. Lett. **98**, 251906 (2011).

[20] G. Zhang, D. Gu, X. Jiang, Q. Chen and F Gan, Solid State Commun. **133**, 209 (2005)

[21] T. Ohta, M. Birukawa, N. Yamada and K Hirao, J. Magn. Magn. Mater. **242,** 108, (2002).

[22] S. M. Wiggins, J. Solis, and C. N. Afonso, Appl. Phys. Lett. **84**, 4445 (2004).

[23] S. K. Sundaram and E. Mazur, Nat. Mater. **1**, 217 (2002).

[24] J. Solis, C. N. Afonso, S. C. W. Hyde, N. P. Barry and P. M. W. French, Phys. Rev. Lett. **76**, 2519 (1996).

[25] R. Merlin, Solid State Commun. **102**, 207 (1997).

[26] G. P Srivastava, "The physics of phonons", Taylor & Francis group, NewYork (1990).

[27] P. Y. Yu and M. Cardona, "Fundamentals of semiconductors", Springer (2010).

[28] G. P. Srivastava, unpublished.

[29] W. Hayes and R. Loudon, "Scattering of Light by Crystals", Dover publications, Inc. NewYork (2004).

[30] P. A. Franken, A. E. Hill, C. W. Peters, and G. Weinreich, Phys. Rev. Lett. **7**, 118 (1961).

[31] R. J. Elliott and A. F. Gibson, "Solid state physics", The Mcmillan Press Ltd, NewYork (1974).

[32] D. A. Kleinman, Phys. Rev. **126**, 1977 (1962)

[33] G. E. H. Reuter and E. H. Sondheimer, Proc. Roy. Soc. London Series A, **195**, 336, 1948.

[34] F. D. Longa, J.T. Kohlhepp, W.J.M. de Jonge, and B. Koopmans, Phys. Rev. B **75**, 224431 (2007)

[35] S. V. Popov, Y. P. Svirko, and N.I. Zheludev, J. Opt. Soc. Am. B **13**, 272 (1996).

[36] R Wilks, N D Hughes and R J Hicken, J. Phys. Condens. Matter **15**, 5129 (2003).

[37] R Wilks and R J Hicken, J. Phys. Condens. Matter **16**, 4607 (2004).

[38] T. C. Damen, S. P. S. Porto and B Tell, Phys. Rev., **142**, 570 (1966).

[39] M. Wuttig and N. Yamada, Nature Mater. **6**, 824, (2007).

[40] M. H. R Lankhorst, B. W. S. M. Ketelaars, and R. A. M. Wolters, Nature Mater. **4**, 347, (2005).

[41] C. D. Wright, Y. Liu, K. I. Kohary, M. M. Aziz, and R. J. Hicken, Adv. Mater. **23**, 3408 (2011).

[42] C. D. Wright, O. Hosseini, and J. A. Vazquez Diosdado, Adv. Funct. Mater. **23**, 2248 (2013).

[43] S. R. Ovshinsky, Phys. Rev. Lett. **21**, 1450 (1968).

[44] M. Wuttig, Nature Mater. **4**, 265 (2005).

[45] N. Yamada, E. Ohno, K. Nishiuchi and N. Akahira, J. Appl. Phys. **69**, 2849 (1991).

[46] J. H. Coombs, A. P. J. M. Jongenelis, W. van Es-Spikeman and B. A. J. Jacobs, J. Appl. Phys. **78**, 4918 (1995).

[47] J. F. Gibbons and W. E. Beadle, Solid State Electron. **7**, 785 (1964).

[48] J. G. Simmons and A. El-Badry, Solid State Electron. **20**, 955 (1977).

[49] F. Argall, Solid State Electron. **11**, 535 (1968).

[50] A. Pirovano, A. L. Lacaita, A. Benvenuti, F. Pellizzer and R. Bez, IEEE Transactions on electronic devices, **51**, 3, (2004)

[51] I. Friedrich, V. Weidenhof, W. Njoroge, P. Franz, M. Wuttig, J. Appl. Phys. **87**, 4130 (2000)

[52] W. K. Njoroge, H. Woltgens and M. Wuttig, J. Vac. Sci. Technol. A **20**, 230 (2002)

[53] M. Wuttig, D. Lusebrink, D. Wamwangi, W. Welnic, M. Gilleben and R. Dronskowski, Nature Mater. **6**, 122 (2007).

[54] A. V. Kolobov, P. Fons, A. I. Frenkel, A. L. Ankudinov, J. Tominaga and T. Uruga, Nature Mater. **3**, 703 (2004).

[55] J. K. Olson, H. Li, and P. C. Taylor, J. Ovonics Res. **1**, 1 (2005)

[56] D. A. Baker, M. A. Paesler, G. Lucovsky, S. C. Agarwal and P. C. Taylor, Phys. Rev. Lett. **96**, 255501 (2006)

[57] D. Lencer, M. Salinga and M. Wuttig, Adv Mat. **23**, 2030 (2011)

[58] J. Hegedüs & S. R. Elliott, Nat. Materials **7**, 399 (2008).

[59] L. Huang, P. Callan, E. N. Glezer, and E. Mazur, Phys. Rev. Lett. **80**, 185, (1998).

[60] C. W. Siders, A. Cavalleri, K. Sokolowski-Tinten, C. Toth, T. Guo, M. Kammler, M. H. von Hoegen, K. R. Wilson, D. von der Linde, and C. P. J. Barty, Science **286**, 1340, (1999).

[61] A. Rousse, C. Rischel, S. Fourmaux, I. Uschmann, S. Sebban, G. Grillon, P. Balcou, E. Foster, J. P. Geindre, P. Audebert, J. C. Gauthier, and D. Hulin, Nature, **410**, 65, (2001).

[62] J. W. Graham, "Arbitrarily oriented biaxially anisotropic media: wave behaviour and microstrip antennas", PhD thesis, Syracuse university (2012).

[63] M. Born and E. Wolf, "Principles of Optics: Electromagnetic Theory of Propagation, Interference and Diffraction of Light", Cambridge University Press (1999).

[64] J. Lekner, J. Phys.: Condens. Matter, **3**, 6121 (1991)

[65] B Koopmans, M van Kampen and W J M de Jonge, J. Phys.: Condens. Matter, 15, 723 (2003).

[66] R. Wilks, PhD Thesis, University of Exeter (2002).

[67] A. V. Kimel, F. Bentivegna, V. N. Gridnev, V. V. Pavlov, R. V. Pisarev, T. Rasing, Phys. Rev. B **63**, 235201 (2001).

[68] M. Först, T. Dekorsy, C. Trappe, M. Laurenzis, H. Kurz, and B. Béchevet, Appl. Phys. Lett. **77**, 1964 (2000).

[69] M. Hase, Y. Miyamoto, and J. Tominaga, Phys. Rev. B **79**, 174112 (2009).

[70] Y. Li, V. A. Stoica, L. Endicott, G. Wang, C. Uher, and R. Clarke, Appl. Phys. Lett. **97**, 171908 (2010).

[71] K. Makino, J. Tominaga, and M. Hase, Opt. Express, **19**, 1260 (2011).

[72] W. Braun, R. Shayduk, T. Flissikowski, M. Ramsteiner, H. T. Grahn, H. Riechert, P. Fons and A. Kolobov, Appl. Phys. Lett. **94**, 041902 (2009).

[73] T. Dekorsy, G. C. Cho, and H. Kurz, Topics in Appl. Phys. **76**, 169 (2000).

[74] G. C. Cho, W. Kütt, and H. Kurz, Phys. Rev. Lett. **65**, 764 (1990).

[75] J. Qi, X. Chen, W. Yu, P. Cadden-Zimansky, D. Smirnov, N. H. Tolk, I. Miotkowski, H. Cao, Y. P. Chen, Y. Wu, S. Qiao, and Z. Jiang, Appl. Phys. Lett. **97**, 182102 (2010).

[76] W. S. Pelouch, and L. A. Schlie, Appl. Phys. Lett. **66**, 82 (1995).

[77] O. B. Wright, U. Zammit, M. Marinelli, and V. E. Gusev, Appl. Phys. Lett. **69**, 553 (1996).

[78] A. J. Sabbah, and D. M. Riffe, Phys. Rev. B **66**, 165217 (2002).

[79] G. A. Garrett, T. F. Albrecht, J. F. Whitaker, and R. Merlin, Phys. Rev. Lett. **77**, 3661 (1996).

[80] J. K. Miller, J. Qi, Y. Xu, Y. J. Cho, X. Liu, J. K. Furdyna, I. Perakis, T. V. Shahbazyan, and N. Tolk, Phys. Rev. B **74**, 113313 (2006).

[81] T. Pfeifer, W. Kütt, H. Kurz, and R. Scholz, Phys. Rev. Lett. **69**, 3248 (1992).

[82] T. Dekorsy, T. Pfeifer, W. Kütt, and H. Kurz, Phys. Rev. B **47**, 3842 (1993).

[83] K. J. Yee, K. G. Lee, E. Oh, D. S. Kim, and Y. S. Lim, Phys. Rev. Lett. **88**, 105501 (2002).

[84] M. Cardona, Top. Appl. Phys. **50**, 19 (1982).

[85] R. Ferrini, M. Galli, G. Guizzetti, M. Patrini, A. Bosacchi, S. Franchi, and R. Magnanini, Phys. Rev. B **56**, 7549 (1997).

[86] M. K. Farr, J. G. Traylor, and S. K. Sinha, Phys. Rev. B **11**, 1587 (1975).

[87] www.luxpop.com

[88] K. Shportko, S. Kremers, M. Woda, D. Lencer, J. Robertson and M. Wuttig, Nat. Mat. **7**, 653 (2008)

[89] J. C. Decius and R. M. Hexter, "Molecular vibration in crystals", McGraw-Hill, (1970).

[90] V. Heine, "Group theory in quantum mechanics", Pergamon Press, (1960).

[91] Y. Liu, M. M. Aziz, A. Shalini, C. D. Wright and R. J. Hicken, J. Appl. Phys. **112**, 123526 (2012).

[92] J. Siegel, W. Gawelda, D. Puerto, C. Dorronsoro, J. Solis, C. N. Afonso, J. C. G. de Sande, R. Bez, A. Pirovano, and C. Wiemer, J. Appl. Phys. **103**, 023516 (2008).

[93] R. L. Colton and J. Siegel, J. Appl. Phys. **112**, 123520 (2012).

[94] K. Ishioka, M. Kitajima, and O. V. Misochko, J. Appl. Phys. **103**, 123505 (2008).

[95] S. Barman and G. P. Srivastava, Phys. Rev. B **69**, 235208 (2004)

[96] V V Kruglyak, R J Hicken, M Ali, B J Hickey, A T G Pym, B K Tanner, Phys. Rev. B **71**, 233104, 2005.

[97] G. C. Sosso, S. Caravati, R. Mazzarello and M. Bernasconi, Phys. Rev. B **83**, 134201 (2011).

[98] P. Nemec, V. Nazabal, A. Moreac, J. Gutwirth, L. Benes and M. Frumar, Materials Chemistry and Physics **136**, 935 (2012).

[99] S. Raoux and M. Wuttig, "Phase Change Materials: Science and Applications" Springer (2008).

[100] N. Yamada, and T. Matsunaga, J. Appl. Phys. **88**, 7020 (2000).

[101] V. Weidenhof, I. Friedrich, S. Ziegler, and M. Wuttig, J. Appl. Phys. **89**, 3168 (2001).

[102] J. Siegel, A. Schropp, J. Solis, C. N. Afonso, and M. Wuttig, Appl. Phys. Lett. **84**, 2250 (2004).

[103] C. H. Chu, C. D. Shiue, H. W. Cheng, M. L. Tseng, H. P. Chiang, M. Mansuripur, and D. P. Tsai, Optics Express **18**, 18383 (2010).

[104] S. M. Huang, Z. Sun, C. X. Jin, S. Y. Huang, and Y. W. Chen, Trans. Nonferrous Met. Soc. China **18**, s226 (2006).

[105] K. Sokolowski-Tinten, J. Solis, J. Bialkowski, J. Siegel, C. N. Afonso, and D. von der Linde, Phys. Rev. Lett. **81**, 3679 (1998).

[106] B. S. Lee, G. W. Burr, R. M. Shelby, S. Raoux, C. T. Rettner, S. N. Bogle, K. Darmawikarta, S. G. Bishop, and J. R. Abelson, Science **326**, 980 (2009).

[107] G. Zhang, F. Gan, S. Lysenko, and H. Liu, J. Appl. Phys. **101**, 033127 (2007).

[108] J. Kalb, F. Spaepen, and M. Wuttig, J. Appl. Phys. **93**, 2389 (2003).

[109] N. Ohshima, J. Appl. Phys. **79**, 8357 (1996).

[110] K. Zhang, S. Li, G. Liang, H. Huang, Y. Wang, T. Lai, and Y. Wua, Physica B **407**, 2447 (2012).

[111] G. M. Fischer, B. Medower, R. Revay, and M. Mansuripur, Appl. Opt. **41**, 1998 (2002).

[112] H. Huang, F. Zuo, F. Zhai, Y. Wang, T. Lai, Y. Wu, and F. Gan, J. Appl. Phys. **106**, 063501 (2009).

[113] H. Cheng, S. Raoux, and Y. Chen, J. Appl. Phys. **107**, 074308 (2010).

[114] E. R. Meinders, A. V. Mijiritskii, L. van Pieterson, and M. Wuttig, "Optical Data Storage: Phase-change media and recording", Springer (2006).

[115] Operator's manual, The Coherent Model 9800/9850, Optical Parametric Amplifier (OPA).

[116] D. R. Lide, "Handbook of Chemistry and Physics", CRC, 2006.

[117] F. L. Pedrotti and L. S. Pedrotti, "Introduction to Optics", Prentice Hall

International, Inc., 1996.

[118] S. Lai and T. Lowrey, International Electron Devices Meeting Technical Digest, **36** (2001).

[119] D. M. Pozar, “Microwave Engineering”, John Wiley & Sons, Inc, 1998.

[120] G. Bruns, “Electronic switching in phase-change materials”, PhD thesis, RWTH Aachen University, 2012.